Application of Disposable Chiral Plasmonics for Biosensing and Raman Spectroscopy

Martin Kartau

Submitted in fulfilment of the requirements for the Degree of Doctor of Philosophy

School of Chemistry

College of Science and Engineering

University of Glasgow

September 2023

Abstract

This thesis explores the capabilities of disposable chiral plasmonic metafilm assays, termed Disposable Plasmonic Assays, as a promising platform for biosensing and surface-enhanced Raman spectroscopy. The sensing and Raman properties of these metafilms arise from the excitation of surface plasmons when exposed to incident light. These plasmonic properties strongly depend on the geometric characteristics of the constituent nanostructures found in the metafilms. Specifically, the primary nanostructure employed throughout this research is the chiral 'shuriken' star, which generates chiral electromagnetic fields exhibiting greater chiral asymmetry than circularly polarized light.

Monitoring changes in the resonance positions of the characteristic optical rotatory dispersion spectra produced by the Disposable Plasmonic Assays allows for the observation of surface binding events. By measuring resonance shift data and through the utilisation of various gold film functionalisation techniques, these assays are demonstrated as versatile, label-free biosensing platforms capable of specifically detecting a wide range of target proteins and virus particles from complex solutions. Furthermore, the multiplexing performance of these assays is showcased, enabling the detection of multiple different antigens and virions in a single experiment. These results highlight the potential of plasmonic metafilms as rapid and disposable point-of-care immunoassays for diagnostic applications.

In addition to biosensing, the chiral geometry of Disposable Plasmonic Assays is exploited for the chiral discrimination of metal nanoparticles and small molecules using Surface Enhanced Raman Spectroscopy (SERS). By linking helicoid shaped gold nanoparticles to the metafilm surface via a dithiol linker, the chiral properties of both nanoparticles and metafilms combine, resulting in the creation of differential electromagnetic 'hotspot' regions based on their symmetry combinations. The electromagnetic intensity in these regions corresponds to the SERS signal obtained from the achiral dithiol linker molecule, facilitating a deeper understanding of the chirally dependent SERS phenomenon. These findings serve to validate and explain the differential SERS data obtained enantiomers of biomolecules and drug molecules from silver modified Disposable Plasmonic Assays.

Table of Contents

Contents

Acknowledgements

There are a great number of people that I wish to acknowledge and thank for their support throughout my PhD journey. Naturally, the largest portion of my appreciation with regards to this work must be handed to my PhD supervisor Dr. Affar Karimullah. He is one of the most knowledgeable men that I know, and his help has been invaluable for everything presented here. If I could become a researcher who is a fraction as skilled as he is, I would hold myself proud. Dr. Karimullah was always ready to help with any problems I had, of which there were many, and he would often go above and beyond his responsibilities. I would also like to thank my secondary supervisor, Professor Malcolm Kadodwala, for his expertise and feedback. Without him, the feat of having my publications submitted would have been a much greater struggle.

In addition, much of this work would not be possible without the help from collaborators at the University of Chemistry and Technology Prague (UCTP), who I had the great pleasure of visiting as part of a Saltire Research Exchange Programme. In particular, I would like to acknowledge Dr. Olga Guselnikova and Anastasia Skvortsova for their collaboration, and for teaching me about surface enhanced Raman Spectroscopy.

One of my greatest supporters has always been my wonderful partner in life Zoe. Without her support and photography skills this journey would have been infinitely more difficult. For every hardship I encountered she was always there to comfort me, and my written words alone cannot express the immense feelings of gratitude I hold for her.

I would also like to thank my friends and family. My mother and father for raising me to always be curious and supporting me in everything I chose and choose to do. My biases aside, I believe them to be the best parents I could have hoped for. My brother must also be commended, for it is his exceptional skills in mathematics and statistics which aided me with any queries I had on such matters.

Finally, I give thanks to all the wonderful people based at the University of Glasgow and my colleagues and peers of which there are too many to name.

Thesis Contributions

Some of the work presented in this thesis was performed in collaboration with others. The details of collaboration are listed below:

- Isolation of SARS-CoV-2 virus particles was performed at the Centre for Virus Research at the University of Glasgow.
- Synthesis of gold helicoid nanoparticles was performed by Polina Bainova at the University of Chemistry and Technology Prague.
- Zika virus antibodies were provided by Dr. Arvind Patel from the Centre for Virus Research at the University of Glasgow.
- Silver coating and SERS optimisation of DPA samples was performed by Dr. Olga Guselnikova at the University of Chemistry and Technology Prague.
- AFM measurements of DPA shurikens before and after silver deposition were performed by Dr. Oleksiy Lyutakov at the University of Chemistry and Technology Prague.
- SERS measurements of cysteine, methionine, thalidomide, and DNA molecules on DPA samples were performed by Dr. Olga Guselnikova at the University of Chemistry and Technology Prague.
- SEM images, EDX, and XRD measurements of cysteine-coated silver DPA samples were performed by Dr. R. Elashnikov at the University of Chemistry and Technology Prague.
- SERS mapping measurements were performed by Dr. Olga Guselnikova at the University of Chemistry and Technology Prague.
- Gold nanorod simulations were performed by Dr. Cameron Gilroy at the University of Glasgow.

Author's Declaration

I declare that, except where explicit reference is made to the contribution of others, that this dissertation is the result of my own work and has not been submitted for any other degree at the University of Glasgow or any other institution.

Printed Name: MARTIN KARTAU

Signature: _____

Published Work

Kartau, M., Skvortsova, A., Tabouillot, V., Chaubey, S.K., Bainova, P., Kumar, R., Burtsev, V., Svorcik, V., Gadegaard, N., Im, S.W., Urbanova, M., Lyutakov O., Kadodwala, M., and Karimullah, A. S. *Chiral Metafilms and Surface Enhanced Raman Scattering for Enantiomeric Discrimination of Helicoid Nanoparticles.* Advanced Optical Materials, 2023. **11**(9): p. 2202991.

Guselnikova, O., Elashnikov, R., Svorcik, V., Kartau, M., Gilroy, C., Gadegaard, N., Kadodwala, M., Karimullah, A.S. and Lyutakov, O., 2023. *Coupling of plasmonic hot spots with shurikens for superchiral SERS-based enantiomer recognition*. Nanoscale Horizons, 2023. **8**(4), pp. 499-508.

Wallace, S., Kartau, M., Kakkar, T., Davis, C., Szemiel, A., Samardzhieva, I., Vijayakrishnan, S., Cole, S., De Lorenzo, G., Maillart, E., Gautier, K., Lapthorn, A. J., Patel, A. H., Gadegaard, N., Kadodwala, M., Hutchinson, E., and Karimullah, A. S. *Multiplexed Biosensing of Proteins and Virions with Disposable Plasmonic Assays*. ACS Sensors, 2023. DOI: 10.1021/acssensors.2c02238

List of Abbreviations Used

- AFM – Atomic force microscopy
- BPDT - Biphenyl-4,4’-dithiol
- CD – Circular dichroism
- CPL – Circularly polarised light
- DPA – Disposable Plasmonic Assay
- EBL – Electron beam lithography
- EDX – Energy dispersive X-ray
- EM - Electromagnetic
- FEM – Finite-element method
- Hb – Haemoglobin
- His – Histidine
- HOMO – Highest occupied molecular orbital
- HNP – Helicoid nanoparticle
- Hp – Haptoglobin
- LCP – Left circularly polarised
- LFD – Lateral-flow device
- LH – Left-handed
- LoD – Limit of detection
- LOMO – Lowest occupied molecular orbital
- LPL – Linearly polarised light
- LSPR – Localised surface plasmon resonance
- NTA – Nitrilotriacetic acid
- OR – Optical rotation
- ORD – Optical rotatory dispersion
- PCR – Polymerase chain reaction

- RCP – Right circularly polarised
- RH – Right-handed
- ROA – Raman optical activity
- SAM – Self-assembled monolayer
- SEM – Scanning electron microscopy
- SEROA – Surface enhanced Raman optical activity
- SERS – Surface enhanced Raman spectroscopy
- SPP – Surface plasmon polariton
- VLP – Virus-like particle
- XRD – X-ray diffraction

Chapter 1 – Introduction

1.1 Thesis Overview

Electromagnetic (EM) fields, commonly known as light, possess the ability to interact with matter, which forms the foundation for numerous material and molecular analysis techniques [1]. These techniques, by measuring detectable signals, have achieved remarkable levels of precision and sensitivity in the detection of biomolecules. Light-based methods, ranging from fluorescence labelling techniques to plasmonic interactions, have revolutionized the exploration of biomolecular interactions and processes, playing pivotal roles in medical diagnostics, drug discovery, and biotechnology [2-4].

The emergence of optical-based techniques and sensors offers a promising solution to address the increasing demand for improved and faster biosensors. This need has been highlighted by the recent COVID-19 pandemic, which emphasised the importance of diagnostic tests capable of effectively serving large populations [5]. Many current diagnostic biosensors often rely on multiple experimental steps, molecular labelling, and intricate analysis, resulting in prolonged turnaround times for obtaining results [6]. Although rapid diagnostic kits based on lateral flow are available, they can usually only detect a limited number of pathogens or disease markers [7].

This thesis focuses on addressing these challenges by harnessing the potential of chiral metamaterial gold film nanostructure arrays, referred to as Disposable Plasmonic Assays (DPAs). The aim is to develop a cost-effective, label-free optical biosensor with multiplexing capabilities. The chosen platform for DPAs consists of "shuriken" star-shaped nanostructures, which exhibit distinctive resonance features in their Optical Rotatory Dispersion (ORD) spectra due to their chiral geometry. The shifts in these resonance positions serve as indicators to monitor binding events of target antigens on the DPA surface. The first of the results chapters, Chapter 4, focuses on achieving homogeneous coverage of streptavidin protein on a biotinylated Self-Assembled Monolayer (SAM) DPA surface. Subsequently, the detection of disease-specific targets, including SARS-CoV-2 spike (S1) proteins, inactivated virus particles, norovirus Virus-Like Particles (VLPs), and live Zika virus, is investigated. Additionally, multiplexed, meaning the ability to detect more than one antigen in a single experiment, experiments involving all the aforementioned targets are showcased.

The second of the results chapters, Chapter 5, explores the applicability of DPAs as Surface Enhanced Raman Spectroscopy (SERS) substrates. SERS offers distinct advantages over using ORD, namely detailed information regarding the chemical structure of the surface bound materials, and near field sensitivity [8]. The chiral geometry of the nanostructures leads to differential Raman signal intensities based upon particle or molecular handedness; a phenomenon defined as chirally dependent SERS. This effect is reported in two separate experimental systems. Firstly, an achiral dithiol reporter molecule is employed to link the DPA surface with chiral Helicoid Nanoparticles (HNPs), forming diastereomeric symmetry combinations which exhibit distinct EM field enhancements. Secondly, chirally dependent SERS is demonstrated with molecular enantiomers and biomolecules, such as cysteine and DNA, which were deposited onto silver sputter coated DPA samples. Understanding this effect can pave the way for rapid enantiomeric discrimination of molecules, benefiting pharmaceutical and industrial applications.

The initial chapters of this thesis guide the reader through the general theory related to EM waves, chiroptical activity, chirality, chiral plasmonics and the methodologies employed for creating and functionalizing DPA samples. Chapter 2 begins with an introduction to light by describing Maxwell's equations. This is followed by the description of the wave nature of light and its various polarization states. Subsequently, Circular Dichroism (CD) and Optical Rotation (OR) phenomena, which occur when polarized light interacts with optically active materials, are described. The theory of plasmonics is then introduced by describing the Lorentz and Drude oscillator models, which describe electron motion in response to light for dielectrics and metals, respectively. The concepts of optical activity and plasmonics are then integrated to describe the theory of chiral plasmonics. Biosensors are then introduced, followed by brief literature reviews of plasmonic biosensors. Chapter 2 concludes with concise reviews on Raman spectroscopy, SERS, and chiral discrimination of enantiomers using SERS.

Chapter 3 provides a comprehensive overview of the equipment, methods, and chemical functionalisation strategies employed in this work. It encompasses the manufacturing process and layout of DPA samples, as well as the various gold surface chemical functionalization strategies used to bind the different antigen targets. In addition, simulation work involving EM modelling using the Finite Element Method is described. Finally, schematics, photographs, and descriptions of the instruments utilised in this work, including two polarimetry microscopes and two Raman spectrometers, are presented.

1.2 References

1. Kliger, D.S. and J.W. Lewis, *Polarized light in optics and spectroscopy*. 2012: Elsevier.
2. Canziani, G., et al., *Exploring biomolecular recognition using optical biosensors.* Methods, 1999. **19**(2): p. 253-269.
3. Citartan, M., et al., *Label-free methods of reporting biomolecular interactions by optical biosensors.* Analyst, 2013. **138**(13): p. 3576-3592.
4. Sun, Y.-S., *Optical biosensors for label-free detection of biomolecular interactions.* Instrumentation Science & Technology, 2014. **42**(2): p. 109-127.
5. Rasmi, Y., et al., *Emerging point-of-care biosensors for rapid diagnosis of COVID-19: current progress, challenges, and future prospects.* Analytical and bioanalytical chemistry, 2021. **413**(16): p. 4137-4159.
6. Mercer, T.R. and M. Salit, *Testing at scale during the COVID-19 pandemic.* Nature Reviews Genetics, 2021. **22**(7): p. 415-426.
7. Mohd Hanafiah, K., et al., *Development of multiplexed infectious disease lateral flow assays: challenges and opportunities.* Diagnostics, 2017. **7**(3): p. 51.
8. Santinom, A., et al., *Surface-enhanced Raman scattering (SERS) as probe of plasmonic near-field resonances.* Vibrational Spectroscopy, 2018. **99**: p. 34-43.

Chapter 2 – Background and Theory

This chapter outlines the background and theory related to the techniques utilised throughout this thesis. This includes the theory and polarisation states of EM light, chirality, optical activity, plasmonics, Raman spectroscopy, and SERS. Brief reviews regarding plasmonics based optical biosensors and chiral analysis using SERS are also provided.

2.1 Maxwell's Equations

The propagation of light, or electromagnetism, is governed by some of the most influential equations in all of physical science: Maxwell's equations. These are a set of four partial differential equations that describe the interplay between changing electric and magnetic fields and currents [1]:

1. Gauss's law for electric fields
2. Gauss's law for magnetic fields
3. Faraday's Law
4. Ampère-Maxwell's Law

These equations were first published in the mid-19th century by James Clerk Maxwell, who was the first to describe light as an EM phenomenon [2]. Using these equations, a wide range of EM behaviours can be described and predicted, such as electric fields, magnetic fields, electric currents, and EM waves. Through the understanding of Maxwell's equations, many technologies were able to be developed, including radio, lasers, and television [3].

Maxwell's equations are generally represented in two forms – the Integral and Differential forms. The integral forms describe EM behaviour over surfaces or closed loops, whereas the differential forms describe EM behaviour at individual points in space.

2.1.1 Integral Form of Maxwell's Equations

The integral forms of Maxwell's equations are the most general. Gauss's law for electric fields in integral form is given as [1]:

$$\oint_S \vec{E} \cdot \hat{n}\, da = \frac{q_{enc}}{\varepsilon_0} \tag{2.1.1}$$

The left side of Equation 2.1.1 describes the electric flux; or the number of electric field, $\vec{E}$, lines passing through a closed surface, *S*. $\hat{n}$ represents the unit vector normal to the surface. The right side of the equation describes the total charge enclosed within the surface, q_{enc}, divided by the permittivity of free space, ε_0. Effectively, Gauss's law for electric fields in this form states that electric charges produce an electric field, and that the flux of this field passing through a surface is proportional to the total charge.

Gauss's law for magnetic fields in integral form:

$$\oint_S \vec{B} \cdot \hat{n}\, da = 0 \tag{2.1.2}$$

The left side Equation 2.1.2 describes the magnetic flux; similar to that of Equation 2.1.1. However, instead of electric field lines this equation refers to magnetic field, $\vec{B}$, lines passing through a closed surface *S*. The right side is simply zero, with the implication of this being that the total magnetic flux passing through a closed surface is always zero. In other words, for every magnetic line passing through the surface into a defined volume, there must be a corresponding magnetic field line exiting that volume. Therefore, magnetic monopoles are forbidden and cannot exist.

The third of Maxwell's equations is known as Faraday's Law:

$$\oint_C \vec{E} \cdot d\vec{l} = -\int_S \frac{\partial \vec{B}}{\partial t} \cdot \hat{n}\, da \tag{2.1.3}$$

The left side of Equation 2.1.3 describes the circulation of the electric field around a closed path of *C*. $\vec{l}$ represents a segment along the path of *C*. The right side describes the time-varying magnetic flux through a surface *S* with the boundary of *C*. The fundamental concept of this equation is that a change in magnetic flux through a surface creates an electromotive force in the

boundary path of the surface. Additionally, this equation states that a time-varying magnetic field induces a circulating electric field.

The last of Maxwell's equations is what is known as the Ampère-Maxwell Law:

$$\oint_C \vec{B} \cdot dl = \mu_0 \left(I_{enc} + \varepsilon_0 \frac{d}{dt} \int_S \vec{E} \cdot \hat{n}\, da \right) \tag{2.1.4}$$

Similar to Faraday's Law, the right side of the Ampère-Maxwell Law describes the circulation of a field around a closed path *C*, but instead of an electric field in this case it is the circulation of a magnetic field. There are two contributors to this phenomenon; an induction current I_{enc} and a changing electric field flux through a surface *S* enclosed by a closed boundary *C* – all multiplied by the permeability of free space, μ_0. This law states that an electric current and/or a time-varying electric flux through a surface *S* creates a circulating magnetic field around any path around the boundary *C* of the surface.

2.1.2 Differential Form of Maxwell's Equations

Maxwell's equations may also be written in their differential forms. The frequency-domain differential forms are the most common and the easiest to work with due to their relative simplicity. Gauss's law for electric fields in differential form [1]:

$$\vec{\nabla} \cdot \vec{E} = \frac{\rho}{\varepsilon_0} \tag{2.1.5}$$

Where *E* is electric field, ρ is the electric charge density, and ε_0 is the vacuum permittivity. $\vec{\nabla}$ is a vector differential operator *del*, which along with the *dot* product represents what is called *divergence*. Divergence is a mathematical operator which defines the "flow" of a vector field at a point [1]. A point with positive divergence is defined as a *source*, while a point with negative divergence is defined as a *sink*. In the case of electric charges, a positive charge would be a source and a negative charge would be a sink. The differential equation of Gauss's Law for electric fields therefore states that electric fields diverge from positive charges and converge at negative charges at points in space. Divergence can only be zero if there are no charges present.

Gauss's Law for magnetic fields:

$$\vec{\nabla} \cdot \vec{B} = 0 \tag{2.1.6}$$

Where *B* is the magnetic field. The differential form of Gauss's Law for magnetic fields states that there are no magnetic monopoles or magnetic charges. The divergence of magnetic field lines is always zero, meaning that for a point in space an entering magnetic field must also exit.

Faraday's Law:

$$\vec{\nabla} \times \vec{E} = -\frac{\partial \vec{B}}{\partial t} \tag{2.1.7}$$

Where *t* is time. In the case of Faraday's Law and the following Ampère-Maxwell Law, the del operator is combined with a cross, which together represents *curl*. The curl of the vector field is a measure of the tendency for the field to circulate around a point [1]. Thus, the differential form of Faraday's Law states that a circulating electric field is created by a changing magnetic field over time.

Ampère-Maxwell Law:

$$\vec{\nabla} \times \vec{B} = \mu_0 \left(\vec{J} + \varepsilon_0 \frac{\partial E}{\partial t} \right) \tag{2.1.8}$$

Where μ_0 is the vacuum permeability and *J* is electric current density. The differential form of Ampère-Maxwell's Law states that a circulating magnetic field induces an electric field and electric current which changes over time. This principle is used to generate electricity several renewable energy sources such as windmills and dams, where wind or water energy is used to spin strong permanent magnets to create electric current [4].

Maxwell used his equations to derive the EM wave equation which describes a propagating wave, given as [1]:

$$\nabla^2 \vec{E} = \mu_0 \varepsilon_0 \frac{\partial^2 \vec{E}}{\partial t^2} \tag{2.1.9}$$

Using the wave equation, it is possible to accurately calculate the speed of light in free space using the μ_0 and ε_0 constants as:

$$c = \frac{1}{\sqrt{\varepsilon_0 \mu_0}} \tag{2.1.10}$$

$$= 2.99792458 \times 10^8 \, m \, s^{-1}$$

Utilising Maxwell's equations it is possible to accurately describe and predict the nature of EM fields in free space. Maxwell's equations can also be applied computationally to numerical methods to simulate the interaction of light with a wide range of materials and structures.

Looking at Maxwell's equations, it is apparent that they only contain field terms. Material properties are not present in these equations; therefore, they do not directly tell us how EM waves interact with or behave in materials. Such information is held in other equations which are often called the constitutive relations [5]:

$$\vec{D} = \varepsilon\vec{E} \tag{2.1.11}$$

$$\vec{B} = \mu\vec{H} \tag{2.1.12}$$

Where *D* represents dielectric displacement, and ε represents permittivity, which describes the electric response of a material. In this case *B* is used to represent magnetic flux density, *H* the magnetic field, and μ represents permeability, which describes the magnetic response of materials. To fully describe classical electromagnetics the Lorentz force law is required as well, which describes the force that electric and magnetic fields put on a charged particle such as an electron or proton [6].

2.2 Polarisation States of Light

EM radiation is a wave that consists of an electric and magnetic component which are orthogonal to one another [7]. The polarisation state of light is the property of the EM wave which describes the time-varying direction and magnitude of the electric field vector. The magnetic field vector is usually ignored when describing polarisation as it is always orthogonal to the electric field. From a light source such as the sun, light travels with random polarisations. A single plane of EM radiation oscillating in a specific plane is considered as *plane polarised*, or *linearly polarised light*, and can be described as follows [7]:

$$\vec{E} = E_0 \cos(kz - \omega t) \tag{2.2.1}$$

Where E_0 is the amplitude of the electric field, k is the wave vector, ω is the angular frequency, and z is the propagation direction. Linearly polarised light (LPL) can also be described in terms of two electric field components oscillating in phase, with the plane of polarisation being the sum of the relative phases of both components (Equation 2.2.2) (Figure 2-1):

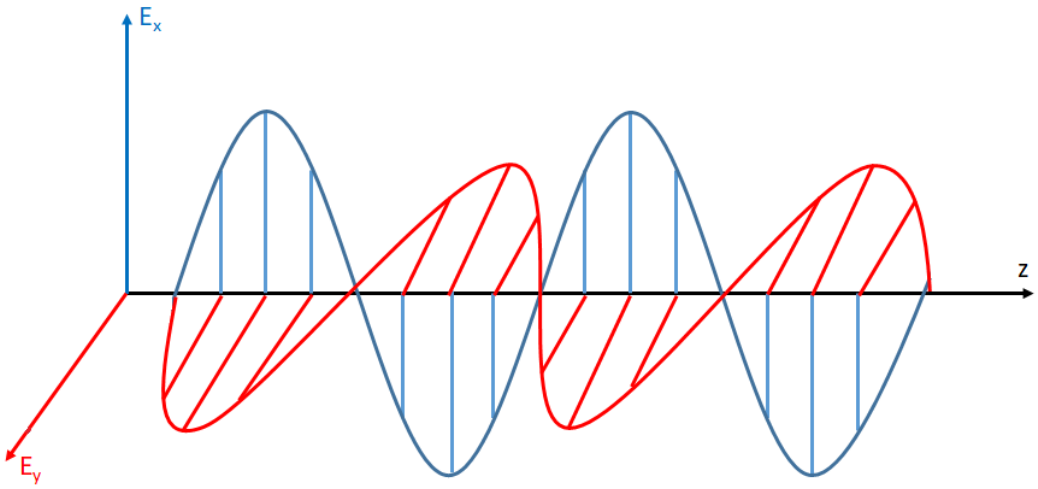

Figure 2-1 Linearly polarised light travelling in the z direction.

$$\vec{E} = \left(E_{0,x} + E_{0,y}\right)\cos(kz - \omega t) \tag{2.2.2}$$

The resultant electric field vector will propagate along the z-direction at a 45° angle between the x- and y-axes.

In 1825 Fresnel discovered the existence of circularly polarised light (CPL) from light refracting at the interfaces of a composite quartz prism with quartz of opposite handedness, known now as a "*Fresnel triprism*" [8] [9]. For CPL the tip of the electric field vector traces a circle as it propagates over time. Conventionally, in the fields of optics and physics, CPL is referred to as right-handed (RH) (positive) when the time-varying electric field vector rotates clockwise when viewed by an observer looking at the source of light. For left-handed (LH) (negative) CPL, the time-varying electric field vector rotates counter-clockwise when viewed from the source [10].

To describe CPL, a phase difference of $\pi/2$, or 45°, must be introduced to the electric field vectors described in Equation 2.2.2 [10]:

$$\vec{E} = E_{0,x}\cos(kz - \omega t) + E_{0,y}\cos\left(kz - \omega t \pm \frac{\pi}{2}\right) \tag{2.2.3}$$

Where E_x and E_y are the x- and y- electric field components of an EM wave where the wave is propagating in the z direction (Figure 2-2) [11].

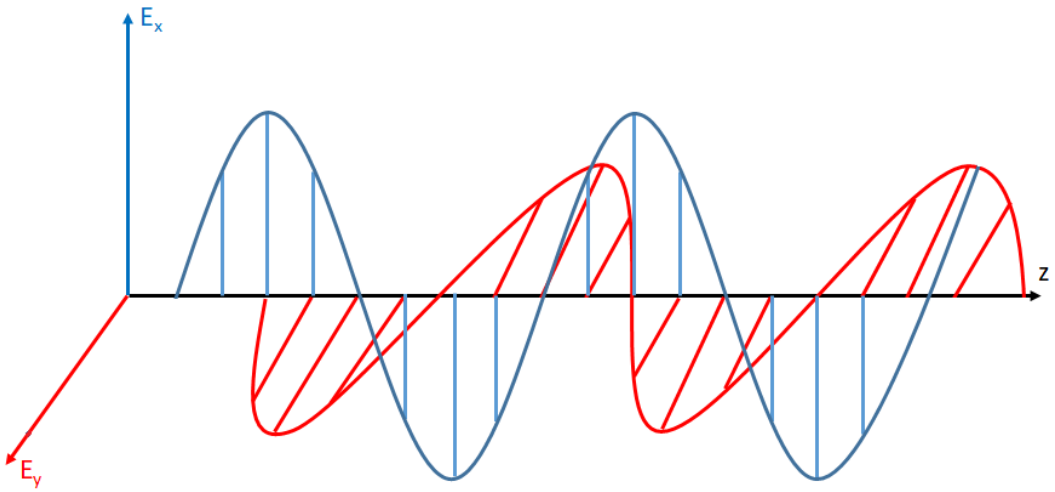

Figure 2-2 Example of LH CPL composed of E_x and E_y electric field components.

An interesting aspect of CPL is that the superposition of LH and RH CPL which are in phase with one another becomes LPL. This can be shown by summing the LH (red) and RH (blue) CPL equations together [10]:

$$E_{0,x}\cos(kz-\omega t)+E_{0,y}\cos\left(kz-\omega t+\frac{\pi}{2}\right)$$

$$+E_{0,x}\cos(kz-\omega t)+E_{0,y}\cos\left(kz-\omega t-\frac{\pi}{2}\right)$$

$$=2E_{0,x}\cos(kz-\omega t) \qquad (2.2.4)$$

The resulting electric field oscillates across a single axis and is thus linearly polarised. This is important in an optically active medium, as the CPL components of LPL will travel at different speeds as well as be absorbed differentially. This results in both the rotation of the electric field vector as well as changes in the electric field component amplitudes. These chiroptical phenomena are called Optical Rotation (OR) and Circular Dichroism (CD), respectively, and will be further discussed in Section 2.4.

2.3 Chirality

Chirality is a fundamental concept used throughout this thesis, which refers to the property of certain objects to exist in mirror image forms. These mirror image forms are known as *enantiomers*. For an object to be chiral, its mirror image must not be super-imposable on its respective pair. Through the lens of group theory, an object can only be chiral if it does not possess improper rotation symmetry elements such as reflection panes, rotation-reflection axes, and centres of inversion [12]. In terms of Chemistry, enantiomers have identical chemical compositions as well as bond connectivity but differ in how their atoms are arranged in space. Just like our hands, which are mirror images of one another, chiral molecules possess this asymmetry. The naming convention for enantiomer configurations are typically given as *R* for *rectus* (right) and *S* for *sinister* (left) for when substituent groups rotate either right or left in order of atomic number [13]. Another similar convention uses the letters *D* for *dexter* (right) and *L* for *laevus* (left), with the difference between the two systems relating to absolute (*S*, *R*) and relative (*L*, *D*) configuration [13].

Despite chiral molecules having the same chemical composition, enantiomers can have drastically different properties when interacting with other chiral molecules. This feature is crucial in the pharmaceutical industry, where chirality is often present in the drug development of pharmaceutical compounds. One of the best-known examples of the role of chirality in drugs is the infamous case of thalidomide (Figure 2-3). Thalidomide exists as a pair of enantiomers, but only one enantiomer (*R*-thalidomide) is therapeutically active against morning-sickness in pregnant women. The other *S*-enantiomer was found to be responsible for teratogenic deformities in children and the drug was resultingly removed from the market in 1961 [14]. Consequently, the chiral analysis of compounds was highlighted.

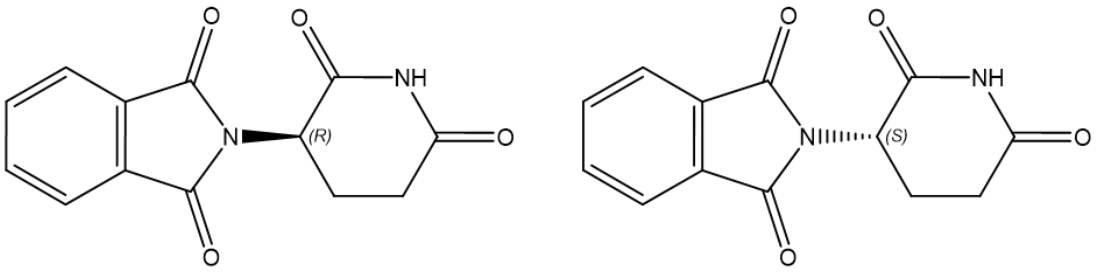

Figure 2-3 Chemical structures of the R- (left) and S- (right) enantiomers of thalidomide.

A compound with two or more chiral centres, or stereocentres, can exist as what are known as *diastereomers*. Unlike enantiomers, diastereomers are not mirror images. An example of diastereomer and enantiomer relationships is shown with the antidepressant drug of setraline in Figure 2-4 [15].

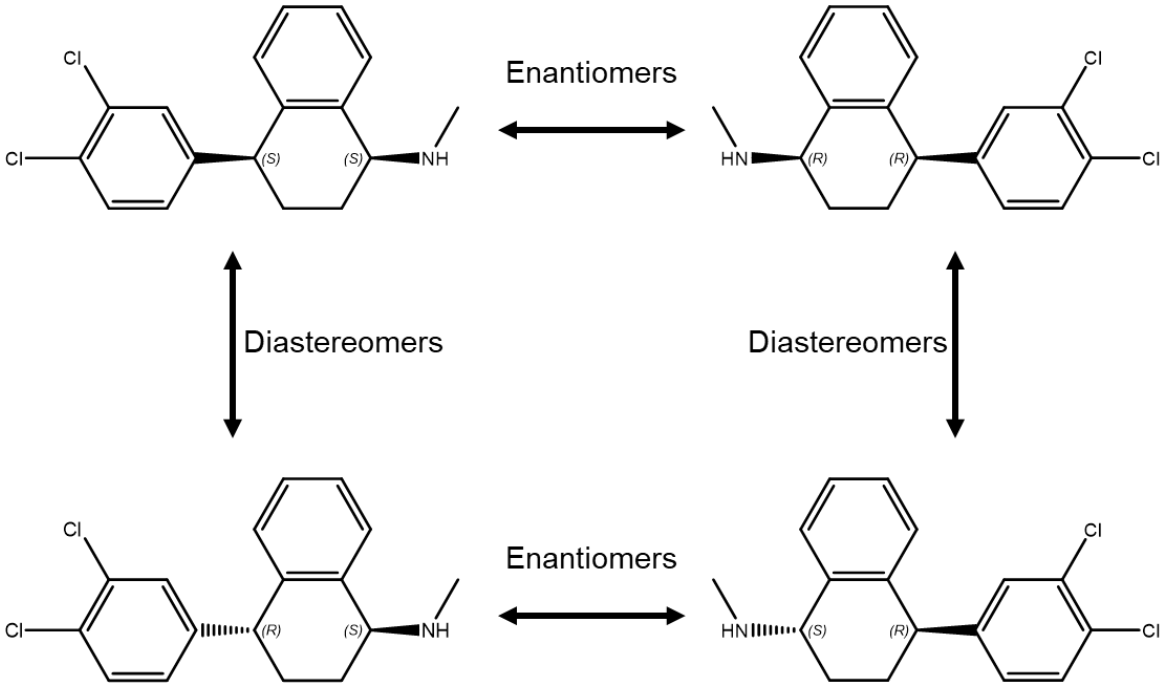

Figure 2-4 Chemical structures of different sertraline conformers, showing enantiomer and diastereomer relationships. Chiral centres defined as "S" or "R".

Chiral analysis of compounds can be performed by taking advantage of the fact that chiral compounds are optically active, meaning they interact differently with different polarisation states of light.

2.4 Optical Activity

A material is defined as being ‘optically active’ when it rotates the plane of polarisation of LPL [12]. In essence, all optical activity of a material is the result of a differential response to LH and RH CPL [16]. The differential optical response between these two polarisations with a chiral material is referred to as a chiroptical (chiral optical) response [11].

The first demonstration of optical activity was first performed by Arago in 1811, who witnessed the different colours of sunlight that passed through a quartz medium in between two polarisers [12]. Biot in 1812 elucidated that these observations arose from two different phenomena: optical rotation of the plane of polarised light; and ORD, the difference in the degree of rotation that is dependent on the wavelength of light [17].

Soon after, the discovery of optical rotation in organic liquids, such as turpentine, aqueous sugar solutions, and tartaric acid led to the understanding that optical activity is dependent on individual molecules that can be randomly orientated in solution, unlike the crystalline lattice of quartz. This eventually culminated in the realisation that natural optical activity arises from *chiral* molecules with opposite *absolute configurations* that rotate plane polarised light in equal but opposite magnitudes.

2.4.1 Optical Rotation (OR)

Optical rotation occurs in an optically active medium when there is a difference in the velocity of propagation of the components of LPL, namely LH and RH CPL [12]. This phenomenon is illustrated in Figure 2-5.

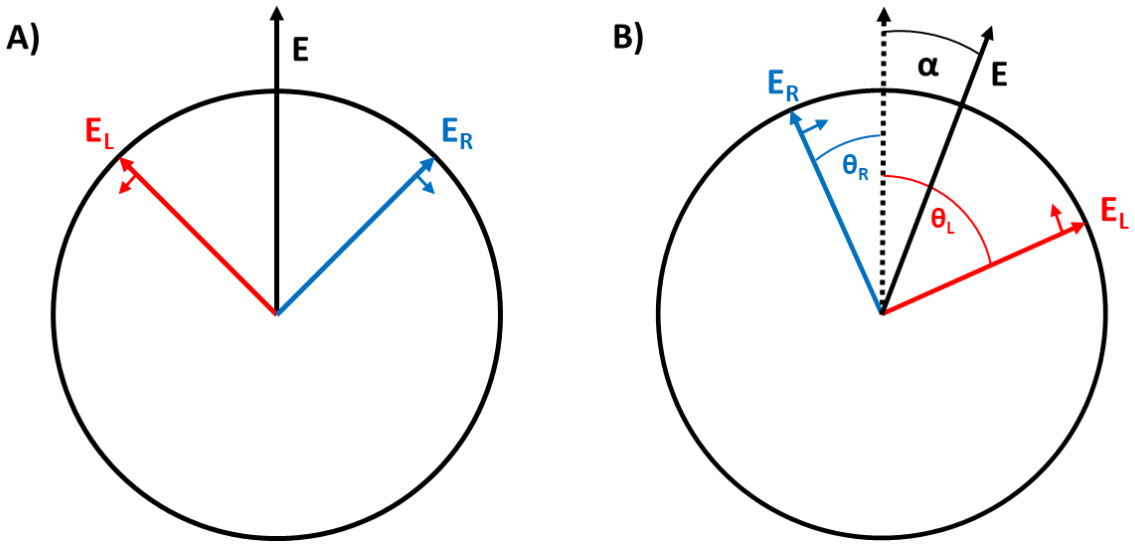

Figure 2-5 Electric field vector decomposed into two equal amplitude LH and RH CPL component vectors. Propagation direction is out of the plane of the paper. B) Rotated electric field vector after passing through an optically active medium [12].

Suppose that LPL with an angular frequency of $\omega = 2\pi c/\lambda$ enters an optically active medium at $z = 0$ *[12]*.

$$\theta_L = \frac{2\pi cl}{\lambda v_L} \quad and \quad \theta_R = \frac{2\pi cl}{\lambda v_R} \tag{2.4.1}$$

Where c is the speed of light, l is the path length of the optically active medium, and v_L and v_R are the velocities of the LH and RH circularly polarised components of light in the medium. The rotation of the electric field vector in radians is then given by:

$$\alpha = \frac{1}{2}(\theta_R + \theta_L) = \frac{\pi cl}{\lambda}\left(\frac{1}{v_L} - \frac{1}{v_R}\right) \tag{2.4.2}$$

Equation 2.4.2 can be simplified using the relationship of refractive index n to velocity v, by $n = c/v$:

$$\alpha = \frac{\pi}{\lambda}(n_L - n_R) \tag{2.4.3}$$

Equation 2.4.3 is a function of the *circular birefringence* of the medium, which is a property where the refractive indices n_L and n_R for LH and RH CPL are different in a material. As OR is a dispersive property dependent on wavelength, measuring OR across a range of wavelengths gives rise to what is known as an ORD spectrum.

A method of calculating ORD involves using a set of values known as the Stokes parameters. These values describe the polarisation state of EM radiation and is performed by measuring the reflectivity the sample at four different angles of polarisation: 0°, 45°, 90° and 135°:

$$ORD = \frac{1}{2} tan^{-1} \frac{(I_{45} - I_{135})}{(I_0 - I_{90})} \tag{2.4.4}$$

2.4.2 Circular Dichroism (CD)

LPL, being a superposition of equal amplitude LH and RH CPL, becomes what is known as *elliptically polarised* when passed through an optically active medium as one circularly polarised component is absorbed more than the other [12]. The ellipticity, given by ψ, is quantified by the ratio of the major and minor axis of the resultant ellipse (Equation 2.4.5 and Figure 2-6):

$$\tan\psi = \frac{(E_R - E_L)}{(E_R + E_L)} \tag{2.4.5}$$

The attenuation of the amplitude of light by an absorbing medium is given by:

$$E = E_0 e^{-\frac{2\pi n' l}{\lambda}} \tag{2.4.6}$$

The attenuation is dependent on the wavelength λ, absorption index n', and path length l of the absorbing medium. Substituting Equation 2.4.6 into Equation 2.4.5:

$$\tan\psi = \frac{\left(e^{-\frac{2\pi n'^R l}{\lambda}} - e^{-\frac{2\pi n'^L l}{\lambda}}\right)}{\left(e^{-\frac{2\pi n'^R l}{\lambda}} + e^{-\frac{2\pi n'^L l}{\lambda}}\right)}$$

$$= \frac{e^{\frac{\pi l(n'^L - n'^R)}{\lambda}} - e^{-\frac{\pi l(n'^L - n'^R)}{\lambda}}}{e^{\frac{\pi l(n'^L - n'^R)}{\lambda}} + e^{-\frac{\pi l(n'^L - n'^R)}{\lambda}}}$$

$$= \tanh\left[\frac{\pi l}{\lambda}(n'^L - n'^R)\right] \tag{2.4.7}$$

Where n'^L and n'^R are the absorption indices of LH and RH CPL, respectively. Equation 2.4.7 shows that the ellipticity as a result of CD is a function of $(n'^L - n'^R)$.

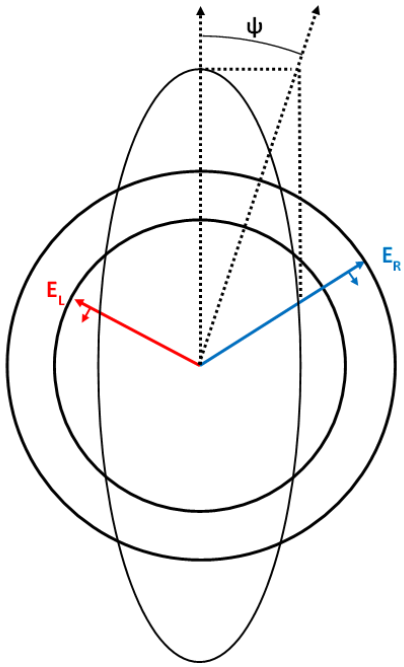

Figure 2-6 Left- (E_L) and right-circular (E_R) polarisation electric field vectors of different amplitudes representing elliptically polarised light. Figure replicated from Barron [12].

Dichroic effects are known to be inherently weak due to the small size of molecules when compared to the length-scales of light. CPL will only twist slightly over molecular dimensions [18].

CD and OR are linked by a bidirectional mathematical relationship known as the Kramers-Kronig relation. This relationship describes the connection between the real (OR) and imaginary (CD) components of linear complex optical functions (Equation 2.4.8) [19].

Furthermore, OR and CR exhibit a relationship known as the Cotton effect [20]. This is represented graphically in Figure 2-7, where the maximum ellipticity of the CD spectrum coincides with the inflexion point of the ORD spectrum. Both OR and CD are expressions which can be used to measure the optical activity of materials and are used to investigate chiral substances. Using the Kramers-Kronig relationship, measuring either the CD or ORD measurement enables the calculation of the corresponding counterpart.

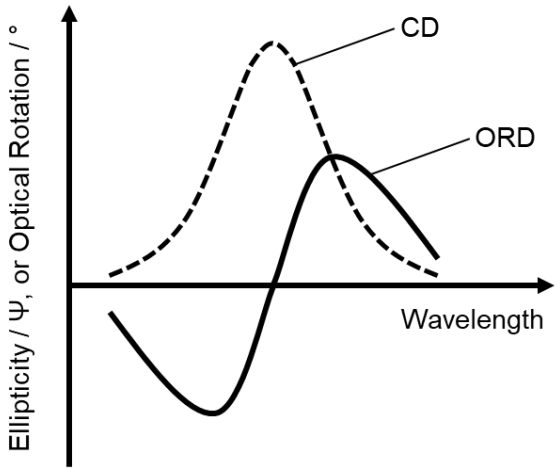

Figure 2-7 Example graph of the relationship between CD and OR, where the ellipticity maximum coincides with the ORD inflexion point.

$$[\phi(\omega)] = \frac{2}{\pi} PV \int_0^\infty \frac{\omega'[\theta(\omega')]}{\omega'^2 - \omega^2} d\omega'$$

$$[\theta(\omega)] = -\frac{2\omega}{\pi} PV \int_0^\infty \frac{[\phi(\omega')]}{\omega'^2 - \omega^2} d\omega' \quad (2.4.8)$$

Where *PV* denotes what is known as the *Cauchy* principal value of the integral [21].

2.4.3 Optical Chirality

Sections 2.4.1 and 2.4.2 have outlined that the interaction between a chiral molecule and a chiral EM field will generate a chiroptical response in the form of OR and CD. A common problem when investigating chiroptical effects of chiral compounds using CPL is that molecules are much smaller than the length scale of CPL. The significance of this is that the analyte molecules do not experience a high degree of 'twist' from the rotating electric field vector of CPL, resulting in fractional differences between optical activity measurements of enantiomers. Indeed, the dissymmetry factor which is used to measure enantioselectivity for chiral molecules is typically in the range of 10^{-5} to 10^{-3} [22]. This dissymmetry factor is often represented by the letter *g*, and is calculated as:

$$g = \frac{A^L - A^R}{\frac{1}{2}(A^L + A^R)} \quad (2.4.9)$$

Where *A* is absorption, and the *L* and *R* superscripts denote LH or RH CPL, respectively.

In 2010, researchers Tang and Cohen considered whether EM fields with greater chiral symmetry than CPL could exist – and if so, whether such fields could enhance chiroptical asymmetry effects [23]. Tang and Cohen's work was preceded by Daniel Lipkin, who in 1964 introduced a conserved quantity of the electromagnetic field using Maxwell's equations, similar to other conserved quantities such as energy and momentum [24]. Lipkin was unaware of the physical significance of his work, and he termed it as 'zilch'. It was not until 2010 that Tang and Cohen discovered that this equation was a descriptor of an EM fields chirality, or optical chirality density [23]. The time-dependent form of this equation is as follows:

$$C = \frac{\varepsilon_0}{2} E \cdot \nabla \times E + \frac{1}{2\mu_0} B \cdot \nabla \times B \tag{2.4.10}$$

Where *E* and *B* are the real time-varying fields. The time-independent expression of Equation 2.4.10 is:

$$C = -\frac{\varepsilon_0 \omega}{2} Im(E^* \cdot B) = -\frac{\varepsilon_0 \omega}{2} |E||B| \cos\left(\beta_{iE,H}\right) \tag{2.4.11}$$

Where ε_0 is the vacuum permittivity, ω is the angular frequency of light, and E^* and *B* are the imaginary components of the complex electric and magnetic field amplitudes, respectively. *C* is ±1 for LH (+) and RH (-) CPL. From Equation 2.4.11, *C* is maximised when the electric and magnetic field lines are parallel and in phase with one another.

Optical chirality density is a pseudoscalar (meaning it behaves like a scalar but changes sign under a parity inversion), and a chiral system is parity odd and even on time-reversal. This means that optical chirality density changes sign if the spatial co-ordinates of a chiral system are inverted (*e.g.*, from x, y, z to -x, -y, -z), but if time *t* is reversed then the chirality retains the original sign. The dissymmetry factor, *g*, was rewritten by Tang and Cohen to include the optical chirality parameter, *C*:

$$g = gCPL \frac{cC}{2U_e \omega} \tag{2.4.12}$$

Where *c* is the speed of light and U_e is the local electric energy density**.** Equation 2.4.12 was the central result of Tang and Cohen's publication in 2010. It shows that chiral asymmetry is

proportional to the product of the chirality of matter as well as the chirality of the EM field. This means that EM fields with greater degrees of asymmetry than CPL are possible. Fields which possess this quality have often been given the distinction of "*superchiral"* light [25].

The significance of Equation 2.4.12 is that the detection sensitivity of chiroptical signals from different enantiomers can be enhanced by manipulating local EM fields so that they possess high *C* values. One way this can be achieved is by using plasmonic metamaterials. Metamaterials are defined as a class of artificial manufactured materials which exhibit unique EM properties unable to be found in nature, and will be discussed further in Section 2.6.1 [26].

2.5 Plasmonics

Before discussing plasmonics in the context of metamaterials and the field of chiral plasmonics, one must first fully comprehend plasmons. Plasmonics is based on the interaction of EM radiation and the free conduction electrons, otherwise known as a *plasma*, of metals [27]. Unlike dielectric or insulating materials, electrons in the *d*-orbital conducting bands surrounding the positive metal nuclei are loosely bound and can move around with relative freedom. A plasmon is defined as a surface and/or volume charge-density oscillation in response to an optical electromagnetic frequency which displaces the metal plasma [28]. These oscillations have a distinct resonance frequency, denoted by ω_p, and are characteristic of metal nanoparticles and nanostructures.

For a plasmon to exist a metal-dielectric interface is required with the respective materials possessing dielectric functions of which the real parts are of opposite sign – with metal typically possessing the negative dielectric. The plasmons at the interface are known to create enhanced optical near-fields and localised charge accumulations in the case of periodic metal nanostructures [28].

To describe plasmons, consider a rigid ionic lattice surrounded by a free electron gas. A collective displacement of the electrons by a small distance of Δx induces a positive charge on the side of the material of $\sigma = ne\Delta x$. Where *n* is electron density, and *e* is elementary charge. The displacement of electrons creates a uniform homogeneous electric field $E = \sigma/\varepsilon_0$. The resultant field and the positive ion cores cause a restoring force on the electrons with the equation of motion:

$$m\ddot{\Delta x} = -eE = -\frac{\Delta x n e^2}{\varepsilon_0} \tag{2.5.1}$$

The solution of this equation is:

$$\Delta z(t) = \Delta z_0 \cos(\omega_p t) \tag{2.5.2}$$

With the plasma frequency, ω_p, of a free electron gas given as:

$$\omega_p = \sqrt{\frac{e^2 n_e}{\varepsilon_0 m_e}} \tag{2.5.3}$$

Where n_e is the concentration of free electrons, m_e is the effective electron mass, ε_0 is the permittivity of free space, and e is charge. Plasmons are dampened by electron collisions with the lattice and other electrons (friction) as well as radiation losses. The plasma frequency can be viewed as the eigenoscillation of the electrons, or a measure of how fast an electron in a material can follow the electric field.

From Equation 2.5.3, it should be noted that the plasma frequency is dependent entirely on the density of electrons in the material as all other variables are constant. For reference, the plasma frequencies ω_p for gold and silver is around 8-9 eV while aluminium has a plasma frequency around 15 eV [29].

2.5.1 Lorentz Model

Before delving deeper into the theory of plasmonics, it must first be understood how materials other than metals, or dielectrics, interact with EM radiation. The complex refractive index, $n + ik$, of materials describes its macroscopic properties and is linked to the atomistic properties (permittivity) by the dielectric function (Equation 2.5.4) [30]. Another way of understanding permittivity is that the composing atoms of a material exposed to an electric field will form opposing dipoles which will reduce the overall electric field strength. A higher permittivity means that the material has a higher resistance to an electric field.

$$n + ik = \sqrt{\varepsilon_1 + i\varepsilon_2} \tag{2.5.4}$$

Where n is the real part of the complex refractive index describing the extent to which light slows down and bends in a material, k is the imaginary component of the complex refractive

index quantifying how much light is absorbed by the material, and ε_1 and ε_2 represent the real and imaginary components of the complex dielectric constant. Permittivity is linked to the electric susceptibility, χ, parameter through the following relation [30]:

$$\varepsilon = \varepsilon_0 \varepsilon_r = (1 + \chi)\varepsilon_0 \tag{2.5.5}$$

The higher the susceptibility, the more resistant a material is to the electric field, resulting in a higher permittivity.

In the macroscopic worldview, Maxwell's equations describe what happens when an EM wave hits a material. The displacement field *D* is linked to the external field *E* via [30]:

$$D = \varepsilon_0 E + P \tag{2.5.6}$$

Where *P* is polarisation. Polarisation *P* relates to the electric field through the following relation:

$$P = \varepsilon_0 \chi \cdot E \tag{2.5.7}$$

Where χ is the susceptibility constant. From these two relations it can be inferred:

$$\begin{aligned} D &= \varepsilon_0 (1 + \chi) E \\ &= \varepsilon_0 \varepsilon E \end{aligned} \tag{2.5.8}$$

The field in the material is connected to the external field by the proportionality constant, $\varepsilon_0 \varepsilon$, where the higher the permittivity the more the electric field is weakened in the material.

To further understand the material parameter of permittivity, ε, it is necessary to investigate the atomic world. The Lorentz oscillator model is used to describe the optical response of bound charges and assumes that the positively charged nucleus and the negatively charged electron are simply connected through electrostatic interactions by a spring constant (Figure 2-8) [30]. Since the electron is significantly lighter than the nucleus, it is easier to displace, with the nucleus effectively remaining stationary. As an incoming EM wave is applied, the electron of the atom is displaced, and this displacement is counteracted by a restoring force. The restoring force can be described by Hooke's Law [30]:

$$F = -kx \tag{2.5.9}$$

Where F is the restoring or spring force, k is the spring constant, and x is the displacement. The spring possesses a natural resonance frequency, which can be described by the time-dependent equation of motion:

$$x(t) = x_0 \cos(\omega_0 t) \tag{2.5.10}$$

Where ω_0 is the resonant frequency of the harmonic oscillator, and is given by:

$$\omega_0 = \sqrt{\frac{k}{m}} \tag{2.5.11}$$

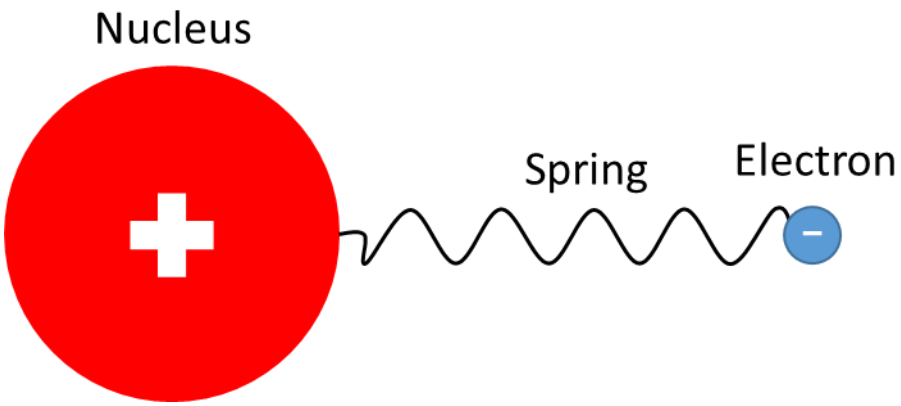

Figure 2-8 Lorentz model diagram of a negatively charged electron attached to a much larger positively charged proton by a theoretical spring.

To connect the macroscopic and atomic worlds, it becomes apparent that the macroscopic polarisation, P, must result from the interaction of all atoms in the material from the interaction with an electromagnetic wave:

$$P = N \cdot p = N \cdot q \cdot r \tag{2.5.12}$$

Where N is the number of atoms, p is the dipole induced displacement, q is charge, and r is the displacement. Looking at the harmonic oscillator, it is desirable to find an equation that balances all the forces between the electron and the nucleus when an electromagnetic wave interacts with the atom. The forces involved are the electromagnetic wave $F = qE$, a restoring force $-kx$, and dampening from other nuclei electrons which creates losses. The dampening is related to the mass, m, and dampening constant, γ [30]:

$$m \cdot \gamma \cdot \frac{\partial r}{\partial t} \tag{2.5.13}$$

To balance the forces:

$$F = m \cdot a = m\frac{\partial^2 r(t)}{\partial t^2} = -kr - m\gamma\frac{\partial r}{\partial t} + q \cdot E(t) \tag{2.5.14}$$

Rearranging:

$$\frac{q}{m}E(t) = \frac{\partial^2 r(t)}{\partial t^2} + \gamma\frac{\partial r}{\partial t} + \omega_0^2 r \qquad where\ \omega_0 = \sqrt{\frac{k}{m}} \tag{2.5.15}$$

Equation 2.5.15 is a partial differential equation (PDE) which describes the electron movement around a nucleus. To solve the PDE 2.5.15, a general solution must be found. As the electric field can be described as complex exponential function (Equation 2.5.16), and as the electrons are driven in response to this electric field, the general solution should follow the same function:

$$E(t) = E_0 \exp(i\omega t) \tag{2.5.16}$$

Since the electric field fluctuates over time, so will electron displacement *r*:

$$r(t) = r \exp(i\omega t) \tag{2.5.17}$$

Applying the general solution Equations 2.5.16 and 2.5.17 into Equation 2.5.15:

$$\frac{q}{m}E_0 \exp(i\omega t) = -\omega^2 r \exp(i\omega t) + \gamma i\omega r \exp(i\omega t) + \omega_0^2 r \exp(i\omega t) \tag{2.5.18}$$

The exponential functions cancel out to give the solution:

$$\frac{q}{m}E_0 = -\omega^2 r + \gamma i\omega r + \omega_0^2 r \tag{2.5.19}$$

Equation 2.5.19 can be rearranged to isolate *r* to obtain the expression for the frequency dependent oscillation of the electron as it is displaced and restored by the nucleus:

$$r(\omega) = \frac{q}{m}\frac{E_0}{(\omega_0^2 - \omega^2) + i\gamma\omega} \tag{2.5.20}$$

From Equation 2.5.20, an important feat to note is that at resonance frequency, ω_0, the displacement *r* is maximised. This function for a harmonic oscillator as a function of frequency

can succinctly be illustrated by a cartoon example of a person on a swing with three different applied 'pushing' frequencies (Figure 2-9). Figure 2-9A shows a scenario where the frequency is below that of the resonance frequency. In this case, the person on the swing is slowly pushed forward by the electric field, producing a small displacement. Figure 2-9B shows maximum displacement with the pushing frequency matching that of the resonance frequency. Here, there is a 90° phase difference between *r* and *E* resulting in the highest amplitude as the peak of the push equals to the 0 of displacement. Finally, Figure 2-9C shows what happens when the frequency is much higher than that of the resonance frequency. For high frequencies above resonance $\omega > \omega_0$, Figure 2-9C, there is almost no amplitude as the electric field phase moves too quickly for the electrons to respond. There is a 180° phase difference between *r* and *E*. This is why X-rays are used for imaging in many scenarios, as the high energy EM radiation is unperturbed by most materials [31].

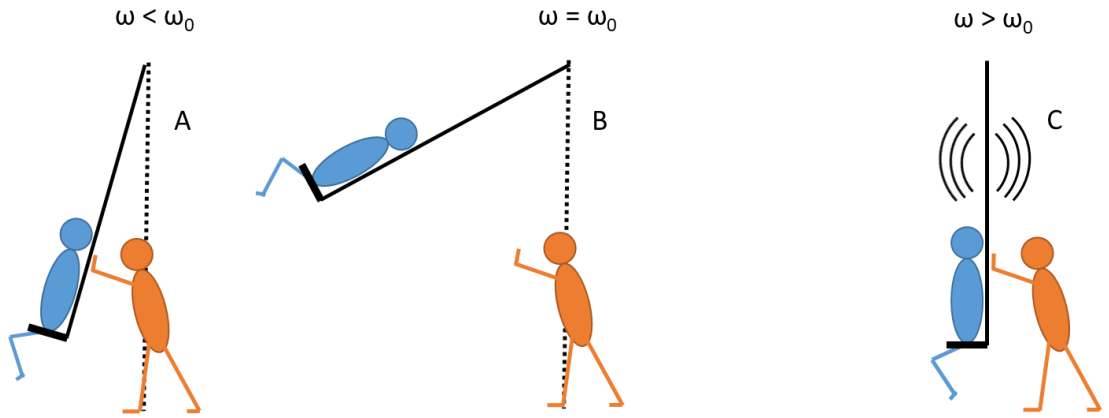

Figure 2-9 Cartoon diagram of a person on a swing being pushed at different frequencies. (A) Frequency below that of resonance frequency. (B) Frequency equal to resonance frequency providing highest displacement. (C) Frequency higher than that of resonant frequency.

To connect Equation 2.5.20 to the macroworld the expression for polarisation P must be calculated:

$$P = \varepsilon_0 \chi E \tag{2.5.21}$$

From Equation 2.5.12 it is already known that:

$$P = Np_i = Nqr(\omega) \tag{2.5.22}$$

Substituting $r(\omega)$ from Equation 2.5.20:

$$Nqr(\omega) = \frac{Nq^2}{m}\frac{E_0}{(\omega_0^2 - \omega^2) + i\gamma\omega} \tag{2.5.23}$$

Susceptibility χ can now be calculated by dividing Equation 2.5.21 with ε_0 and *E*. It is also known that $\varepsilon = 1 + \chi$, allowing the frequency dependence of the permittivity $\varepsilon(\omega)$ to be derived:

$$\varepsilon(\omega) = 1 + \chi = 1 + \frac{Nq^2}{\varepsilon_0 m}\frac{1}{(\omega_0^2 - \omega^2) + i\gamma\omega} \tag{2.5.24}$$

Knowing that the plasma frequency ω_p is:

$$\omega_p^2 = \frac{Nq^2}{\varepsilon_0 m} \tag{2.5.25}$$

Equation 2.5.24 can be simplified to the more known format:

$$\rightarrow \varepsilon(\omega) = 1 + \frac{\omega_p^2}{(\omega_0^2 - \omega^2) + i\gamma\omega} \tag{2.5.26}$$

The final step is to separate $\varepsilon(\omega)$ into its real ε_1 and imaginary ε_2 components. To accomplish this, Equation 2.5.26 can be rationalised as [32]:

$$\varepsilon(\omega) = 1 + \frac{\omega_p^2(\omega_0^2 - \omega^2) - i\gamma\omega}{(\omega_0^2 - \omega^2)^2 + \gamma^2\omega^2} \tag{2.5.27}$$

$$\varepsilon(\omega) = \varepsilon_1 + i\varepsilon_2 \tag{2.5.28}$$

$$\varepsilon_1 = 1 + \frac{\omega_p^2(\omega_0^2 - \omega^2)}{(\omega_0^2 - \omega^2)^2 + \gamma^2\omega^2} \tag{2.5.29}$$

$$\varepsilon_2 = \frac{\omega_p^2(\gamma\omega)}{(\omega_0^2 - \omega^2)^2 + \gamma^2\omega^2} \tag{2.5.30}$$

A noteworthy observation regarding Equations 2.5.29 and 2.5.30 is that at resonance condition where $\omega = \omega_0$ the real component ε_1 becomes small, whereas the imaginary component ε_2 becomes large. This means that losses occurring in the dielectric function through absorption of energy in the material is encoded in the imaginary part but not in the real part. ε_1 and ε_2 can now be used to determine the refractive index of a material at a certain frequency. By graphing ε_1 and

ε_2 against frequency, the trends in both dielectric functions as they approach and move away from the resonance frequency can be observed (Figure 2-10):

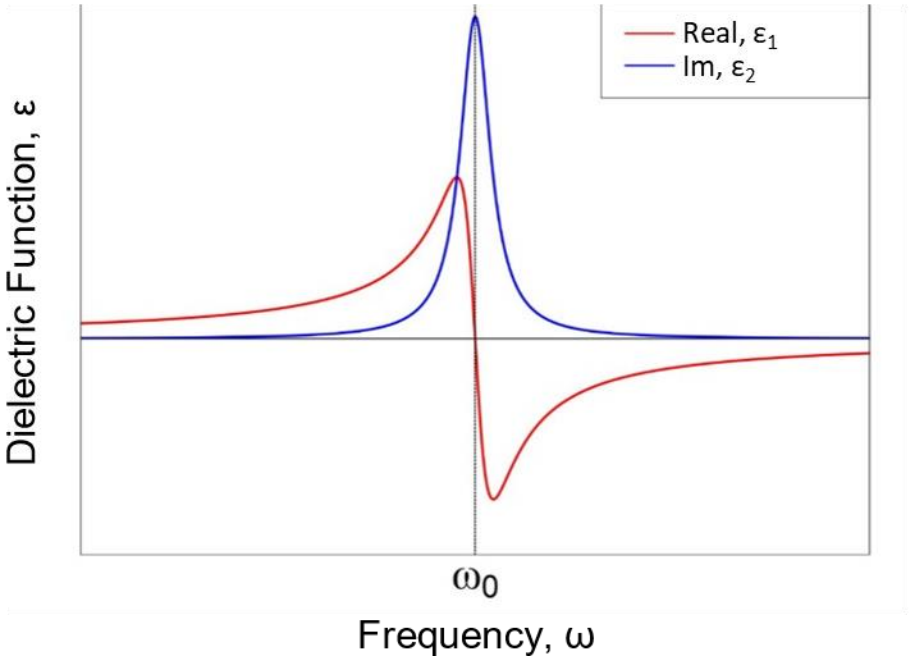

Figure 2-10 Real (red) and imaginary (blue) dielectric functions according to the Lorentz model.

2.5.2 Drude Model for Metals

To investigate the behaviour of electrons in response to EM radiation in metals, and by extension in metal nanostructures, bulk properties need to be established. Important questions to ask are why metals behave differently compared to dielectrics, and how their differences relate to their respective dielectric functions. The answers to these questions can be explained adequately by the Drude model [32]. This model accurately explains how metals possess their characteristic optical properties such as colour and reflectivity.

Similar to the Lorentz model, The Drude model describes the dielectric function, or the response to light, for metallic materials. As discussed, prior in Section 2.5, the conducting electrons within a metal lattice can freely move in response to an electric field. The strategy for deriving the dielectric function with the Drude model is similar to the derivation of the Lorentz model. The equation of motion for the atomic world is first derived, which includes the following terms [32]:

$$Acceleration: F = ma = m\frac{\partial^2 r}{\partial t^2} \tag{2.5.31}$$

$$E - field: F = qE_0\, exp(i\omega t) \tag{2.5.32}$$

$$Dampening: F = m\gamma \frac{\partial r}{\partial t} \tag{2.5.33}$$

The restoring force $F = -kr$ in the Lorentz model does not exist in the Drude model as it is assumed that the electrons are free to move in the material. Thus, the equation of motion for a metal according to the Drude model becomes:

$$m\frac{\partial^2 r}{\partial r^2} = qE_0 \exp(i\omega t) - m\gamma \frac{\partial r}{\partial t} \tag{2.5.34}$$

To solve this PDE it is necessary to find a generic solution that can always replicate itself and insert it into the equation to determine parameters/factors. A shortcut can be applied by noticing that Equation 2.5.36 is similar to the Lorentz model of motion, with the difference being the lack of a restoring force term. This means that there is no resonance. Therefore, the solution of the Lorentz model (Equation 2.5.26) can be taken and the resonance factor, ω_0, can be discarded [5]:

$$\varepsilon(\omega) = 1 + \frac{\omega_p^2}{(\cancel{\omega_0^2} - \omega^2) + i\gamma\omega}$$

$$\rightarrow \varepsilon(\omega) = 1 + \frac{\omega_p^2}{i\gamma\omega - \omega^2} \tag{2.5.35}$$

This is the dielectric function according to the Drude model. To reiterate, Equation 2.5.35 describes the reaction of a metal when a light of a certain frequency impinges on a metal. From this we can derive several material properties such as refractive index. Recall that the plasma frequency is:

$$\omega_p^2 = \frac{Nq^2}{m_e \varepsilon_0} \tag{2.5.36}$$

The physical significance of the plasma frequency is aided by visualising an electric field with varying frequency, or speed. At low frequencies, the electrons in a material can easily follow the oscillating electric field. As the electric field frequency increases, eventually the inertia of the electrons becomes too high, and they will be unable to follow the electric field. This turning point limit is given by the plasma frequency, the flip in the behaviour of electrons in response to light with varying frequencies.

Considering the metal as a free electron gas and that there is no dampening, or $i\gamma\omega = 0$, Equation 2.5.35 can be simplified to [5]:

$$\varepsilon(\omega) = 1 - \frac{\omega_p^2}{\omega^2} \tag{2.5.37}$$

It is known that the refractive index of a plasma is $n = \sqrt{\varepsilon}$, therefore [33]:

$$n = \sqrt{1 - \frac{\omega_p^2}{\omega^2}} \tag{2.5.38}$$

Consequently, for frequencies smaller than the plasma frequency $\omega < \omega_p$ the expression in Equation 2.5.38 becomes negative and must therefore be a complex number, $N = n + ik$, which is dominated by *k*. This means that the electrons can move and absorb the electric field. In the case of $\omega > \omega_p$ the square root in Equation 2.5.38 is positive and the refractive index is dominated by the real component, n. In this situation the metal essentially behaves as a dielectric as there are almost no losses. The electrons cannot follow the oscillations of the electric field anymore and behave as though they are bound to the nucleus.

These observations can be related to reflectivity. Metals are known to be highly reflective at visible frequencies. Reflectivity is given by [34]:

$$R = \frac{(n-1)^2 + k^2}{(n+1)^2 + k^2} \tag{2.5.39}$$

Where *n* is the real part of the refractive index and *k* is the imaginary part. For frequencies below the plasma frequency $\omega < \omega_p$, it can be assumed that the real part n is neglected ($n \approx 0$):

$$R = \frac{1 + k^2}{1 + k^2} = 1 \tag{2.5.40}$$

A reflectivity of 1 means all light is reflected. For $\omega > \omega_p$ we assume $n \approx 1$ and $k \approx 0$:

$$R = \frac{0}{1} = 0 \tag{2.5.41}$$

Thus, a shift from complete reflectivity at frequencies below the plasma frequency to completely transparent behaviour at frequencies above plasma frequency can be seen. It should be noted this

is not the complete physical picture as the assumption of a metal being a completely free electron gas is not entirely accurate at all frequencies.

The complete dielectric function includes the dampening of electrons. The dampening is caused by electrons colliding with each other as well as lattice ions [5]:

$$\varepsilon(\omega) = 1 + \frac{\omega_p^2}{i\gamma\omega - \omega^2} \tag{2.5.42}$$

As described earlier, γ is the collision frequency. This can similarly be expressed by the time between two collisions, which is called the electron relaxation time τ, which is usually around 10^{-14} seconds. τ is related to collision frequency γ by:

$$\tau = \frac{1}{\gamma} \tag{2.5.43}$$

Replacing collision frequency γ in Equation 2.5.42 by relaxation time τ:

$$\varepsilon(\omega) = 1 + \frac{\tau\omega_p^2}{\tau\left(i\frac{\omega}{\tau} - \omega^2\right)} = 1 + \frac{\tau\omega_p^2}{i\omega - \tau\omega^2} \tag{2.5.44}$$

This result places τ and γ in the same product of the denominator, producing a unitless value that is important for later. Rationalising Equation 2.5.44 by multiplying with $i\omega + \tau\omega^2$:

$$1 + \frac{\tau\omega_p^2(i\omega + \tau\omega^2)}{\tau(i\omega - \tau\omega^2)(i\omega + \tau\omega^2)} \tag{2.5.45}$$

$$= 1 + \frac{\tau\omega_p^2(i\omega + \tau\omega^2)}{-\omega^2 - \tau^2\omega^4} \tag{2.5.46}$$

Finally, the real $\varepsilon_1(\omega)$ and imaginary $\varepsilon_2(\omega)$ components can now be separated:

$$\varepsilon_1(\omega) = 1 + \frac{\tau^2\omega_p^2\omega^2}{-\omega^2(1 + \tau^2\omega^2)} \tag{2.5.47}$$

$$\rightarrow \varepsilon_1(\omega) = 1 - \frac{\tau^2\omega_p^2}{1 + \tau^2\omega^2} \tag{2.5.48}$$

Having frequency ω (units of s^{-1}) and collision frequency τ (units of s) in the denominator allows the ability to make certain observations. If:

$$\omega > \tau \ \rightarrow \omega\tau > 1 \tag{2.5.49}$$

For the case of visible frequencies, frequency ω will approximately be 10^{15} s^{-1}, so the 1 term in Equation 2.5.48 can be ignored as it becomes negligible, and the equation can be simplified to:

$$\varepsilon_1(\omega) \approx 1 - \frac{\omega_p^2}{\omega^2} \tag{2.5.50}$$

For the imaginary part $\varepsilon_2(\omega)$:

$$\varepsilon_2(\omega) = \frac{\omega\tau\omega_p^2}{\omega^2(1+\tau^2\omega^2)} = \frac{\tau\omega_p^2}{\omega(1+\tau^2\omega^2)} \tag{2.5.51}$$

The same approximation as in Equation 2.5.50 can be made here:

$$\varepsilon_2(\omega) \approx \frac{\omega_p^2}{\tau\omega^3} \; for \; \omega > \tau \tag{2.5.52}$$

Graphing $\varepsilon_1(\omega)$ and $\varepsilon_2(\omega)$ with regards to frequency (Figure 2-11):

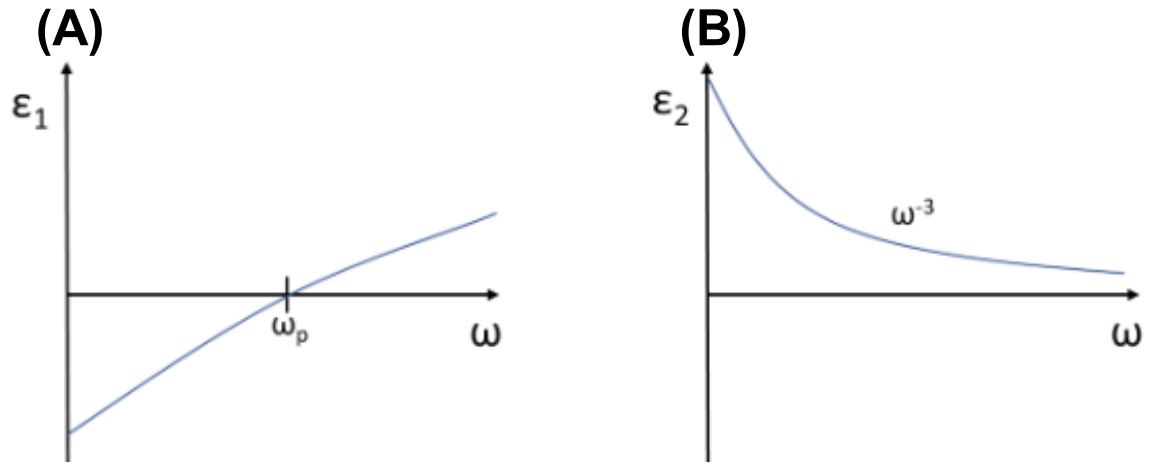

Figure 2-11 Real (A) and imaginary (B) dielectric functions according to the Drude model.

The significance of the dielectric function for the real component $\varepsilon_1(\omega)$ of the Drude model is that it is negative up until the plasma frequency ω_p. This is the primary reason metals behave differently from dielectrics and is one of the reasons why metals can support surface plasmons. The imaginary component is proportional to ω^{-3} so is generally large over a wide frequency range, which leads to high k, or losses in a material. At lower frequencies, the Drude model can

describe the dielectric properties of metals, such as gold, with surprising accuracy (Figure 2-12).

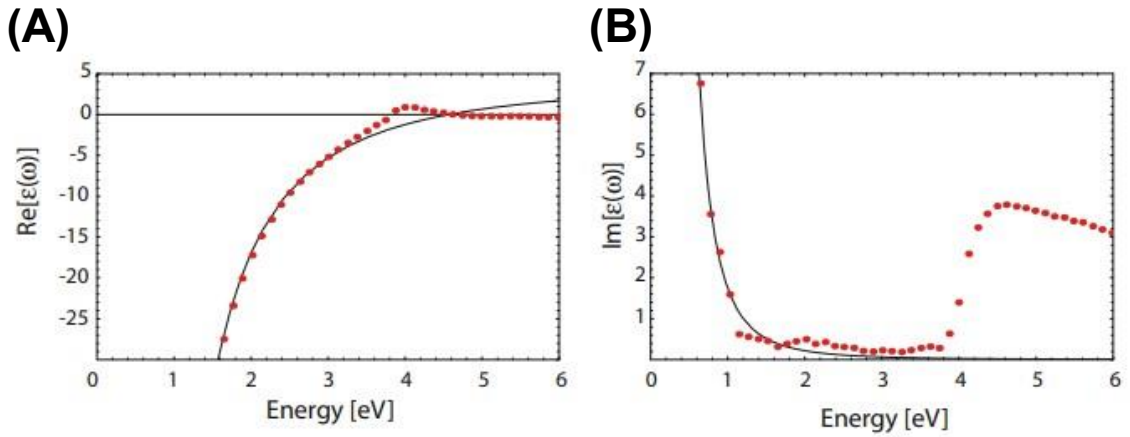

Figure 2-12 Real (A) and imaginary (B) components of the dielectric function of a free electron gas as described by the Drude model (solid lines). Dotted values represent the dielectric data for gold [35]. Image from [5].

From Figure 2-12 it is evident that the Drude model does not perfectly describe reality for non-main group metals at higher frequencies. These differences arise from higher losses (ε_2) than what the Drude model accounts for. The increase in ε_2 means that the energy is being dissipated through other mechanisms, namely the presence of *d*-orbital electrons which can be excited from the 3*d* band into the unoccupied 4*s* band. These *interband transitions* are responsible for the higher losses in ε_2 as well as the colours of non-main group metals such as gold and copper [5].

To account for the complete optical properties of transition metals, the Drude model describing the conducting electrons, and the Lorentz model describing the bound electrons can be combined (Figure 2-13):

$$\varepsilon_1(\omega) = 1 - \frac{\tau^2\omega_p^2}{1+\tau^2\omega^2} + \frac{\omega_p^2(\omega_0^2-\omega^2)}{(\omega_0^2-\omega^2)^2-\gamma^2\omega^2} \tag{2.5.53}$$

$$\varepsilon_2(\omega) = \frac{\tau\omega_p^2}{\omega(1+\tau^2\omega^2)} + \frac{\omega_p^2(\gamma\cdot\omega)}{(\omega_0^2-\omega^2)^2-\gamma^2\omega^2} \tag{2.5.54}$$

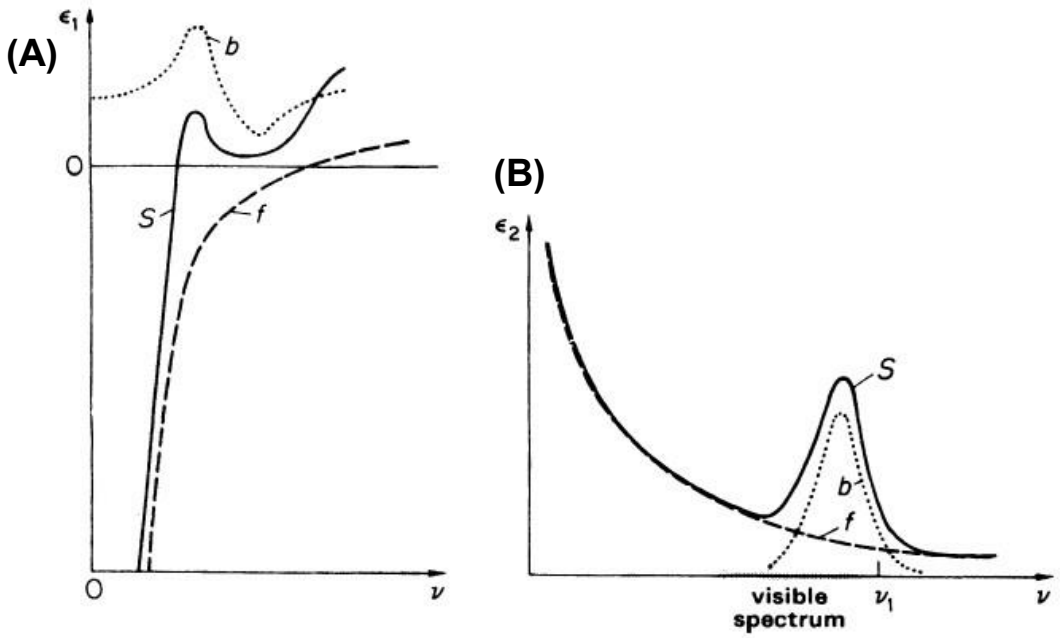

Figure 2-13 ε_1 (A) and ε_2 (B) dielectric functions of free (f, dashed) Drude electron model, bound (b, dotted) Lorentz electron model, and combined summary (S, solid) model curves plotted against frequency, v. Image from Hummel [30].

Graphing the wavelength dependence of the real (ε_1) and imaginary (ε_2) components of the new Drude-Lorentz dielectric function now shows that it fits the experimentally observed data of gold adequately (Figure 2-14).

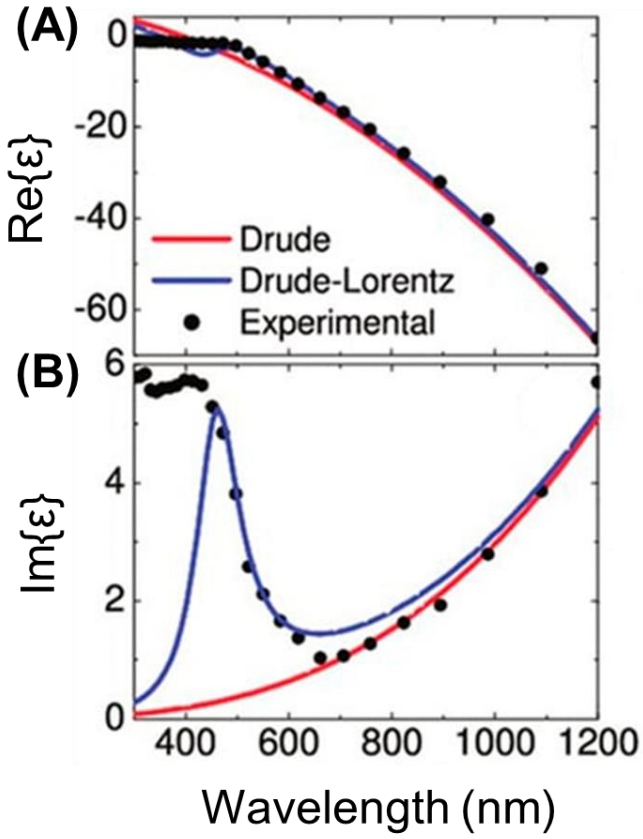

Figure 2-14 Real (A) and imaginary (B) components of the dielectric function of gold, with experimental values (dots), and as described by the Drude (red) and Drude-Lorentz model (blue). Image from Giannini et al [36].

2.5.3 Surface Plasmon Polaritons

Since the discovery of plasmons, different types of plasmons have been identified. Surface Plasmon Polaritons (SPPs) are one type of plasmons that are supported specifically on a metal-dielectric interface. SPPs are electronic excitations which propagate perpendicularly along a metal-dielectric interface in an evanescent field consisting of surface charges (Figure 2-15), arising from the coupling between the incident EM fields to the bulk metal electron plasma oscillations [37].

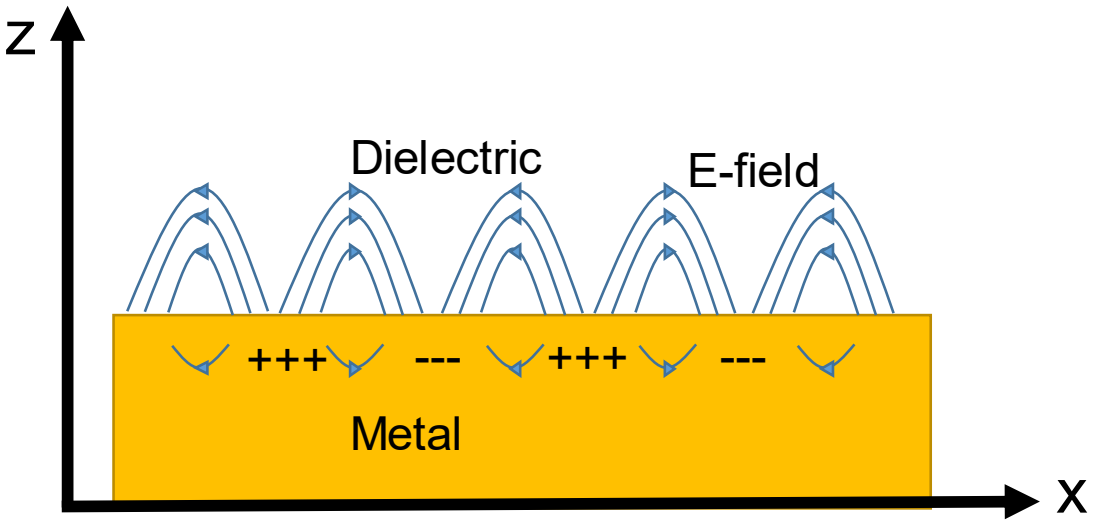

Figure 2-15 Diagram of surface charge propagation of an SPP at a metal-dielectric interface.

The coupled SPP wave possesses a different frequency to that of the incident light, given by:

$$\omega_{spp} = \frac{\omega_p}{\sqrt{1+\varepsilon_d}} \tag{2.5.55}$$

Where ω_p is the bulk plasmon frequency and ε_d is the relative permittivity of the dielectric medium. The SPPs continue to propagate along the metal-dielectric interface, gradually decaying due to ohmic losses in the metal. The SPP evanescent field decays exponentially both into the metal and the dielectric (Figure 2-16). This resonant coupling present in SPPs significantly enhances optical near fields around the metal [5].

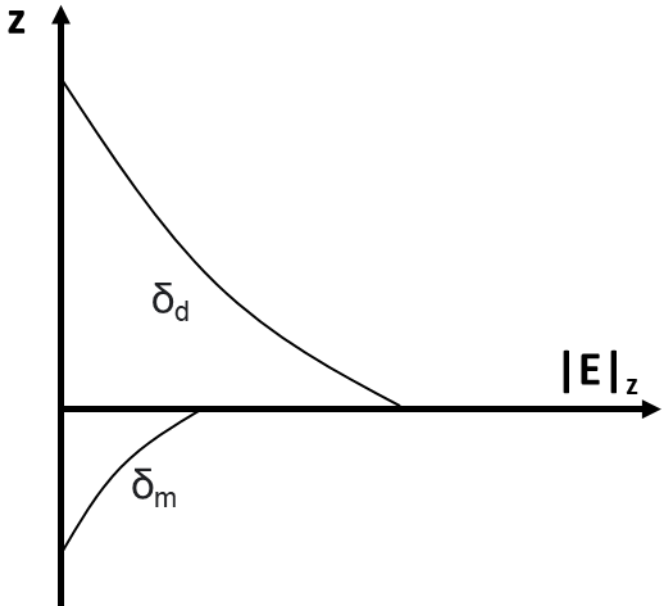

Figure 2-16 Shows the SPP electric field strengths in the metal (σ_m) and dielectric (σ_d) in the z direction.

Equation 2.5.55 shows that the SPP frequency is dependent on the bulk plasma frequency, ω_p, and the relative permittivity of the dielectric, ε_d. It also reveals that SPP frequencies are lower in energy than those of the bulk plasma and can thus be excited at lower energies.

The method of exciting SPPs is an important aspect as they possess a higher momentum compared to the momentum of the respective propagating EM wave in a low RI medium such as air. By utilising Maxwell's equations, the dispersion relation of SPPs can be derived to confirm this [37]:

$$k_{SPP} = k\sqrt{\frac{\varepsilon_d \varepsilon_m}{\varepsilon_d + \varepsilon_m}} \tag{2.5.56}$$

Where k_{SPP} is the SPP wavevector, k is the wavevector of free-space light, and ε_d and ε_m are the relative permittivities of the dielectric and the metal, respectively. This momentum mismatch signifies that an incident EM wave in air cannot excite a SPP in a metal on its own, and this effect is illustrated by graphing the dispersion relations in Figure 2-17.

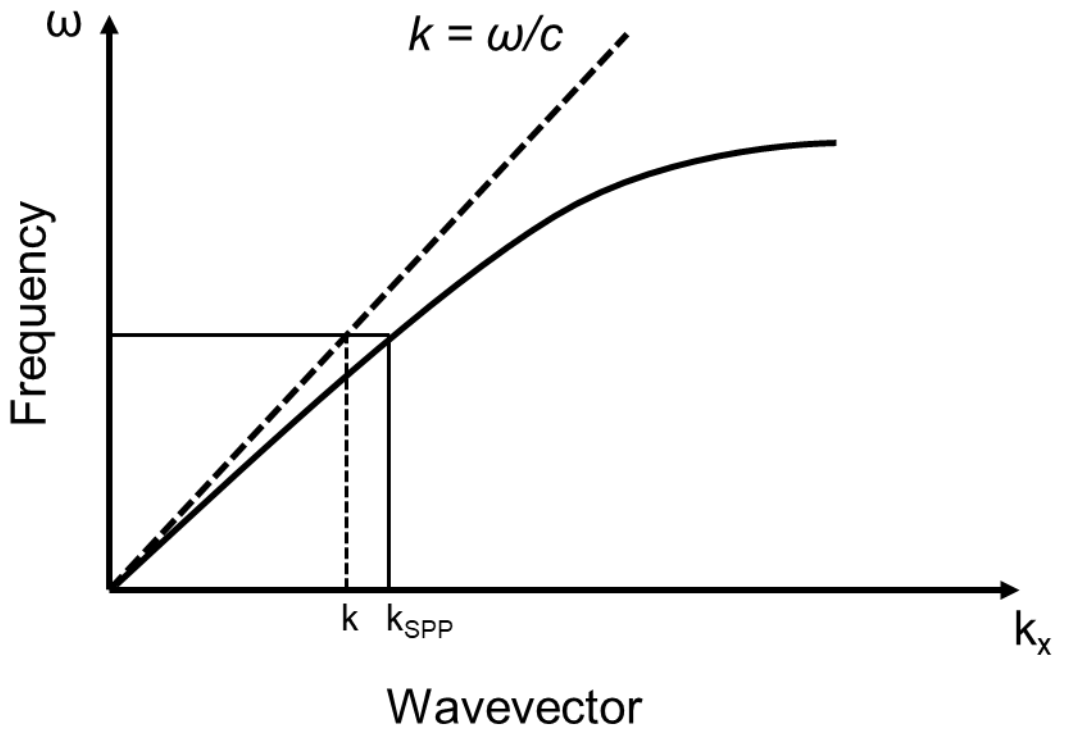

Figure 2-17 Dispersion curves of the free-space (dotted line) and SPP (solid line) wavevectors.

To excite SPPs on a metal interface this momentum mismatch needs to be overcome. One method of achieving this would be to use a higher RI dielectric medium such as glass and an angle of light greater than the critical angle. The critical angle is the point at which the angle of refraction of light passing through one RI medium to another is 90°. Beyond this angle all light is reflected in a phenomenon known as Total Internal Reflection (TIR) [38]. With these conditions the parallel component of the wave vector of glass k_{SiO_2} can be modified to equal that of k_{spp}, which would effectively lower the slope of the free space dispersion curve in Figure 2-17, creating an intercept at which the two momentums would match and resulting in SPP excitation. One such popular configuration is the Kretschmann geometry, which uses a glass prism with a deposited metal layer (Figure 2-18) [37].

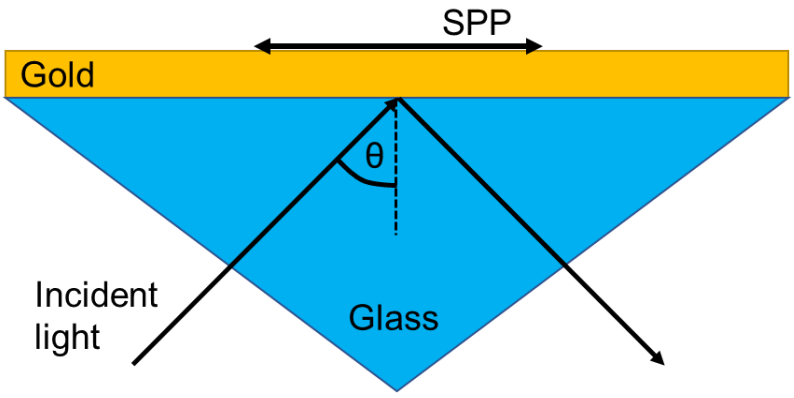

Figure 2-18 Diagram of a Kretschmann configuration set-up for SPP excitation at a metal-dielectric interface.

An alternative approach to excite SPPs, which holds greater relevance within the scope of this thesis, involves utilizing grating coupling. A grating is simply a periodic array of lines or nanostructure, such as which are present in metamaterials. The grating itself possesses its own wavevector, *G* (Equation 2.5.57), which adds its momentum to the parallel component of the incident plane wavevector to match that of the SPP (Equation 2.5.58) [5] [39].

$$G = \frac{2\pi}{P} \tag{2.5.57}$$

$$k_{SPP} = k \pm mG \tag{2.5.58}$$

Where m is the different diffraction orders $m = 1, 2, 3, \ldots$ generated by the grating, and *P* is the periodicity of the grating. Through the combination of the grating vector and wavevector of free space light, a SPP can be generated.

The propagation length of a SPP depends on the metal, dielectric, and the incident wavelength of light. The plasmon oscillations extend into both the metal and dielectric in what is called the *near field* region and are said to be evanescent.

2.5.4 Localised Surface Plasmon Resonance

In contrast to SPPs, plasmons can also be non-propagative, or localised. An electric field that is incident on a metal particle will displace electrons, creating a separation of charge to create a dipole. This effect is illustrated with metal nanoparticles in Figure 2-19.

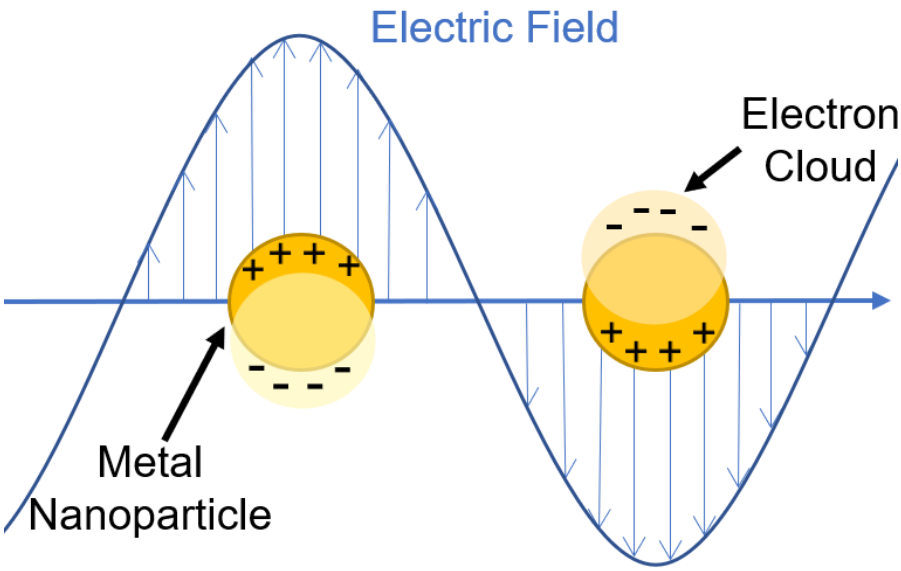

Figure 2-19 Diagram of LSPR with two spherical metal nanoparticles experiencing a time-varying electric field.

As the electric field wave moves across the nanoparticles the electrons continuously oscillate. This induced oscillation of charges generates a new electric field that is radiated, or scattered, outwards. The scattering of light depends upon the polarisability of the metal particles, and is given by [5]:

$$\alpha = 4\pi d^3 \frac{\varepsilon_{particle} - \varepsilon_{medium}}{\varepsilon_{particle} + 2\varepsilon_{medium}} \tag{2.5.59}$$

It is also known that the cross-section for scattering is proportional to polarisability by $C_{Scattering} \propto |\alpha|^2$. Considering that the dielectric function of a dielectric material such as air or water is always greater than one, and that the dielectric function of metal particles can be negative (leading to a denominator that can approach zero in Equation 2.5.59), it is possible for the polarisability, α, term for a metal particle to become significantly large. Thus, the scattering

becomes large as a result from approaching resonance. This is only possible for metals, and not dielectrics.

The condition for resonance occurs when the denominator in Equation 2.5.59 is minimised, which transpires when:

$$\varepsilon_{particle} = -2\varepsilon_{medium} \tag{2.5.60}$$

This is known as the *Fröhlich* condition, and it is in this situation that strong resonance and scattering of light is expected [5]. To find the frequency or wavelength that satisfies this condition, the real component of the dielectric function $\varepsilon_1(\omega)$ for metals from Equation 2.5.50 must equal to the dielectric function of the dielectric medium multiplied by negative two:

$$-2\varepsilon_{medium} = 1 - \frac{\omega_p^2}{\omega^2} \tag{2.5.61}$$

Where ω is given by:

$$\omega = \sqrt{\frac{\omega_p^2}{1 + 2\varepsilon_{medium}}} \tag{2.5.62}$$

This resonance frequency, ω, is what is called the *Localised Surface Plasmon Resonance* (LSPR). It is localised as it is confined to a small particle in the quasi-static dipole approximation.

2.5.5 Refractive Index Based Sensing

Both SPPs and LSPRs can be used to detect changes in the refractive index at a surface before and after molecule adsorption. This lends these techniques suitable for sensing purposes, especially considering the sharp resonance features possible. The equation for resonance shift, $\Delta\lambda$, in response to a change in RI, Δn, for LSPR is presented in Equation 2.5.63:

$$\Delta\lambda = m\Delta n\left[1 - \exp\left(\frac{-2d}{l_d}\right)\right] \tag{2.5.63}$$

The resonance wavelength is affected by Δn. d is the molecular layer thickness, and l_d is the spatial evanescent decay of local fields. The parameter m represents the sensitivity of the nanomaterial towards changes in local RI and will be different for each surface plasmon mode.

This forms the basis of SPR sensors, which are sensitive to surface changes due to the enhancement and confinement of light fields arising from plasmonic interactions. A simplified example of a resonance shift due to molecular absorption is presented in Figure 2-20.

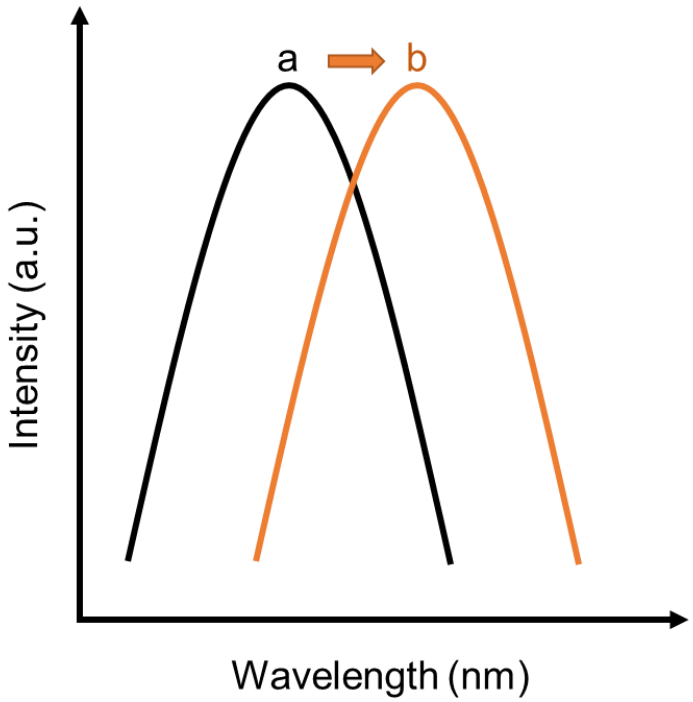

Figure 2-20 Example of a LSPR/SPR resonance before (a) and after (b) introduction of a surrounding higher refractive index medium.

Neighbouring nanoparticles or nanostructures which also possess plasmon modes may couple to each other to further enhance electromagnetic fields. This, however, typically broadens resonances as a result from strong radiative damping [40].

2.5.6 Plasmonic Hybridisation

Plasmonic metamaterials can possess more than one type of resonance, and these may also couple to one another, or hybridise. A useful analogy to better understand the plasmon response of metal-based nanostructures is to compare plasmons to molecular orbitals of atoms. Molecular orbital theory dictates that atomic orbitals can hybridise with neighbouring atoms to form bonds. In a similar fashion, plasmonic oscillations from metallic particles or structures can also hybridise to form new resonances [41] [42]. Therefore, group theory can be utilised to describe and better understand plasmonic modes.

A metamaterial comprised of a periodic array of metallic nanostructures can generate both SPP and LSPR resonance phenomena. With the correct lattice parameters, these resonances can couple to one another to create hybridised plasmon modes [43]. A simplified example of this hybridisation model has been demonstrated by investigating the dipole-dipole interactions between a metallic nanorod dimer (Figure 2-21).

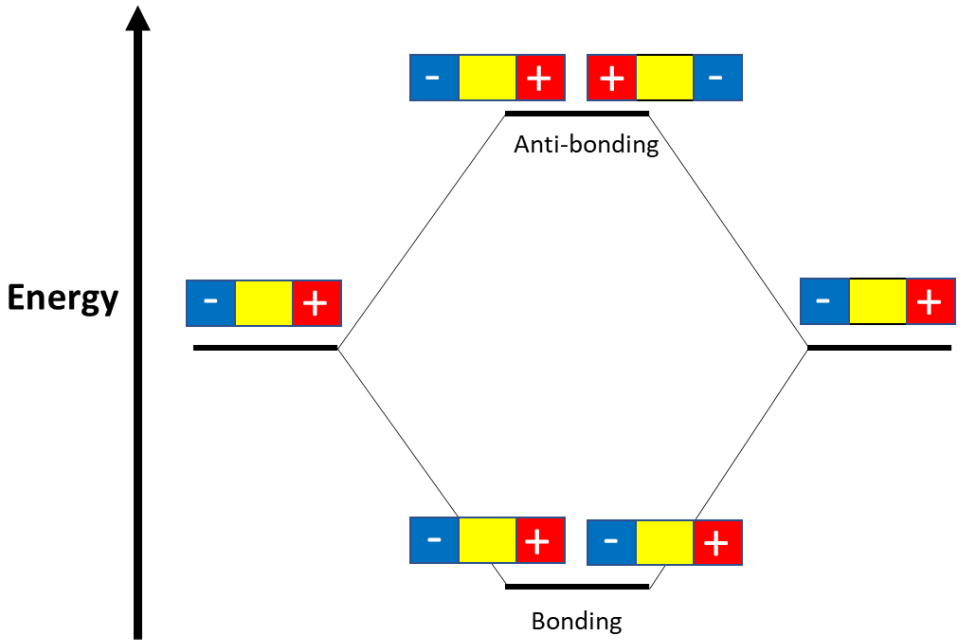

Figure 2-21 Shows the hybridisation of the dipolar plasmonic modes of two individual nanorods in proximity. The plasmonic oscillations generate charged regions which can couple to the neighbouring nanorod in a favourable (bonding) interaction or unfavourable (anti-bonding) interaction.

The gap between the nanorod dimers is small enough to allow for overlap of the plasmon modes, creating a strong near field interaction. When plasmon oscillations are in-phase with one another a symmetric mode occurs. Conversely, out-of-phase dimers will possess an anti-symmetric mode. Analogous to molecular orbitals, these modes will differ in energies, with the in-phase mode acting as a lower energy 'bonding' mode and possessing a higher enhanced EM field in the gap between the dimer [43]. The in-phase and out-of-phase modes are typically referred to as bright and dark modes respectively; arising from the fact that the in-phase mode has a strong dipole moment and interacts strongly with incident light, whereas the out-of-phase mode has a small dipole moment which does not interact strongly with incident light.

This simplified model can be extended to more complex nanostructures such as the shurikens on DPAs. The interaction between the present bright and dark modes leads to interesting interference effects, such as Fano Resonances and Plasmonic Induced Transparency windows [44, 45].

2.6 Chiral Plasmonics

In this thesis the phenomena of optical activity and plasmonics is brought together in a field regarded as *Chiral Plasmonics*. Light in of itself cannot be chiral as it possesses no geometry. However, the chirality of light can be defined through the rotating electric and magnetic field vectors present in LCP, RCP, and elliptical light, as described earlier in Section 2.4. To describe the phenomenon of a chiral plasmonic response, a metallic nanoparticle/nanostructure can be considered. The electric dipole moment, p, of said particle, when using the quasistatic approximation, can be written as:

$$p = \alpha_E E \tag{2.6.1}$$

Where α_E is the electric dipole polarisability. The quasistatic approximation assumes that the EM field acting on metallic particles remains constant across the entire particle. This is a useful tool, but the approximation is only accurate for simple geometries and when the dimensions of the metallic particle are significantly smaller than the wavelength of light [46]. The chiral plasmonic effect occurs when there is magnetoelectric cross-coupling, which can be expressed in matrix-form as [47-49]:

$$\begin{pmatrix} p \\ m \end{pmatrix} = \begin{pmatrix} \alpha_E & ia_C \\ -ia_C & \alpha_H \end{pmatrix} \begin{pmatrix} E \\ H \end{pmatrix} \tag{2.6.2}$$

Where α_c and α_H are the chiral and magnetic dipole polarisabilities, respectively. As the magnetic dipole moment in metallic structures may be reduced or suppressed significantly compared to its counterparts, it is often approximated as zero. Therefore, a chiral metallic nanoparticle can be modelled as:

$$p = \alpha_E E + ia_C H \tag{2.6.3}$$

Here, the i represents the phase shift between the electric and magnetic dipole moments. The magnetoelectric dipole polarisability term a_C represents the chiral character of the oscillating EM

fields. The resultant phase shift between the electric and magnetic dipole moments is responsible for the creation of chiral EM fields, which is generated by the chiral geometry of the theoretical nanoparticle or nanostructure [47]. Another characterisation of chiral plasmonics presented by Wu and Pauly is that a chiral particle can be described as a coupled system with phase shifted electric and magnetic dipoles, which interact differentially with LCP or RCP light [50]. The much larger magnitudes of the electric and magnetic dipole moments of chiral plasmonic metallic particles or structures compared to that of chiral molecules is what leads to the observed greater chiroptical effects.

A visual way of understanding chiral plasmonics is to visualise chiral nanoparticles interacting with an electromagnetic wave (Figure 2-22). In the case of a spherical achiral nanoparticle (A), a LSPR mode will arise in the quasi-static dipole limit. The same particle interacting with CPL (B) will attain a plasmon that follows a helical path. Imposing chiral properties to the nanoparticle as in (C) and (D) creates a scenario where only one handedness of CPL will induce a plasmon that can accommodate the structure. The energy mismatch between (C) and (D) is the principle of chiral plasmonics and illustrates the differential interaction with CPL.

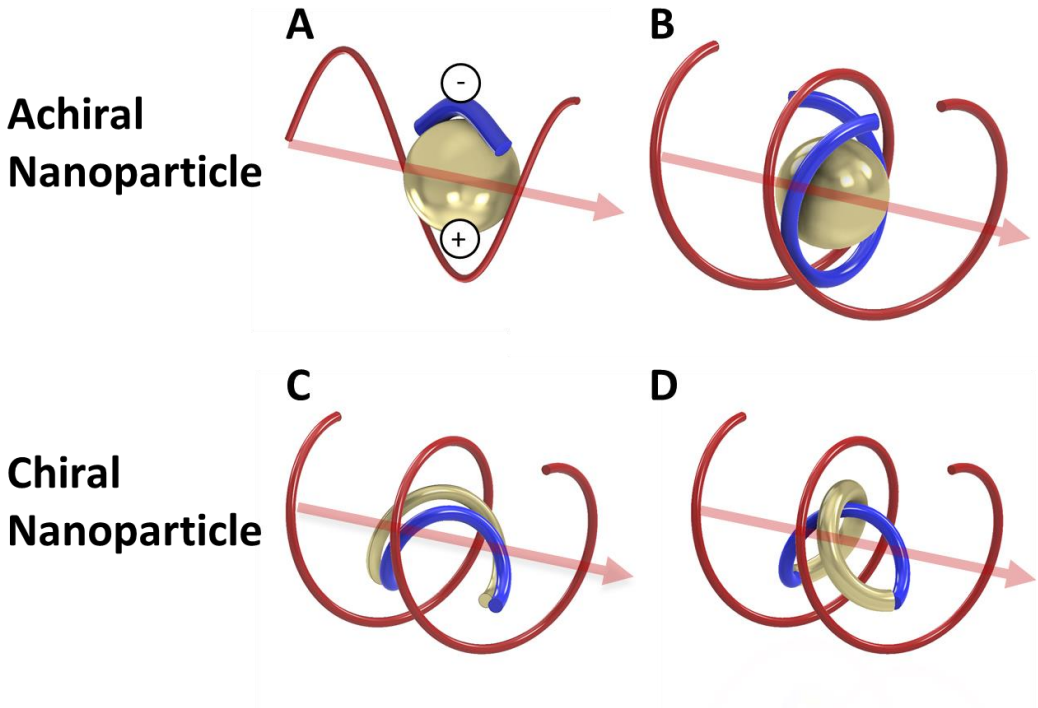

Figure 2-22 Achiral and Chiral gold nanoparticles interaction with LPL and CPL, where the red faded arrow represents direction of travelling EM wave and solid red lines represent the electric field component. A) Achiral nanoparticle illuminated by LPL exhibits a dipolar LSPR response. B) Electrons in an achiral nanoparticle follow a helical path under CPL illumination. C) Electrons in a RH chiral nanoparticle can follow the shape of the structure under LH-CPL. D) Electrons are unable to follow the path of a LH chiral nanoparticle under LH-CPL, resulting in a weak chiroptical interaction. Image adapted with permission from Valev [51].

2.6.1 Chiral Metamaterials

Chiral plasmonics have been used extensively in metamaterials. Metamaterials are artificial fabricated materials with exotic properties undetected in nature. These materials have garnered much interest in the scientific community over the past decades in several different fields. The typical defining characteristics of metamaterials are periodically or randomly arranged nanostructures with sizes and spacings smaller than the wavelength of interest [52-54]. Carefully choosing the design parameters of metamaterials has allowed for the exploration of many interesting phenomena, including but not limited to negative refractive indices [55], artificial magnetism [56], and low frequency plasmons [57].

Imposing chiral features onto the nanostructures created a subset of metamaterials known as *chiral metamaterials*. Plasmonic chiral metamaterials have attracted much interest due to the produced chiral EM fields when interacting with light, which have been shown to possess strong optical activity [58-60]. In addition, the chiral EM fields produced by chiral metamaterials have been shown to greatly increase asymmetrical effects between light and chiral molecules, improving chiroptical detection by several orders of magnitude [59, 61].

Several different nanostructure geometries have been utilised for chiral metamaterials. A classical shape is the three-dimensional helix structure. In a study by Gansel *et al*., researchers fabricated such helices using direct laser writing and gold plating on a glass substrate (Figure 2-23) [62].

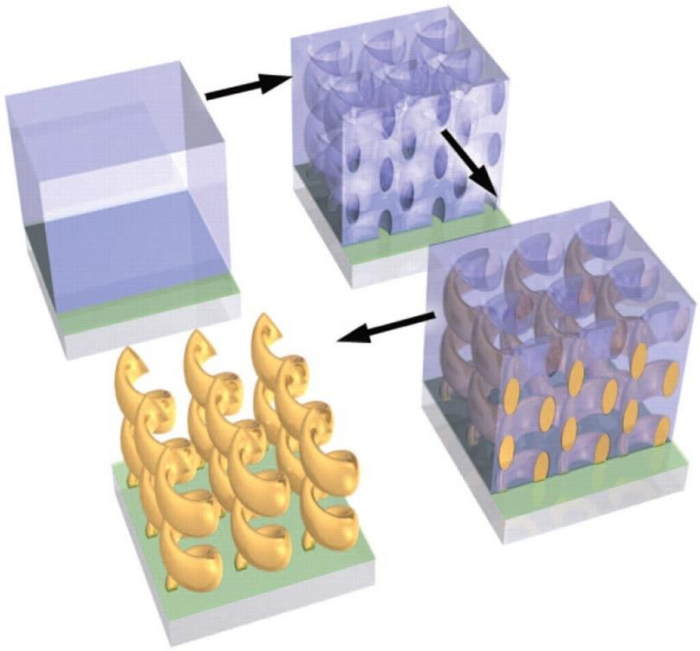

Figure 2-23 3D helix metamaterial fabrication using a positive photoresist, which after direct laser writing and development is formed into an array of air helices. Gold plating in an electrolyte and polymer removal results in final helix structures. Image from Gansel et al [62].

Another alternative building block for chiral metamaterial arrays - and the type used for this thesis - are planar chiral nanostructures. Such geometries involve “flat” chiral shapes which possess no line of symmetry in the plane [63]. The initial study investigating planar chiral metamaterials by Papakostas *et al.* was conducted using arrays of LH and RH gammadions,

which showed handedness dependent optical rotation and circular dichroism responses diffracted from the nanostructured arrays (Figure 2-24) [63].

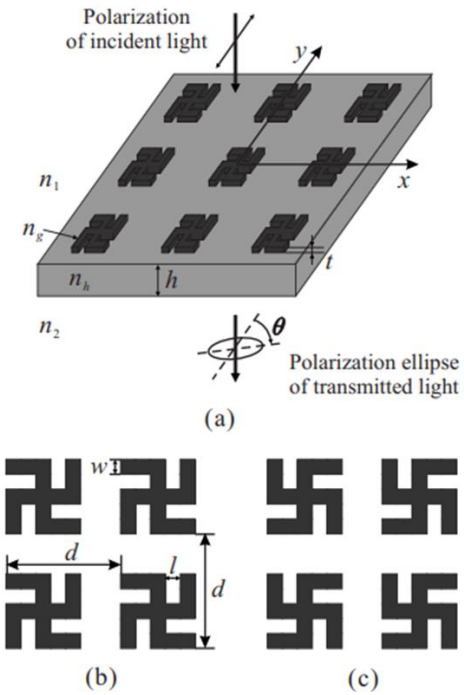

Figure 2-24 (A) Geometry of a planar chiral metamaterial array consisting of gammadion nanostructures, with the polarisation rotation of transmitted light shown. (B) and (C) Top-views of LH and RH gammadion nanostructures, respectively. Image from Bai et al.[64]

The geometry employed throughout this thesis is the "shuriken" star shape, which is used in a continuous plasmonic metafilm in a periodic array arrangement to create the DPA (Figure 2-25). The shuriken metafilms are fabricated using nanoindented polycarbonate substrates with a deposited gold layer on top. Further details regarding DPA fabrication is presented in Chapter 3. The optical properties of these shuriken assays can be controlled by modifying gold layer thickness, shuriken geometry, as well as periodicity [65].

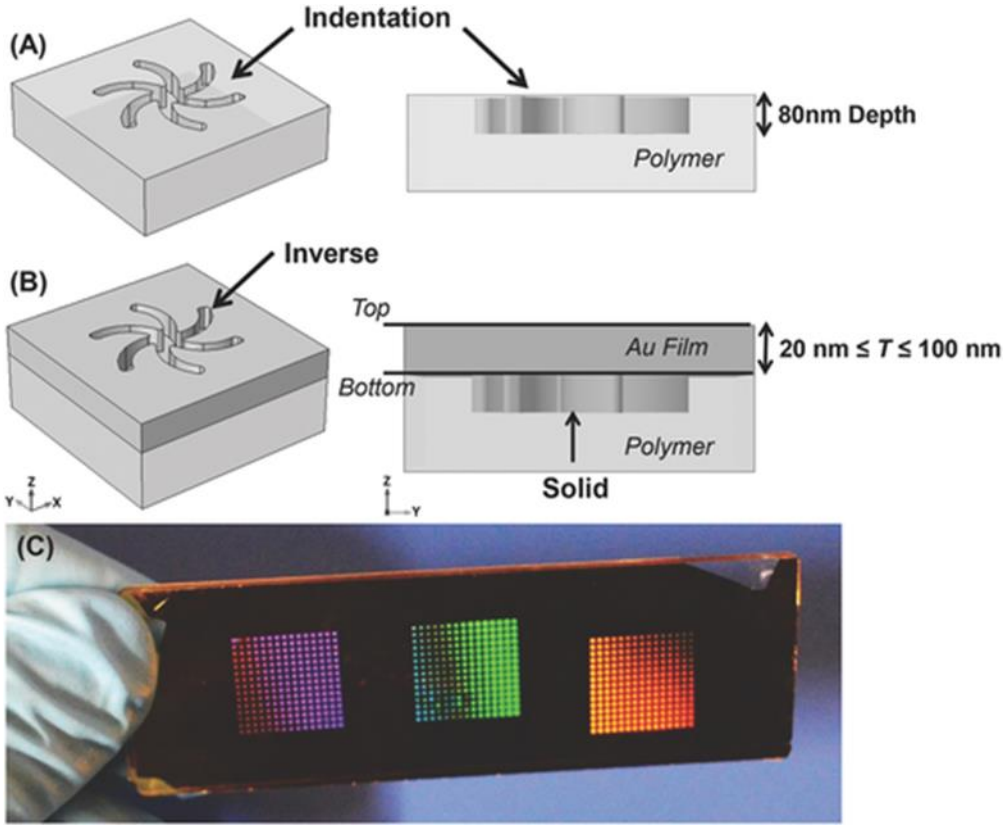

Figure 2-25 Diagrams of polycarbonate (A) and gold-coated polycarbonate (B) substrates showing single shuriken geometries. (C) Photograph of gold-coated polycarbonate slide with numerous shuriken arrays. Different colours are produced by different shuriken geometries. Image from Karimullah et al [65].

2.7 Biosensors

By utilising plasmonic materials and their unique capabilities to condense EM fields to dimensions significantly smaller than that of the incident wavelength, therefore increasing light-matter interactions, as well as possessing specific resonance frequencies which can be measured, these substrates have been proven valuable as biosensors. The term *biosensor*, encompasses a wide range of technologies that are used to study the interactions between biomolecules, detect analytes from bodily fluids, manufacturing processes, and environmental samples. Accordingly, this versatility makes biosensors useful for a wide range of fields including life science research, pharmaceuticals, medical diagnostics, and food/water safety [66].

Historically, biological research and sensing has relied on labels physically attached to the molecule/cell/virus that is being studied to detect them. Commonly used labels are fluorophores, which emit light upon excitation with certain light frequencies. Observing the corresponding fluorescence is an indicator which confirms the presence of the analyte which is conjugated to the fluorophore. Other possible labels include nanoparticles, enzymes, and radioactive isotopes [67-69].

Though the use of molecular labels has been immensely useful for the research of biological systems, there are cases in which the incorporation of labels can pose problems: Fluorophores are prone to photobleaching over time, nanoparticle tags are often significantly larger than the systems that are desired to be studied, radiolabelled compounds need to be synthesised in specialised labs and have specific disposal regulations. The label itself may influence the experiment and assays must be developed to assure non-interference. Due to these considerations, the interest in label free assays and biosensors has risen significantly in the recent decades [70]. Removing labels allows for higher throughput experiments, while also reducing assay complexity and the quantity of reagents. Label-free systems are especially important for pharmaceutical companies who require a large number of assays at low costs and with high throughput to develop novel therapeutic compounds [66].

A label-free biosensor is an analytical device that uses biological or chemical receptors to detect analytes in a sample by converting a biological response into an observable signal. Typically, the response signal is proportional to the concentration of target analyte. A basic biosensor consists of the following elements (Figure 2-26):

1. **Analyte:** The target substance/molecule that is measured or detected. For example, the analyte for blood glucose monitors is simply glucose.
2. **Bioreceptor:** Component of the biosensor which selectively binds to the analyte to elicit a response. Examples of bioreceptors are antibodies, acute phase proteins, and aptamers.
3. **Transducer:** The transducer is responsible for signalisation; converting the change induced by analyte binding into a measurable response, such as electrical or optical signals. In the case of DPAs, these are classified as an optical bio-transducer type, as they convert the binding of analyte into optical signals that can be measured through changes in ORD.

4. **Readout/Display:** A System which visualises the final result, such as a computer screen.

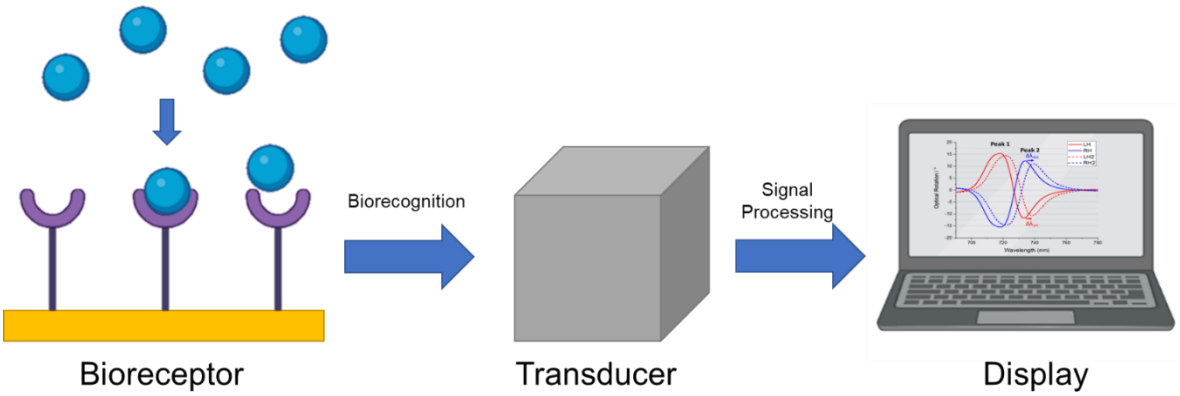

Figure 2-26 Schematic diagram of basic biosensor elements.

Label-free biosensors detect signals based on the material qualities of the analyte(s). These qualities can include atomic mass, surface charges, electrical impedance - or more relevantly to this thesis - index of refraction [71]. As there are several properties which can be measured without the requirement of labels, it follows that there are a diverse range of label-free biosensing technologies. These can be broadly categorised as either optical or non-optical methods [72].

Some examples of common non-optical methods include Lateral Flow Devices (LFDs), which are paper based and use capillary action to move liquid sample along a strip containing detection reagents [73], Enzyme-Linked Immunosorbent Assay (ELISA), an immunoassay which uses antibodies linked with enzymes to produce a colorimetric response in the presence of target proteins or antigens [74], and Polymerase Chain Reaction (PCR), which amplifies DNA segments for DNA detection and quantification [75]. Optical sensing methods commonly rely on plasmonic interactions, with two established techniques being that of SPR and LSPR.

2.7.1 SPR Biosensors

Surface plasmon resonance (SPR) technology is the most common optical biosensor based tool relying on plasmonic interactions [76]. SPR relies on SPPs, most commonly generated using prism-metal interfaces or metal surface gratings, with their specific resonance frequency modified once the biomolecular surface recognition elements on the metal surface capture the

desired analyte and the local refractive index increases. This spectral shift can then be measured to confirm the presence of the analyte of interest. This concept is illustrated in Figure 2-27.

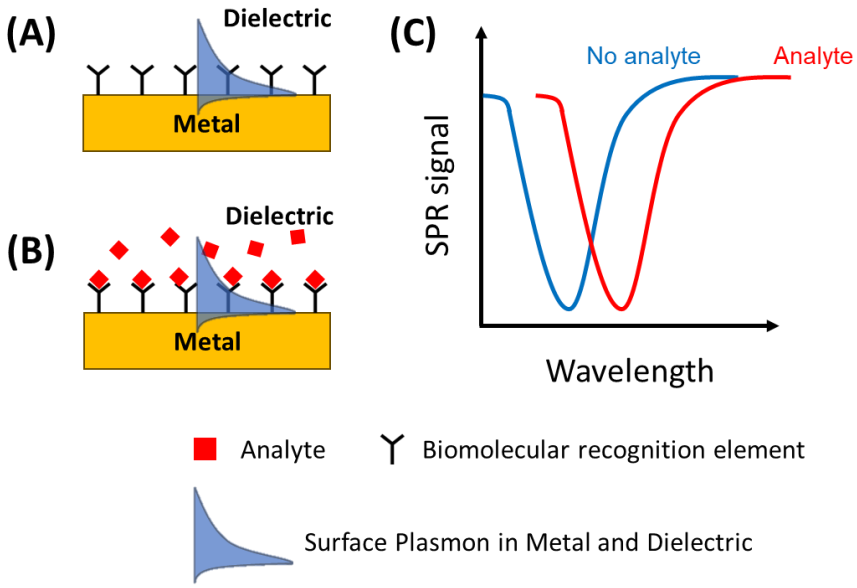

Figure 2-27 Schematic of SPR principle, with biomolecular recognition elements functionalised on a metal without (A) and with (B) analyte. The resultant increase in RI in the presence of analyte leads to a SPR signal shift (C).

The first demonstration of SPR for biosensing was performed by Liedberg *et al.* in 1983, who adsorbed Human IgG antibody onto a metal surface followed by an injection of anti-IgG into the fluid cell [77]. Using a prism and a He-Ne laser, a resultant shift in the SPR resonance angle was recorded upon anti-IgG addition. Since this time, SPR has been advanced to include various types of biorecognition elements, surface functionalisation methods, and different measurement formats to improve sensor response [76]. These advancements have greatly diversified SPR applications. Additionally, by monitoring the change in SPP resonance position over time, SPR allows for the extraction of valuable kinetic information.

Chip-SPR devices are one of the types of SPR instruments used today by several companies, such as Biacore, BioNavis, Reichert Technologies, and Biosensing Instruments [78]. These are prism-based setups effective at studying biomolecular interactions and are usually operated using one of three parameters to excite SPPs, namely angle, intensity, and wavelength modulation.

For angle-based systems, monochromatic light is utilised and the reflectance spectrum of the prism-metal chip is recorded as a function of angle. This system has been successfully

commercialised by Biacore instruments, and is regarded as the gold-standard of SPR systems today [79]. Intensity based SPR (iSPR) devices keep angle and wavelength constant, and only measure the changes in reflectivity intensities upon analyte addition. iSPR devices possess typically lower sensitivities than angle-based systems, but can be used in conjunction with a Charged-Coupled Device (CCD) camera to create a single chip with several biorecognition elements and measure multiple regions at a time [79]. Wavelength based SPR setups keep angle constant and use polychromatic light sources, obtaining reflectance spectra as a function of wavelength. This method is mostly used with Fiber Optic SPR (FO-SPR) systems, where polychromatic light is transmitted through a metal-coated fibreoptic cable to generate the SPPs. These devices are typically cheaper and less bulky than Chip-SPR platforms [79].

To present an overview of the versatility of SPR systems available, Table 2-1 presents examples of various biomolecular interactions available with Biacore chips.

Chip Substrate	Ligand	Analyte	K_d	Applications	Ref
Au	Rat sCD4	RNA-aptamer	Nanomolar order	Affinity and specificity	[80]
Au	Tat-peptide	RNA-aptamer	31 µM	TAT and Zn2+ dependent aptamer interactions	[81]
Au	DNA-Aptamer	Retinol binding protein (RBP4)	200 nM	Aptamer-based sensor for early diagnostics	[82]
Au	Thiolated DNA	DNA, RNA, and protein	-	Comparative studies	[83]
SA	Setrol carrier protein-2 (SCP-2)	Lipids	38-2060 nM	Lipid transfer protein binding of natural lipids	[84]
SA	RNA-aptamer	Anti-GST Rabbit IgG	15 pM	Binding and Kinetics	[85]
SA	RNA-aptamer	Tumor necrosis factor (TNF) proteins	0.11-960 nM	Analysis of complex formation	[86]
C1	HIV TAR	HIV-TAR	1.58 nM	Kinetics and stabilisation	[87]
CM3	Synaptic vesicle	Annexin V	0.46 nM	Real-time analysis of intact organelle binding	[88]
CM5	Anti-Human Fc	Antibody	Low nanomolar	Antigen-antibody interactions	[89]

Table 2-1 Examples of studies using Biacore SPR chips to investigate various biomolecular interactions.

From Table 2-1, an SA SPR chip is a gold chip coated with a carboxymethyl (CM) dextran matrix covalently bonded with streptavidin (SA) molecules and is used to study biotinylated moieties. C1, CM3, and CM5 have the CM dextran of different dextran chain lengths on the gold

surface and are suitable for specific ligand functionalisation. From these examples, it is evident that SPR is possesses a diverse range of applications. Using peptides, aptamers, which are short sequences of oligonucleotides that specifically bind to targets such as proteins [90], and DNA/RNA sequences, it is possible to study most biomolecular binding processes and measure kinetic data.

2.7.2 LSPR Biosensors

LSPR is the counterpart technique to SPR, relying instead on localised plasmons as opposed to propagating ones. As described earlier in Section 2.5.5, sensing using LSPR with noble metal nanoparticles relies on changes in refractive index upon analyte binding, which in turn modifies the plasmon resonance frequency.

LSPR possesses certain advantages over SPR. Firstly, LSPR is considered less susceptible to changes in bulk refractive index, and is therefore more sensitive, as the plasmons do not extend as far into bulk media of the surrounding dielectric. Typically, SPPs possess evanescent fields which extend hundreds of nanometres into the dielectric medium, whereas for LSPR this value is in the order of tens of nanometres [91]. However, this does limit LSPR to sensing relatively smaller molecules. Secondly, as LSPR does not require prism-based or fibreoptic setups to induce surface plasmons, LSPR instruments are generally more compact and simpler in design, making the sensors more portable [92]. Thirdly, LSPR sensors can be used on a broader range of substrates compared to SPR, such as silica, indium tin oxide, and quartz, again underscoring that they are not restricted to prism or fibre optic set-ups [93].

In principle an LSPR biosensor functions similar to SPR, with metal nanoparticles able to be functionalised with various bioreceptors. The initial LSPR resonance position can be controlled by adjusting the shape, size, and material of the nanoparticles [94], allowing for the tuning of the sensor for optimum performance, depending on the optical properties of the materials, detection requirements, and compatibility with biological samples. For biological applications, the resonances in the visible and near-infrared regions are most commonly preferred [95]. LSPR sensors are commonly created by coating or nanofabricating nanoparticles onto a suitable substrate. A schematic of a general LSPR biosensing set-up is presented in Figure 2-28 [96].

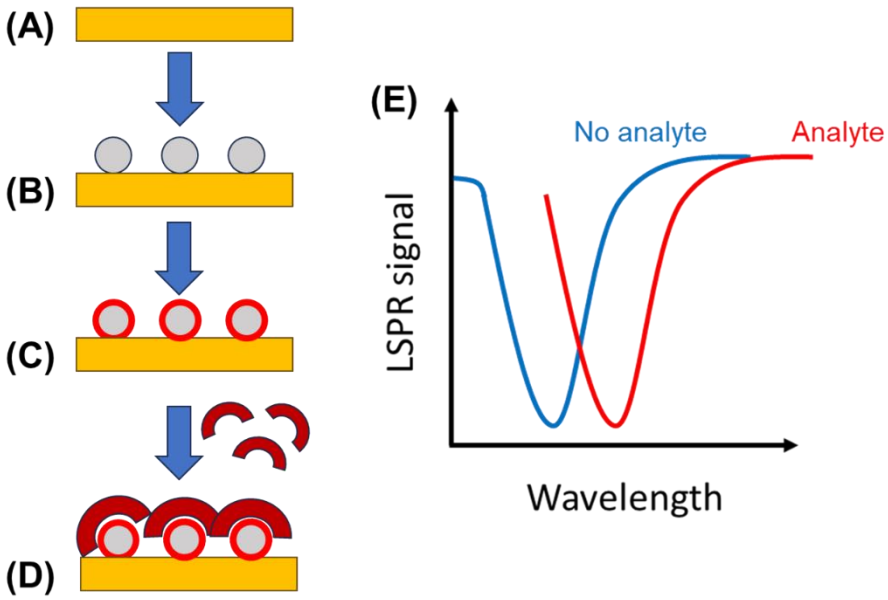

Figure 2-28 Schematic representation of simple LSPR biosensing. (A) A suitable substrate is chosen. (A) Noble metal nanoparticles are attached to the substrate. (C) Nanoparticles are functionalised with desired analyte linkers. (D) Analyte is introduced, binding to the nanoparticles and inducing a resonance shift (E).

In addition to placing nanoparticles on a substrate, LSPR sensing can also be accomplished with nanoparticles in solutions, gels or polymers, and liquid crystal matrices [97, 98].

As with SPR, the sensing capabilities are extensive given the availability of various bioreceptors. With LSPR, the choice of nanoparticle geometry also allows for added tunability to create sensors with optimised surface plasmon enhancement effects. Table 2-2 presents an overview of studies on LSPR-based biosensors, highlighting the technique's versatility.

Nanoparticle	Ligand	Analyte	Ref
Au Nanorods	anti-Hepatitis B antibody	Hepatitis B surface antigen	[99]
Hollow Au spike-NPs	Multi-functional DNA	Avian Influenza H5N1	[100]
Au coated silica NPs	GBP protein	Avian Influenza H5N1	[101]
Au NPs	Aptamer	Human Norovirus	[102]
Ag nanotriangles	Amyloid β-derived diffusible (ADDL)	ADDL-antibody	[103]

Table 2-2 Examples of studies using LSPR to investigate various biomolecular interactions using different gold (Au) and silver (Ag) nanoparticles.

Due to the geometry of the DPA nanostructures, which will be described in the following chapter, DPAs generate both SPP and LSPR plasmons, which may also hybridise. As a result, the DPA platform may be considered a hybrid between a SPR and LSPR biosensor.

2.8 Raman Spectroscopy and SERS

Raman spectroscopy is a widely used technique used to study the chemical structure and composition of molecules [104]. Most photons that interact with matter are scattered elastically (Rayleigh scattering), where the kinetic energy of the particle is conserved. Raman spectroscopy relies on inelastically scattered photons from molecules which are excited into a *virtual energy state*, where the primary photon loses or gains energy due to an interaction with the analyte molecule. The scattering of photons possessing lower energies than the original photons is known as *Stokes Raman scattering*, while scattering of photons which gain energy from the bond of a molecule in an initially excited virtual state is known as *Anti-Stokes Raman scattering* (Figure 2-29). The source of photons arrives from a monochromatic light source, which is typically a laser.

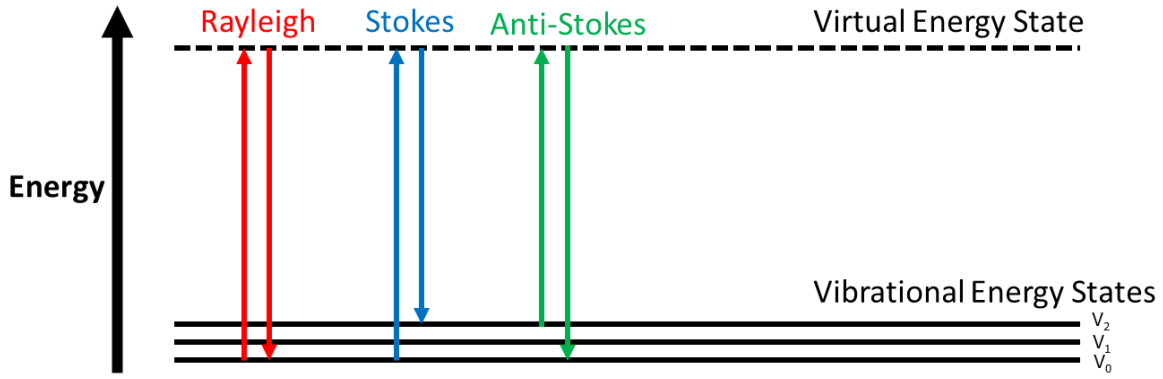

Figure 2-29 Energy level diagram depicting Rayleigh, Stokes Raman, and Anti-Stokes Raman scattering.

Due to the relatively low likelihood of inelastic scattering events as a result of low scattering cross-sections for non-resonant excitation [104], Raman spectroscopy requires high concentrations of analyte. In 1973, it was discovered that inelastic scattering events could be significantly enhanced by bringing analyte molecules into close proximity with roughened silver surfaces [105].

2.8.1 Theory of Raman Spectroscopy

An incident EM wave induces a dipole moment in matter. The strength of the induced dipole moment, *P*, is dependent on the polarizability of matter, and is given as [106]:

$$P = \alpha E \tag{2.7.1}$$

Where α is the material polarizability and *E* is the electric field amplitude of the incident EM wave. Polarisability is a material property which depends on the constituent molecules and how they are arranged in space. The electric field in and EM field may be described as:

$$E = E_0 \cos(2\pi \nu_0 t) \tag{2.7.2}$$

Where ν_0 is the angular frequency of the incident EM ($\nu_0 = c/\lambda$). We can substitute Equation 2.7.2 into Equation 2.7.1 to yield the time-dependent induced dipole moment:

$$P = \alpha E_0 \cos(2\pi \nu_0 t) \tag{2.7.3}$$

We also know that all molecular bonds are confined to quantised vibrational modes with specific energies. The vibrational energy of a mode is given as:

$$E_{vib} = \left(j + \frac{1}{2}\right) h\nu_{vib} \tag{2.7.4}$$

Where *j* is the vibrational quantum number, *h* is the Planck constant, and ν_{vib} is the vibrational mode frequency. The physical displacement of the atoms from their equilibrium position may be denoted as dQ:

$$dQ = Q_0 \cos(2\pi \nu_{vib} t) \tag{2.7.5}$$

Where Q_0 is the maximum displacement about the equilibrium position. The displacement of atoms is generally small, which allows for the polarisability to be approximated by what is known as a Taylor series expansion (an expansion of a function into an infinite sum of terms) to provide:

$$\alpha = \alpha_0 + \frac{\partial \alpha}{\partial Q} dQ \tag{2.7.6}$$

Where α_0 is the polarisability of the molecule at its equilibrium position. Based on the vibrational displacement Equation 2.7.5, the polarisability may now be given as:

$$\alpha = \alpha_0 + \frac{\partial \alpha}{\partial Q} dQ \cos(2\pi \nu_0 t) \tag{2.7.7}$$

Equation (2.7.7) may be substituted into Equation (2.7.3):

$$P = \alpha_0 E_0 \cos(2\pi\nu_0 t) + \frac{\partial\alpha}{\partial Q} Q_0 E_0 \cos(2\pi\nu_0 t)\cos(2\pi\nu_{vib} t) \quad (2.7.8)$$

Using two trigonometric identities, Equation 2.7.8 can be rewritten as:

$$P = \alpha_0 E_0 \cos(2\pi\nu_0 t) + \left(\frac{\partial\alpha}{\partial Q}\frac{Q_0 E_0}{2}\right)\{cos[2\pi(\nu_0 - \nu_{vib})t] + \cos[2\pi(\nu_0 + \nu_{vib})t]\} \quad (2.7.9)$$

The trigonometric identities use can be found in Appendix A.

From Equation 2.7.9 it can be deduced that induced dipole moments are created at three distinct frequencies: ν_0, $(\nu_0 - \nu_{vib})$, and $(\nu_0 + \nu_{vib})$ which result in scattered light. The first frequency, ν_0, corresponds to elastically scattered light (Mie or Rayleigh), which has the same frequency as the incident EM light. The other two frequencies, $(\nu_0 - \nu_{vib})$ and $(\nu_0 + \nu_{vib})$, are shifted to either lower or higher frequencies and are therefore inelastic processes. These changes in frequency are what is observed as Raman scattering.

One important detail from Equation 2.7.9 is that a necessary condition for Raman scattering is that the term $\partial\alpha/\partial Q$ must be non-zero. This means that for a molecular vibration to be Raman active, the vibrational displacement of the atoms must result in a change in polarisability. This condition is considered as the *Raman selection rule* [106].

Discrete vibrational energy states are also commonly used to describe Raman scattering. This can be represented by a vibrational energy well diagram (Figure 2-30).

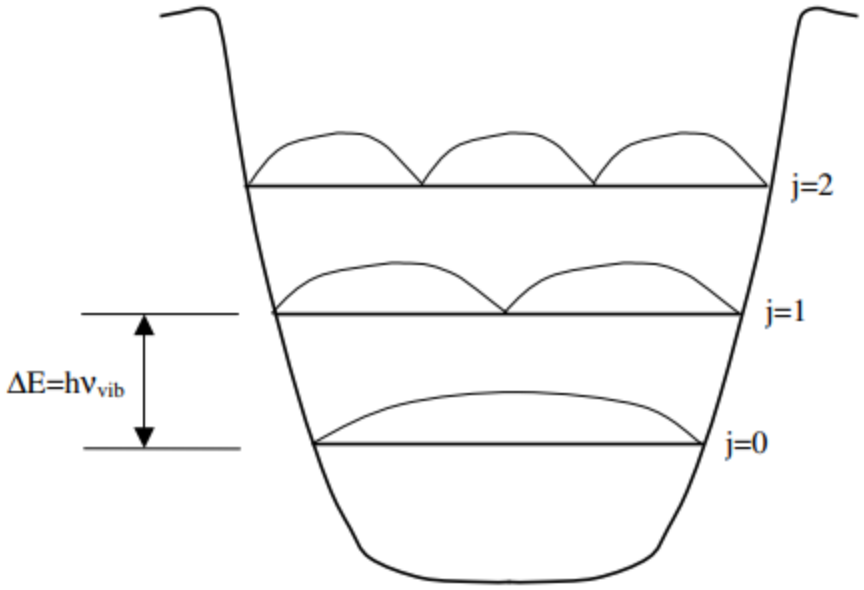

Figure 2-30 Vibrational energy well showing discrete molecular vibrational states. Figure from Hahn [106].

Every vibrational state, *j,* corresponds to a vibrational quantum number described by Equation 2.7.4. The ground state at $j = 0$ is the most favoured for a population of molecules at low temperatures in accordance with the Boltzmann distribution. Introducing an incident EM wave to the molecule generates an oscillating dipole moment, as discussed above, which places the molecule into what is called a *virtual energy state* (Figure 2-31). The energy of this state is higher than the vibrational energy states, but lower than electronic energy states - it exists in between, and the molecule remains in its ground state.

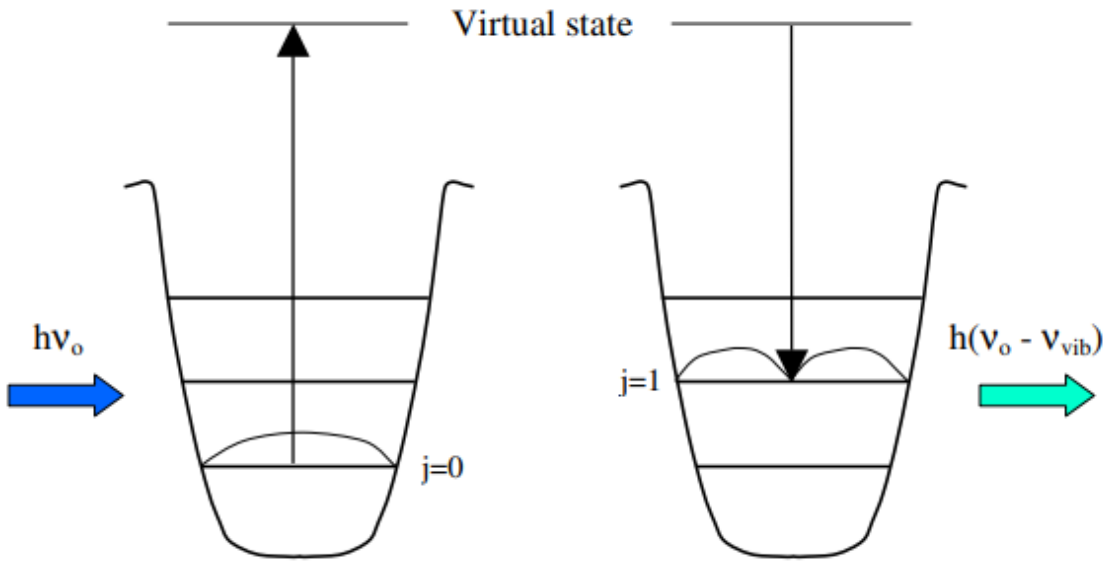

Figure 2-31 Vibrational energy wells showing the conservation of energy for Stokes shift Raman scattering. Figure from Hahn [106].

Upon relaxation from the excited virtual state back to a vibrational state a quantum of energy may be transferred to the molecule if it relaxes into a higher vibrational energy state ($j > 0$). This results in an inelastically scattered photon with lower energy equal to that of the energy gap between vibrational states. Due to the likelihood of most molecules residing in their ground states because of the Boltzmann distribution, most inelastically scattered light will possess less energy than the incident light with $h = (\nu_0 - \nu_{vib})$ (Stokes scattering). In some cases, molecules which are in an excited vibrational state ($j > 0$) will be further excited into a virtual state and relax into the ground state, resulting in an emitted photon that has gained energy $h = (\nu_0 + \nu_{vib})$ (Anti-Stokes scattering). In a Raman spectrum both Stokes and Anti-Stokes scattering is observed, with Anti-Stokes signals being lower in their respective intensities.

Raman shifts are typically presented in wavenumbers of inverse length, cm^{-1}, which is given by:

$$\Delta\tilde{\upsilon} = \left(\frac{1}{\lambda_0} - \frac{1}{\lambda}\right) \tag{2.7.10}$$

Where $\Delta\tilde{\upsilon}$ is the wavenumber, λ_0 is the excitation wavelength, and λ is the Raman spectrum wavelength.

The difference in the likelihoods of Raman scattering (inelastic) and Rayleigh scattering (elastic) events can be observed by comparing the respective cross-sections of a simple diatomic molecule such as N_2. When measuring scattering events using a 488 nm laser, the Raman scattering cross-section yields a value of 5.5×10^{-31} cm^2 sr^{-1}, which is 3 orders of magnitude lower than the Rayleigh scattering cross-section of 8.9×10^{-28} cm^2 sr^{-1} [106]. The 'sr' unit stands for *steradian*, which refers to solid angle in 3D space, and is used to measure the direction of scattered radiation. This difference in scattering intensities is further increased when investigating solids [106].

2.8.2 Surface Enhanced Raman Spectroscopy

Raman scattering is a highly unlikely process when compared with its counterpart of Rayleigh scattering. An extremely useful discovery related to Raman scattering was that this likelihood could be vastly increased by changing the local environment of the analyte, in a phenomenon now known as Surface Enhanced Raman Spectroscopy (SERS). SERS occurs with molecules in the vicinity of plasmonic materials, where the collective oscillations of electrons generate strong electromagnetic fields which can couple with the vibrational modes of the deposited molecules adsorbed on the surface, leading to enhanced Raman signals [107-109].

SERS was initially reported by Fleischmann *et al.* in 1974 [105], who observed significant increases in Raman scattering intensities from pyridine which was adsorbed onto a roughened silver substrate. Further work from Jeanmaire and Van Duyne [110], as well as Albrecht and Creighton [111] postulated that the increase in Raman signal intensity could not purely be from the increase in adsorbed molecules due to the increase in surface area from the deposited silver, but that the enhancement of scattering intensity occurred in the adsorbed state [112]. These studies sparked discussions about the mechanism(s) of SERS. Eventually, the so-called Electromagnetic Model (EM) was developed in 1980 by several groups to explain the effect [113, 114], which can account for all major SERS observations [115]. Additionally, the role of the Chemical complexation Mechanism (CM) of the analyte molecule to the plasmonic metal surface with regards to SERS has been identified. Together, the EM and CM models are the two fundamental mechanisms responsible for the vast SERS enhancement compared to conventional Raman (Figure 2-32).

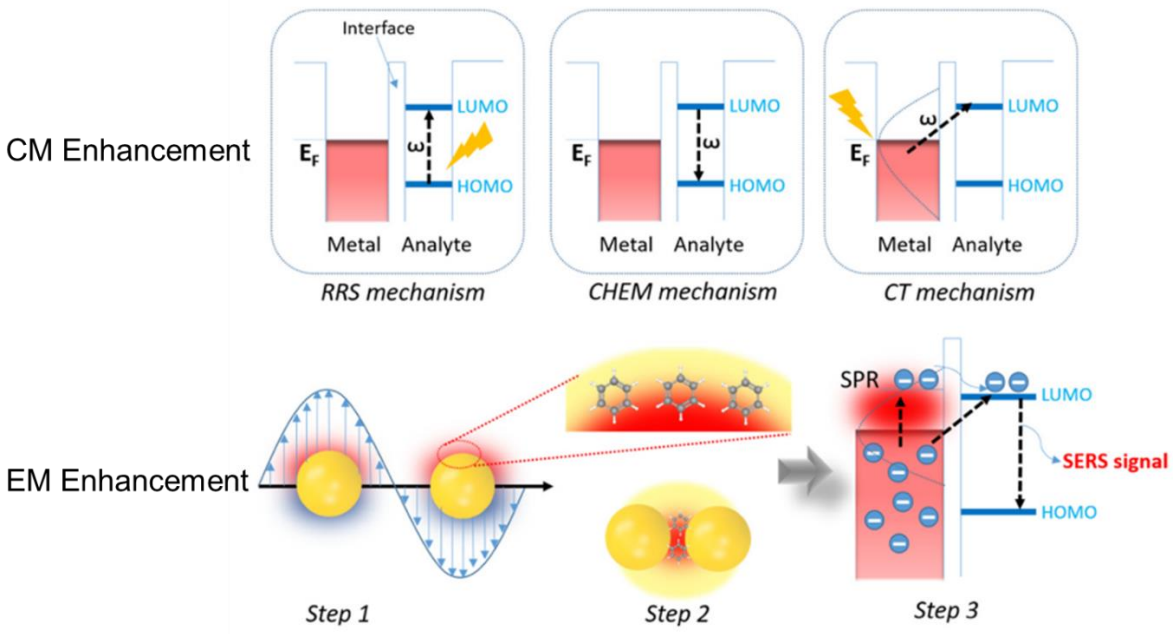

Figure 2-32 Diagram of CM and EM SERS enhancement mechanisms. Figure from Mai et al [107].

There are three contributions to the short-ranged CM effect [107]: (1) Molecular Resonance Raman Scattering (RRS), which occurs when the excitation laser is in resonance with the intermolecular vibrational transition between the Highest Occupied Molecular Orbital (HOMO) and the Lowest Unoccupied Molecular Orbital (LUMO). This mechanism has been reported to be enhanced in the presence of a metal substrate [107]. (2) Non-resonant chemical mechanism (CHEM), which is a small enhancement arising from the relaxation of the electronic structure of the molecule. (3) Charge-Transfer (CT), which results from electron transfer from the metal to the molecule from a plasmon induced hotspot through SPR.

EM is a relatively longer ranged effect when compared with CM. The overall mechanism can be understood as a three-step process [107]: (1) Plasmon oscillation induced by EM wave. (2) Local field enhancement. (3) Charge exchange between metal and the HOMO-LUMO of the molecule.

One drawback of SERS is that it is difficult to obtain SERS active substrates that have good reproducibility between samples [116]. Utilising metamaterials with their patterned arrangement of nanostructures such as the ones found in DPA samples is one way to ensure a regular distribution of active hot spots for more reproducible results. An additional benefit of molecular detection using SERS is that it is a non-intrusive and label-free technique.

The SERS spectrum of a molecule may differ from a classical Raman spectrum. The molecular vibrations closest to the metal surface will constitute the majority of the vibrational bands. SERS spectra can also possess additional vibrational modes from the sample absorbed to the substrate. An example of a Raman spectrum of a thiophenol molecule compared to a SERS measurement is presented in Figure 2-33.

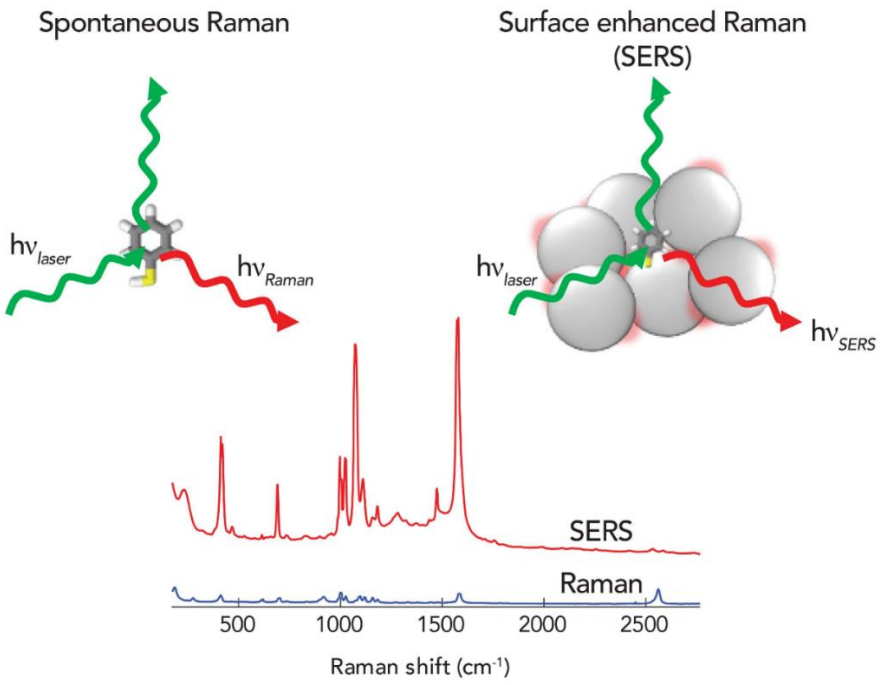

Figure 2-33 Example of regular Raman and SERS scattering of a thiophenol molecule. Image from Shultz [117].

2.8.3 Raman Optical Activity

Results Chapter 5 explores the phenomenon of chirally dependent SERS, which can be easily confused with Surface Enhanced Raman Optical Activity (SEROA). To distinguish between the two effects, this section will briefly detail SEROA and its difference to chirally dependent SERS.

When illuminating enantiomers of chiral molecules with LH or RH circularly polarised laser light, small differences in Raman scattering intensities can be detected – a technique termed Raman Optical Activity (ROA). Similar to CD measurements, the disadvantage of ROA is that signals are weak, around 3-5 orders of magnitude smaller than the already weak conventional Raman signal [118]. This necessitates high concentrations of samples and lengthy data collection times to achieve adequate results, which significantly limits ROA applications. Efrima was the

first to suggest that by using plasmonic metal surfaces or nanoparticles, SERS and ROA can be combined to perform SEROA [119].

The unit for (SE)ROA measurements is Circular Intensity Difference (CID), and is defined as:

$$\Delta = \frac{(I_{RH} - I_{LH})}{(I_{RH} + I_{LH})} \tag{2.7.11}$$

Where I_{RH} and I_{LH} are the intensities of inelastically scattered light for RH and LH CPL respectively.

The analysis of SEROA measurements is complex in comparison with ROA, as plasmon resonances and the anisotropic environment of metal-analyte interface can severely impact ROA scattering. Additionally, even with enhancement, SEROA measurements are still relatively weak, and the acquisition of results can thus be time consuming [120].

These complications are not present when chirally dependent SERS is investigated, as SERS intensity differences arise from the differential interplay between the chiral materials being analysed and the chiral EM fields generated by the nanostructures, as opposed to measured intensity differences of LH and RH CPL excitation.

2.8.4 Chiral Discrimination Using SERS

To enhance of the chiral discrimination capabilities from ROA and increase reproducibility of SEROA, chiral metamaterials – such as DPAs – can be utilised to enhance signals and create consistent regions of chiral EM fields. This can be accomplished using either circularly or linearly polarised light with the combination of a suitable metamaterial. In both cases the general mode of action is to excite chiral plasmons, which interact differentially with deposited enantiomers based on the enantiomer and handedness of the metamaterial units. There are several proposed mechanisms for this response, and these will be discussed further in Chapter 5.

One of the first studies related to this field was conducted by Kalachyova *et al*., who prepared a polymer surface with a deposited gold surface capable of supporting SPPs [121]. The surfaces of these substrates were then functionalised with chiral (M- or P-) helicenes, which are organic molecules characterised by their helical arrangement of carbon atoms (Figure 2-34). M-helicenes

rotate clockwise and P-helicenes rotate counter-clockwise. Helicenes possess high values of optical activity, and these were shown to influence the SPPs to give them chiral character.

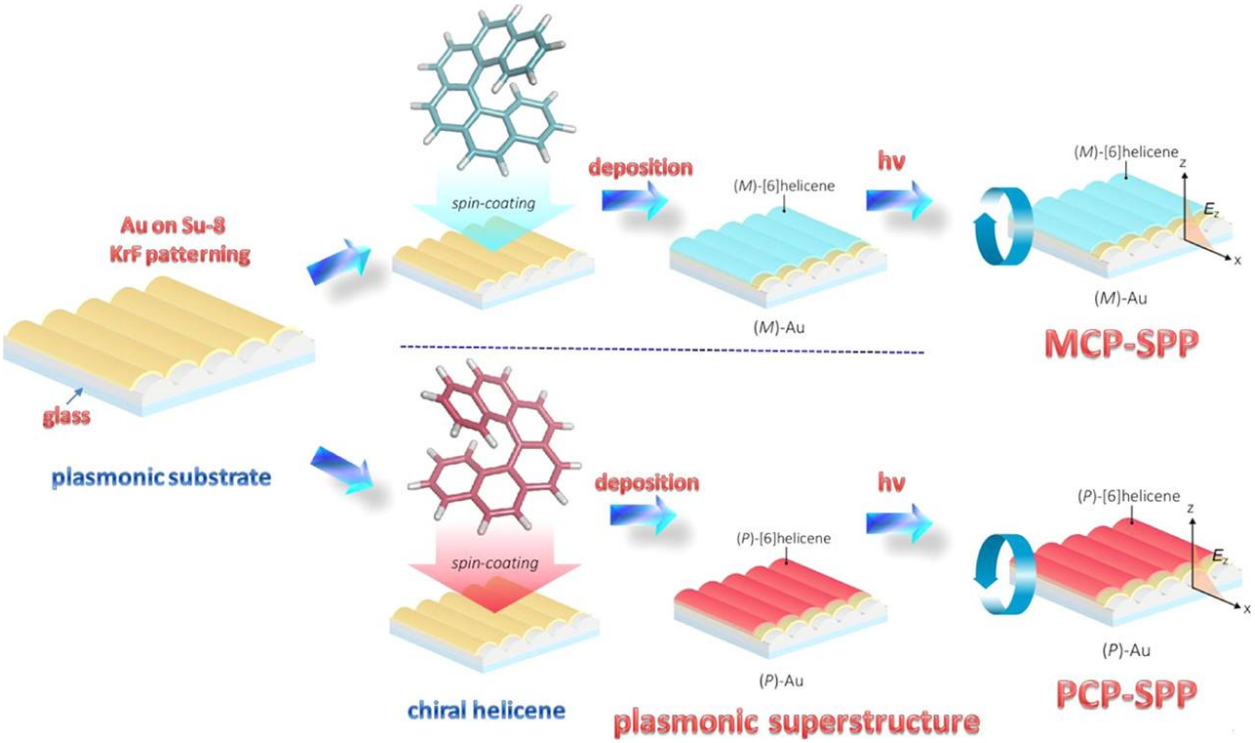

Figure 2-34 Schematic representation of the chiral plasmonic substrate preparation, with substrates coated with either M- (top) or P-helicenes (bottom) from study by Kalachyova et al. Upon excitation with light, chiral SPPs are generated. Image from Kalachyova et al.

This gold-helicene plasmonic hybrid structure was shown to achieve SERS enantioselective discrimination for many different enantiomeric compounds, such as cysteine, tartaric acid, and dihydroxyphenylalanine. These compounds were drop-deposited on the prepared M- or P-helicene substrates, and differences in SERS spectra identified. The SERS results for cysteine are presented in Figure 2-35.

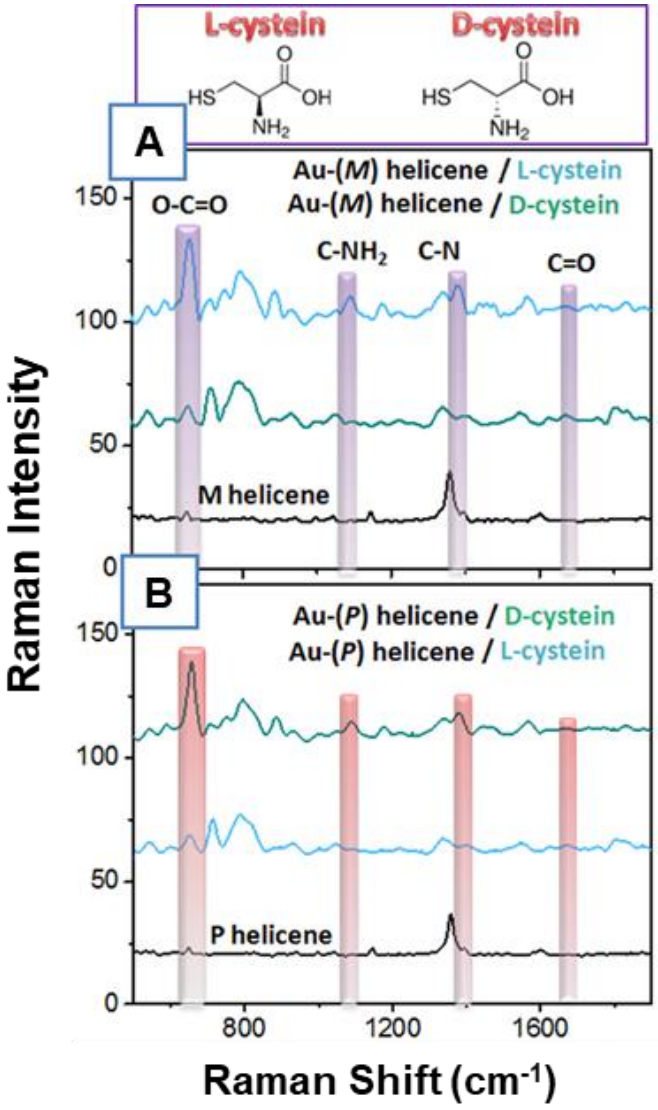

Figure 2-35 SERS spectra of L- (blue) and D-cysteine (green) enantiomers deposited on M-helicene (A) and P-helicene (B) gold substrates. Black lines represent SERS measurements from helicene coated samples before enantiomer introduction. Image from Kalachyova et al.

The differences between the SERS spectra of L- and D-cysteine are evident, with L-cysteine possessing higher intensities of characteristic Raman bands on M-helicene coated substrates. This effect was found to be reversed on the P-helicene coated substrate, confirming that these results arise from the interplay between the chirality of the helicene and enantiomer in question.

In another study, Sun *et al*. fabricated chiral silver nanorods which could remotely enhance Raman and ROA signals of chiral molecules [122]. The propagation direction of the chiral plasmons could be controlled by altering the polarisation of incident light, allowing for the accurate excitation and enhancement of the Raman and ROA signals. Zhang *et al*. utilised chiral

crescent shaped nanostructures to also perform enantiomeric discrimination of cysteine, with the crescent tips possessing sub-10 nm gaps creating regions of EM hotspots with enhanced chiroptical properties [123]. These are some examples of the versatility of chiral metamaterials, and how they can be applied for SERS applications and enantiomeric discrimination.

2.9 References

1. Fleisch, D., *A student's guide to Maxwell's equations*. 2008: Cambridge University Press.
2. Maxwell, J.C., *VIII. A dynamical theory of the electromagnetic field.* Philosophical transactions of the Royal Society of London, 1865(155): p. 459-512.
3. Wang, Z.L., *On the first principle theory of nanogenerators from Maxwell's equations.* Nano Energy, 2020. **68**: p. 104272.
4. Prentiss, M., *Energy revolution: The physics and the promise of efficient technology*. 2015: Harvard University Press.
5. Maier, S.A., *Plasmonics: fundamentals and applications*. Vol. 1. 2007: Springer.
6. Graneau, P., *Ampere and Lorentz forces.* Physics Letters A, 1985. **107**(5): p. 235-237.
7. Cloude, S., *Polarisation: applications in remote sensing*. 2009: OUP Oxford.
8. Silverman, M., *Differential amplification of circularly polarised light by enhanced internal reflection from an active chiral medium.* Optics communications, 1989. **74**(3-4): p. 134-138.
9. Arteaga, O., E. Garcia-Caurel, and R. Ossikovski, *The Fresnel triprism and the circular polarization of light.* Photoniques, 2019: p. 44-45.
10. Goldstein, D.H., *Polarized light*. 2017: CRC press.
11. Collins, J.T., et al., *Chirality and chiroptical effects in metal nanostructures: fundamentals and current trends.* Advanced Optical Materials, 2017. **5**(16): p. 1700182.
12. Barron, L.D., *Molecular light scattering and optical activity*. 2009: Cambridge University Press.
13. Riehl, J.P., *Mirror-image asymmetry: An introduction to the origin and consequences of chirality*. 2010: John Wiley & Sons.
14. Vargesson, N. and T. Stephens, *Thalidomide: history, withdrawal, renaissance, and safety concerns.* Expert Opinion on Drug Safety, 2021. **20**(12): p. 1455-1457.
15. He, Q., et al., *Sertraline racemate and enantiomer: solid-state characterization, binary phase diagram, and crystal structures.* Crystal growth & design, 2010. **10**(4): p. 1633-1645.
16. Nafie, L.A., *Vibrational optical activity: Principles and applications*. 2011: John Wiley & Sons.
17. Biot, L., *Observations médicales, recueillies dans une petite contrée du pays de Liège, depuis 1800 jusqu'en 1808, etc*. 1812.
18. Mason, S.F. and S.F. Mason, *Molecular optical activity and the chiral discriminations*. 1982: Cambridge University Press.
19. Lucarini, V., et al., *Kramers-Kronig relations in optical materials research*. Vol. 110. 2005: Springer Science & Business Media.
20. Kuball, H.-G. and J. Altschuh, *Optical activity of oriented molecules. comparison of the optical rotatory dispersion and the circular dichroism through the kramers-kronig transform.* Chemical Physics Letters, 1982. **87**(6): p. 599-603.
21. Chen, X., et al., *Kramers–Kronig receivers for 100-km datacenter interconnects.* Journal of Lightwave Technology, 2018. **36**(1): p. 79-89.
22. Nagata, Y. and T. Mori, *Irreverent nature of dissymmetry factor and quantum yield in circularly polarized luminescence of small organic molecules.* Frontiers in Chemistry, 2020. **8**: p. 448.

23. Tang, Y. and A.E. Cohen, *Optical chirality and its interaction with matter*. Physical review letters, 2010. **104**(16): p. 163901.
24. Lipkin, D.M., *Existence of a new conservation law in electromagnetic theory*. Journal of Mathematical Physics, 1964. **5**(5): p. 696-700.
25. Tang, Y. and A.E. Cohen, *Enhanced enantioselectivity in excitation of chiral molecules by superchiral light.* Science, 2011. **332**(6027): p. 333-336.
26. Bilotti, F. and L. Sevgi, *Metamaterials: Definitions, properties, applications, and FDTD-based modeling and simulation.* International Journal of RF and Microwave Computer-Aided Engineering, 2012. **22**(4): p. 422-438.
27. Maier, S.A., *Plasmonics: fundamentals and applications*. 2007: Springer Science & Business Media.
28. Novotny, L. and B. Hecht, *Principles of nano-optics*. 2012: Cambridge university press.
29. Gérard, D. and S.K. Gray, *Aluminium plasmonics.* Journal of Physics D: Applied Physics, 2014. **48**(18): p. 184001.
30. Hummel, R.E., *Electronic properties of materials*. 2011: Springer Science & Business Media.
31. Assmus, A., *Early history of X rays.* Beam Line, 1995. **25**(2): p. 10-24.
32. Bohren, C.F. and D.R. Huffman, *Absorption and scattering of light by small particles*. 2008: John Wiley & Sons.
33. Gerardo, J. and J. Verdeyen, *Plasma refractive index by a laser phase measurement.* Applied Physics Letters, 1963. **3**(7): p. 121-123.
34. Hummel, R.E. and R.E. Hummel, *Electrical properties of materials.* Understanding Materials Science: History· Properties· Applications, 1998: p. 180-216.
35. Johnson, P.B. and R.-W. Christy, *Optical constants of the noble metals.* Physical review B, 1972. **6**(12): p. 4370.
36. Giannini, V., et al., *Plasmonic nanoantennas: fundamentals and their use in controlling the radiative properties of nanoemitters.* Chemical reviews, 2011. **111**(6): p. 3888-3912.
37. Zhang, J., L. Zhang, and W. Xu, *Surface plasmon polaritons: physics and applications.* Journal of Physics D: Applied Physics, 2012. **45**(11): p. 113001.
38. Bhattacharjee, P.R., *Refinement of the definitions of angles of incidence, reflection, refraction, and critical angle in ray optics.* Optik, 2018. **172**: p. 1187-1192.
39. Ramanandan, G., et al., *Emission of terahertz pulses from nanostructured metal surfaces.* Journal of Physics D: Applied Physics, 2014. **47**(37): p. 374003.
40. Rodriguez, S.R.K., et al., *Coupling bright and dark plasmonic lattice resonances.* Physical Review X, 2011. **1**(2): p. 021019.
41. Prodan, E., et al., *A hybridization model for the plasmon response of complex nanostructures.* science, 2003. **302**(5644): p. 419-422.
42. Hentschel, M., et al., *Transition from isolated to collective modes in plasmonic oligomers.* Nano letters, 2010. **10**(7): p. 2721-2726.
43. Abdulla, H.M., R. Thomas, and R.S. Swathi, *Overwhelming analogies between plasmon hybridization theory and molecular orbital theory revealed: The story of plasmonic heterodimers.* The Journal of Physical Chemistry C, 2018. **122**(13): p. 7382-7388.
44. Lovera, A., et al., *Mechanisms of Fano resonances in coupled plasmonic systems.* ACS nano, 2013. **7**(5): p. 4527-4536.
45. Zentgraf, T., et al., *Ultranarrow coupling-induced transparency bands in hybrid plasmonic systems.* Physical Review B, 2009. **80**(19): p. 195415.

46. Kelly, K.L., et al., *The optical properties of metal nanoparticles: the influence of size, shape, and dielectric environment*. 2003, ACS Publications. p. 668-677.
47. Goerlitzer, E.S., et al., *The Beginner's Guide to Chiral Plasmonics: Mostly Harmless Theory and the Design of Large-Area Substrates.* Advanced Optical Materials, 2021. **9**(16): p. 2100378.
48. Lindell, I., et al., *Electromagnetic waves in chiral and bi-isotropic media*. 1994: Artech House.
49. Sersic, I., et al., *Ubiquity of optical activity in planar metamaterial scatterers.* Physical review letters, 2012. **108**(22): p. 223903.
50. Wu, W. and M. Pauly, *Chiral plasmonic nanostructures: recent advances in their synthesis and applications.* Materials Advances, 2022. **3**(1): p. 186-215.
51. Valev, V.K., *Chiral nanomaterials and chiral light.* Optics and Photonics News, 2016. **27**(7): p. 34-41.
52. Wang, Z., et al., *Optical chiral metamaterials: a review of the fundamentals, fabrication methods and applications.* Nanotechnology, 2016. **27**(41): p. 412001.
53. Liu, Y. and X. Zhang, *Metamaterials: a new frontier of science and technology.* Chemical Society Reviews, 2011. **40**(5): p. 2494-2507.
54. Smith, D.R., J.B. Pendry, and M.C. Wiltshire, *Metamaterials and negative refractive index.* Science, 2004. **305**(5685): p. 788-792.
55. Smith, D.R. and N. Kroll, *Negative refractive index in left-handed materials.* Physical review letters, 2000. **85**(14): p. 2933.
56. Pendry, J.B., et al., *Magnetism from conductors and enhanced nonlinear phenomena.* IEEE transactions on microwave theory and techniques, 1999. **47**(11): p. 2075-2084.
57. Pendry, J.B., et al., *Extremely low frequency plasmons in metallic mesostructures.* Physical review letters, 1996. **76**(25): p. 4773.
58. Rogacheva, A., et al., *Giant gyrotropy due to electromagnetic-field coupling in a bilayered chiral structure.* Physical review letters, 2006. **97**(17): p. 177401.
59. Schäferling, M., et al., *Tailoring enhanced optical chirality: design principles for chiral plasmonic nanostructures.* Physical Review X, 2012. **2**(3): p. 031010.
60. Zhang, S., et al., *Negative refractive index in chiral metamaterials.* Physical review letters, 2009. **102**(2): p. 023901.
61. Warning, L.A., et al., *Nanophotonic approaches for chirality sensing.* ACS nano, 2021. **15**(10): p. 15538-15566.
62. Gansel, J.K., et al., *Gold helix photonic metamaterial as broadband circular polarizer.* science, 2009. **325**(5947): p. 1513-1515.
63. Papakostas, A., et al., *Optical manifestations of planar chirality.* Physical review letters, 2003. **90**(10): p. 107404.
64. Bai, B., et al., *Optical activity in planar chiral metamaterials: Theoretical study.* Physical Review A, 2007. **76**(2): p. 023811.
65. Karimullah, A.S., et al., *Disposable plasmonics: plastic templated plasmonic metamaterials with tunable chirality.* Advanced Materials, 2015. **27**(37): p. 5610-5616.
66. Cooper, M.A., *Label-free biosensors: techniques and applications*. 2009: Cambridge University Press.
67. Cao, X., Y. Ye, and S. Liu, *Gold nanoparticle-based signal amplification for biosensing.* Analytical biochemistry, 2011. **417**(1): p. 1-16.

68. Er, O., et al., *Investigation of vipera anatolica venom disintegrin via intracellular uptake with radiolabeling study and cell-based electrochemical biosensing assay.* Applied biochemistry and biotechnology, 2019. **187**: p. 1539-1550.
69. Wu, Y., C. Chen, and S. Liu, *Enzyme-functionalized silica nanoparticles as sensitive labels in biosensing.* Analytical Chemistry, 2009. **81**(4): p. 1600-1607.
70. Rapp, B.E., F.J. Gruhl, and K. Länge, *Biosensors with label-free detection designed for diagnostic applications.* Analytical and bioanalytical chemistry, 2010. **398**(6): p. 2403-2412.
71. Samuel, V.R. and K.J. Rao, *A review on label free biosensors.* Biosensors and Bioelectronics: X, 2022: p. 100216.
72. Sang, S., et al., *Progress of new label-free techniques for biosensors: a review.* Critical reviews in biotechnology, 2016. **36**(3): p. 465-481.
73. Budd, J., et al., *Lateral flow test engineering and lessons learned from COVID-19.* Nature Reviews Bioengineering, 2023. **1**(1): p. 13-31.
74. Peng, P., et al., *Emerging ELISA derived technologies for in vitro diagnostics.* TrAC Trends in Analytical Chemistry, 2022. **152**: p. 116605.
75. Rahman, M.T., et al., *Polymerase chain reaction (PCR): a short review.* Anwer Khan Modern Medical College Journal, 2013. **4**(1): p. 30-36.
76. Guo, X., *Surface plasmon resonance based biosensor technique: a review.* Journal of biophotonics, 2012. **5**(7): p. 483-501.
77. Liedberg, B., C. Nylander, and I. Lunström, *Surface plasmon resonance for gas detection and biosensing.* Sensors and actuators, 1983. **4**: p. 299-304.
78. Kuncová-Kallio, J., et al., *Optical and Acoustic Label-free Instrumentation for Molecular Detection with a Focus on Food.* Rapid Antibody-based Technologies in Food Analysis, 2019: p. 223-255.
79. Qu, J.-H., et al., *Advancements in SPR biosensing technology: An overview of recent trends in smart layers design, multiplexing concepts, continuous monitoring and in vivo sensing.* Analytica Chimica Acta, 2020. **1104**: p. 10-27.
80. Kraus, E., W. James, and A.N. Barclay, *Cutting edge: novel RNA ligands able to bind CD4 antigen and inhibit CD4+ T lymphocyte function.* The Journal of Immunology, 1998. **160**(11): p. 5209-5212.
81. Kawakami, J., et al., *In vitro selection of aptamers that act with Zn2+.* Journal of Inorganic Biochemistry, 2000. **82**(1-4): p. 197-206.
82. Lee, S.J., et al., *ssDNA aptamer-based surface plasmon resonance biosensor for the detection of retinol binding protein 4 for the early diagnosis of type 2 diabetes.* Analytical chemistry, 2008. **80**(8): p. 2867-2873.
83. Gopinath, S.C., et al., *Monitoring biomolecular interactions on a digital versatile disk: A BioDVD platform technology.* ACS nano, 2008. **2**(9): p. 1885-1895.
84. Kernstock, R.M. and A.W. Girotti, *Lipid transfer protein binding of unmodified natural lipids as assessed by surface plasmon resonance methodology.* Analytical biochemistry, 2007. **365**(1): p. 111-121.
85. Yoshida, Y., et al., *Rabbit antibody detection with RNA aptamers.* Analytical Biochemistry, 2008. **375**(2): p. 217-222.
86. Mori, T., et al., *RNA aptamers selected against the receptor activator of NF-κB acquire general affinity to proteins of the tumor necrosis factor receptor family.* Nucleic acids research, 2004. **32**(20): p. 6120-6128.

87. Nair, T.M., D.G. Myszka, and D.R. Davis, *Surface plasmon resonance kinetic studies of the HIV TAR RNA kissing hairpin complex and its stabilization by 2-thiouridine modification.* Nucleic Acids Research, 2000. **28**(9): p. 1935-1940.
88. Ferracci, G., et al., *Real time analysis of intact organelles using surface plasmon resonance.* Analytical biochemistry, 2004. **334**(2): p. 367-375.
89. Canziani, G.A., S. Klakamp, and D.G. Myszka, *Kinetic screening of antibodies from crude hybridoma samples using Biacore.* Analytical biochemistry, 2004. **325**(2): p. 301-307.
90. Keefe, A.D., S. Pai, and A. Ellington, *Aptamers as therapeutics.* Nature reviews Drug discovery, 2010. **9**(7): p. 537-550.
91. Kim, D.M., et al., *Biosensing applications using nanostructure-based localized surface plasmon resonance sensors.* Sensors, 2021. **21**(9): p. 3191.
92. Singh, P., *LSPR Biosensing: Recent Advances and Approaches.* Reviews in Plasmonics 2016, 2017: p. 211-238.
93. Szunerits, S. and R. Boukherroub, *Sensing using localised surface plasmon resonance sensors.* Chemical Communications, 2012. **48**(72): p. 8999-9010.
94. Xu, T. and Z. Geng, *Strategies to improve performances of LSPR biosensing: Structure, materials, and interface modification.* Biosensors and Bioelectronics, 2021. **174**: p. 112850.
95. Wang, B., et al., *Design of aluminum bowtie nanoantenna array with geometrical control to tune LSPR from UV to near-IR for optical sensing.* Plasmonics, 2020. **15**: p. 609-621.
96. Sepúlveda, B., et al., *LSPR-based nanobiosensors.* nano today, 2009. **4**(3): p. 244-251.
97. Chen, Y.-C., et al., *Plasmonic gel films for time-lapse LSPR detection of hydrogen peroxide secreted from living cells.* Sensors and Actuators B: Chemical, 2021. **336**: p. 129725.
98. Yakovkin, I. and V. Reshetnyak. *Controlling Plasmon Resonance of Gold and Silver Nanoparticle Arrays with Help of Liquid Crystal*. in *Photonics*. 2023. MDPI.
99. Wang, X., et al., *Gold nanorod-based localized surface plasmon resonance biosensor for sensitive detection of hepatitis B virus in buffer, blood serum and plasma.* Biosensors and Bioelectronics, 2010. **26**(2): p. 404-410.
100. Lee, T., et al., *Label-free localized surface plasmon resonance biosensor composed of multi-functional DNA 3 way junction on hollow Au spike-like nanoparticles (HAuSN) for avian influenza virus detection.* Colloids and Surfaces B: Biointerfaces, 2019. **182**: p. 110341.
101. Park, T.J., et al., *Development of label-free optical diagnosis for sensitive detection of influenza virus with genetically engineered fusion protein.* Talanta, 2012. **89**: p. 246-252.
102. Weerathunge, P., et al., *Ultrasensitive colorimetric detection of murine norovirus using NanoZyme aptasensor.* Analytical chemistry, 2019. **91**(5): p. 3270-3276.
103. Haes, A.J., et al., *A localized surface plasmon resonance biosensor: First steps toward an assay for Alzheimer's disease.* Nano letters, 2004. **4**(6): p. 1029-1034.
104. Sackmann, M. and A. Materny, *Surface enhanced Raman scattering (SERS)—a quantitative analytical tool?* Journal of Raman Spectroscopy: An International Journal for Original Work in all Aspects of Raman Spectroscopy, Including Higher Order Processes, and also Brillouin and Rayleigh Scattering, 2006. **37**(1-3): p. 305-310.
105. Fleischmann, M., P.J. Hendra, and A.J. McQuillan, *Raman spectra of pyridine adsorbed at a silver electrode.* Chemical physics letters, 1974. **26**(2): p. 163-166.

106. Hahn, D.W., *Raman scattering theory.* Department of Mechanical and Aerospace Engineering, University of Florida, 2007.
107. Mai, Q.D., et al., *Silver Nanoparticles-Based SERS Platform towards Detecting Chloramphenicol and Amoxicillin: An Experimental Insight into the Role of HOMO–LUMO Energy Levels of the Analyte in the SERS Signal and Charge Transfer Process.* The Journal of Physical Chemistry C, 2022. **126**(17): p. 7778-7790.
108. Pérez-Jiménez, A.I., et al., *Surface-enhanced Raman spectroscopy: benefits, trade-offs and future developments.* Chemical science, 2020. **11**(18): p. 4563-4577.
109. Pilot, R., et al., *A review on surface-enhanced Raman scattering.* Biosensors, 2019. **9**(2): p. 57.
110. Jeanmaire, D.L. and R.P. Van Duyne, *Surface Raman spectroelectrochemistry: Part I. Heterocyclic, aromatic, and aliphatic amines adsorbed on the anodized silver electrode.* Journal of electroanalytical chemistry and interfacial electrochemistry, 1977. **84**(1): p. 1-20.
111. Albrecht, M.G. and J.A. Creighton, *Anomalously intense Raman spectra of pyridine at a silver electrode.* Journal of the american chemical society, 1977. **99**(15): p. 5215-5217.
112. Campion, A. and P. Kambhampati, *Surface-enhanced Raman scattering.* Chemical society reviews, 1998. **27**(4): p. 241-250.
113. Gersten, J.I., *The effect of surface roughness on surface enhanced Raman scattering.* The Journal of Chemical Physics, 1980. **72**(10): p. 5779-5780.
114. McCall, S. and P. Platzman, *Raman scattering from chemisorbed molecules at surfaces.* Physical Review B, 1980. **22**(4): p. 1660.
115. Kneipp, K., M. Moskovits, and H. Kneipp, *Surface-enhanced Raman scattering: physics and applications*. Vol. 103. 2006: Springer Science & Business Media.
116. Kalachyova, Y., et al., *Surface plasmon polaritons on silver gratings for optimal SERS response.* The Journal of Physical Chemistry C, 2015. **119**(17): p. 9506-9512.
117. Schultz, Z., *SERS and TERS.* 2020.
118. Pour, S.O., S.E. Bell, and E.W. Blanch, *Use of a hydrogel polymer for reproducible surface enhanced Raman optical activity (SEROA).* Chemical Communications, 2011. **47**(16): p. 4754-4756.
119. Efrima, S., *The effect of large electric field gradients on the Raman optical activity of molecules adsorbed on metal surfaces.* Chemical physics letters, 1983. **102**(1): p. 79-82.
120. Abdali, S. and E.W. Blanch, *Surface enhanced Raman optical activity (SEROA).* Chemical Society Reviews, 2008. **37**(5): p. 980-992.
121. Kalachyova, Y., et al., *Helicene-SPP-based chiral plasmonic hybrid structure: toward direct enantiomers SERS discrimination.* ACS applied materials & interfaces, 2018. **11**(1): p. 1555-1562.
122. Sun, M., et al., *Remotely excited Raman optical activity using chiral plasmon propagation in Ag nanowires.* Light: Science & Applications, 2013. **2**(11): p. e112-e112.
123. Zhang, W., et al., *Plasmonic chiral metamaterials with sub-10 nm nanogaps.* ACS nano, 2021. **15**(11): p. 17657-17667.

Chapter 3 – Experimental

This chapter outlines the fabrication and experimental methods employed throughout this thesis. This includes the nanofabrication of DPAs, chemical surface functionalisation techniques, and the experimental procedures used to measure spectroscopic data from the samples, such as ORD, reflectivity, and Raman spectroscopy. Examples of DPA optical properties and characterisation of electric fields using EM simulations are also provided.

3.1 Nanostructure Fabrication

3.1.1 Electron-Beam Lithography

Lithography is a useful technique used to transfer designs onto a base substrate [1]. Electrons in Electron-Beam Lithography (EBL) can be used in a focused beam to write incredibly small and precise patterns onto a surface, ideal for the nanostructures used in the DPA samples of this thesis. The energetic electrons are used to modify the chemical composition of a surface mask, making it either more or less soluble than unwritten regions of the mask. Once the surface mask is submerged in a developing solution, the written pattern is obtained as either extrusions or intrusions depending on the type of mask used. A positive resist changes the chemical mask structure so that it becomes more soluble, whereas a negative resist mask will become cross-linked in the written sections and become insoluble (Figure 3-1). Using electrons instead of visible-UV light allows for a much more focused beam, which can achieve sub-10 nm resolutions [2]. Some disadvantages of EBL to be mindful of are the significantly low throughput times, high costs, and proximity effects. The proximity effect occurs when electrons ‘spill over’ into adjacent regions of the resist mask, enlarging the image and reducing its contrast.

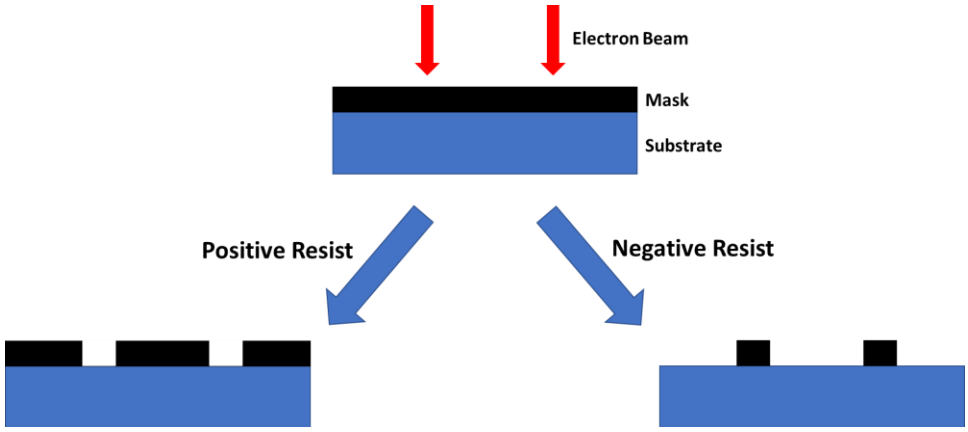

Figure 3-1 Diagram depicting a simple pattern after EBL using either a positive resist mask or a negative resist mask.

EBL is ideal for generating chiral metamaterial surfaces. For DPA samples, a nickel metal master template - or shim - with the pattern of nanostructures etched on, is used in conjunction with a Victory 28, Engel GmbH injection moulder (Figure 3-2) to generate a large quantity of polycarbonate slides with the inverse pattern of the shim. A thin layer of gold - 120 nm - is then evaporated onto the polycarbonate slides using physical vapour deposition to create the final DPA sample. This high-throughput method of fabrication allows for the creation of multiple samples with high pattern reproducibility.

To create the nickel shim, a silicon wafer is first cleaned with acetone, methanol, and isopropyl alcohol (IPA), followed by sonication, and drying with N_2 gas. A common positive photoresist PMMA (Poly(methyl methacrylate)) is then spin coated onto the wafer to achieve a resist thickness of 110 nm. The coated wafer is then ‘baked’ on a hotplate at 180 °C for 5 minutes to allow for drying. This step removes any remaining solvent. The nanostructure patterns are then etched with an electron beam writer (Vistec VB6), which breaks down PMMA polymer chains in the exposed regions. The substrate is then developed in IPA:MIBK (methyl isobutyl ketone) (2.5:1 v/v ratio) for 60 seconds at 23.7 °C to remove the exposed and now soluble PMMA. The final stages of nickel shim production are to electroplate the substrate with 1 mm of nickel and perform a metal lift-off (Figure 3-3).

Figure 3-2 Front view stock image of an Engel Victory 28 injection moulder used to create polycarbonate DPA templates.

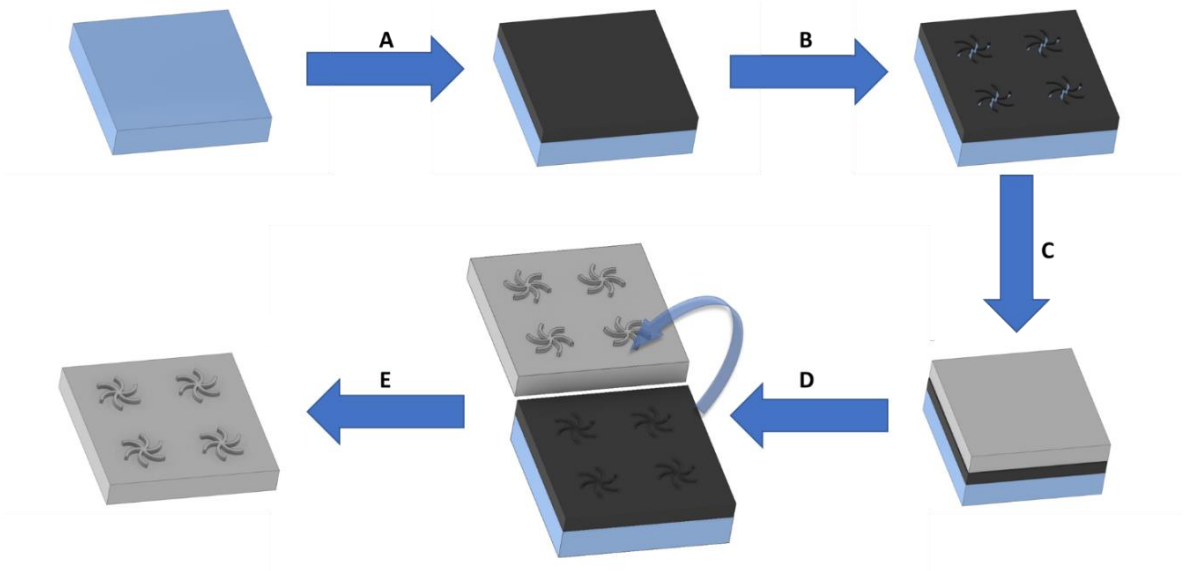

Figure 3-3 Schematic of Electron Beam Lithography (EBL) process for the fabrication nickel shim with shuriken-shaped nanostructures. A) Spin Coating of PMMA onto a cleaned silicon wafer. B) EBL etching and development with IPA:MIBK. C) Nickel metal plating. D) Lift-off of nickel shim. E) Cleaning of shim for final product.

Using the nickel shim, injection moulding with polycarbonate is performed using the hydraulic injection moulder to replicate the nanostructure features onto a clear polycarbonate template (Figure 3-4A). A temperature of 280 °C is used to melt polycarbonate pellets, which is then injected into the mould at an injection speed of 50 cm^3 s^{-1}. This is then cooled for 10 seconds after which the imprinted polycarbonate slide is ejected from the machine. This process is usually repeated to produce 100-200 samples at a time. The flow, temperature, and cooling parameters of the molten polycarbonate are carefully chosen to ensure high-quality nanostructure duplication [3]. Once cooled, the polycarbonate slides can be prepared for gold evaporation. Slides are rinsed with IPA, dried under N_2 gas, and placed inside an electron beam evaporator (Plassys MEB) under a vacuum of 3×10^{-6} mbar. An electron gun fires electrons into a gold containing crucible, which evaporates the gold. Based on the design of the crucible and the machine chamber, gold is directionally evaporated towards the sample holder with the secured polycarbonate template. The crucible directs the evaporated gold onto the template slide at a rate of 0.3 nm s^{-1} until the final 120 nm thickness is reached. This process yields the final DPA sample (Figure 3-4B).

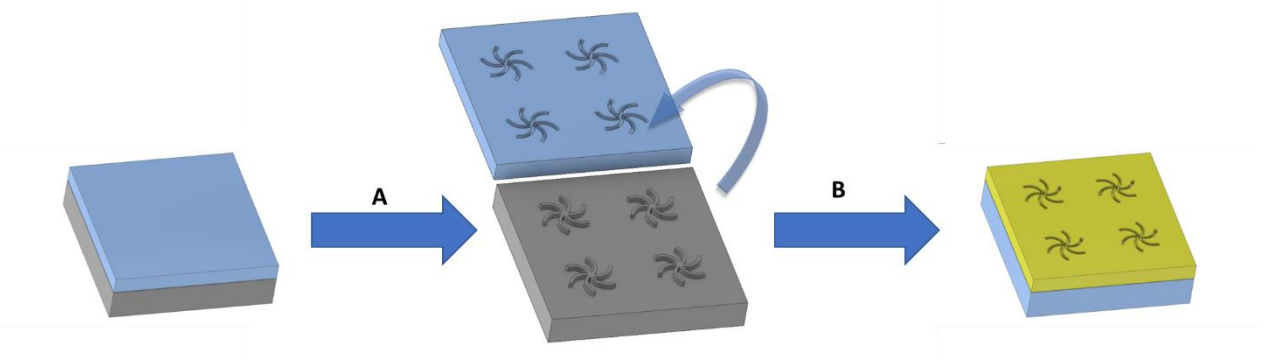

Figure 3-4 (A) Injection moulding using nickel shim to generate polycarbonate slide followed by (B) gold metallisation.

3.1.2 DPA Nanostructure Design and Geometry

The final shuriken nanostructure geometry on the DPA samples is dependent on the original design pattern on the nickel shim master. The original shuriken design is first created using Tanner L-edit (Layout Editor) software (Version 2016.2) by drawing a reference circle with a diameter equal to the shuriken length of 520 nm. A toroidal curve of selected width is then added, extending from the circle origin to the edge. This toroid is then mirrored, and the process

repeated until the final six-armed shuriken shape is achieved (Figure 3-5). This shuriken unit is then repeated into an array in the software, which transfers the design data to the EBL tool (Raith, EBPG 5200).

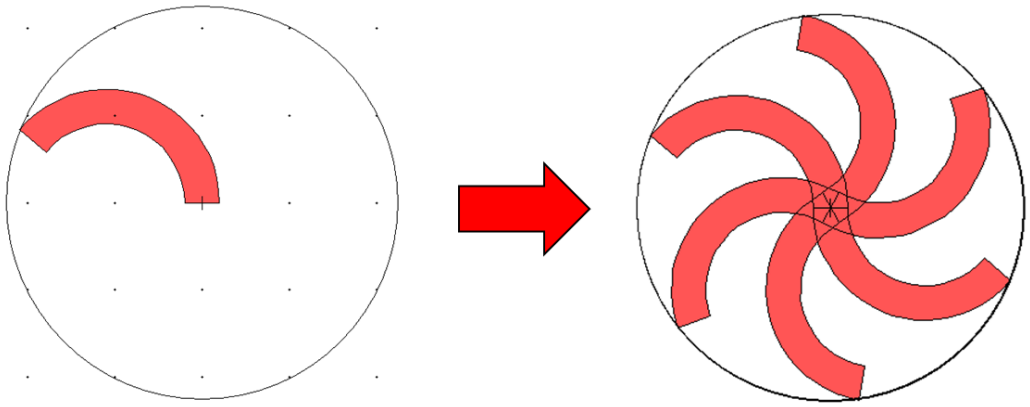

Figure 3-5 Illustration of DPA shuriken design using L-Edit. Using a reference circle, a toroid is drawn to the edge. This process is repeated to achieve the final shuriken shape.

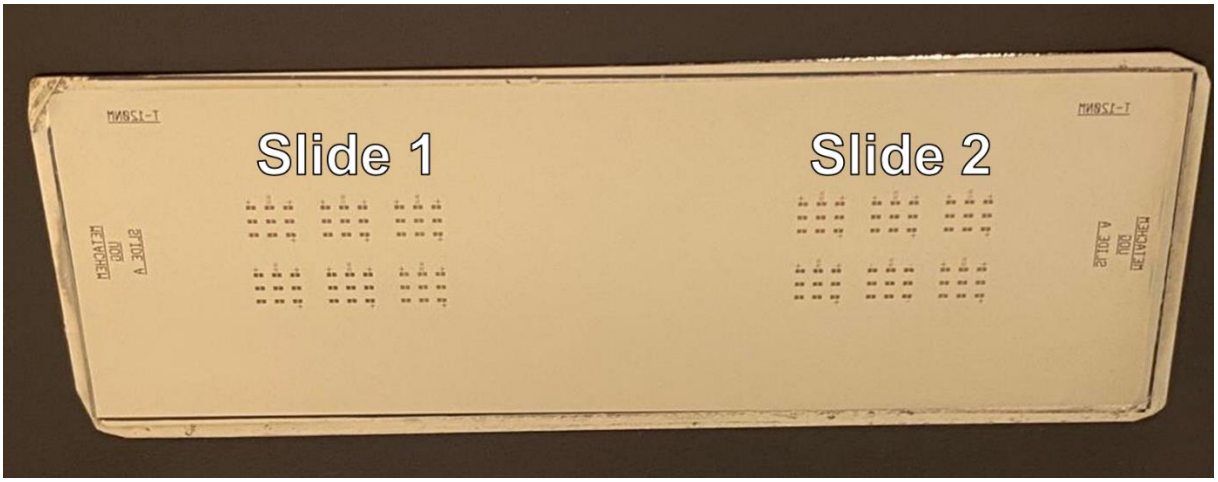

Figure 3-6 Nickel shim master used in injection moulding to generate polycarbonate DPA slides prior to gold coating.

The manufactured nickel shim for DPA production is comprised of two identical slides (Slide 1 and Slide 2) (Figure 3-6). Each slide possesses six regions of slightly varying nanostructures labelled P1-P6, and each of these regions has 9 array pairs of LH and RH shuriken nanostructures labelled A-I.

A photograph of a Slide 1 DPA polycarbonate slide generated from the nickel shim which has been coated with gold is shown in Figure 3-7A, and a descriptive diagram outlining the slide features is shown in Figure 3-7B. The distance between the marker crosses is 3 mm. Each LH or RH shuriken array has an area of 300 × 300 μm. As the length and periodicity of the shuriken nanostructures is 520 and 720 nm respectively, this results in approximately 330,000 nanostructures per array. SEM images of LH P1-P6 shuriken nanostructures are displayed in Figure 3-8. The shuriken dimensions between P1-P6 regions possess small differences in their arm widths and inner circle diameters, visible in the SEM images and outlined in Table 3-1. These structures and geometries were chosen because of the strong chiroptical signals and sharp ORD resonance features they possess.

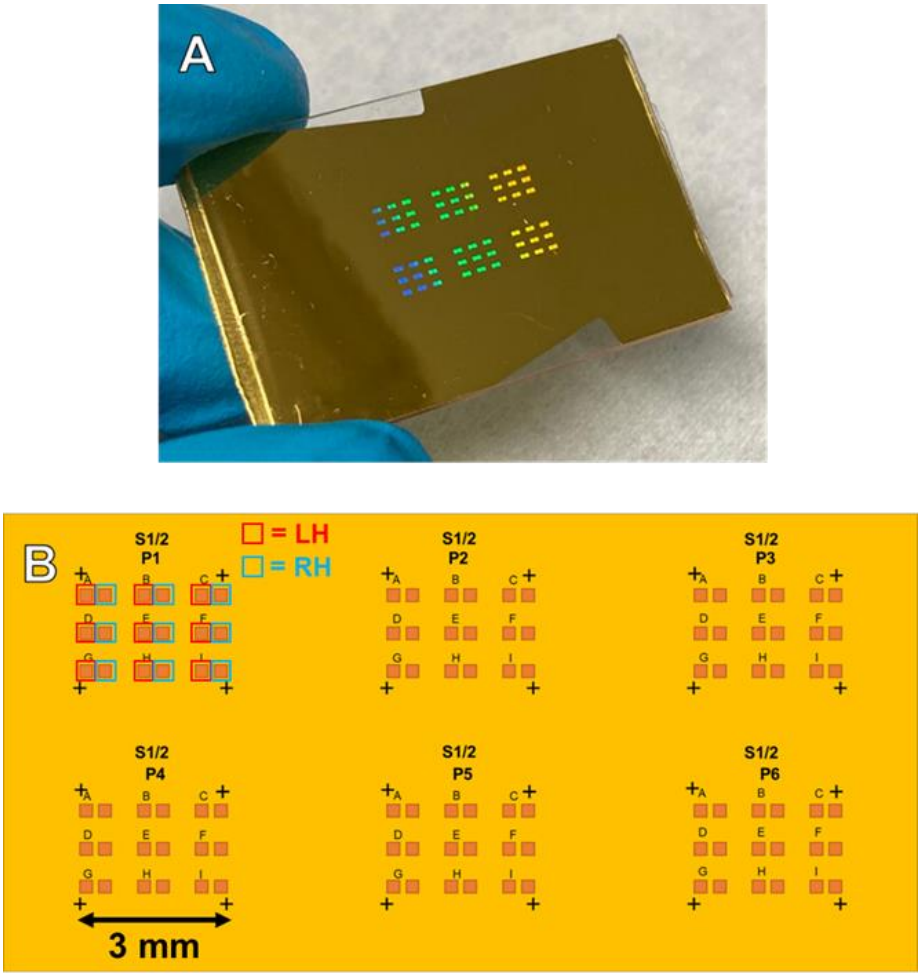

Figure 3-7 (A) Photograph of final gold coated DPA slide and (B) schematic diagram of DPA P1-P6 regions and A-I array locations with LH and RH arrays defined for P1 array.

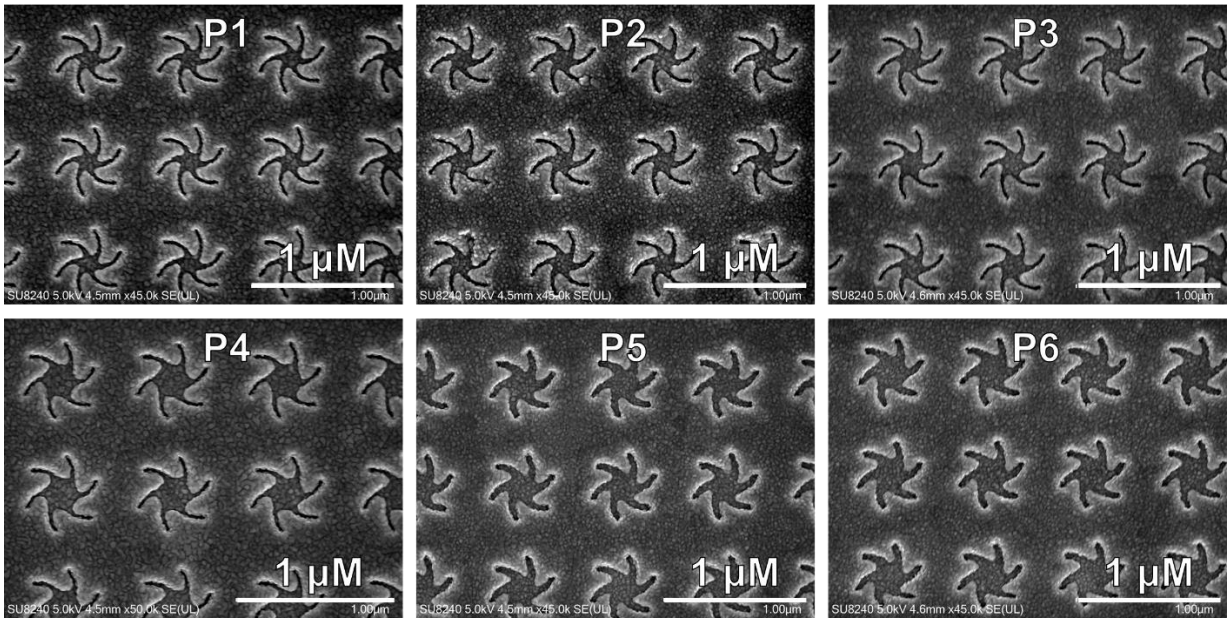

Figure 3-8 SEM images of LH shurikens from DPA slide from each P1-P6 regions showcasing differences between nanostructures.

Location	Arm Width (nm)	Centre Radius (nm)
P1	30	0
P2	30	50
P3	30	75
P4	30	100
P5	50	0
P6	50	75

Table 3-1 Shuriken arm width and centre radius values for each DPA shurikens in each region/location. A centre radius of zero indicates that the shuriken centre diameter is resultant purely from the shuriken arms converging in the EBL design.

3.2 Chemical Functionalisation

The various DPA surface passivation and chemical functionalisation strategies, as well as virus isolation methodology used for the biosensing experiments presented in Chapter 4 are as follows.

3.2.1 Surface Passivation

Preventing non-specific adsorption of material in a multi-constituent analyte solution to the surface of any biosensor is significant. Resultingly, surface passivation techniques are required to maximise the sensitivity, specificity, and selectivity of a biosensor to the target analyte(s) of interest [4].

A suitable surface technique that is widely used with metal surfaces is that of Self-Assembled Monolayers (SAMs). SAMs are defined as ”*organic assemblies formed by the adsorption of molecular constituents from solution or the gas phase onto the surface of solids or in regular arrays on the surface of liquids”* [5]. The incorporation of monolayer components containing different functional head and tail groups allows for the chemical control and tailoring of metal-surface properties. This capability diversifies SAM applications to include such fields as biosensing [6], catalysis [7], and molecular electronics [8].

Probably the most researched type of SAM and the ones employed throughout this thesis are that of alkanethiols onto elemental gold. The inherent inertness of gold, and the strong affinity of sulfur to gold makes it an ideal system to study and prepare SAMs. Thiols have even been known to displace adventitious materials from the gold surface [5]. The exact nature of the sulfur-gold interaction is still unclear, though the general consensus is that the sulfhydryl group is first deprotonated to form a sulfhydryl radical ($RS\cdot$), which then covalently chemisorbs to the gold surface - usually as Au(111) or Au(100) - whilst liberating H_2 [5].

SAMs have been widely utilised for biosensor applications due to their ease of manufacture, stability, uniformity, and passivation properties. Examples include SPR based [9] and electrochemical sensors [10]. SAMs were employed throughout most of the biosensing experiments involving DPAs. Preliminary experiments to optimise SAM protocols discovered that relatively high concentrations of thiols were required to fully passivate the surface (Figure 3-9). DPA samples were first plasma cleaned for 105 seconds at 100 W with 0.1 bar O_2 gas. Samples were then placed in different concentrations (0, 10, and 100 mM) of aqueous methyl-PEG-4 thiol ($MT(PEG)_4$) solutions for 18 hours. Samples were rinsed with deionised water and immersed for 1 hour in aqueous 1 µM Alexa-Fluor 647 fluorophore tagged Bovine Serum Albumin (BSA) protein. Samples were rinsed with deionised water and fluorescence images acquired.

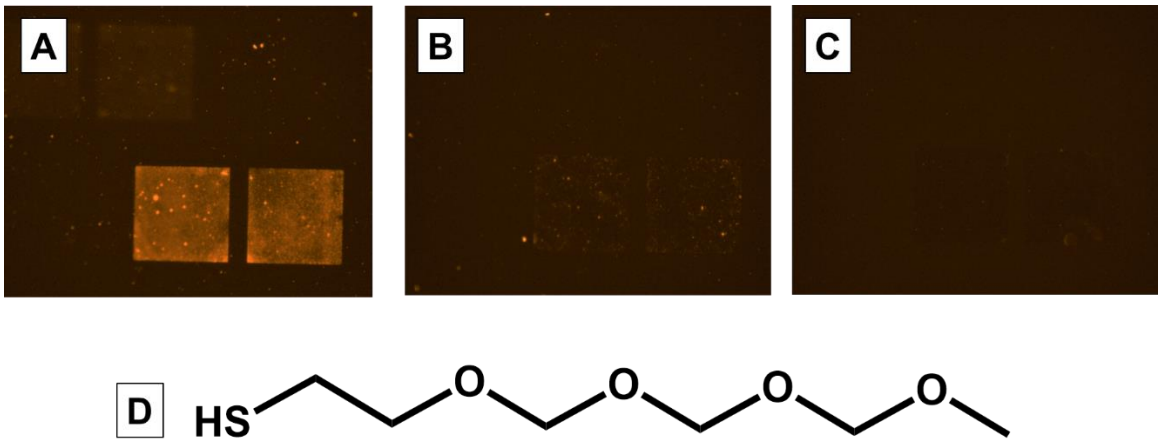

Figure 3-9 Fluorescence microscope images of 3 sets of LH/RH DPA nanostructure arrays taken at 10× magnification treated with different concentrations of aqueous $MT(PEG)_4$ thiol solutions, followed by treatment with Alexa-Fluor 647 tagged BSA. (A) Control sample with no SAM. (B) Sample treated with 10 mM $MT(PEG)_4$. (C) Sample treated with 100 mM $MT(PEG)_4$. (D) $MT(PEG)_4$ molecular structure.

Fluorescence images indicate that for DPA samples untreated with $MT(PEG)_4$ there is a large amount of surface-bound protein. Fluorescence is amplified on the nanostructure regions due to an effect known as plasmon enhanced fluorescence, which increases enhances fluorescence emission and decreases of lifetimes [11]. For samples treated with $MT(PEG)_4$, fluorescence decreases dramatically. For the 10 mM treated sample (Figure 3-9B) there are still some regions of fluorescence because of non-specific adsorption visible. At a concentration of 100 mM, there is almost no fluorescence (Figure 3-9C).

These results were surprising considering that most studies based on gold SAMs generally deal with thiol concentrations in the range of 1 mM, and these SAMs have been shown to be highly packed with few surface defects using several diffraction and vibrational techniques [5] [12] [13]. Possible explanations for the higher concentration requirement are that the DPA gold evaporation and subsequent plasma cleaning processes do not yield a perfectly smooth Au(111) surface. Common surface cleaning or smoothing techniques such as annealing, piranha and aqua regia solutions used to generate pristine Au(111) surfaces are incompatible with DPA samples due to their harsh properties which would damage the nanostructures or the polycarbonate template. Plasma cleaning may be adequate in removing surface adventitious material, but if the

gold evaporation leaves a slightly roughened gold surface the quality of SAM may be too poor at only 1 mM concentrations. Experiments for the detection of streptavidin (Section 4.2) and haptoglobin (Section 4.5) were thus conducted using 100 mM thiol concentrations.

3.2.2 Streptavidin Experiments

For streptavidin protein and biotinylated SAM experiments presented in Section 4.2, the methodology of surface functionalisation used is as follows.

Solutions for SAM functionalisation were prepared using a 1:4 molar ratio of biotin(PEG)-thiol: MT(PEG)$_4$ thiol (Polypure, 41156-1095; ThermoFisher, 26132) with the constituents having a 100 mM total concentration in phosphate buffer saline (PBS, ThermoFisher). The DPA sample was incubated in this solution for 24 hours, followed by rinsing with PBS and optical measurements taken in PBS for the starting reference values. Streptavidin (ThermoFisher, 21122), at 1 μM, was prepared in PBS and added to the sample for 2 hours. Optical measurements were taken pre- and post-rinsing using PBS. 1 μM Atto-655-Biotin (Sigma-Aldrich 06966) was also prepared in PBS and added to the sample for a further 2-hour period (Figure 3-10). Optical measurements were taken pre- and post-rinsing using PBS.

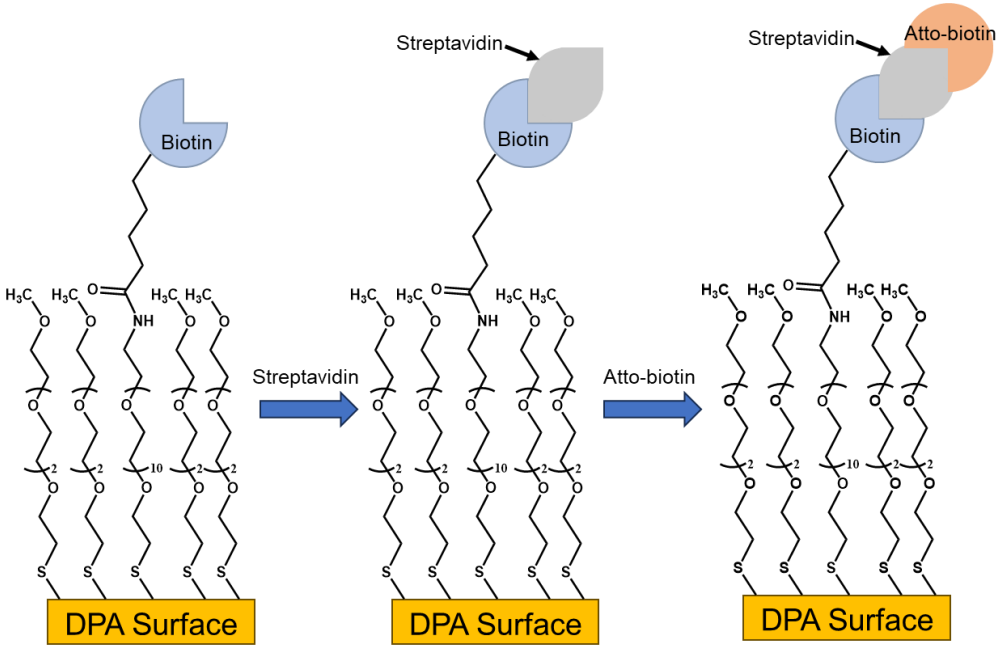

Figure 3-10 Functionalisation scheme showing prepared biotin-PEG-thiol and MT(PEG)$_4$ spacer SAM, binding of streptavidin, and binding of Atto-biotin.

3.2.3 Functionalisation – NTA SAM for His-tagged Proteins

For the experiments using His-tagged COVID-19 S1 and streptavidin proteins in Section 4.3, the methodology of surface functionalisation used is as follows.

Histidine, or polyhistidine, amino acid tags (His-tagged) are commonly used for the purification and detection of recombinant proteins due to their high affinity to immobilised chelating metal ions such as Ni^{2+} or Cu^{2+} [14]. To specifically bind His-tagged proteins onto DPA sample surfaces, thiolated nitrilotriacetic acid (NTA) was co-adsorbed with triethylene glycol mono-11-mercaptoundecyl (EG-thiol) to create a mixed SAM. The samples are then immersed in a 95% ethanol solution of 0.1 mM NTA and 0.9 mM EG-thiol and left for 4 hours. Samples are then removed from the solution, rinsed with 95% ethanol, and dried with N_2 gas. Samples are then incubated in a 1 mM NaOH solution for 5 minutes, removed from solution, and rinsed with DI water and dried with N_2 gas. Samples are then incubated in a 40 mM solution of $NiSO_4$ for 1 hour to introduce the Ni^{2+} ions into the NTA chelating ligand (Figure 3-11). Finally, samples are removed from solution, rinsed with HEPES buffer solution followed by DI water, and dried with N_2 gas. Further details regarding the addition of His-tagged proteins, such as protein concentration, is presented in the results chapter in Section 4.3.

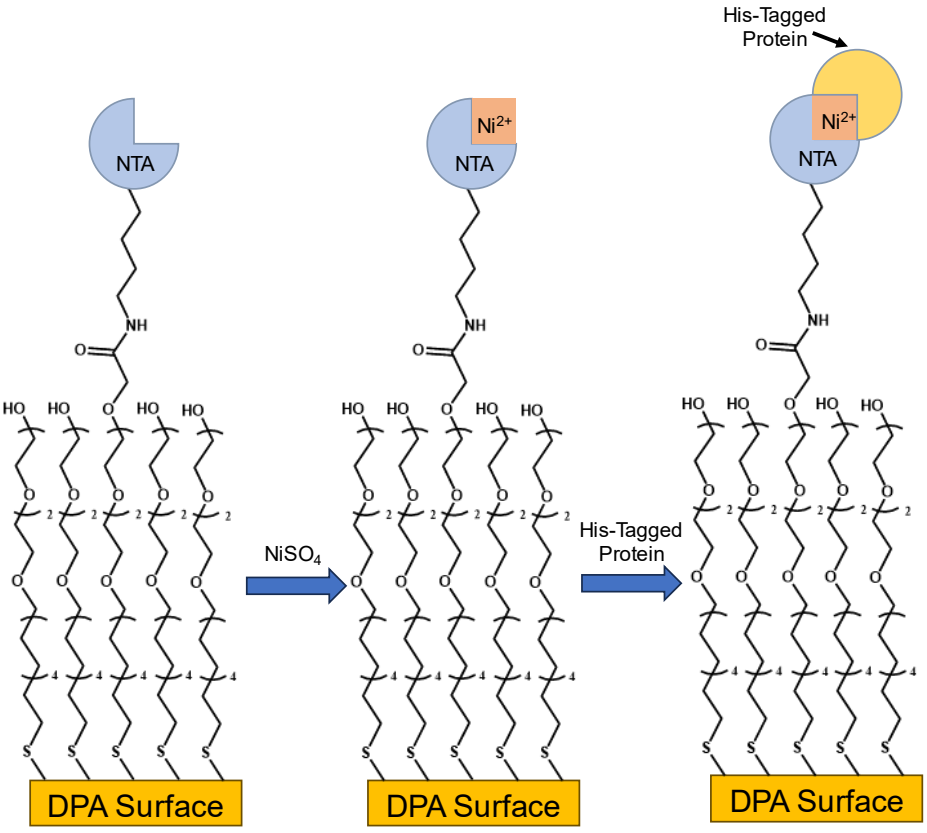

Figure 3-11 Functionalisation scheme showing NTA SAM, binding of Ni^{2+} from $NiSO_4$, followed by binding of His-tagged protein.

3.2.4 Isolation of SARS-CoV-2 Virus from Clinical Samples

For SARS-CoV-2 virus experiments in Section 4.4.1, the virions were isolated and inactivated as follows.

SARS-CoV-2 virus (the clinical isolate Gla8) was isolated from nasal swabs of SARS-CoV-2-infected individuals that were obtained in viral transport medium (VTM) mixed 1:4 (v:v) in Dulbecco's Modified Eagle Medium supplemented with 2% fetal calf serum, 1% Penicillin-Streptomycin and 250 ng ml^{-1} Amphotericin B (ThermoFisher scientific: 0566016, 10499044, 15140122 and 15290018, respectively). The mixture was clarified at 3000 rpm for 10 minutes and then used to inoculate Vero E6 cells (African Green monkey kidney cell line, from Michelle Bouloy, Institute Pasteur, France) in a 6 well plate. Samples were harvested between 48- and 96-hours post-infection, depending on the extent of cytopathic effect. Viral presence was determined

using a NEB Luna Universal Probe One-Step RT-qPCR Kit (New England Biolabs, E3006) and 2019-nCoV CDC N1 primers and probes (IDT: 10006713) and infectious titres by plaque assay.

The clinical isolate of SARS-CoV-2 virions was amplified to a titre of 7.3×10^5 plaque forming units (pfu) ml^{-1}. The virions were inactivated in formaldehyde for 30 minutes to allow safe handling, after which the excess formaldehyde was quenched by diluting the virus solution 1:1 (v:v) with 50 mM Tris buffer resulting in final sample with $\sim 3 \times 10^5$ inactivated virions ml^{-1}.

3.2.5 Antibody Fragment Functionalisation

Antibody-based biosensors have garnered significant interest due to the naturally high specificity of the antibody to its associated antigen target and the availability of recombinant antibody engineering. Due to the relatively large size of antibodies - 150 kDa on average for the most common IgG antibody type - [15] antibody cleaving and fragmentation techniques have been developed to minimize molecular size while maintaining antigen binding specificity by only keeping antibody sections which contain the antigen binding sites.

Fragmentation of immunoglobulin type antibodies is performed using proteases to digest and cleave specific antibody regions. There are two groups of antibody fragments: namely the Fab antigen binding and non-antigen binding Fc fragments (Figure 3-12). There are several variations of Fab fragments which can be produced, with different digestive enzymes fragmenting the antibodies at different sections. However, what they all have in common is that they contain the variable regions of the heavy and light antibody chains. For the work presented in this thesis, only $F(ab')_2$ fragments were used, which are generated by antibody digestion using a pepsin resin. Pepsin is a non-specific endopeptidase which produces one $F(ab')_2$ fragment and several Fc fragments, which can be separated using affinity column chromatography.

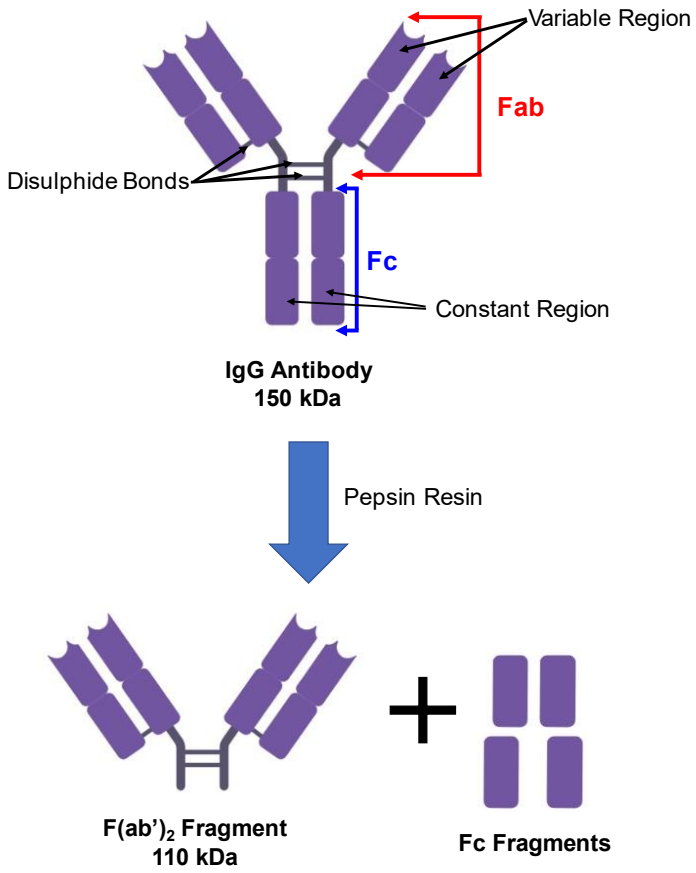

Figure 3-12 Schematic diagram of antibody fragmentation process using a pepsin resin, resulting in F(ab')$_2$ and Fc antibody fragments.

The F(ab')$_2$ fragments are held together by disulphide bridges, which dissociate into two Fab' fragments after immobilisation to the DPA gold surface (Figure 3-13) [16]. These antibody fragments allow for better alignment of the epitopes on the DPA surface. Other advantages of fragmentation include the reduction of non-specific interactions associated with Fc fragments as well as higher sensitivity for antigen detection from reduced steric hindrance effects due to the smaller size of the fragment compared to the full antibody.

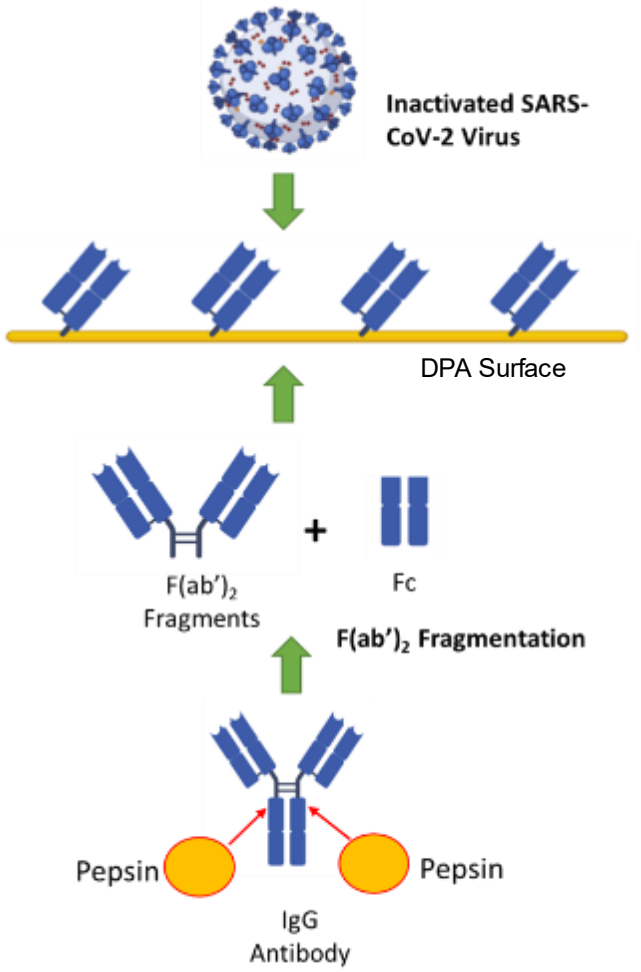

Figure 3-13 F(ab')2 antibody fragmentation and its functionalisation to the DPA sample which is then used for detecting inactivated SARS-CoV-2 Virus. The MT(PEG)4 spacer is not shown for clarity.

The antibody fragmentation protocol used for F(ab')$_2$ biosensing to detect SARS-Cov-2 virions is outlined below:

Anti-SARS-CoV-2 Spike Glycoprotein S1 antibody (Abcam ab275759) was cleaved using a Pierce F(ab')$_2$ Micro Preparation kit (Thermofisher 44688) following manufacturer instructions:

1. Pipette was used to deposit a 50% pepsin slurry into a spin column and column centrifuged at 5000 × *g* for 1 minute and buffer discarded.
2. Pepsin resin was washed with digestion buffer and column centrifuged again at 5000 × *g* for 1 minute and buffer discarded. Pepsin resin spin column set aside.

3. To prepare any IgG type antibody, a desalting column was prepared by removing storage solution by centrifuging at 1000 × *g* for 2 minutes.
4. Digestion buffer was added to the desalting column, and the column centrifuged at 1000 × *g* for 2 minutes to remove buffer. This step was repeated three time to equilibrate the column with buffer discarded each time.
5. 25-50 μg of IgG type antibody sample was added to the desalting column and centrifuged at 1000 × *g* for 2 minutes to collect the sample. Desalting column was then discarded.
6. Prepared IgG type antibody sample was added to immobilised pepsin spin column and the column placed in a shaker at 37 °C for 2 hours for the digestion reaction to take place.
7. Pepsin immobilised spin column was then centrifuged at 5000 × *g* for 1 minute to separate the digest.
8. Pepsin resin was then washed with PBS and centrifuged at 5000 × *g* for 1 minute. This step was repeated once, and wash fractions containing $F(ab)_2$ fragments combined.
9. To purify the $F(ab)_2$ fragment solution and remove Fc fragments, a NAb Protein A plus column was used. Protein A is a bacterial surface protein with high affinity for Fc antibody regions. The Protein A column was centrifuged at 1000 × *g* for 1 minute to remove storage solution and equilibrated with PBS and centrifuged at 1000 × *g* for 1 minute with flow-through discarded.
10. $F(ab)_2$ fragment solution was added to protein A column and the column resin resuspended through inversion. The column was incubated at room temperature with manual end-over-end inversion for 10 minutes.
11. Protein A column was then centrifuged 1000 × *g* for 1 minute to collect the purified $F(ab)_2$ fragment solution.

The estimated antibody fragmentation is between 50-70%. Concentration calculations assume a 50% conversion rate going forward. Following this preparation, the $F(ab')_2$ fragment solution was added onto the DPA surface for 2 hours, and optical measurements taken. A 2 mM $MT(PEG)_4$ spacer solution was prepared in PBS and was added for 2 hours to the DPA surface to passivate any gold surface regions left uncovered by the Fab' antibody fragments. Optical measurements were then taken pre- and post-rinsing in PBS. SARS-CoV-2 (prepared in Section 3.2.4) virus in 6% formaldehyde was diluted 1:1 with TRIS buffer to quench the formaldehyde prior to application and 0.2% (w/v) mucin protein was added to mimic clinical nasopharyngeal

samples. The SARS-CoV-2 inactivated virus solution was added to the DPA fluidic chamber for 1 hour, and optical measurements taken pre- and post-rinsing with PBS.

3.2.6 Protein A/G Functionalisation for Virus Experiments

While the fragmentation of antibodies has useful advantages, the use of whole IgG class antibodies for biosensing purposes has also been trialled in this thesis. The orientation of capture antibodies is highly important for biosensor functionality. Antibodies which are orientated end-on retain function as their antigen binding sites are still available. Side-on orientation may retain some functionality, whereas head-on orientation loses all function. To ensure orientated immobilization of capture antibodies Fragment Crystallizable (Fc) Binding (FCB) proteins are often used, such as Protein A, Protein G, and Protein A/G.

Protein A and Protein G are both bacterial cell wall proteins with high affinities with the Fc regions of IgG molecules [17]. Protein A/G is a gene fusion result of Protein A and Protein G with a total of seven IgG-binding domains and is superior to the individual protein counterparts; possessing higher IgG binding affinity while also being less pH dependent (works in a pH range of 5-8).

For virus experiments presented in Section 4.4.2, the surface functionalisation methodology used is as follows.

A Protein A/G SAM was prepared using a 1:30 ratio of Protein A/G Cys-tagged recombinant protein (Prospec pro-1928, concentration of 6.3 μM) and $MT(PEG)_4$ spacer (189 μM, Thermofisher, 26132) in ultrapure water. Following an incubation time of 16 hours, the sample was rinsed with PBS.

Mouse anti-Norovirus GI antibody (NativeAntigen MAB12495-100) at 1 μM, and anti-Zika virus antibody (prepared at the Centre for Virus Research (CVR) in Glasgow) at 1 μM, were prepared in PBS and added to separate regions of the DPA sample for 2 hours using a 2-well culture well insert to isolate the regions. The sample was rinsed with PBS, and SEA blocking buffer (Thermo 37527) added to the sample for 30 minutes. The sample was rinsed with PBS, a fluidic chamber attached, and optical measurements taken. Zika virus solution, provided by the CVR, was added to the sample for 1 hour. The sample was rinsed with PBS and optical

measurements performed. Norovirus VLP solution (NativeAntigen REC31722-100) was added to the sample for 1 hour. The sample was rinsed with PBS and optical measurements performed.

3.2.7 Functionalisation – EDC/NHS Protein Conjugation

For haemoglobin-haptoglobin experiments presented in Section 4.5, EDC/NHS protein conjugation protocols were performed as follows:

Carboxylic acid groups can be conjugated with primary amines using common water-soluble conjugation reagents 1-Ethyl-3-(3-dimethylaminopropyl)carbodiimide (EDC) and (N-hydroxysulfosuccinimide (NHS). NHS, in the presence of EDC, reacts with carboxylic acid (-COOH) functional groups to form semi-stable NHS esters, which are susceptible to nucleophilic attack by primary amine ($-NH_2$) groups to form strong amide crosslinks [18]. 1-(2-Aminoethyl)maleimide hydrochloride (AEM) was found to increase conjugation efficiency.

Sulfo N-hydroxysulfosuccinimide (sulfo-NHS) and EDC were purchased from ThermoFisher. AEM was purchased from Sigma-Aldrich.

DPA samples were treated with 50 mM $MT(PEG)_4$ and 50 mM $CT(PEG)_{12}$ thiols overnight at room temperature. The DPA sample was then rinsed, and optical measurements taken. DPA samples were then treated with 180 mM EDC and 180 mM sulfo-NHS in 2-morpholinoethanesulfonic acid (MES) buffer (pH 6.5) for 15 minutes. The conjugation solution was removed and replaced with 180 mM AEM for 30 minutes. The final step of conjugation is to add the desired protein solution (Figure 3-14). Further details of protein concentrations and duration of protein conjugation is discussed in the results chapter in Section 4.5.

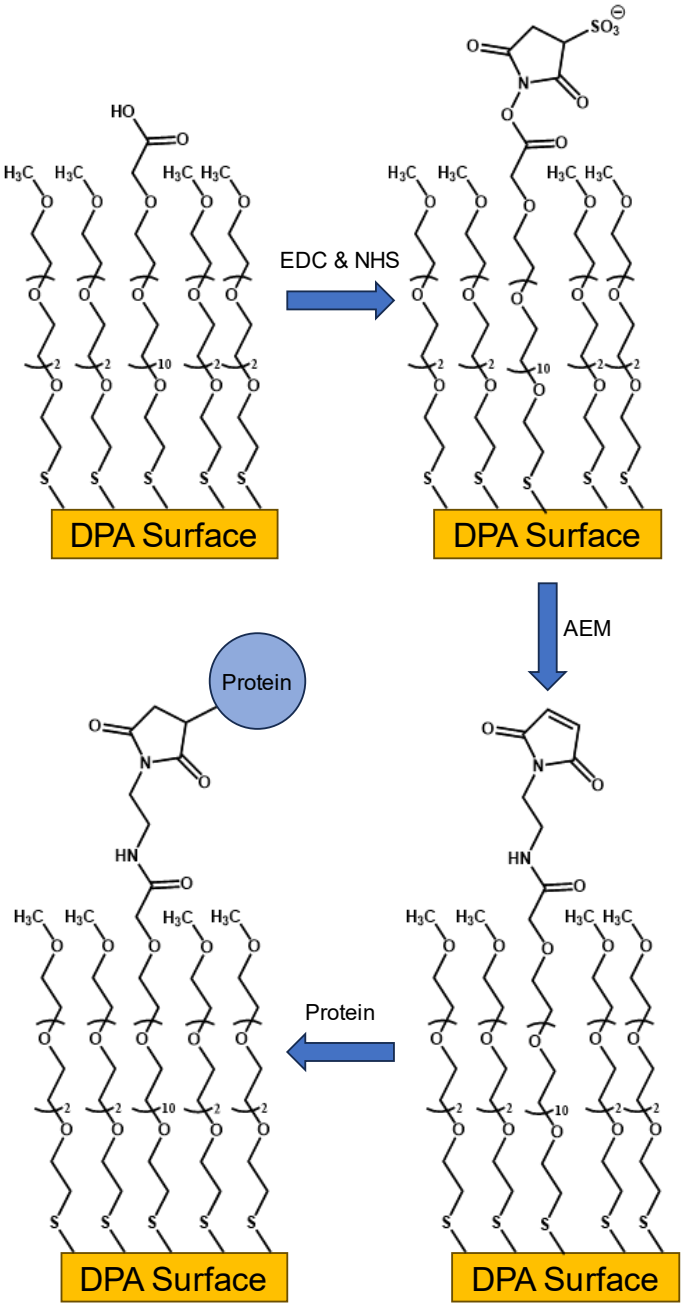

Figure 3-14 Functionalisation scheme showing $CT(PEG)_{12}$ and $MT(PEG)_4$ SAM formation, NHS ester formation, maleimide formation upon AEM addition, and protein conjugation.

3.3 Recording of Optical and Raman Measurements

ORD and reflectivity measurements from DPA samples were recorded using two different custom built polarisation microscopes, referred to as the *imaging polarimetry microscope system*, and the *single-spot polarimetry microscope system*. The general schematic for both polarisation microscopes is presented in Figure 3-15, with further details regarding the respective systems provided in Section 3.3.1 and Section 3.3.2.

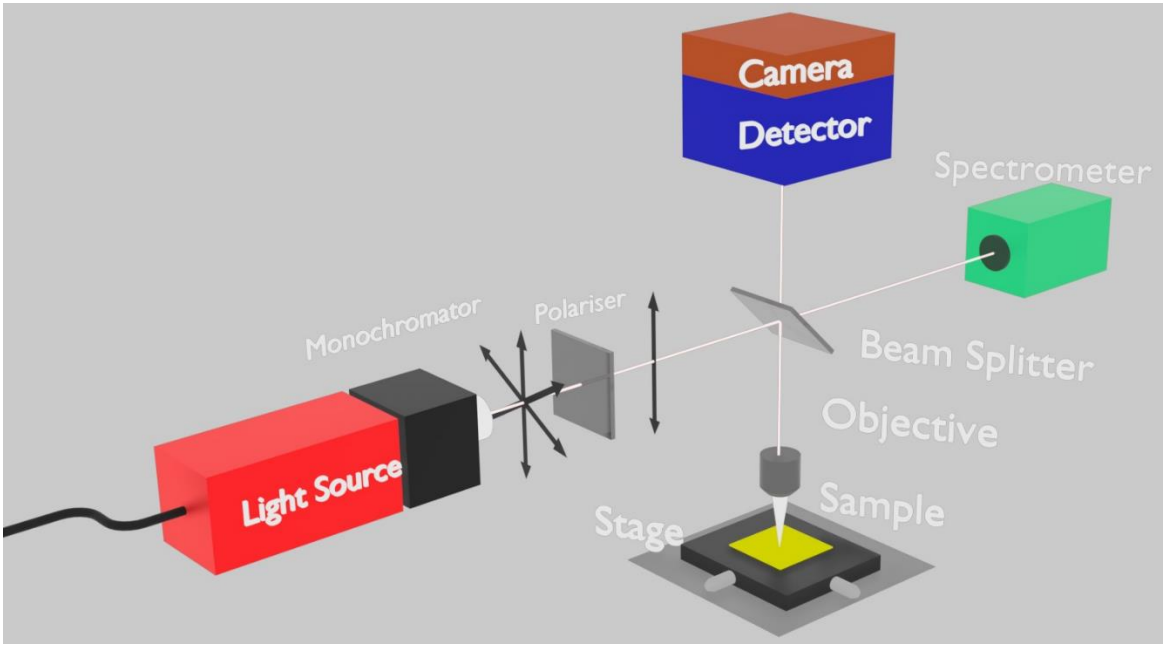

Figure 3-15 Diagram of imaging polarimetry set-up used to measure ORD.

For all biosensing experiments presented in Chapter 4, ORD results were collected using the imaging polarimetry microscope with a 2× objective lens capable of collecting ORD data from 18 nanostructured arrays at a time on a DPA region.

For all Raman experiments presented in Chapter 5, ORD and reflectivity results were collected using the single-spot polarimetry microscope with a 10× objective lens. This reduces data collection to one nanostructured array at a time, though provides sharper resolution of spectral features desired for reflectivity measurements.

3.3.1 Description of Imaging Polarimetry Microscope

A custom-built polarimetry microscope is used to image the DPA surfaces using a polarisation sensitive camera (FLIR), which simultaneously acts as the detector, and a monochromatic light source (Spectral Photonics) (Figure 3-16). The sensor in the polarisation sensitive camera is comprised of several megapixels; each individual pixel has 4 polarising filters which are orientated at 0°, 45°, 90°, and 135°. This set-up allows for the rapid computing of Stokes parameters at a defined location to provide polarisation information and the degree of optical rotation.

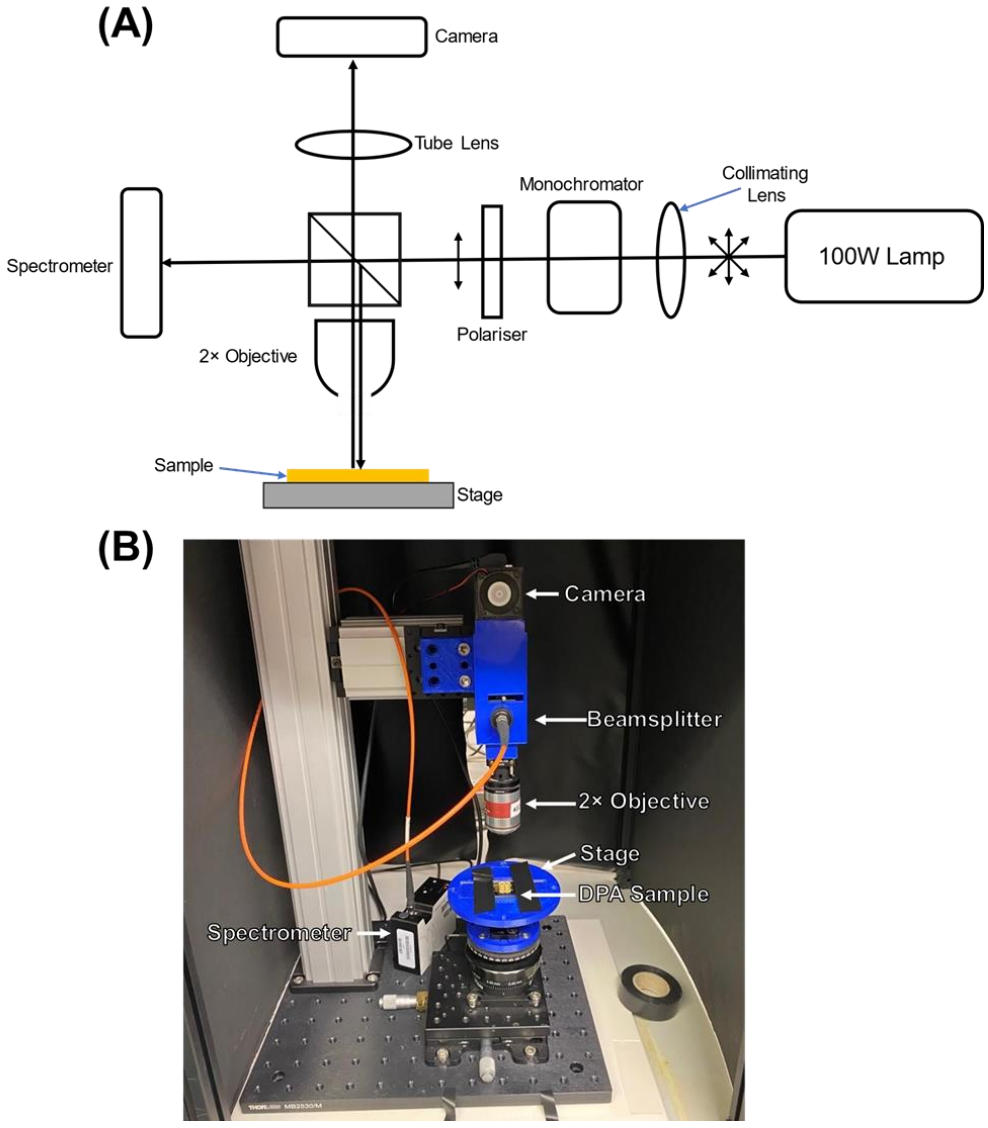

Figure 3-16 (A) Schematic representation, and (B) photograph of the imaging polarimetry microscope set-up used to measure ORD.

The spectral data is captured using a spectrometer (Ocean Optics)**.** A series of lenses and a polarises (Thorlabs) are used to direct the now polarised monochromatic light through a 2× objective (Thorlabs) and onto the DPA sample, and the reflected light is captured by the camera. For ORD measurements, DPA samples were fitted with a fluidic chamber insert (Figure 3-17).

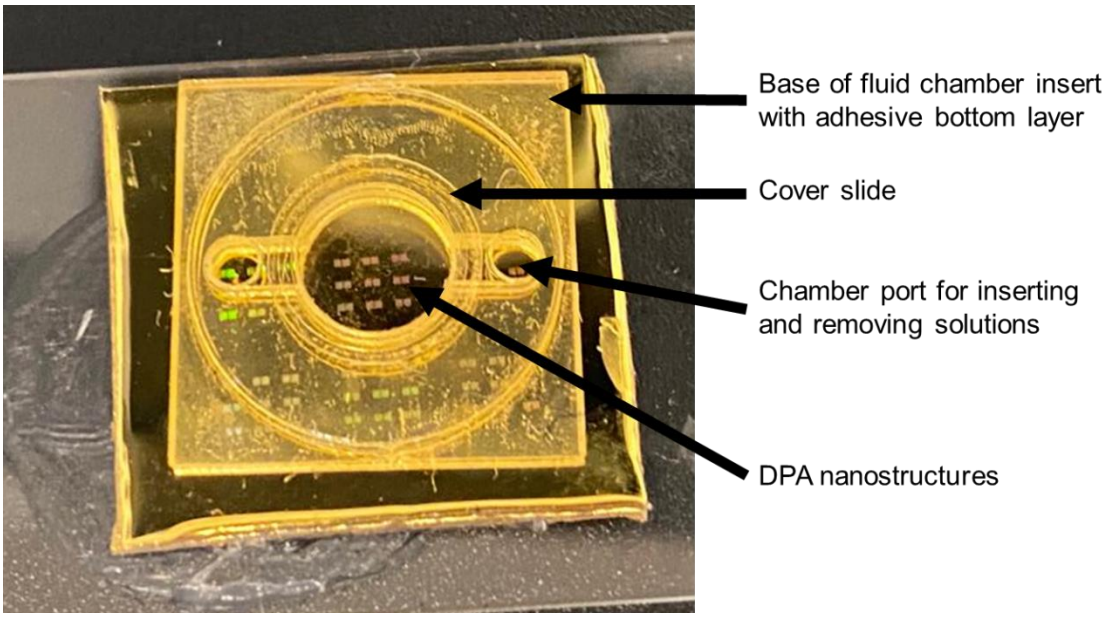

Figure 3-17 DPA slide with fluidic chamber insert applied for optical measurements taken in solution.

LabVIEW software is used to control the light source wavelength and to capture data from 18 locations in the camera image, corresponding to the nanoarrays on the DPA, and generate ORD spectra. The software calculates the *maxima* and *minima* ORD peak positions using a max-min function to generate a table providing resonance peak wavelength values for all 18 arrays. DPA samples are placed on a stage with multi-axis alignment features and each sample is aligned to achieve even illumination. Array regions are then selected from which the software measures ORD (Figure 3-18).

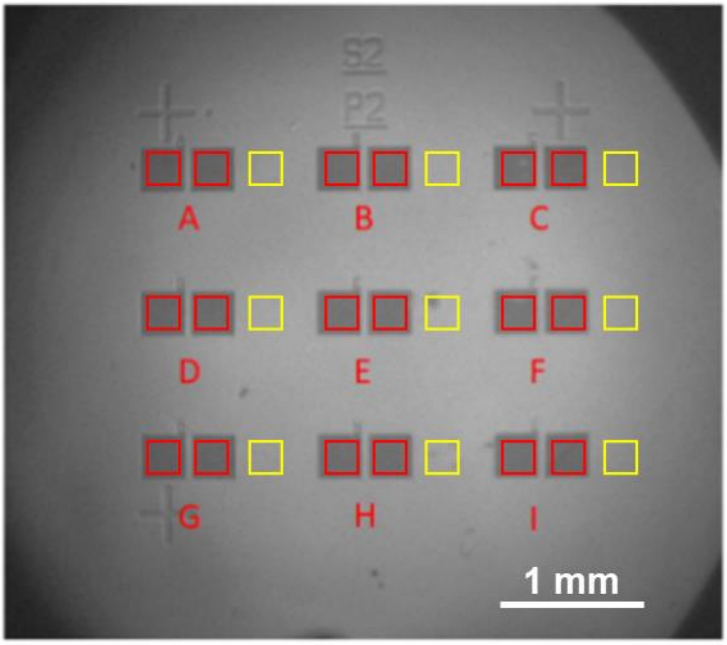

Figure 3-18 Camera image captured using the 2× objective lens of DPA surface. P2 region shown with A-I array labels added for clarity. Red boxes indicate regions from which ORD is measured. Yellow squares indicate background ORD measurement locations taken from plain gold surfaces adjacent to nanostructure arrays, which is subtracted from the respective ORD measurements.

3.3.2 Description of Single-Spot Polarimetry Microscope

A custom built polarimeter, equipped with a tungsten halogen light source (Thorlabs), polarisers (Thorlabs), and a 10× objective (Olympus) was used for measurements of ORD and reflectivity optical spectra. The samples were positioned with the aid of a camera (Thorlabs) and the spectrum was measured using a compact spectrometer (Ocean Optics) (Figure 3-19). For reflectivity measurements plain gold surfaces were used as a background.

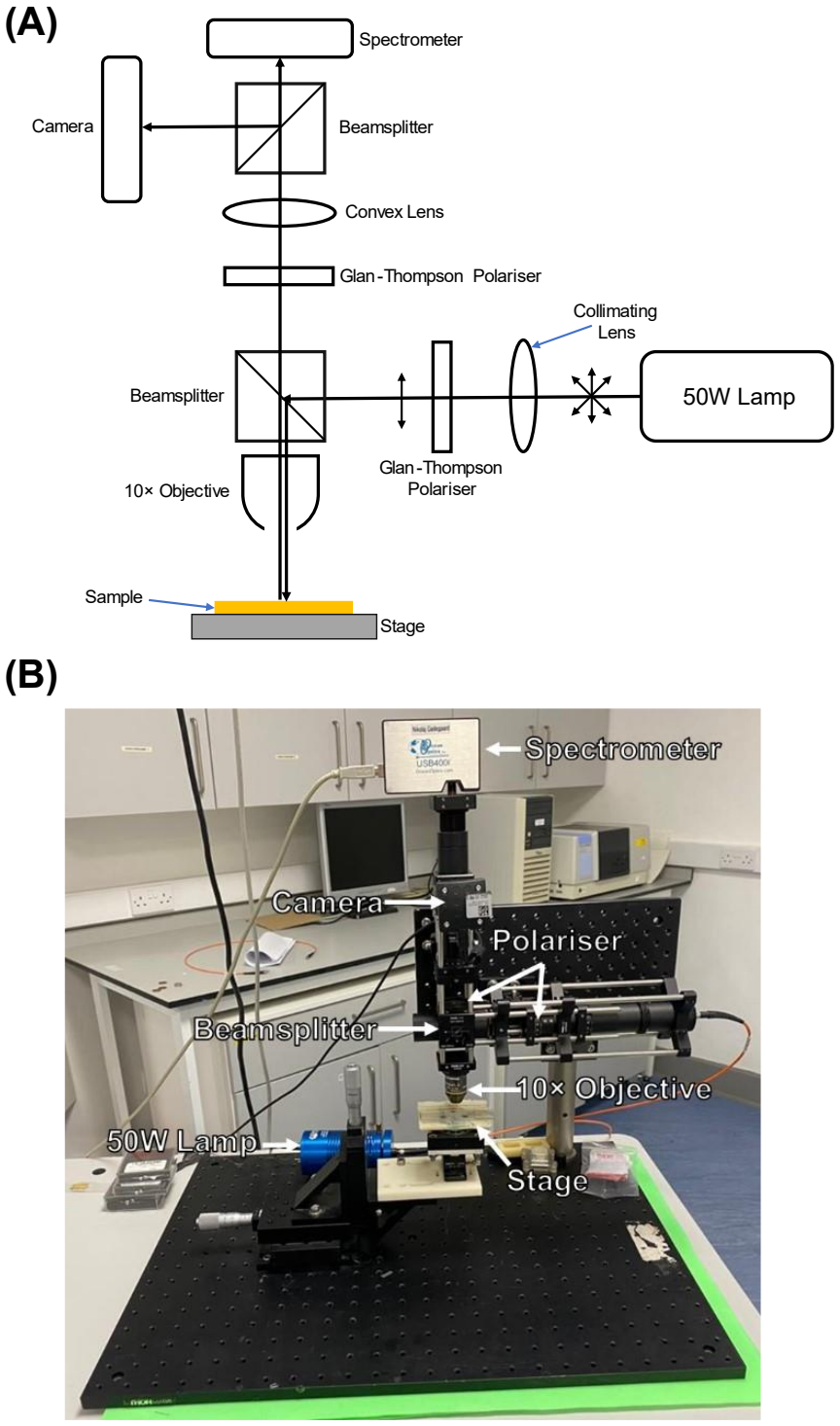

Figure 3-19 (A) Schematic representation, and (B) photograph of the single spot polarimetry microscope set-up used to measure ORD and reflectivity.

3.3.3 DPA Optical Properties

DPA samples possess unique ORD and reflectivity optical properties. The resonance mode wavelength positions from each array of P1-P6 shurikens is dependent on their diameter and periodicity, which remains constant in all arrays, contributing to relatively similar resonance positions for all structures. Measured in water, the DPA display bisignate ORD with two peaks labelled Peak 1 and Peak 2, with the peaks residing around 720 and 740 nm, respectively. However, the differences in arm width and centre circle diameters between P1-P6 cannot be neglected as they do contribute to small changes in resonance positions and peak shape, as can be seen in the ORD graphs presented in Figure 3-20.

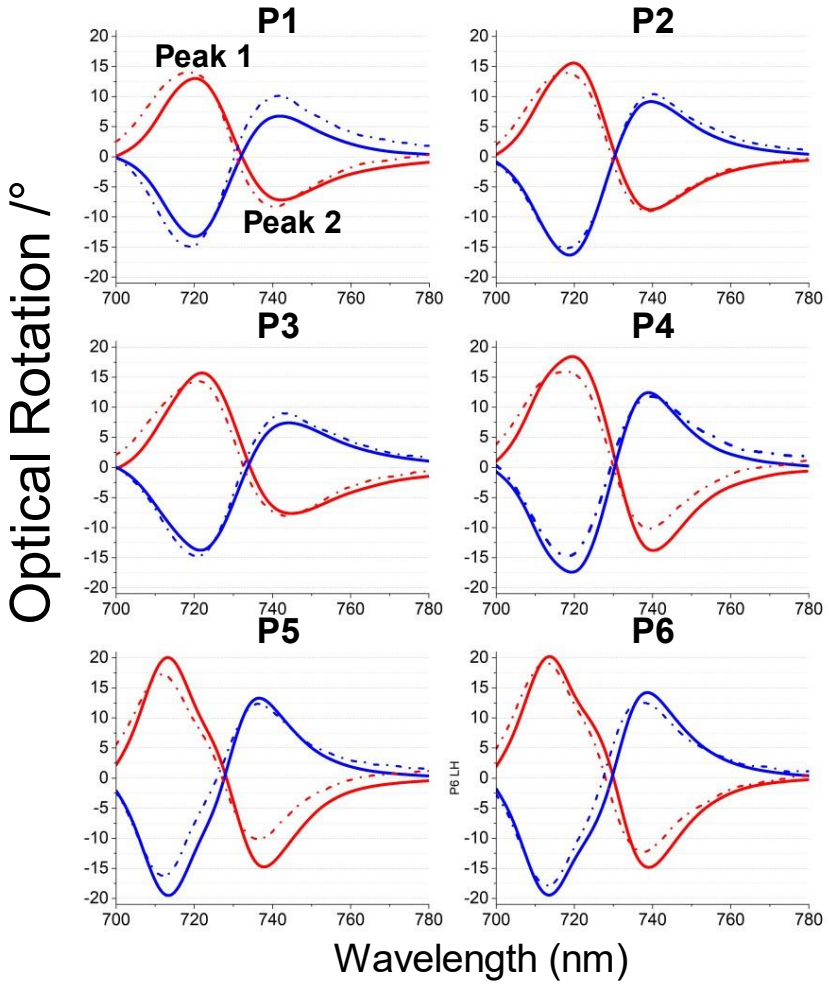

Figure 3-20 ORD spectra collected from all P1-P6 array regions using the imaging (solid lines) and single-spot (dashed) polarimetry microscopes for LH (red) and RH (blue) nanostructures. Peak 1 and Peak 2 labelled for P1 graph.

The ORD measurements between the imaging and single-spot polarimetry microscopes are in good accordance with one another as resonance positions for Peak 1 and Peak 2 are similar. Minor differences in peak shape and position can possibly be attributed to different numerical apertures between the objectives of the two polarimeters, polariser differences, different degrees of illumination and collimation. The ORD amplitudes for P5 and P6 regions are significantly higher than others, which arises from the wider shuriken arm widths. Considering the higher ORD amplitudes and sharper peaks, P5 was chosen for all biosensing experiments presented in this thesis to be used with the imaging polarimetry microscope. P6 was disregarded as it was found that nanofabrication defects were more likely to be found on the edges of the polycarbonate substrates.

Reflectivity measurements in air were collected for the SERS results chapter of this thesis, Chapter 5, using the single-spot polarimetry microscope. As DPA P3 regions showed the highest SERS enhancement, which will be discussed further in Section 5.3.1, the P3 reflectivity spectra in air is shown in Figure 3-21.

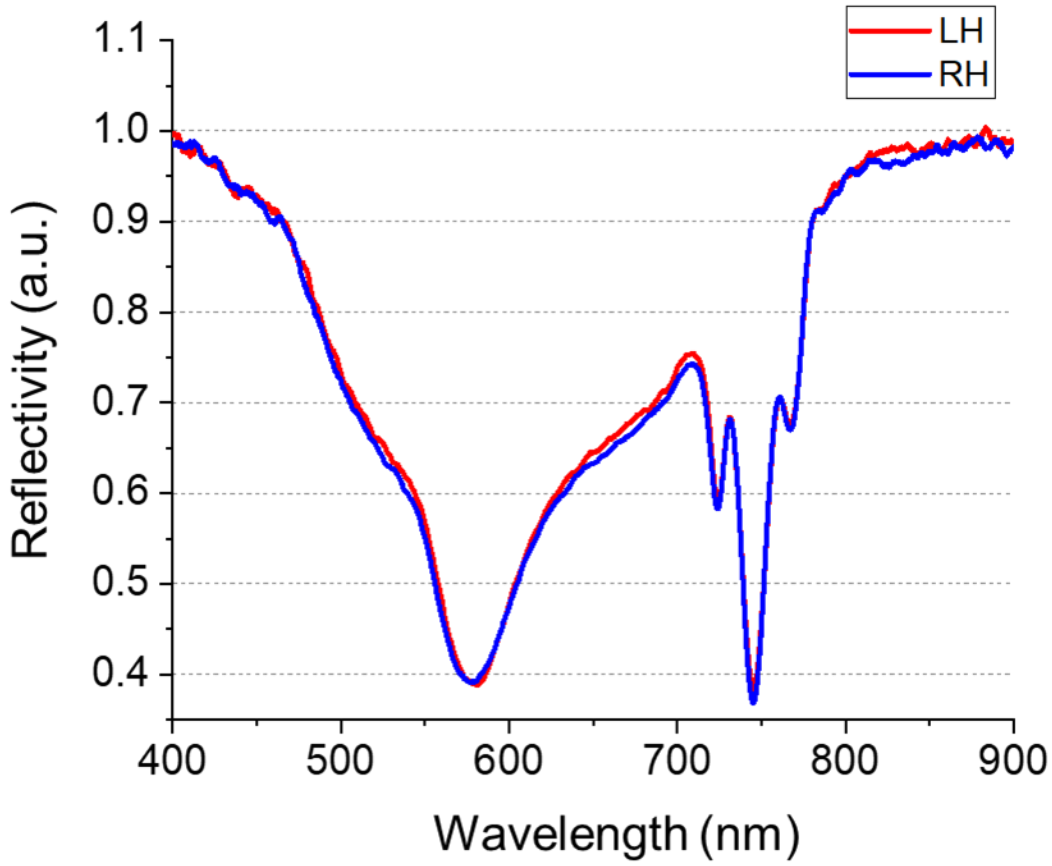

Figure 3-21 Reflectivity spectra of P3 LH (red) and RH (blue) DPA nanostructures using the single-spot polarimetry microscope.

In air, the P3 reflectivity spectra display a broad resonance around the 550-630 nm region, and sharp distinct resonances between the 720-760 nm region. These sharper resonant features arise from Fano-coupling between multiple modes. Fano-coupling, also referred to as Fano resonance or Fano interference, produces asymmetric line-shapes in resonance features through the coupling of background and resonant scattering processes [19].

The single-spot polarimetry microscope was chosen for these measurements due to the relative ease of alignment for a single set of nanostructures as opposed to 9 sets with the imaging polarimetry system. Additionally, the single-spot polarimetry system was found to possess sharper reflectivity peaks.

3.3.4 Raman Spectroscopy Measurements – Glasgow

All Raman spectroscopic measurements recorded in Glasgow were recorded using a NT-MDT NTEGRA Probe NanoLaboratory Raman microscope, as shown in Figure 3-22 and Figure 3-23, using a 633 nm laser excitation (35 mW power) with a 10 second accumulation time. Excitation and collection of Raman scattered light was done using a 20× objective with an estimated spot size of 100 µm. For analysis, the mean and standard error of the SERS intensity values were calculated.

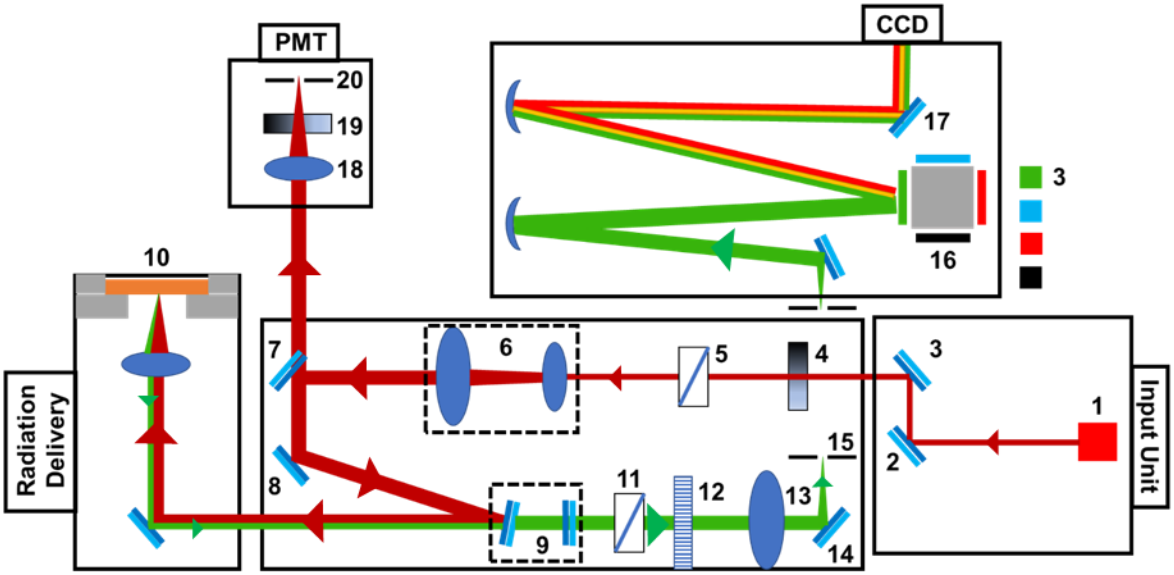

Figure 3-22 Simplified optical schematic of the NTEGRA Spectra Raman system. 1 – laser input unit; 2, 3, 8, 14, 17 – mirrors; 4, 19 – adjustable density neutral filter; 5, 11 – polariser; 6 – beam expander; 7 – 97% mirror; 9 – notch filters; 10 – DPA sample; 12 – filter cartridge; 13, 18 – lenses; 15, 20 – adjustable pinhole; 16 – diffraction gratings. Arrows indicate laser and reflected light travel path.

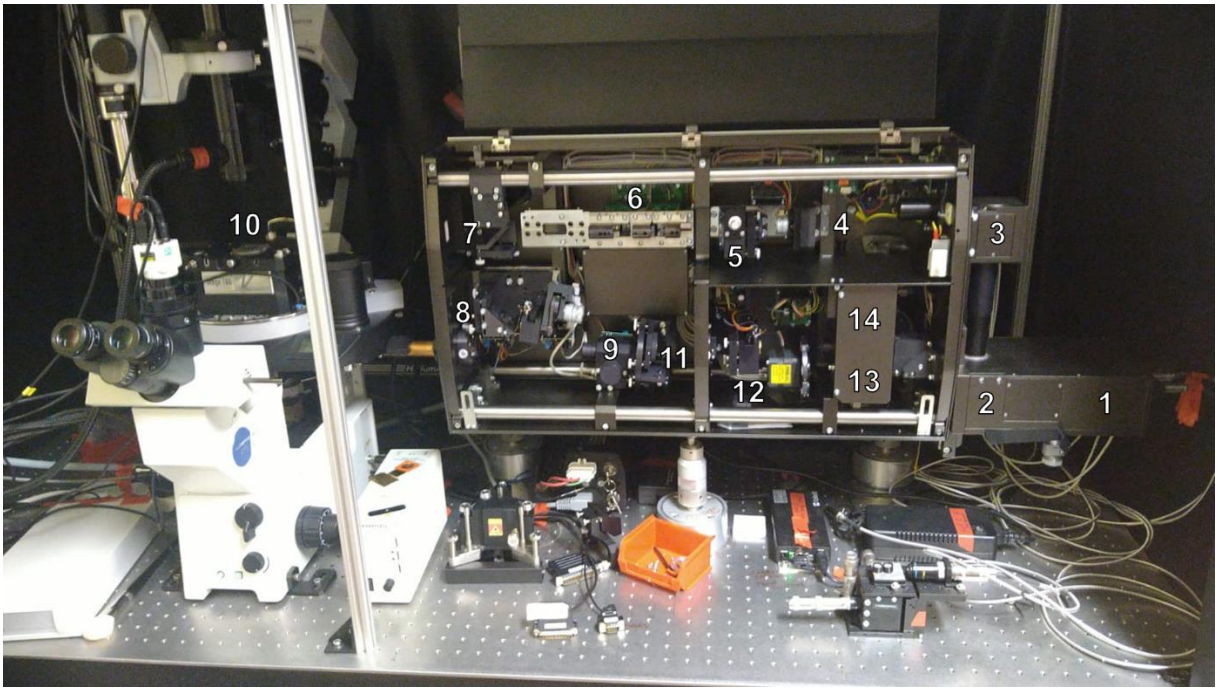

Figure 3-23 Photograph detailing the NTEGRA Spectra Raman system. Numbers indicate the visible instrument components as from Figure 3-22.

The laser beam is transferred from the input unit using mirrors 2 and 3 through the adjustable density neutral filter 4 and a polariser 5 to the beam expander 6. The automatically adjusted laser beam expander 6 provides control of laser beam diameter adjustment and collimation. Mirrors 7 and 8 direct the laser beam onto the notch filter 9. The beam reflected from the notch filter 9 runs to the radiation delivery system and is passed through the measuring head lens to be focused on the DPA sample 10.

The beam reflected from the sample is recorded in two ways. The first path is the laser optical scheme, which is designed to produce a confocal picture of the sample from laser light. The laser light is reflected from the sample passing through the measuring head lens, which is then reflected from notch filter 9 and mirror 8. A small portion of the light (3%) passes through mirror 7 and passes into the reflection unit. Lens 18 focuses the beam through pinhole 20 into the Photo-Multiplier Tube (PMT) to produce a scatter diagram.

The second path is the spectral optical scheme, which is designed to produce a confocal picture of the sample from the light of secondary radiation. The Raman light emitted by the sample is collimated by the measuring head lens and polariser 11 and filter cartridge 12 after which it is

directed into an adjustable pinhole 15 installed at the monochromator entrance. Diffraction gratings 16 separate the light into its spectral components, which can then be with the CCD-camera after being directed by mirror 17.

3.3.5 Raman Spectroscopy Measurements – UCTP Prague

Raman and SERS spectra were recorded using various Raman spectrometers for different laser excitation wavelengths. All spectra data collection was performed using experimental conditions (laser power, collection time), optimized for each used wavelength. The spectrometers used and their associated lasers and laser powers are as follows (Table 3-2):

Spectrometer	Laser Wavelength (nm)	Power (mW)
Thermo Scientific DXR Raman Microscope	532	1
Renishaw inVia Reflex Raman Microscope	633	5
ProRaman-L spectrometer	785	15
Renishaw inVia Reflex Raman Microscope	830	25

Table 3-2 Raman spectrometers used at UCTP with their associated laser wavelength and power.

From each DPA sample, 10 random points were analysed on each shuriken array and the result mean calculated. All spectra were baseline corrected and smoothed using an 11-point averaging smoothing algorithm to reduce baseline variability in 450–2000 cm^{-1} region using Omnic Professional Software Suite (Thermo Scientific, Inc., Madison, WI).

3.4 Finite Element Method for Electromagnetics

The development of novel photonic devices can be an arduous process involving design, fabrication, and characterisation of optical properties. Not to mention the consequent redesigns required to optimise any new device. Utilising the power of computational modelling and simulation tools can significantly reduce the time required to create such devices.

Many natural and physical phenomena operate via gradients. Mathematically, these can be represented as gradients, differential equations, or PDEs. Maxwell's equations are a good example of a set of PDEs. For engineering problems, additional constraints called *boundary conditions* are also added, which when coupled with differential equations lead to what is known as a *boundary value problem*. The solutions to these problems using analytical methods such as direct integration is only possible for simple geometries. To solve for complex geometries, *numerical methods* must be applied to obtain approximate solutions to the given boundary value problem. The finite element method (FEM) is one type of numerical method used. The FEM works by converting a boundary value problem into a linear system of equations of the form $Ax = b$, where A is a matrix that represents the coefficients of the unknowns in the equations, x is a column vector of the unknowns that are being solved, and b is the resultant column vector [20].

The FEM and how it is employed to EM simulations can be divided into the following steps:

1. **Simulation set-up**: The geometry of the simulation domain is first constructed. This includes defining the materials present, such as gold, water, air, or polycarbonate. Domain boundaries and periodic conditions are also applied.
2. **Material properties**: To all domains, the appropriate material properties are assigned. These properties include parameters such as permittivity, permeability, chirality tensors.
3. **Meshing**: Simulation domains are divided into smaller *finite elements*. A great advantage of FEM is that element sizes and shapes can be chosen to accommodate complex geometries, such as the shuriken 'star' shape used in DPA samples. Some examples of available shapes are triangles, quadrilaterals, and tetrahedrons [21]. The way the FEM breaks apart a complex problem domain into smaller elements is often referred to as a "divide and conquer" technique [20].

4. **Equation formulation**: Maxwell's equations are then applied to each element, with the material properties taken into account.
5. **Weak formulation**: Maxwell's differential equations are transformed into what is called the *weak form*, which is accomplished by multiplying the differential equations with test functions to convert them to integral form across each element. These give approximate solutions to the EM equations but are simpler to solve.
6. **Piecewise interpolation**: The weak form equations are combined with *shape functions*. These are typically polynomial functions designed to satisfy certain conditions and provide a way to approximate the EM solutions between element nodes. When multiplying the shape functions with the integral weak form equations and integrating across the element, a linear system of equations is created for each element.
7. **Assembly**: The contribution of all elements is assembled to obtain a linear system of equations for the whole simulation domain, which can be solved the EM field representation for the entire domain.
8. **Result analysis**: The simulation results can now be analysed, and parameters such as EM field strength and reflectivity obtained. If possible, results should be validated with experimental data.

A benefit to the FEM is the flexibility in the choice of discretisation parameters. Meshing elements size can be chosen according to the domains. Regions of interest with more complex geometries typically have smaller mesh to provide a more accurate image of the electromagnetic fields, whereas larger simpler domains can have larger mesh elements to cut down on computing times. The multitude of element shapes available in FEM is also of great importance as it allows for the accurate representation of complex geometries, such as shuriken shaped nanostructures.

The unit cell of the simulated DPA metasurface containing the shuriken nanostructure is generally split into domains of varying thickness (Figure 3-24A). The top 200 nm of the cell is what is referred to as a Perfectly Matched Layer (PML), which serves the purpose of absorbing all reflections from the nanostructure surface. Below the PML exists the incident light port from where collimated light of a specified polarisation and power originates. 100 nm below the incident light port an integration surface is added, which calculates the power of reflected light. The nanostructure being simulated is located at the centre of the unit cell. Moving further down

the unit cell another integration surface is added which calculates the transmitted power. The exiting light port is placed 200 nm from the bottom of the unit cell, which is followed by another PML. Floquet periodic conditions are applied to the unit cell to simulate a periodic array of nanostructures found in a metasurface array. The Floquet theorem states solutions to a wave equation in a periodic structure can be represented by the product of a periodic function and a plane wave. allowing for the modelling of EM waves in periodic array structures [22]. The domains surrounding the nanostructure are selected as specific materials. Typically, above the nanostructure and within the nanostructure cavity the domains are simulated as water or air, with parameters such as refractive index and permittivity values chosen accordingly. Similarly, below the nanostructure gold metal layer the material is appropriately chosen as polycarbonate.

The refractive index values for gold and polycarbonate were chosen from reports by Johnson and Christy [23], and Sultanova *et al* [24], respectively. Refractive index values for air were simply chosen to be 1 and zero for the real and imaginary components, respectively, as in air these values remain relatively constant in the wavelength ranges studied. Finally, simulations using water as the dielectric had refractive index values chosen from the available material database of the software utilised for simulations. For all simulation results presented in this thesis, a commercial finite element package (COMSOL V6.0 Multiphysics Software, Wave Optics Module) was used. The number of mesh elements for a single simulation is tuned by choosing element size for each domain. Generally, the desired number of elements is around 500,000 per simulation to achieve accurate results.

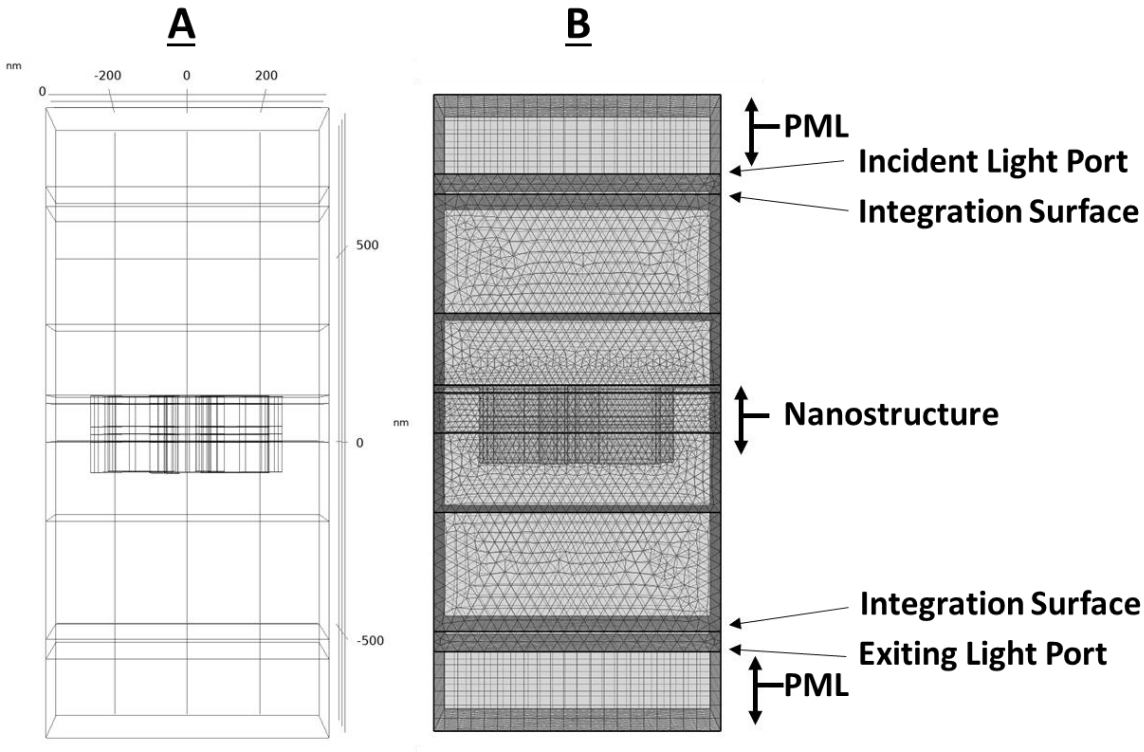

Figure 3-24 (A) Side-view of simulation unit cell. (B) Rendered meshing shown in geometry.

An example of a unit cell with material domains specified for a simulated periodic LH shuriken metafilm is presented in Figure 3-25. This unit cell was used for simulations presented in Section 5.3.6 to study optical chirality, *C*, parameters generated by the DPA shuriken structure. The polarisation of incident light for all simulations was selected to be along the y-axis (Figure 3-25B), which is in accordance with all experimental measurements. Wavelengths chosen for simulation were dependent on the experiment and are defined in subsequent chapters.

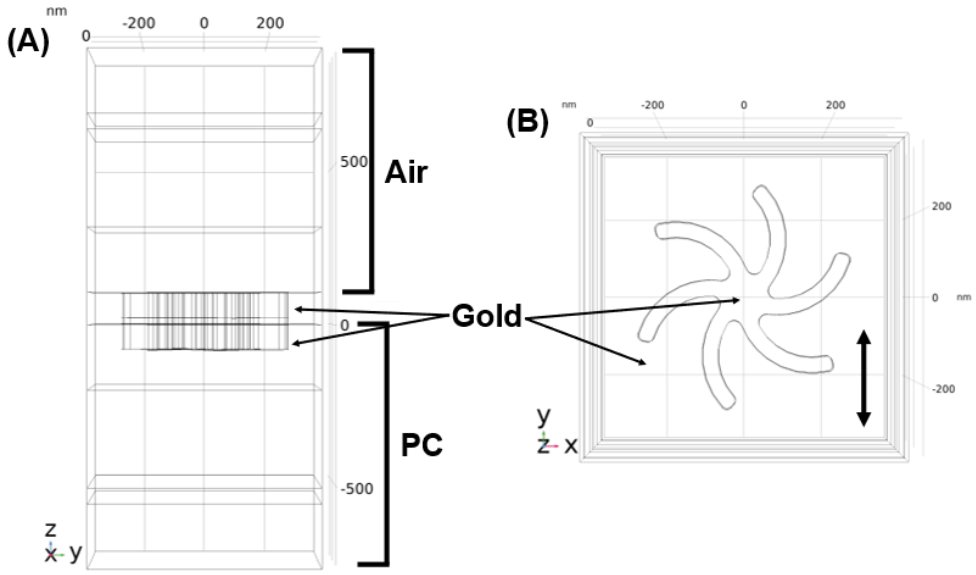

Figure 3-25 Side (A) and top (B) view of an example LH shuriken unit cell used for simulations, with air, gold, and polycarbonate (PC) domains shown. Grid units in nm. Double-headed arrow indicates electric field polarisation direction of incident light.

3.4.1 Modelling of Chiral Protein Layers

To simulate chiroptical interactions between chiral metamaterial nanostructures and deposited chiral dielectric materials, such as proteins, a commonly used approach is to apply a chiral isotropic layer [25, 26]. The effect of this chiral layer on optical properties is modelled using what is known as the *constitutive equations* for a chiral material, which contains the second rank tensor χ^{iso} [27, 28]:

$$D = \varepsilon_0 \varepsilon E + i\chi^{iso} B \tag{2.8.1}$$

$$H = \frac{B}{\mu_0 \mu} + i\chi^{iso} E \tag{2.8.2}$$

Where ε_0 is the permittivity of free space, ε is the relative permittivity, E is the complex electric field, D is the electric displacement field, μ_0 is the permeability of free space, μ is the relative permeability, B is the complex magnetic flux density, and H is the magnetic field. The letter χ is a dimensionless magneto-electric parameter which represents the reciprocity of a material. Reciprocity in this context means that a material will interact with an EM field the same way when the magnetic and electric fields are interchanged [29].

In this case χ^{iso} will only be non-zero and non-reciprocal for chiral dielectric materials. Achiral materials will experience no change in phase between electric and magnetic fields as $\chi = 0$.

The second rank tensor components for χ^{iso} are only determined by electric dipole and magnetic dipole interactions, leaving the non-diagonal elements as zero [30]:

$$\chi^{iso} = \begin{bmatrix} \chi_{xx}^{iso} & 0 & 0 \\ 0 & \chi_{yy}^{iso} & 0 \\ 0 & 0 & \chi_{zz}^{iso} \end{bmatrix} \tag{2.8.3}$$

Where $\chi_{xx}^{iso} = \chi_{yy}^{iso} = \chi_{zz}^{iso}$.

For an ordered layer of proteins, chiral interactions with EM fields will not be the same in all directions as the layer is anisotropic, so the χ tensor must be modified. For a chiral medium of adsorbed biomolecules that are well-orientated with respect to the surface, but rotationally isotropic, the layer can be assumed to have C_∞ symmetry [26]. In a study by Theron and Cloete, the chiral tensor was modified to account for such symmetry [31]:

$$\chi^{aniso} = \begin{bmatrix} \chi_{xx}^{ani} & \chi_{xy}^{ani} & 0 \\ -\chi_{xy}^{ani} & \chi_{yy}^{ani} & 0 \\ 0 & 0 & \chi_{zz}^{ani} \end{bmatrix} \tag{2.8.4}$$

The diagonal elements are no longer equal as the chiral layer molecules are aligned in a linear fashion, resulting in $\chi_{xx}^{iso} = \chi_{yy}^{iso} \ll \chi_{zz}^{iso}$. The contribution of the electric dipole-electric quadrupole interaction to optical activity cannot be ignored in an anisotropic chiral medium and is thus represented by the χ_{xy}^{ani} element [31].

The effect of a chiral protein layer on the optical properties of DPA shurikens, and the significance of well-ordered anisotropic protein layers is further investigated further in Section 4.2.1.

3.5 DPA Testing and Characterisation

3.5.1 Noise and Sensitivity

After optimising surface functionalisation and passivation protocols, the next stage of experimentation was to estimate the performance of the DPA sample with the imaging polarimetry microscope by evaluating the noise performance and establishing the error limitations which impact the sensitivity and performance limits of the platform.

Multiple ORD measurements of water, followed by 2 M $MgSO_4$, were performed to estimate the measurement error and potential drifts when no changes are made in the fluidic chamber (Figure 3-26 and Table 3-3). An initial reference measurement of water was taken at 0 minutes, and every 30 minutes thereafter until 3 hours. Then, the 2 M $MgSO_4$ solution was added, and ORD measurements taken every 30 minutes until 3 hours passed. Box plots were chosen as a suitable format to present the resonance shift, $\Delta\lambda$, data as they adequately show the spread of data obtained from each DPA P5 region A-I array locations. The central small square in the box plot represents the mean, with the surrounding box showing the range between the lower and upper quartiles. The whiskers represent the minimum and maximum data points.

Results show that the largest maximum-minimum (max-min) range for resonance shifts is 0.3 nm or less for both water and salt. Hence, the estimated instrument error is $\pm$ 0.15 nm for the $\Delta\lambda$ of both peaks. Results also show that the errors are larger when the media is changed and resonance shifts occur, roughly giving an error in $\Delta\lambda$ of $\pm$ 0.3 nm (Figure 3-26C). This increased variation may occur due to changes in incident light wave fronts, temperature and concentration gradients, or changes on the metal-liquid interface (electrical double layer) over the 3×3 mm measurement area that have been shown previously to affect plasmonic sensing [32, 33]. Another useful parameter to consider is the spacing in the wavelength values between the two peaks (represented by S). ΔS is the change in the spacing in comparison to the initial measurement and this has previously been used as an additional parameter to measure protein interactions at the surface [26, 34]. The large ~20 nm resonance shift due to $MgSO_4$ is accompanied by a slight increase in spacing (ΔS) between Peak 1 and Peak 2 of 0.2-0.3 nm, indicating a slight difference in terms of the sensitivity to refractive index changes. However, for proteins and buffer solutions, we expect resonance shifts to be an order smaller as the proteins form at most only a

monolayer and the buffer solutions are far lower in salt concentration than the $MgSO_4$ solutions used here. The differences in sensitivity, and hence ΔS, seen in the salt solutions would be near negligible when resonance shifts are in the order of ~2-5 nm.

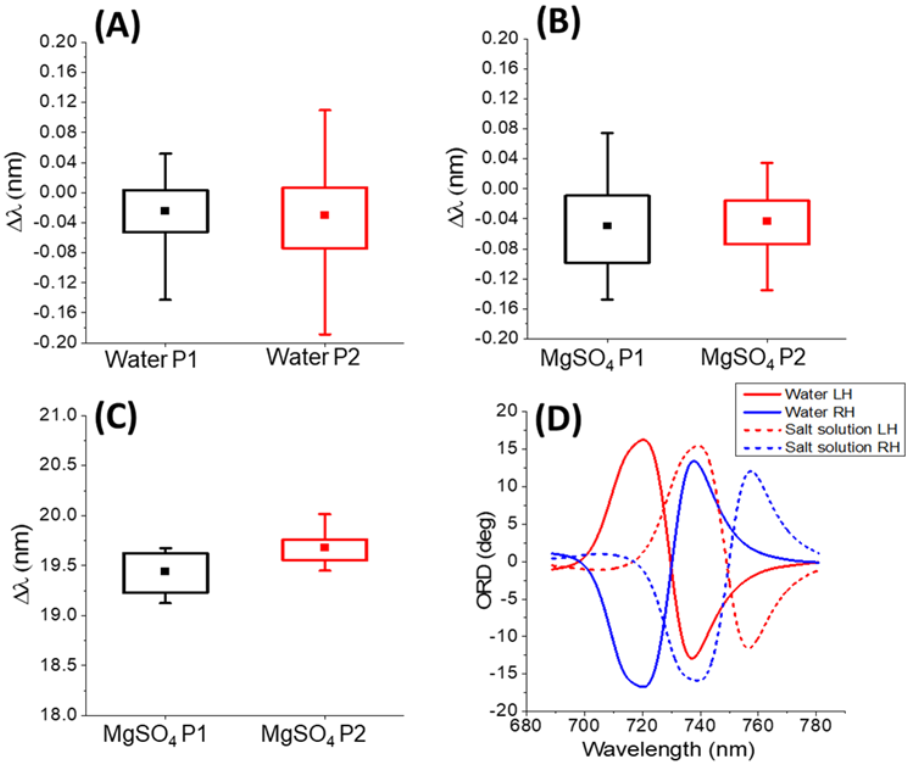

Figure 3-26 Δλ values from Peak 1 (black) and Peak 2 (red) of (A) water measurements and (B) repeat $MgSO_4$ measurements, comparing resonance shifts from initial 0 min and 3-hour periods. (C) Δλ obtained for $MgSO_4$ relative to water following 3 hours, with (D) change in ORD for LH (red) and RH (blue) structures.

Values in nm	Δλ of Water Over 3 hours		Δλ of $MgSO_4$ Relative to Water		Δλ of $MgSO_4$ Over 3 hours	
	P1	P2	P1	P2	P1	P2
Mean Δλ	-0.02	-0.03	19.44	19.68	-0.06	-0.04
St. Dev. Δλ	0.04	0.06	0.20	0.16	0.06	0.04
Range Δλ	0.19	0.30	0.55	0.57	0.22	0.17
Mean ΔS	-0.01	-	0.24	-	0.01	-
St. Dev. ΔS	0.07	-	0.21	-	0.07	-

Table 3-3 Δλ values of data shown in Figure 3-26. Changes in ORD spacing (ΔS) also shown. Values in nm. Standard deviation (St. Dev.) values calculated from all 9 LH and 9 RH (18 total) array locations.

The sensing performance of DPA samples was also characterised through ORD measurements of sucrose solutions (Figure 3-27). Compared to baseline water measurements, ORD peak positions for the sucrose solution are red-shifted approximately 10 nm because of the higher RI compared to water - 1.355679 against 1.334, respectively. The refractive index sensitivity, commonly measured in Refractive Index Units (RIU) and defined as the ratio of the change in resonance peak wavelength ($\Delta\lambda$) to the bulk refractive index variation (Δn) was calculated [35]:

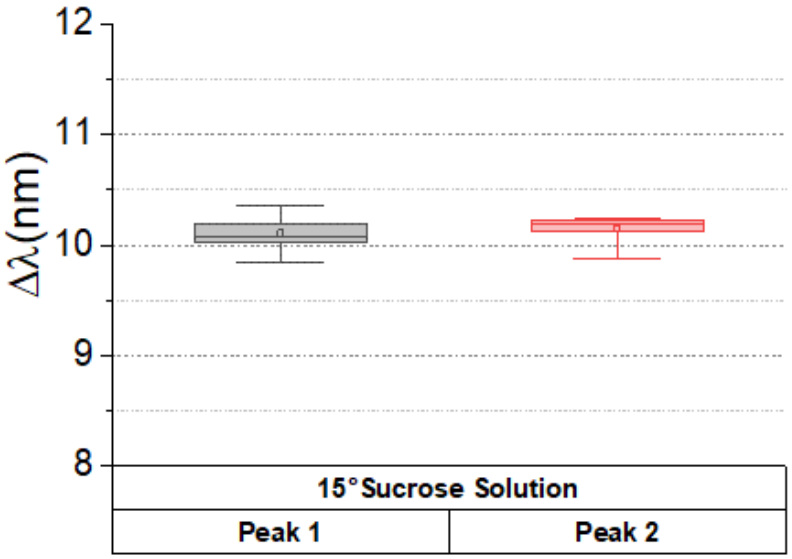

Figure 3-27 ORD Δλ results for Peak 1 and Peak 2 of sucrose solution measurements used to measure refractive index sensitivities.

$$RIU\ (Peak\ 1) = \frac{\Delta\lambda}{\Delta n} = \frac{10.11\ nm}{0.021679} = 466\ nm/RIU \quad (3.4.1)$$

$$RIU\ (Peak\ 2) = \frac{\Delta\lambda}{\Delta n} = \frac{10.15\ nm}{0.021679} = 468\ nm/RIU \quad (3.4.2)$$

These RIU values are generally in between the sensitivity values of SPR (>1000 nm/RIU) and LSPR (around 100 nm/RIU) [36, 37], indicating that DPAs are comparable with other plasmonic based sensors.

3.5.2 DPA Surface Sensitivity Characterisation Using EM Simulations

To characterise how the EM fields decay with distance from the DPA nanostructure surface, and therefore the region in which plasmon-matter interactions occur, EM simulations of LH and RH DPA nanostructures were performed using the FEM.

The shuriken unit cell utilised for LH DPA simulations is shown in Figure 3-28. The diameter of the shuriken centre radius and arm width is 100 and 35 nm, respectively. The depth of the shuriken well is 100 nm. The optical properties of the dielectric on top of the shuriken were chosen in accordance with water, and polycarbonate below the shuriken. The top of the shuriken indentation and polycarbonate surface were assigned the properties of gold. The simulated wavelength range was $620 - 780$ nm in single steps, and the obtained ORD spectra for both LH and RH simulations are presented in Figure 3-29.

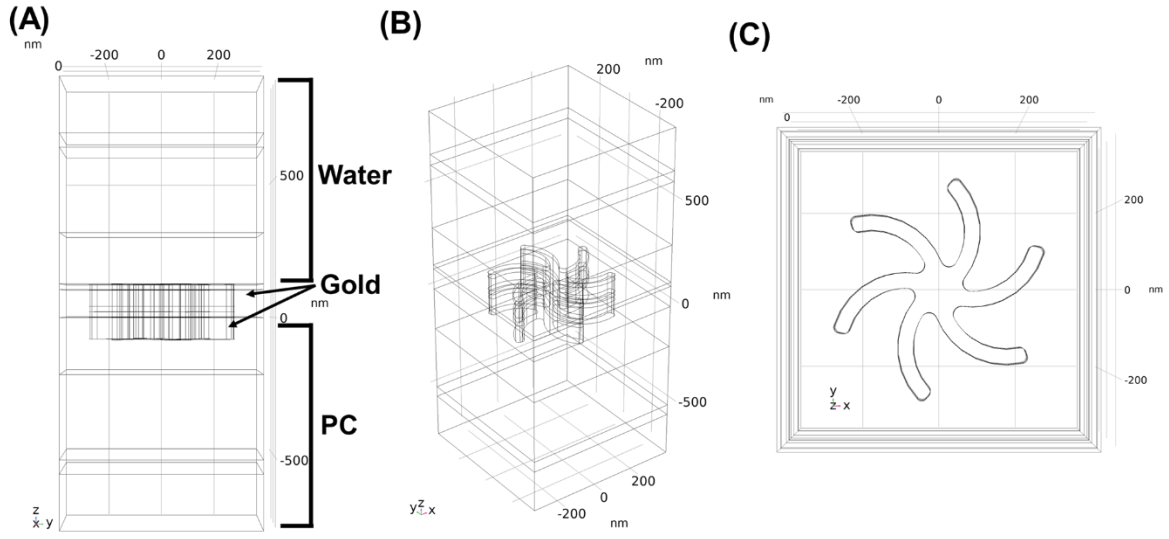

Figure 3-28 Side (A), diagonal (B), and top (C) views of the simulated LH DPA shuriken unit cell, with water, gold, and polycarbonate (PC) domains defined.

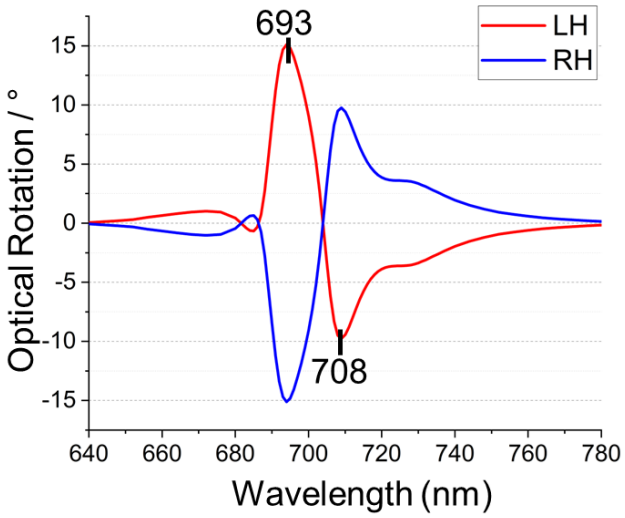

Figure 3-29 Simulated ORD spectra from LH (red) and RH (blue) DPA nanostructures, with Peak 1 and Peak 2 resonance positions highlighted.

The simulated ORD spectra display the characteristic bisignate line shapes, which are equal and opposite in magnitude. Peak 1 and Peak 2 resonance positions were found to be at 693 and 708 nm, respectively. There is a small resonance feature around 730 nm, which is thought to arise from the idealised simulation edges of the DPA shuriken. In reality, the nanofabrication processes lead to smoothed edges, resulting only in a bisignate ORD line shape. The electric field intensities of these resonance positions were investigated by measuring the maximum electric field values in the xy-plane along the lateral z-axis direction, moving from the bottom of the shuriken nanostructure indentation (at $z = 20$ nm) up to 230 nm from the surface (at $z = 250$ nm) (Figure 3-30). z = 0 nm is located at top-most point of the polycarbonate domain.

For Peak 1, Figure 3-30A, two lateral points are observed which have the highest E fields; one inside the indentation and one on the surface at $z = 100$ nm. Peak 2, Figure 3-30B, has a peak only at the surface at $z = 100$ nm. Both resonant modes show that the electric fields decay to less than 15% of the maximum value by approximately 25 nm above the surface ($z = 125$ nm). This indicates that the DPA samples possess sensitivity to material up to $20 - 30$ nm above the shuriken surface. The significance of these results is that the nanostructures will not be strongly affected by the bulk media 30 nm above the gold surface. Based on these observations, the near-field sensitivity of DPA is estimated to range up to 30 nm.

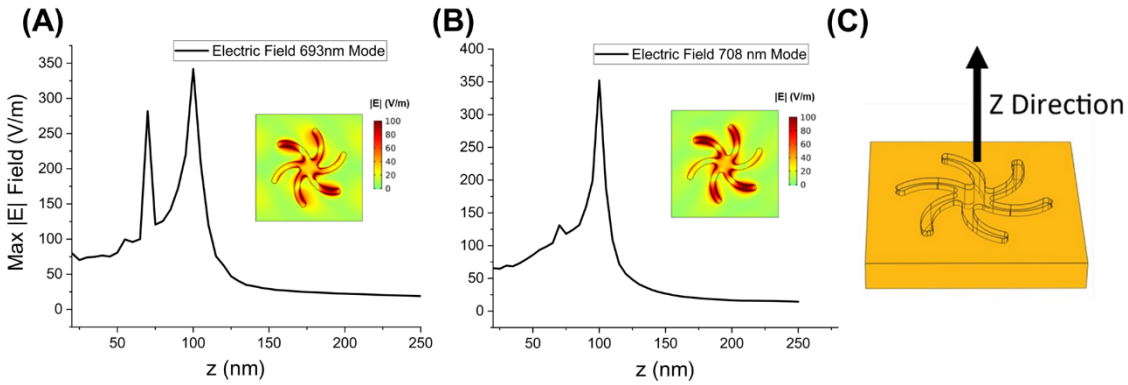

Figure 3-30 Electric field magnitude, |E| (V/m), along the z-axis above shuriken nanostructures for two separate modes: 693 nm (A) and 708 nm (B). Inset shows the 2D surface plots for |E| values on gold surface ($z = 100$ nm) at these two modes. (C) z-axis direction diagram.

When comparing these E-field decay length results to other RI based sensors, it was found that DPA structures have significantly lower decay lengths than SPR sensors (>100 nm) and slightly higher decay lengths than LSPR sensors (~ 5-10 nm) [38].

The electromagnetic confinement shown by LSPR techniques and DPA samples make them less susceptible to bulk changes due to effects such as temperature changes or additional non-target proteins expected in complex serum-like samples. It also potentially provides increased sensitivity to small molecules at low concentrations [39, 40]. Hence, from these results it can be inferred that the DPA shuriken metafilms combine the sensing benefits of both traditional LSPR and SPR biosensors.

3.6 References

1. Nayfeh, M.H., *Fundamentals and applications of nano silicon in plasmonics and fullerines: current and future trends.* 2018.
2. Vieu, C., et al., *Electron beam lithography: resolution limits and applications.* Applied surface science, 2000. **164**(1-4): p. 111-117.
3. Stormonth-Darling, J.M. and N. Gadegaard, *Injection moulding difficult nanopatterns with hybrid polymer inlays.* Macromolecular materials and engineering, 2012. **297**(11): p. 1075-1080.
4. Reimhult, E. and F. Höök, *Design of surface modifications for nanoscale sensor applications.* Sensors, 2015. **15**(1): p. 1635-1675.
5. Love, J.C., et al., *Self-assembled monolayers of thiolates on metals as a form of nanotechnology.* Chemical reviews, 2005. **105**(4): p. 1103-1170.
6. Chaki, N.K. and K. Vijayamohanan, *Self-assembled monolayers as a tunable platform for biosensor applications.* Biosensors and Bioelectronics, 2002. **17**(1-2): p. 1-12.
7. Pieters, G. and L.J. Prins, *Catalytic self-assembled monolayers on gold nanoparticles.* New Journal of Chemistry, 2012. **36**(10): p. 1931-1939.
8. Aswal, D., et al., *Self assembled monolayers on silicon for molecular electronics.* Analytica chimica acta, 2006. **568**(1-2): p. 84-108.
9. Friggeri, A., F.C. van Veggel, and D.N. Reinhoudt, *Recognition of Steroids by Self-Assembled Monolayers of Calix [4] arene–Resorcin [4] arene Receptors.* Chemistry–A European Journal, 1999. **5**(12): p. 3595-3602.
10. Jin, W., et al., *Construction and characterization of a multi-layer enzyme electrode: Covalent binding of quinoprotein glucose dehydrogenase onto gold electrodes.* Biosensors and Bioelectronics, 1995. **10**(9-10): p. 823-829.
11. Li, J.-F., C.-Y. Li, and R.F. Aroca, *Plasmon-enhanced fluorescence spectroscopy.* Chemical Society Reviews, 2017. **46**(13): p. 3962-3979.
12. Watcharinyanon, S., *Structure of Self-Assembled Monolayers on Gold Studied by NEXAFS and Photoelectron Spectroscopy*. 2008, Karlstads universitet.
13. Vericat, C., et al., *Self-assembled monolayers of thiols and dithiols on gold: new challenges for a well-known system.* Chemical Society Reviews, 2010. **39**(5): p. 1805-1834.
14. Gaberc-Porekar, V. and V. Menart, *Potential for using histidine tags in purification of proteins at large scale.* Chemical Engineering & Technology: Industrial Chemistry-Plant Equipment-Process Engineering-Biotechnology, 2005. **28**(11): p. 1306-1314.
15. Janeway Jr, C.A., et al., *The structure of a typical antibody molecule*, in *Immunobiology: The Immune System in Health and Disease. 5th edition*. 2001, Garland Science.
16. Kakkar, T., et al., *Superchiral near fields detect virus structure.* Light: Science & Applications, 2020. **9**(1): p. 195.
17. Eliasson, M., et al., *Chimeric IgG-binding receptors engineered from staphylococcal protein A and streptococcal protein G.* Journal of Biological Chemistry, 1988. **263**(9): p. 4323-4327.
18. Jazayeri, M.H., et al., *Various methods of gold nanoparticles (GNPs) conjugation to antibodies.* Sensing and bio-sensing research, 2016. **9**: p. 17-22.
19. Khanikaev, A.B., C. Wu, and G. Shvets, *Fano-resonant metamaterials and their applications.* Nanophotonics, 2013. **2**(4): p. 247-264.

20. Polycarpou, A.C., *Introduction to the finite element method in electromagnetics*. 2022: Springer Nature.
21. Wai, C., A. Rivai, and O. Bapokutty. *Modelling optimization involving different types of elements in finite element analysis*. in *IOP Conference Series: Materials Science and Engineering*. 2013. IOP Publishing.
22. Hakoda, C., et al. *Using Floquet periodicity to easily calculate dispersion curves and wave structures of homogeneous waveguides*. in *AIP Conference Proceedings*. 2018. AIP Publishing.
23. Johnson, P.B. and R.-W. Christy, *Optical constants of the noble metals.* Physical review B, 1972. **6**(12): p. 4370.
24. Sultanova, N., S. Kasarova, and I. Nikolov, *Dispersion properties of optical polymers.* Acta Physica Polonica A, 2009. **116**(4): p. 585-587.
25. Gilroy, C., et al., *Roles of superchirality and interference in chiral plasmonic biodetection.* The Journal of Physical Chemistry C, 2019. **123**(24): p. 15195-15203.
26. Kelly, C., et al., *Chiral plasmonic fields probe structural order of biointerfaces.* Journal of the American Chemical Society, 2018. **140**(27): p. 8509-8517.
27. Cho, K., *Dispersion relation in chiral media: Credibility of Drude–Born–Fedorov equations.* Electromagnetic Metamaterials: Modern Insights into Macroscopic Electromagnetic Fields, 2019: p. 189-199.
28. Govorov, A.O., et al., *Theory of circular dichroism of nanomaterials comprising chiral molecules and nanocrystals: plasmon enhancement, dipole interactions, and dielectric effects.* Nano letters, 2010. **10**(4): p. 1374-1382.
29. Wang, B., et al., *Chiral metamaterials: simulations and experiments.* Journal of Optics A: Pure and Applied Optics, 2009. **11**(11): p. 114003.
30. Govorov, A.O. and Z. Fan, *Theory of chiral plasmonic nanostructures comprising metal nanocrystals and chiral molecular media.* ChemPhysChem, 2012. **13**(10): p. 2551-2560.
31. Theron, I.P. and J.H. Cloete, *The electric quadrupole contribution to the circular birefringence of nonmagnetic anisotropic chiral media: A circular waveguide experiment.* IEEE Transactions on microwave theory and techniques, 1996. **44**(8): p. 1451-1459.
32. Kötz, R., D. Kolb, and J. Sass, *Electron density effects in surface plasmon excitation on silver and gold electrodes.* Surface Science, 1977. **69**(1): p. 359-364.
33. Wang, S., et al., *Electrochemical surface plasmon resonance: basic formalism and experimental validation.* Analytical chemistry, 2010. **82**(3): p. 935-941.
34. Kelly, C., et al., *Controlling metamaterial transparency with superchiral fields.* Acs Photonics, 2018. **5**(2): p. 535-543.
35. Gómez-Castaño, M., et al., *Electrodeposited negative index metamaterials with visible and near infrared response.* Advanced Optical Materials, 2020. **8**(19): p. 2000865.
36. Chung, T., et al., *Plasmonic nanostructures for nano-scale bio-sensing.* Sensors, 2011. **11**(11): p. 10907-10929.
37. Guo, L., et al., *Strategies for enhancing the sensitivity of plasmonic nanosensors.* Nano Today, 2015. **10**(2): p. 213-239.
38. de Almeida, M.P., et al., *Gold nanoparticles as (bio) chemical sensors*, in *Comprehensive analytical chemistry*. 2014, Elsevier. p. 529-567.
39. Lopez, G.A., et al., *Recent advances in nanoplasmonic biosensors: applications and lab-on-a-chip integration.* Nanophotonics, 2017. **6**(1): p. 123-136.

40. Luchansky, M.S., et al., *Characterization of the evanescent field profile and bound mass sensitivity of a label-free silicon photonic microring resonator biosensing platform.* Biosensors and Bioelectronics, 2010. **26**(4): p. 1283-1291.

Chapter 4 – Biosensor Applications

This chapter will detail DPA platforms as a candidate for a rapid, low-cost, biosensor platform with added multiplexing (multiple biomarker detection) capabilities for diagnostic applications. Various biosensing experiments and their respective results are presented. This includes the initial detection of the biotin-streptavidin protein-ligand interaction, COVID-19 spike (S1) protein, SARS-CoV-2 and Zika virus, Noro Virus-Like-Particles (VLP), and haptoglobin protein detection.

4.1 Background

4.1.1 DPAs as Biosensors

Current diagnostic biosensor methods, such as PCR, often rely on multiple steps, molecular labelling, and complex analysis which increases result turnaround times [1]. The technique of PCR is also susceptible to oligonucleotide reagent shortages, as occurred in the SARS-CoV-2 pandemic [2]. Existing rapid diagnostic platforms which are based on lateral flow devices (LFDs) provide results faster than PCR but are limited in detecting one, or at most a handful of biomarkers at a time.

The ORD spectra generated by DPAs and subsequent resonance shifts ($\Delta\lambda$) from surface binding events of biomolecules serves as the basis for a biosensing platform. The DPA samples display bisignate ORD with 2 peaks in the 700-800 nm spectral window when measured in aqueous conditions, which are labelled Peak 1 and Peak 2. These ORD peaks experience resonance shifts from the increase in local refractive index upon the addition of material on the sample surface (Figure 4-1). In addition to $\Delta\lambda$ values, chiral asymmetry parameters ($\Delta\Delta\lambda$) can be calculated from the difference between the shifts of the LH and RH ORD spectra, which can possess valuable information:

$$\Delta\Delta\lambda = \Delta\lambda_{LH} - \Delta\lambda_{RH} \tag{4.1.1}$$

Where $\Delta\lambda_{LH}$ and $\Delta\lambda_{RH}$ are the ORD resonance shifts for LH and RH nanostructures, respectively. Using this technique, previous studies using chiral gammadions have shown sensitivity to secondary structures of protein macromolecules. For example, proteins possessing a higher ratio of β-sheets such as concanavalin A and β-lactoglobulin exhibit high and positive $\Delta\Delta\lambda$ values – whereas proteins with higher proportions of α-helices such as bovine serum albumin and haemoglobin had significantly smaller $\Delta\Delta\lambda$ [3].

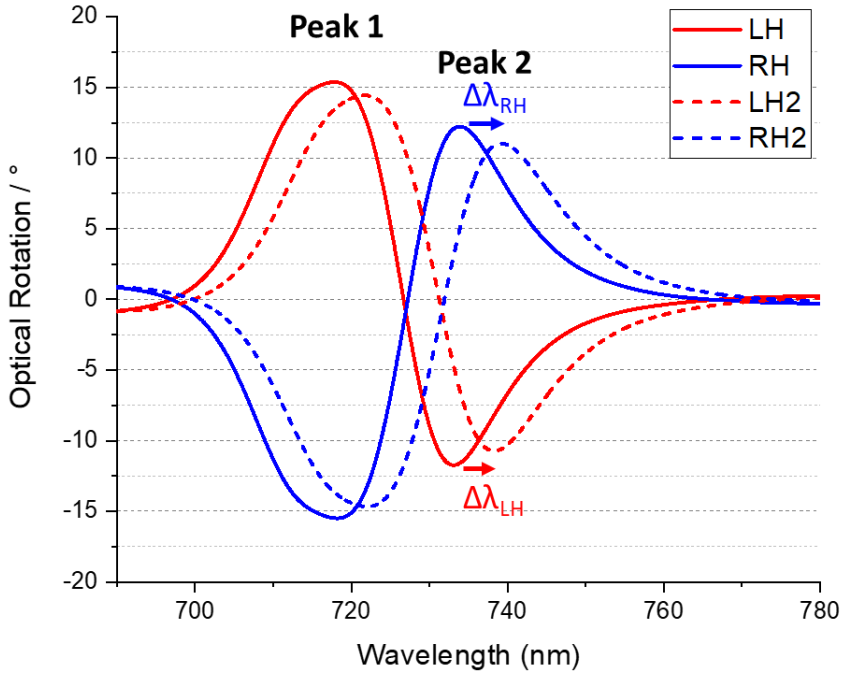

Figure 4-1 Example ORD spectra from LH (red) and RH (blue) DPA structures in water (solid lines) and a higher refractive index solution (dashed line).

Other work using the DPA shuriken or nanostructure indentations has been performed to study the chiroptical effects and characterise higher order (tertiary and quaternary) shikimate kinase and enolpyruvylshikimate 3-phosphate synthase proteins [4], as well as turnip yellow mosaic virus particles [5].

4.1.2 SARS-CoV-2 Pandemic

The global COVID-19 pandemic has sparked a tremendous increase in demand for rapid virus on-site diagnostic tests. The ability to accomplish this without the requirement of lysing agents would reduce experimental steps and reagent requirements. Currently, PCR diagnostic approaches are viewed as the gold standard of infectious disease diagnostics due to their high

sensitivity, specificity, and reproducibility attributes [6]. The drawbacks associated with PCR detection techniques are their cost and relatively high turnaround times which range from 2-3 hours – making PCR impractical for use in large scale routine testing. Additionally, a compounding problem experienced during the pandemic was the limited supply of diagnostic resources such as nucleotide reagents required for PCR, creating shortages of available diagnostic tests [7, 8]. To improve on result turnaround times, rapid and economical detection of some pathogen components and biomarkers is performed using lower sensitivity tests such as LFDs and traditional immunoassays, such as Enzyme-Linked Immunosorbent Assays (ELISA), which are now well established for non-PCR based diagnostics.

Given the significance and the readily available of the related antigen and antibody reagents, COVID-19 emerged as one of the main targets for detection using the DPA platform.

The infamous virus responsible for the COVID-19 pandemic is the Severe Acute Respiratory Syndrome Coronavirus 2 (SARS-CoV-2). It is a highly infectious viral disease that has spread worldwide and resulted in a reported death toll of 6.9 million people [9]. The internationalisation and ease of travel in the modern world has facilitated the spread of infection and has highlighted the importance of Point-of-Care (PoC) rapid diagnostic testing for locations such as airports, borders, and test centres for the general populace to monitor, control, and contain the disease.

The structure of SARS-CoV-2 is that of a single-stranded RNA-enveloped virus, covered by a large number of trimeric glycosylated proteins known as ‘spike’ or S-proteins (Figure 4-2) [10] [11]. S-proteins are promising targets for COVID-19 antigen testing present in the nasal mucus of infected individuals, and their antibody tests are useful to evaluate post-infection rates as well. The S-protein is a 1273 amino acid long (180-200 kDa) class I glycoprotein which can be cleaved into two subunits, referred to as spike 1 (S1) and spike 2 (S2) sub-units, which play different roles in viral binding and entry into cells. For experimental procedures, the S1 subunit was used, which consists of an N-terminal domain (NTD; amino acid sequence 14-290), and a receptor binding domain (RBD; amino acid sequence 306-527). The 193-amino acid RBD constituent of the S-protein is responsible for the recognition and binding of the angiotensin-converting enzyme-2 (ACE-2) on host cells [2, 12].

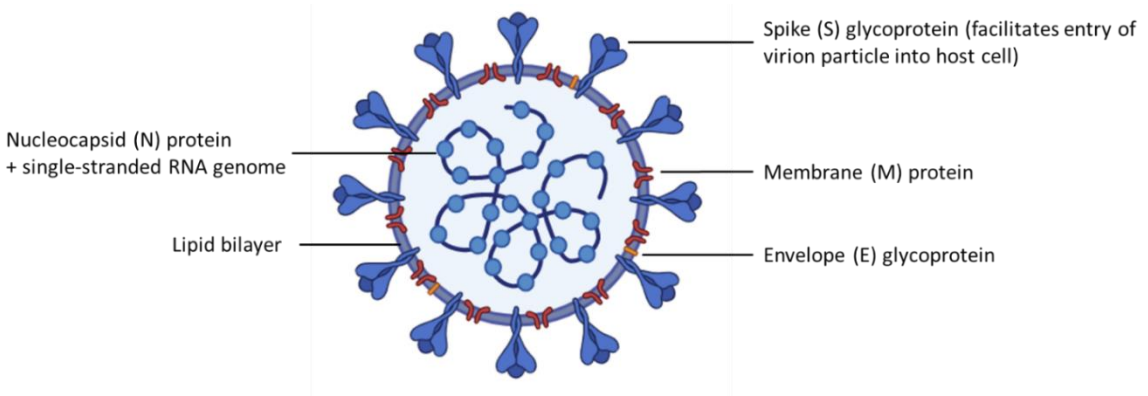

Figure 4-2 SARS-CoV-2 virus structure with major structural proteins depicted. Image adapted from Kuldeep et al. [10].

Before the detection of SARS-CoV-2 virions and S1 proteins, initial experiments using DPA samples were directed towards a simpler test-system – namely the interaction between biotin and streptavidin.

4.2 Biotin-Streptavidin Interaction Using DPAs

Having calibrated the ORD imaging system with salt solutions in Section 3.5.1, a robust protein-ligand system was required to test the DPA sensing platform. The streptavidin protein and its associated biotin ligand was chosen due to their wide-spread use in research and incredibly high binding affinity; streptavidin binding to biotin forms one of the strongest non-covalent interactions in nature, possessing a dissociation constant of $\sim 1 \times 10^{-14}$ M [13].

The protein of streptavidin possesses a tetrameric quaternary protein structure, and thus has 4 binding sites for biotin (Figure 4-3A-B) [14]. Modifying the biotin molecule by adding a PEG-chain with a terminal sulfhydryl group, a biotinylated SAM can be created on the DPA surface which selectively binds streptavidin (Figure 4-3C). Due to the symmetry of the streptavidin structure and the surface density of biotin moieties immobilised in the SAM, streptavidin is likely to only bind to 1 or 2 biotin sites on the DPA surface at any time [15]. Hence, a minimum of 2 vacant biotin binding sites would be expected for the protein, allowing for the potential of introducing additional biotin molecules functionalised with reporter fluorescent dyes to monitor DPA protein surface coverage. Streptavidin is also expected to adopt a more compact structure upon binding to biotin [16]. This conformational change in the protein may be detectable in the ORD spectrum. Considering these versatile characteristics of the streptavidin-biotin complex,

this protein-ligand system becomes an appropriate model to study the performance of the DPA sensor platform [17, 18].

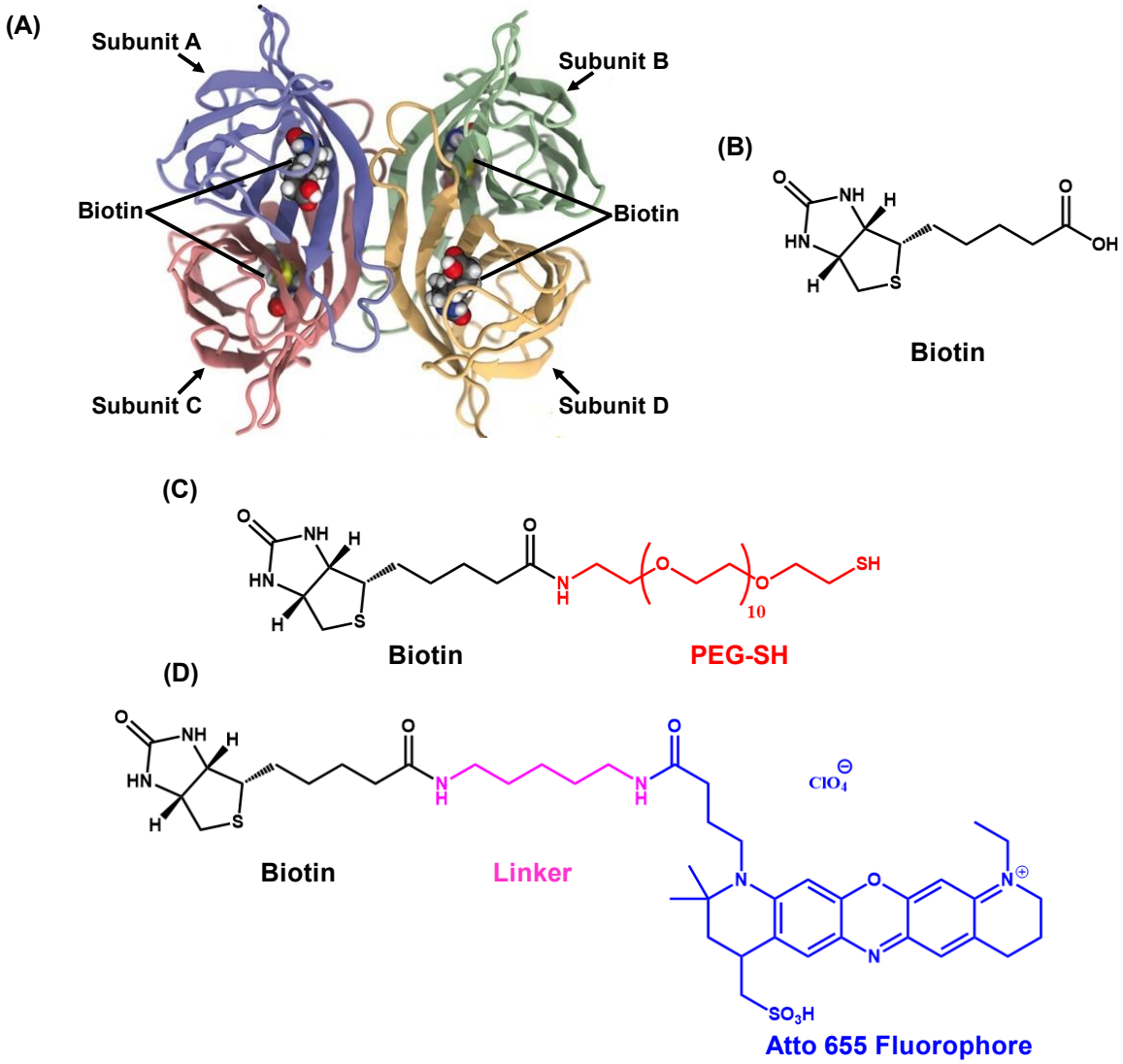

Figure 4-3 (A) Protein crystal structure of streptavidin, comprised of 4 β-barrel sub-units. Protein image from Sedlak et al [14]. (B) Biotin molecule. (C) Biotin-PEG-SH molecule used to create biotinylated SAMs on gold DPA surfaces. (C) Atto-655 fluorophore biotin used to confirm biotin-streptavidin binding with fluorescence images.

Unlike SPR instruments, there is no requirement for kinetic measurements using ORD $\Delta\lambda$ measurements to determine successful ligand/protein binding and experiments are performed by adding the streptavidin to the sample surface for 30 mins**.** The ORD resonance peak values are evaluated by LabView software from the spectra and the resonance values from the first reference water measurements are used to plot the mean $\Delta\lambda$ values.

A DPA sample was functionalised to form a biotinylated SAM as described in Section 3.2.2. To this sample, streptavidin protein solution as well as atto-655 biotin conjugate solution were applied in subsequent steps to investigate DPA performance (Figure 4-4). Figure 4-4B shows the resonance shifts, $\Delta\lambda$, for Peak 2 at each step of the experiment using box plots. Box plots were chosen as the medium to present the $\Delta\lambda$ data from all 9 DPA array pair sites. The square in the box represents the mean value, the line the median, the whiskers the minimum or maximum value, and the box edges the interquartile range. Initial baseline optical measurements were taken in water and then followed by PBS. Hence, all biosensing measurements here are taken relative to water.

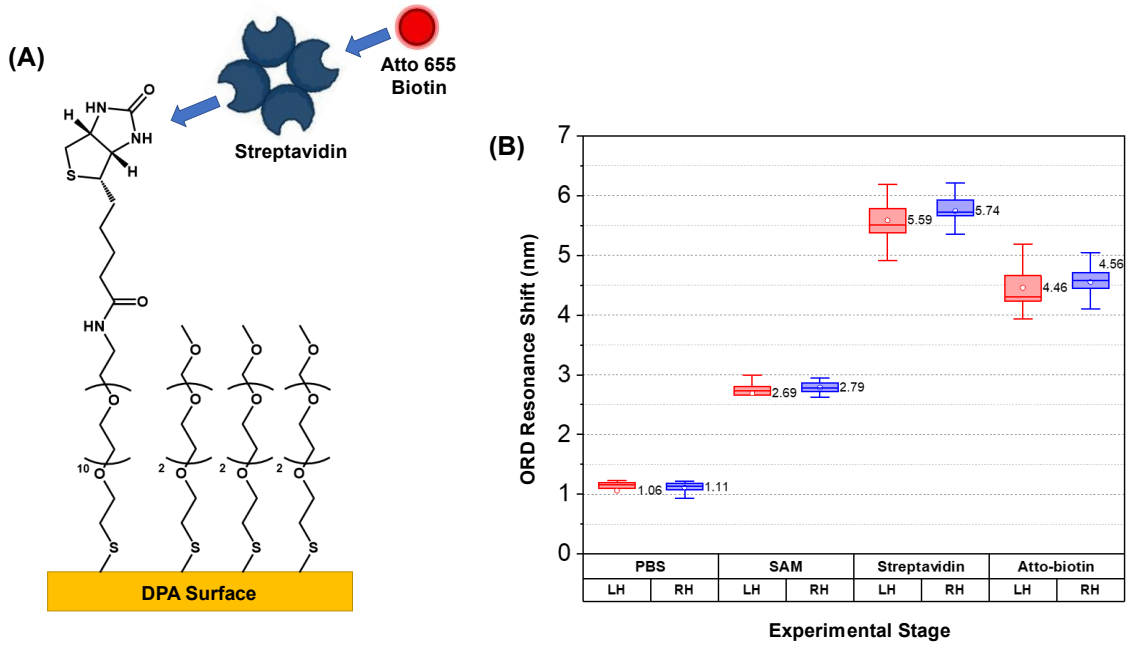

Figure 4-4 (A) Functionalisation and experimental scheme: Biotin PEG Thiol/MT(PEG)$_4$ SAM functionalised to Au surface; binding of Streptavidin to functionalised biotin; binding of Atto-655 labelled biotin to streptavidin. (B) Results for Peak 2 resonance shifts for streptavidin binding to biotin PEG thiol SAM, followed by addition of biotin (Atto-655 conjugated). Values adjacent to box plots show mean $\Delta\lambda$.

Changing solution from water to buffer induces a mean resonance shift of around 1.1 nm, which arises due to the salts present in PBS. The SAM layer shows good adhesion to the surface with a mean $\Delta\lambda$ increase of 1.6 nm for Peak 2 compared to buffer. As streptavidin (~55 kDa) is a medium sized protein considerably larger than SAM molecules, it generates a larger mean resonance shift increase of 3 nm $\Delta\lambda$ shift compared to the SAM. The streptavidin immobilisation

step was followed by the addition of biotin with an Atto-655 conjugate as outlined in Figure 4-4A.

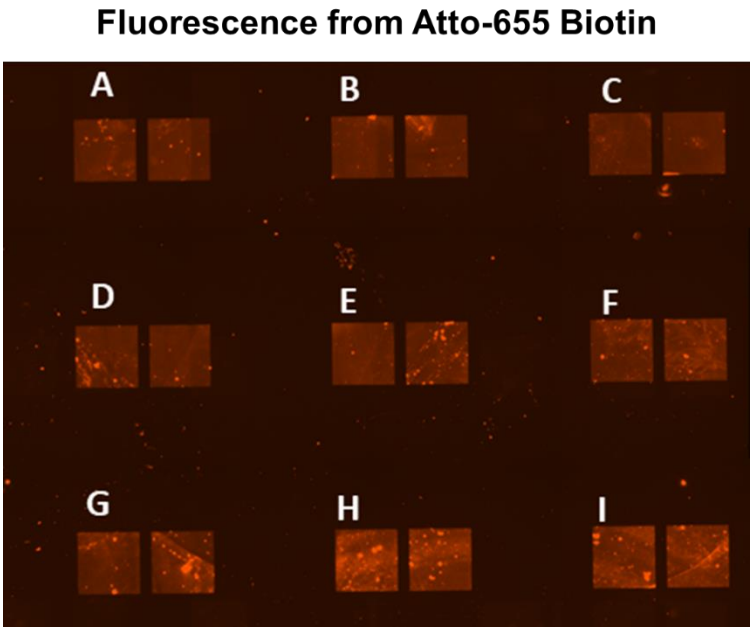

Figure 4-5 Fluorescence image from the final Atto-655 conjugated biotin observed on the nanostructures. Fluorescence over the nanostructures is more prominent due to plasmonic enhanced fluorescence.

Surprisingly, upon the addition of Atto-655 Biotin in the final stage of the experiment the mean Peak 2 ORD resonance shifts negatively by 1.2 nm (~40% change in value) even though the biotin is bound to the surface immobilised tetrameric streptavidin, which is confirmed by the plasmonic enhanced fluorescence image (Figure 4-5) [19]. One explanation for the negative shift could potentially be due to the dissociation of streptavidin from the DPA surface. However, given the extremely low dissociation constant of 10^{-15} M for the streptavidin-biotin complex, this would be highly unlikely.

An alternative reasoning for the negative resonance shift can be explained when looking at the spacing and change in spacing values between Peak 1 and Peak 2 of the ORD spectra, represented by S and ΔS, respectively (Figure 4-6). Following the ΔS values across the experiment, when the relatively large streptavidin protein is added to the biotinylated SAM, the mean ΔS increases by 0.4 nm. In the following atto-biotin addition stage, the mean ΔS only reduces by 0.1 nm, representing a 25% change in value. This 25% change is significantly lower

than the 40% change reflected in the mean $\Delta\lambda$ shifts, indicating that streptavidin protein has likely not unbound from the DPA surface.

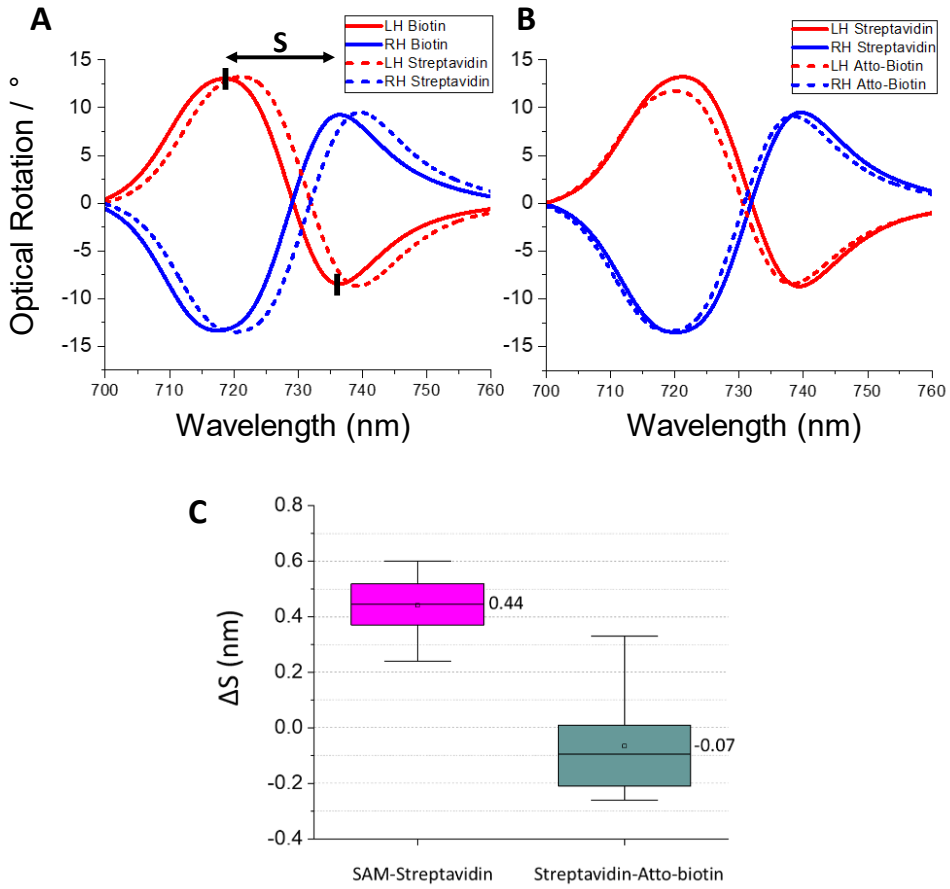

Figure 4-6 (A) Example ORD spectra from E LH (red) and E RH (blue) DPA arrays from biotin SAM (solid line) and streptavidin (dashed line) experiment, which black lines depicting the Spacing, S, parameter between Peak 1 and Peak 2. (B) Example ORD spectra from E LH (red) and E RH (blue) DPA arrays from streptavidin (solid line) and Atto-biotin (dashed line) experiment. (C) Change in ORD spacing (ΔS) from experimental steps boxplot data, with mean values shown.

A previous study by Tullius *et al*. utilised mathematical modelling based on coupled oscillators to show that an increase in the spacing parameter in reflectivity spectra obtained from DPA can be indicative of surface bound material, such as proteins [20].

From the results obtained in this study, spacing in reflectivity spectra were found to increase both experimentally as well as in EM simulations with the addition of protein layers. Thus, it can be hypothesised that spacing in ORD would also be likely to occur. This increase in spacing arises from a process known as plasmonic damping, which broadens spectral resonance features.

Plasmons possess various natural damping and decay mechanisms, such as interband, intraband, radiation, and surface damping [21]. A plasmon in a different chemical environment, such as with an added dielectric protein layer, will experience what is called chemical interface damping, inducing resonance feature broadening [22-24].

4.2.1 Lack of ORD Asymmetry

Another key feature evident from the resonance shift values in Figure 4-4B is that there is no significant difference in ORD resonance shift values between LH and RH structures – in other words the chiral asymmetry parameter $\Delta\Delta\lambda \approx 0$ despite the introduction of chiral molecules. Previous work by Kelly *et al.* using DPA arrays has shown that asymmetry from chiral layers is largely dependent on the alignment of the immobilised chiral biomolecules on the DPA surface [25]. This was shown experimentally with either orientated or disordered layers of IgG antibodies, as well as with EM simulations comparing results using either the isotropic or anisotropic chiral tensor χ, as discussed in Section 3.4.1. It was found that good levels of alignment lead to a more anisotropic chiral dielectric layer surrounding the chiral nanostructures, leading to higher levels of asymmetry. Achieving this level of surface structure and alignment is difficult in most functionalisation strategies and this restricts the practicality of generating assays with multiple binders for multiple targets.

Another complexity in achieving correlation in asymmetry for all DPA array locations is that reflected light is being collected by the imaging polarimetry microscope camera from multiple angles. Angled excitation could potentially impact the plasmonic response(s). This was investigated using numerical EM simulations by simulating DPA shuriken metafilms in water with a 10 nm isotropic chiral dielectric layer deposited on top of the shurikens to represent a protein layer. While a 10 nm thick protein layer is unrealistic for most experimental applications, this thickness is required for simulation purposes due to meshing constraints. The chirality tensor χ value was set to be 1×10^{-3}. This value is considerably higher than that of an actual protein layer, which has been shown to be approximately 5×10^{-4} at a wavelength of 700 nm [26, 27]. A higher χ value was chosen for these simulation purposes to better visualise asymmetry changes between ORD spectra. Three different angles were simulated: 0° (incident), 1°, and 2° degrees (Figure 4-7).

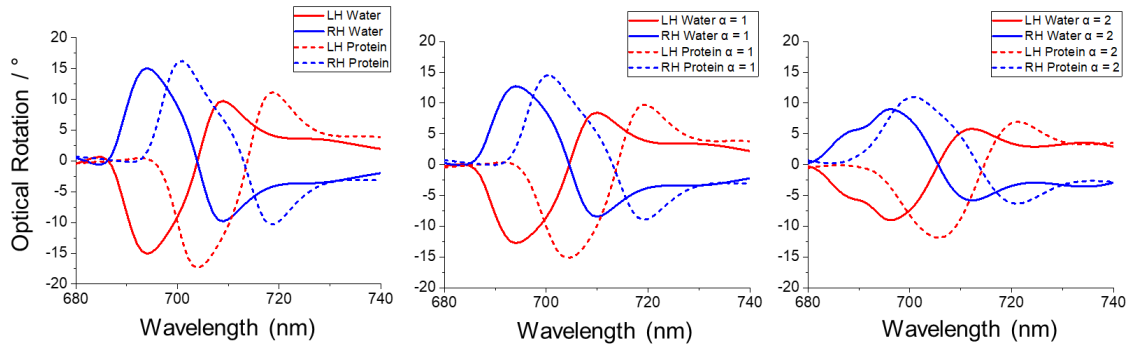

Figure 4-7 Calculated ORD spectra of LH (red) and RH (blue) DPA nanostructures in water (solid lines) and with a 10 nm chiral protein layer (dotted lines) with different angles (α) 0-2° of incident light.

Simulated DPA ORD results show clear differences between light angle changes. Noticeably, ORD amplitudes tend to decrease with increasing angle. This can be attributed to changes in the effective light path length as light travels through different thicknesses of substrate or dielectric, as well as reflection and interference effects which can lead to constructive or destructive interference, changing ORD amplitudes [28]. Another noteworthy feature is the presence of a third weak resonance mode in the 2° simulation around 690 nm. This new mode, or peak, arises from the shuriken film, which is anisotropic, and not from the chiral protein layer which in this case is modelled as an isotropic layer.

The $\Delta\Delta\lambda$ parameters for all ORD spectra in Figure 4-7 were tabulated to observe how asymmetry changes with varying light angles (Table 4-1).

	Angle, α		
	0	**1**	**2**
ΔΔλ Peak 1	3.4	3.7	4.8
ΔΔλ Peak 2	0.0	-0.5	0.3

Table 4-1 Calculated asymmetry parameters $\Delta\Delta\lambda$ (LH-RH) from Figure 4-7 ORD spectra. $\Delta\Delta\lambda$ units in nm.

From the $\Delta\Delta\lambda$ parameters obtained from simulations; it is evident that asymmetry does in fact change with altering light angles. Peak 1 appears to be more sensitive to angle changes, with asymmetry increasing substantially from incident to 2° angled light. Peak 2 shows no visible asymmetry for incident light. At 1°, ORD shows negative asymmetry, whereas at 2° asymmetry

shifts to the positive. These results show the complex nature of concurrently measuring multiple DPA arrays to achieve consistent asymmetry results, as angles of incident and collected light will be slightly different from all A-I regions.

Furthermore, with regards to asymmetry for virus experiments, presented in Section 4.4, different pathogens have different physical properties. One of the major classifications between virus types is the one between enveloped and non-enveloped viruses. Non-enveloped viruses are typically contained in a rigid icosahedral assembly of proteins, and they deliver their viral genome across host cell membranes through a pore created by viral capsid proteins [29]. Some examples of non-enveloped viruses include adeno-, pico-, and noroviruses [30, 31]. Enveloped viruses possess an additional lipid bilayer envelope surrounding the capsid, and they accomplish viral genome transport using a membrane fusion reaction [29]. Examples of enveloped viruses include influenza and SARS-CoV-2 viruses [32, 33]. Enveloped viruses have a more flexible structure and can be physically deformed, resulting in a lack of consistent anisotropy when interacting with DPA gold surfaces. This feature makes the achievement of an anisotropic dielectric layer impractical for rapid diagnostic applications.

In conclusion, although the DPA nanostructures do not consistently exhibit asymmetry between ORD spectra when observed with the imaging polarimetry microscope, there are several reasons why ORD remains a valuable tool in this thesis's biosensing work. Firstly, ORD demonstrates resilience against signal losses and variations caused by absorptive molecules, as the ratio-based Stokes method equally affects all ORD measurement sites, including the background reference measurement sites. Secondly, the well-defined and sharp ORD peaks generated by DPAs facilitate automation and data collection in experiments, allowing for easy monitoring of changes in peak resonance positions. Lastly, ORD exhibits high surface sensitivity, with the EM fields generated by DPA nanostructures decaying significantly within approximately 25 nm above the patterned surface, as shown earlier in Section 3.5.2. This attribute ensures that the surrounding bulk solution has minimal influence on the measured ORD. Consequently, DPAs continue to utilise chiral nanostructures for biosensing experiments, leveraging their distinctive optical properties.

4.3 DPAs for Multiplexed Protein Diagnostics

The imaging polarimetry microscope system discussed in Section 3.3.1 enables the simultaneous measurement of multiple DPA array regions. By applying distinct antigen-binding molecules to individual DPA arrays through chemical functionalization, it becomes possible to detect multiple biological targets within a single measurement. The ability to simultaneously detect multiple antigens is a highly valuable feature in the field of diagnostic tools, known as multiplexing [34, 35]. Multiplexing, as defined by Jarockyte *et al.*, involves the concurrent measurement of multiple analytes in a single experiment and sample, all under the same conditions [36]. In the subsequent sections, the detection and multiplexing capabilities of DPAs are explored, employing various functionalisation strategies.

A multiplexed target diagnostics proof-of-concept with DPAs is performed by demonstrating the detection of two antibody targets to their respective proteins (binders). The first of the two protein binders used was streptavidin. The second protein binder selected was the S1-protein selected to show relevance to diagnostics related for SARS-CoV-2.

In addition to mere protein detection, it is necessary to test protein binding in serum-like media, as samples taken from patients for diagnostic purposes, either from blood or nasopharyngeal swabs, will contain a variety of different proteins and other substances, such as mucin, glycoproteins, cellular debris, antibodies, enzymes, cytokines, and viral or bacterial components [37, 38]. To mimic these conditions, an artificial serum was prepared into which the target proteins were added to.

4.3.1 S1 Protein Antibody Detection

Prior to the use of S1-proteins in a multiplexed DPA experiment alongside streptavidin protein, the detection of anti-S1 antibodies was evaluated. An artificially reconstituted mimic of human mucus serum containing 0.2% mucin, 0.25 mg ml^{-1} haptoglobin, and 0.50 mg ml^{-1} transferrin in PBS was prepared to investigate non-specific interaction effects on S1-protein binding capability. The experimental stages were:

1. Functionalise DPA sample with an NTA/EG-thiol SAM as outlined in Section 3.2.3.
2. Add 1 μM his-tagged S1-protein for 1 hour.
3. Add artificial serum **without** S1-antibody for 15 minutes.

4. Add artificial serum **with** S1-antibody for 1 hour.

ORD measurements were taken at each experimental stage post-rinsing with PBS, and ORD Δλ results presented relative to SAM measurements are presented in Figure 4-8B-C.

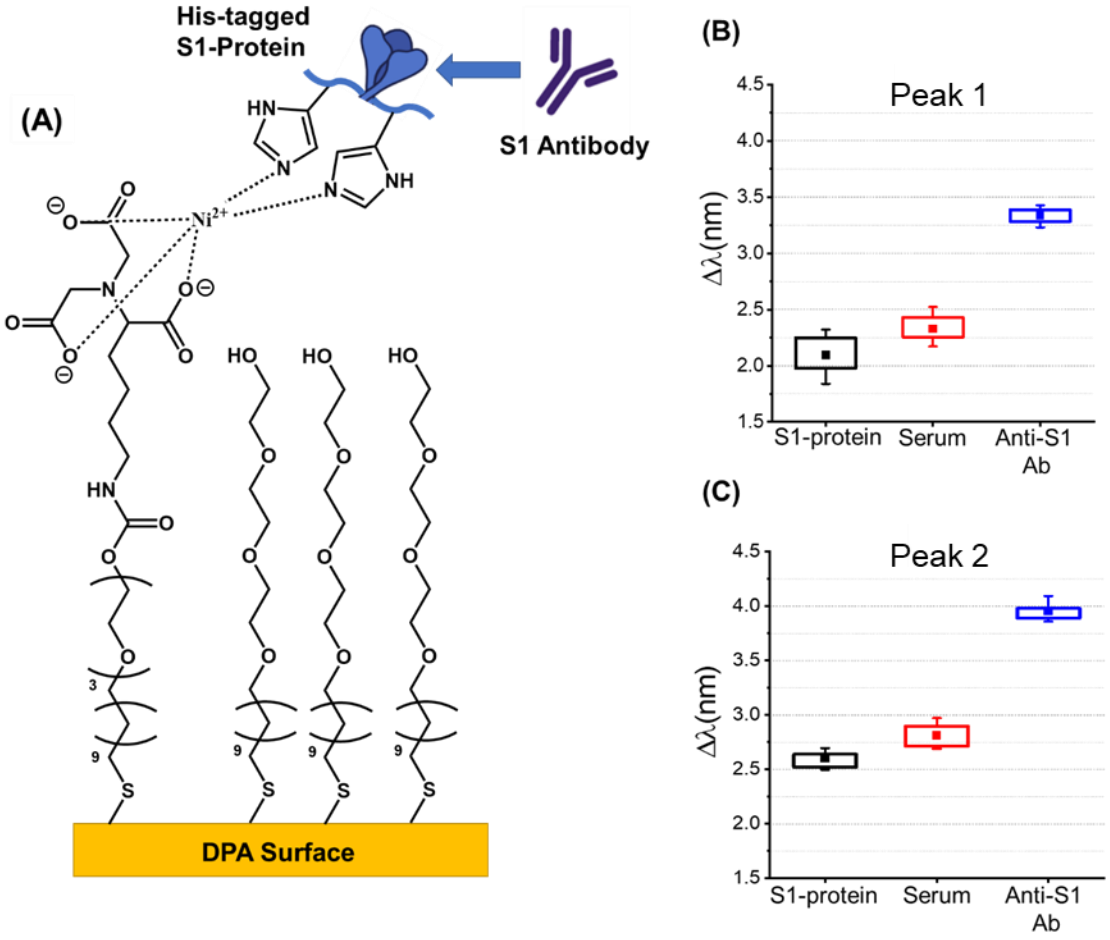

Figure 4-8 (A) Graphical representation of DPA functionalisation with an NTA and spacer SAM, followed by the subsequent additions of his-tagged S1 protein and S1 antibody. (B) Boxplot data for his-tagged S1-Protein binding to pre-functionalised 1:4 NTA/EG-thiol SAM, followed by addition of artificial serum, which was then spiked with 1 μM S1-Antibody. ORD Δλ measurements taken relative to SAM.

Mean $\Delta\lambda$ values of 2.1 and 2.6 nm were obtained for the successful immobilisation of the S1-protein onto the SAM for Peak 1 and Peak 2, respectively. Measurements with the artificial mucus serum without S1-antibody shows small degrees of non-specific binding with $\Delta\lambda$ mean increases of 0.2 nm for both Peak 1 and Peak 2, values which are similar to resonance shift error ($\pm$ 0.3 nm) expected for changes in media (noise) performed in Section 3.5.1. These values are also much smaller than the expected shifts (>2nm) for anti-S1 antibodies that are over 100 kDa in mass. The artificial mucus serum spiked with 1 μM of anti-S1 antibody induced positive shifts of 1.0 and 1.2 nm compared to only serum for Peak 1 and Peak 2, respectively, indicating the binding of anti-S1 antibody to the S1-protein. From the data in Figure 4-8B-C, there is minimal variance across the 9 DPA pair structures, portrayed by the narrow range of the box plots. In particular, the anti-S1 antibody maximum and minimum data lies within a small 0.3 nm range for Peak 2.

4.3.2 Protein Multiplexing

After successful confirmation of the his-tagging immobilisation strategy and testing the specific S1-protein interaction with anti-S1 antibody in artificial mucus, the multiplexing experiment, or multiplexed DPA, was conducted along with his-tagged streptavidin as follows (Figure 4-9A):

1. Functionalise DPA sample with an NTA/EG-thiol SAM as outlined in Section 3.2.3.
2. Drop 500 nL volume of his-tagged streptavidin onto DPA regions A and C and let bind for 1 hour.
3. Drop 500 nL volume of his-tagged S1-protein onto DPA regions G and I and let bind for 1 hour.
4. Rinse DPA sample with deionised water and attach fluid chamber insert.
5. Introduce 1 μM concentrations of binder targets in artificial mucus serum as in Section 4.3.1 to insert chamber sequentially:
    a. Anti-streptavidin antibody for 15 minutes.
    b. Anti-S1-protein antibody for 15 minutes.

ORD measurements were collected post-PBS rinsing for each experimental stage, and all $\Delta\lambda$ values presented are the average of the two array locations for each target relative to the initial PBS buffer measurements. Array locations which were not functionalised (B, D, E, F, and H) were disregarded. Obtained ORD boxplot results are presented in Figure 4-9B and Figure 4-9C for Peak 1 and Peak 2, respectively.

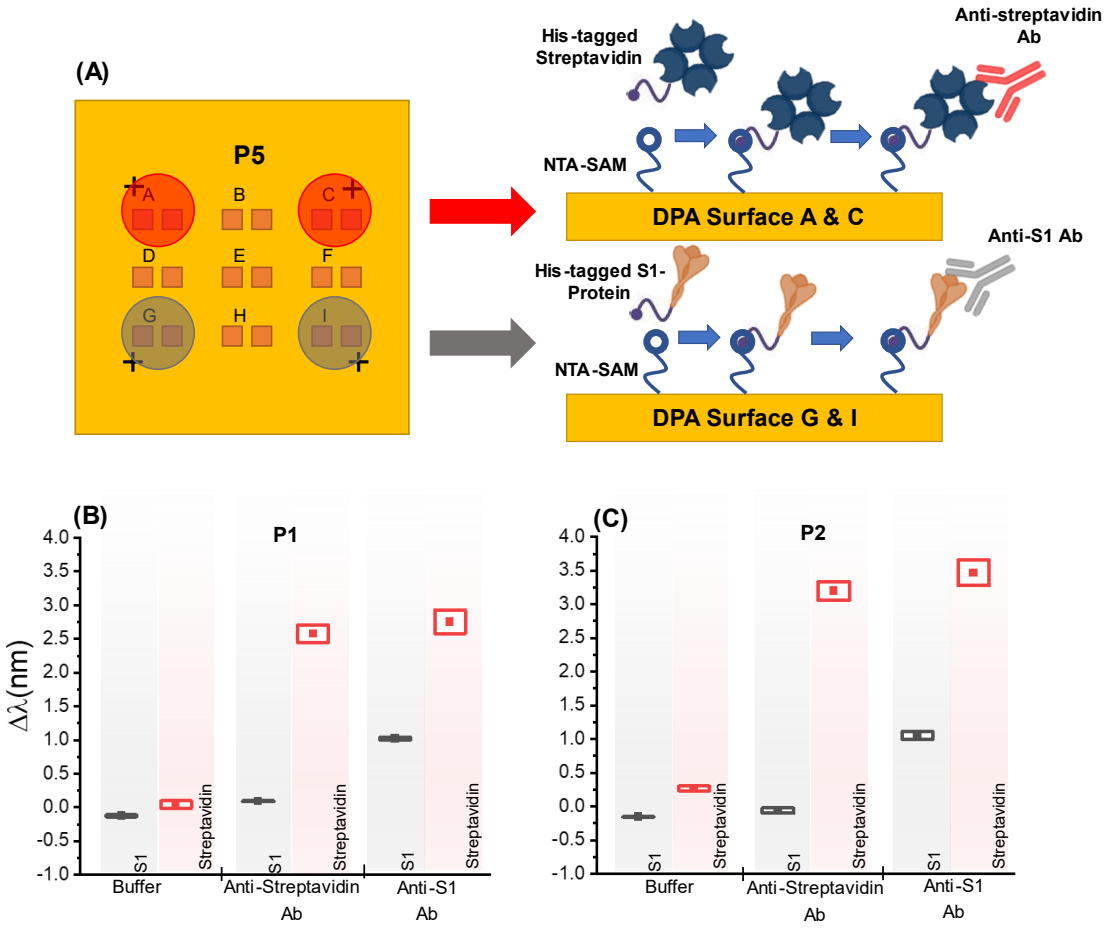

Figure 4-9 (A) Graphical representation of multiplexing experiment stages. Red regions represent NTA/EG-thiol SAM DPA regions functionalised with His-tagged streptavidin binder and anti-streptavidin antibody. Grey regions represent NTA/EG-thiol SAM DPA regions functionalised with His-tagged S1-protein binder and anti-S1 antibody. ORD resonance shift box plots for Peak 1 (B) and Peak 2 (C).

Addition of the anti-streptavidin antibody incurred minimal non-specific binding to the S1 protein, with changes in mean $\Delta\lambda$ of 0.2 and 0.1 nm for Peak 1 and 2 respectively. Conversely, binding of the antibody to streptavidin showed mean $\Delta\lambda$ changes of 2.5 and 2.9 nm, showing a clear specific interaction. Immobilisation of the anti-S1 antibody thereafter bound only to the S1 protein, giving mean $\Delta\lambda$ increases of 0.9 and 1.2 nm while the streptavidin regions showed only minor mean $\Delta\lambda$ increases of only 0.2 and 0.3 nm due to non-specific interactions. These results validate the specific detection capabilities of this DPA multiplexing setup, with the potential to detect various biomolecules within one experimental setup using binders coated onto specific regions without the need of kinetic measurements or flow systems required in SPR.

It should be noted that the $\Delta\lambda$ exhibited for the anti-S1 antibody are significantly smaller in comparison to those obtained for the anti-streptavidin antibody, although both have a similar molecular weight of around 150 kDa [39]. This difference is likely due to the variation of antibody coverage or alignment on the DPA surface between anti-streptavidin and anti-S1. Lower surface coverage would providing fewer epitopes for the antibodies to bind to, and poorer alignment would reduce binding likelihood. These differences are likely to be further compounded by variations in the antibody affinities to their targets.

4.4 DPAs for Multiplexed Virus Diagnostics

After successfully detecting the Covid S1 protein, the subsequent objective was to examine the possibility of detecting complete SARS-CoV-2 virus particles. Given that a SARS-CoV-2 virion is considerably larger and more intricate than an individual protein, direct detection of the virions would eliminate the necessity for sample lysis, thereby reducing processing steps and reagent requirements. To achieve this, DPA samples were functionalised with anti-SARS-CoV-2 Spike Glycoprotein S1 antibody $F(ab')_2$ fragments, following the functionalization protocol outlined in Section 3.2.5.

4.4.1 Detection of Inactivated SARS-CoV-2 Virions

SARS-CoV-2 virus solution was first inactivated to facilitate safe handling, as described in Section 3.2.4. This solution was then added to the $F(ab')_2$ fragment functionalised DPA sample for a duration of 1 hour. ORD measurements with the viral solution on the DPA were taken (concentrated) in addition to a measurement after PBS rinsing. These ORD $\Delta\lambda$ boxplot results are presented in Figure 4-10 and Table 4-2.

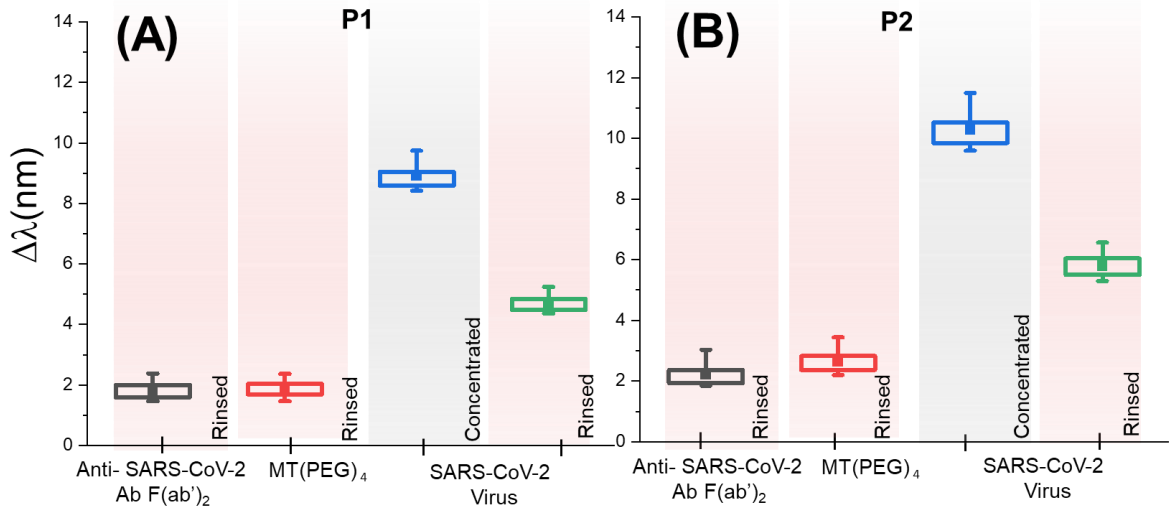

Figure 4-10 ORD box-plot results for inactivated SARS-CoV-2 virion detection for (A) Peak 1 (P1) and (B) Peak 2 (P2). The Δλ results are presented relative to initial PBS measurements.

Units in nm	Anti-SARS-CoV-2 F(ab')2		MT(PEG)$_4$ Spacer		Virus Concentrated		SARS-CoV-2 Virus Rinsed	
	P1	P2	P1	P2	P1	P2	P1	P2
Mean Δλ	1.81	2.21	1.86	2.64	8.92	10.29	4.54	6.45
St. Dev. Δλ	0.31	0.41	0.31	0.43	0.51	0.71	2.38	3.54
Range Δλ	1.00	1.25	1.02	1.41	1.81	3.54	1.41	1.96

Table 4-2 Mean resonance shift (Δλ) values for each experimental stage of SARS-CoV-2 virion detection relative to initial buffer measurements for Peak 1 (P1) and Peak 2 (P2).

Addition of the diluted SARS-CoV-2 solution to the F(ab')$_2$ fragment functionalised DPA yielded a mean $\Delta\lambda$ increase of 7.7 nm when taking a measurement with the virus solution (concentrated) after 1 hour. Rinsing the DPA insert with PBS buffer caused a reduction in resonance peak position by a mean of 3.8 nm. This reduction is indicative of the removal of non-specifically bound virus particles weakly adsorbed to the DPA surface, implying that the final resonance shifts represent specifically bound virus material. For visualisation, the DPA sample used in this experiment was dried, and sputter coated with 9 nm of platinum metal for SEM imaging purposes. The SEM images taken (Figure 4-11) show small spherical particles (~50-100 nm in diameter) on the shuriken structures, indicative of viral particles, further reinforcing the observed resonance shifts obtained post rinsing. Measuring the diameter of multiple virus particles (highlighted in cyan) provides a mean diameter of 70 nm, which is in accordance with other literature measurements [40, 41].

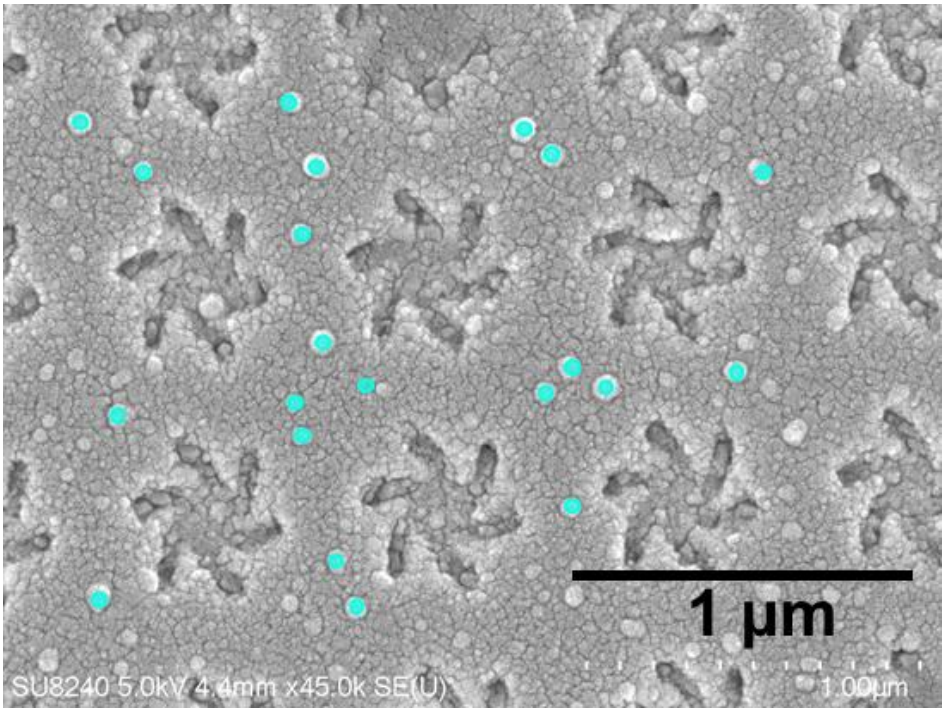

Figure 4-11 SEM image of DPA sample with SARS-CoV-2 virion coverage. Prominent virions are highlighted in false cyan colour.

4.4.2 Virus Multiplexing – Zika and Norovirus

In addition to detection of SARS-CoV-2, other viruses have been trialled – namely Zika and norovirus. Zika virus is an arthropod-borne virus which is usually transmitted through mosquitos, with the most common symptoms being fever, muscle pains, headaches, joint pain, and red eyes [42]. Norovirus is a highly contagious enteric virus spread through stool or vomit, with the most common symptoms being nausea, diarrhoea, and vomiting [43]. While these viruses would not be tested for using nasal swab samples, as is the case with COVID-19, and how the DPA substrates are currently envisioned to be analysed, the work presented here is a proof-of-concept that different viruses can be detected in a specific manner. Additionally, the antibodies for these viruses are readily available for purchase, along with their Virus-Like-Protein (VLP) counterparts.

VLPs are supramolecular protein structures which mimic the viral envelope structure while possessing no viral RNA, making them non-hazardous to work with and a good antigen analogue for testing with antibodies bound to the DPA surface [44]. In this section, the multiplexing

results of a DPA sample treated with Zika and norovirus antibodies, followed by live Zika virus provided by the CVR, and norovirus VLPs is presented.

Following the Protein A/G functionalisation strategy outlined in Section 3.2.6, a DPA sample was then divided into two separate regions using a 2-well fluidic insert, and the regions were functionalised with different monoclonal virus antibodies – namely anti-norovirus and anti-Zika virus antibodies (Figure 4-12B). The 2-well fluidic insert was then removed and replaced with a singular fluidic chamber, which was then filled with live Zika virus (4.8×10^{-5} pfu ml^{-1}). This solution was left to incubate on the DPA sample for 1 hour. Following PBS rinsing, optical measurements were taken. The fluidic chamber was then filled with Norovirus VLPs of approximate 7.7 nM concentration, which was calculated from manufacturer provided information on number of VLP surface antigens, and the solution was left to incubate for 1 hour. Following PBS rinsing, optical measurements were taken. The relative ORD $\Delta\lambda$ are shown in Figure 4-13.

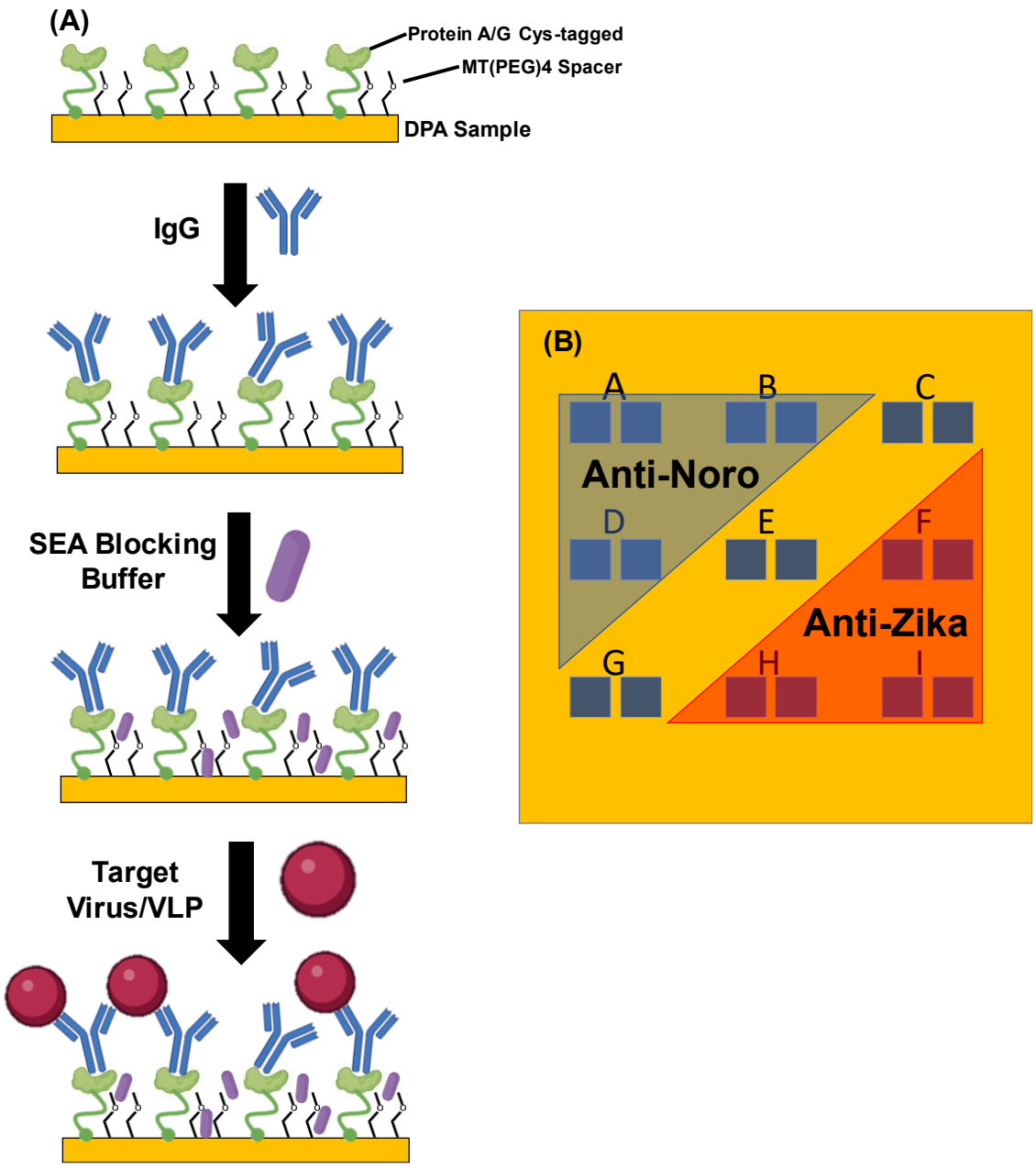

Figure 4-12 (A) Schematic diagram of DPA functionalisation strategy with Protein A/G, IgG, SEA blocking buffer, and target virus or VLP. (B) Diagram of DPA sample with highlighted regions indicating anti-norovirus (blue) and anti-Zika virus (red) functionalised areas on the DPA sample. C, E, and G regions possessed no antibodies.

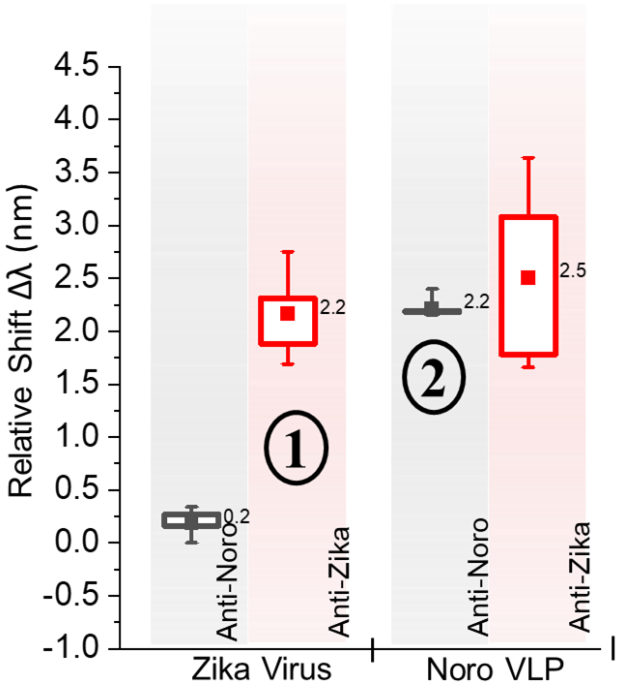

Figure 4-13 Relative ORD Δλ of virus multiplexing experiment. Grey columns show relative Δλ from anti-norovirus sites, and red columns show relative shifts from anti-Zika virus sites. Numbers 1 and 2 represent addition of respective virus targets.

ORD resonance shift results show specific 2.2 nm Δλ mean increases from the respective DPA functionalised regions, where the grey columns represent results from the anti-norovirus regions, and the red columns represent results from the anti-Zika virus regions. Both antibody sites experience minor non-specific binding interactions, with anti-norovirus showing a 0.2 nm mean relative shift upon Zika virus addition, and anti-Zika virus regions showing a 0.3 nm mean relative shift upon norovirus VLP addition. However, these values are much lower compared to mean shifts induced from antibody relative targets.

The overall Δλ means are significantly lower than those obtained from the SARS-CoV-2 virions in Section 4.4.1. The virion and VLP surface coverage was investigated using SEM imaging, which shows less virus coverage in comparison (Figure 4-14). These findings suggest that further optimisation is required for multiplexed DPA virus detection with Zika and norovirus antigens using the Protein A/G functionalisation technique.

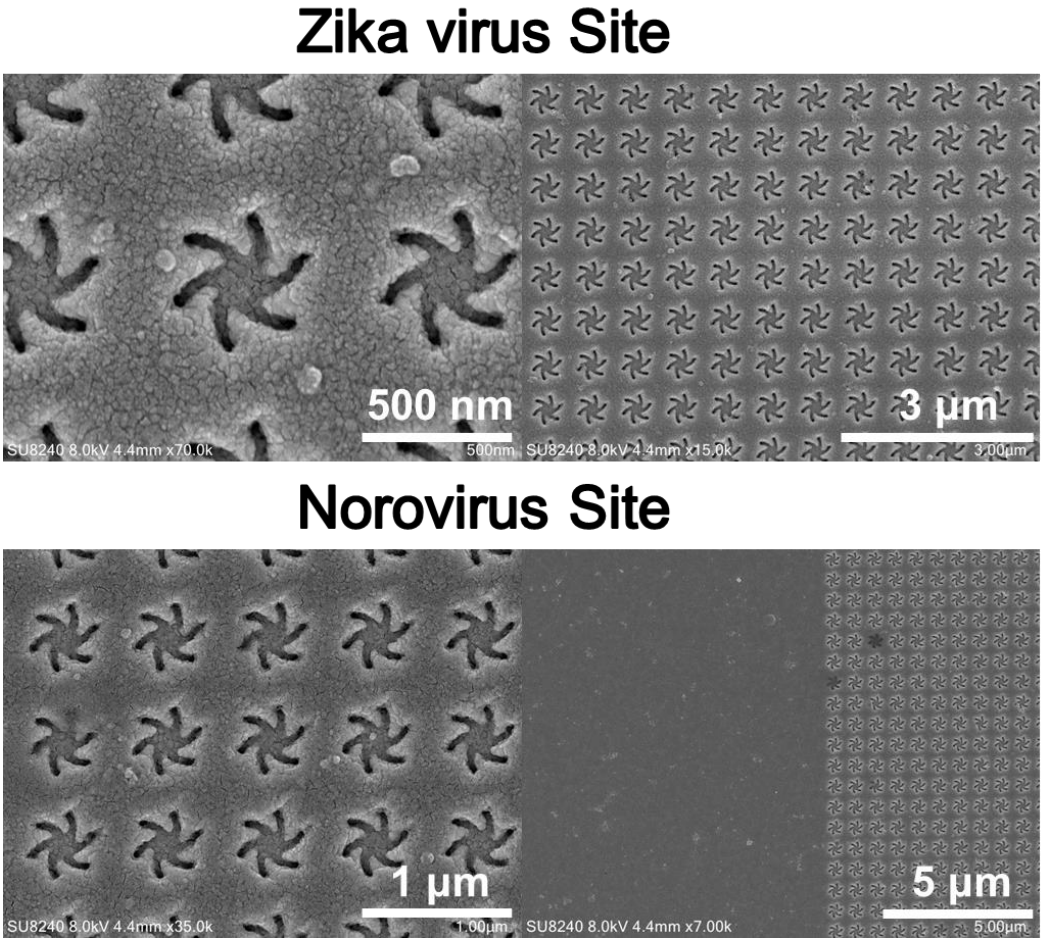

Figure 4-14 SEM images of final multiplexed virus DPA locations showing Zika virus particles and Noro VLPs.

4.4.3 Zika Virus Limit of Detection Using DPAs

An important biosensor parameter is the Limit of Detection (LoD), as it determines sensor sensitivity. The LoD quantifies the lowest analyte target concentration which the sensor can reliably detect and differentiate from noise levels [45]. Lower LoD values are desired as they possess greater sensitivity and a greater diagnostic range, allowing for earlier disease detection and monitoring of disease progression. To estimate the Lod of DPAs with live Zika virus, a concentration curve experiment was performed.

9 DPA samples were prepared following the Protein A/G functionalisation protocol outlined in Section 3.2.6. All samples were rinsed with PBS, and anti-Zika virus antibody at 1 µM prepared in PBS was added to all 9 DPA samples for 2 hours. Following SEA blocking buffer application and PBS rinsing, baseline ORD measurements were performed. 9 Zika virus solutions of various

concentrations ranging from 0.005×10^5 to 6.00×10^5 pfu ml^{-1} were added to the samples for 1 hour to investigate virus concentration dependency on ORD resonance shift values. The samples were rinsed with PBS and ORD measurements for each sample performed (Figure 4-15 and Table 4-3).

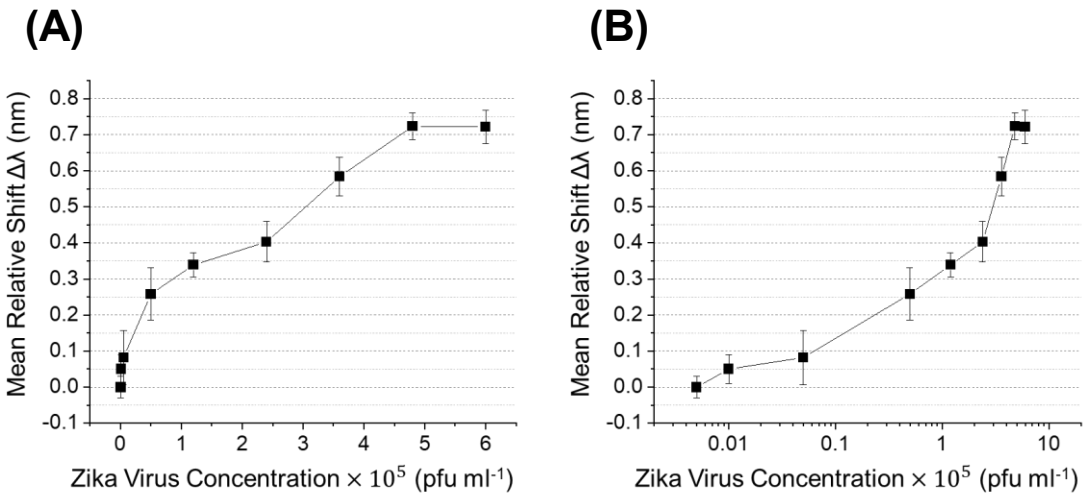

Figure 4-15 Mean Peak 2 Δλ values for Zika virus LoD experiments using varying concentrations of virus. Error bars represent standard error. (A) Graph with linear x-axis and (B) with logarithmic x-axis.

	Zika Virus LoD Experiment								
Concentration (pfu ml^{-1} ×10^5)	**0.005**	**0.01**	**0.05**	**0.5**	**1.2**	**2.4**	**3.6**	**4.8**	**6.0**
Mean Δλ	0.00	0.05	0.08	0.26	0.34	0.40	0.58	0.72	0.72
Standard Error	0.03	0.04	0.08	0.07	0.03	0.06	0.05	0.04	0.05

Table 4-3 Mean Δλ and standard error values from Zika virus LoD experiment.

Standard error is calculated using the equation:

$$\frac{\sigma}{\sqrt{n}} \tag{4.4.1}$$

Where σ is the standard deviation, and *n* is the number of measurements. The measurements for each data set are from the 18 individual nanostructure arrays on the P5 DPA region taken from a single experiment for each concentration.

The lower concentration of 0.005×10^5 Zika virus pfu ml^{-1} did not induce any observable resonance shifts. However, for all higher concentrations, positive $\Delta\lambda$ values were obtained,

which increased nearly linearly until reaching a saturation point at the concentration of 4.8×10^5 pfu ml^{-1}.

Considering the relatively linear response of the DPA Zika virus biosensor at low virus concentrations, the LoD can be calculated as [46, 47]:

$$LoD = \frac{\Delta\lambda_{blank} + 3\sigma_{blank}}{Slope_{linear}} \tag{4.4.2}$$

Where $\Delta\lambda_{blank}$ and σ_{blank} are the mean and standard deviation values of the blank measurement, respectively, and $Slope_{linear}$ is the slope of the line of best fit fitted to the initial data points. Using the blank water measurement values acquired earlier in Section 3.5.1, and evaluating the slope with the first four data points in Figure 4-15A to be 4.9×10^{-6} nm per pfu ml^{-1}, the LoD can be calculated:

$$LoD = \frac{-0.03 + 3(0.06)}{4.9 \times 10^{-6}}$$

$$= 3.1 \times 10^4\ pfu\ ml^{-1} \tag{4.4.2}$$

While studies have reported LoD values lower than the value obtained here in Equation 4.4.2, such as 1.6×10^1 pfu ml^{-1} for SARS-CoV-2 using field-effect graphene based transistors (FET) [48], 24.3 pfu ml^{-1} for Influenza A (H3N2) using colorimetric methods with gold nanoparticles [49], and 113 pfu ml^{-1} for H1N1 using paper-based electrical measurements [50], this result of 3.1×10^4 pfu ml^{-1} obtained here remains comparable to most optical biosensors and LFDs [51, 52]. Moreover, direct comparisons can be challenging due to the various ways of defining LoD. It is also important to mention that LoD is influenced by the performance of the surface-bound antibodies and is subject to variation with different antibodies and target analytes based on surface optimisation.

Considering that the viremia (number of virus particles in blood) of a symptomatic Zika virus-infected patient ranges from 10^3 to 10^6 pfu ml^{-1} [53], it is anticipated that this DPA sensor would primarily detect Zika virus positive patients with higher viral loads. However, when measuring from blood or plasma samples of infected individuals, additional challenges may arise due to non-specific binding effects, potentially influencing the LoD value.

4.5 DPAs for Haptoglobin Detection for Mastitis Diagnostics

The field of veterinary medicine is another area that can benefit from rapid disease diagnosis. Mastitis is a prevalent bacterial disease amongst dairy cattle that causes inflammation of mammary tissue, leading to losses in milk yield and reduced quality. Examples of bacteria that can cause mastitis are *Staphylococcus aureus*, *Streptococcus agalactiae*, and *Corynebacterium bovis* [54] [55]. It is estimated that mastitis costs the dairy industry to be 140£ per cow a year in Scotland in 1996 [56]. Another more recent study in the US evaluated the cost of an average clinical mastitis case to be 435$ [54].

Mastitis infection releases inflammatory cytokines in the affected tissue, which in turn stimulates the increase in the production of Acute Phase Proteins (APPs), one of which is haptoglobin (Hp). Hp is primarily produced in the liver but can also be produced in other tissues such as mammary tissue [57]. Hp has the key role of binding to extracorpuscular haemoglobin (Hb) released during haemolysis. This is important as Hb outside of their native red-blood cell environment is toxic due to the oxidative properties of the haeme iron group [58]. During infection, as a response to inflammatory cytokines, Hp levels increase in blood serum as well as milk as the APP can pass through mammary tissue [59]. In healthy cattle, Hp levels were found to be supra-normal at the 57 mg L^{-1} (663 nM) and 4.3 mg L^{-1} (50 nM) cut-off points for serum and milk, respectively [60]. Post-infection, the highest Hp levels have been reported to range from 960-2190 (11-25 μM) and 52-323 mg L^{-1} (0.6-4.0 μM) for serum and milk, respectively [60]; which is over a ten-fold increase from normal levels in both cases.

Reliable and fast analysis methods of bulk milk Hp levels are desired by the dairy industry to help manage and control the spread of bovine infection. Current methods for identifying mastitis largely rely on the bacteriological culture analysis of milk samples [61]. However, this method is infeasible for large herds as throughput is low and financial costs are high. Culture analysis also does not provide information about the degree of inflammation in infected cattle. PCR tests are another method of mastitis detection. While highly sensitive, it is relatively expensive compared to other tests [62]. California Mastitis Tests (CMTs), which measure the degree of precipitation and gel formation when infected milk is mixed with normal healthy milk to confirm high Somatic Cell Count (SCC) [63], is simple to perform but does not provide quantitative results [59]. The counting of somatic cells, which are mainly milk-secreting epithelial cells which shed

from tissue lining and white-blood cells [64], is another technique that can indicate the presence of mastitis. While more sensitive than CMT, SCC can increase from other conditions such as apocrine secretion and lead to false positive results [65]. Considering these limitations, developing a rapid and sensitive biosensor that is relatively inexpensive would be beneficial for dairy and veterinary industry.

Hp is a suitable biomarker target due to its level increase post-infection as well as high affinity to Hb, with studies reporting remarkably low dissociation constants ranging from 10^{-12} and 10^{-15} M [66] [67]. The Hp protein is comprised of a Complement Control Protein (CCP) domain and a Serine Protease (SP) domain. The serine protease domain is an assembly which is typically found in serine proteases. However, Hp does not belong to the serine protease family as it has an incomplete 'catalytic triad' of amino acids responsible for the catalysis of amide bond lysis [68].

With regards to binding mechanism, once Hb is released into the plasma it dissociates from its tetrameric form into two αβ-dimers, after which it is captured by Hp to form the Hb-Hp complex (Figure 4-16) [68].

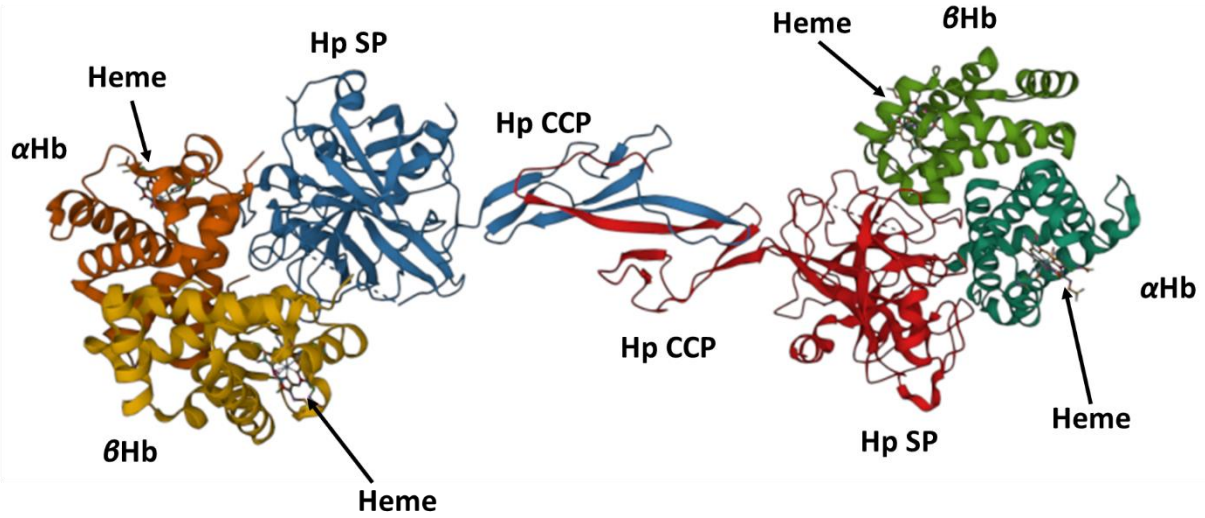

Figure 4-16 Structure of the haemoglobin (Hb)-haptoglobin (Hp) complex. Hp dimer is coloured blue and red. Left-side Hb is coloured orange (αHb) and yellow (βHb). Right-side Hb is coloured turquoise (αHb) and green (βHb). Protein structure from Andersen et al [68].

Hp molecules themselves have been found to dimerise through a β-strand swap prior to Hb binding. The SP domains of Hp are responsible for the strong binding of αHb and βHb sub-units.

The overall shape of the Hb-Hp complex can be described as a barbell with two-fold rotational symmetry.

4.5.1 DPAs for Haptoglobin Detection

To successfully detect Hp in a solution, DPA samples must first be functionalised with Hb as well as a suitable SAM to prevent any non-specific interactions. To accomplish this, a mixed SAM of $MT(PEG)_4$ spacer units and $CT(PEG)_{12}$ thiols were utilised. The terminal carboxylic acid functional group on the $CT(PEG)_{12}$ allows for the conjugation of proteins containing free lysine amino acid residues (containing a primary amine $-NH_2$ group) using EDC/NHS chemistry [69]. The step-by-step experimental stages are outlined below:

1. 5 DPA P5 samples were prepared following the EDC/NHS functionalisation protocol detailed in Section 3.2.7.
    a. ORD baseline measurements taken after $MT(PEG)_4$ and $CT(PEG)_{12}$ mixed SAM preparation and prior to EDC/NHS addition.
2. 1 µM Hb (Sigma-Aldrich) in PBS was added to each sample for 1 hour to complete the conjugation reaction and create a haemoglobin functionalised surface.
3. DPA samples were rinsed with PBS, and ORD measurements taken.
4. Different Hp concentrations of 0.05, 0.5, 1, 5, and 10 µM in PBS were added to the Hb functionalised DPA samples for 1 hour.
5. DPA samples were rinsed with PBS, and ORD measurements taken.

The ORD spectra for each experimental stage from a DPA P5 EL and ER region treated with 10 µM Hp is displayed in Figure 4-17, and the resonance peak wavelength values are presented in Table 4-4.

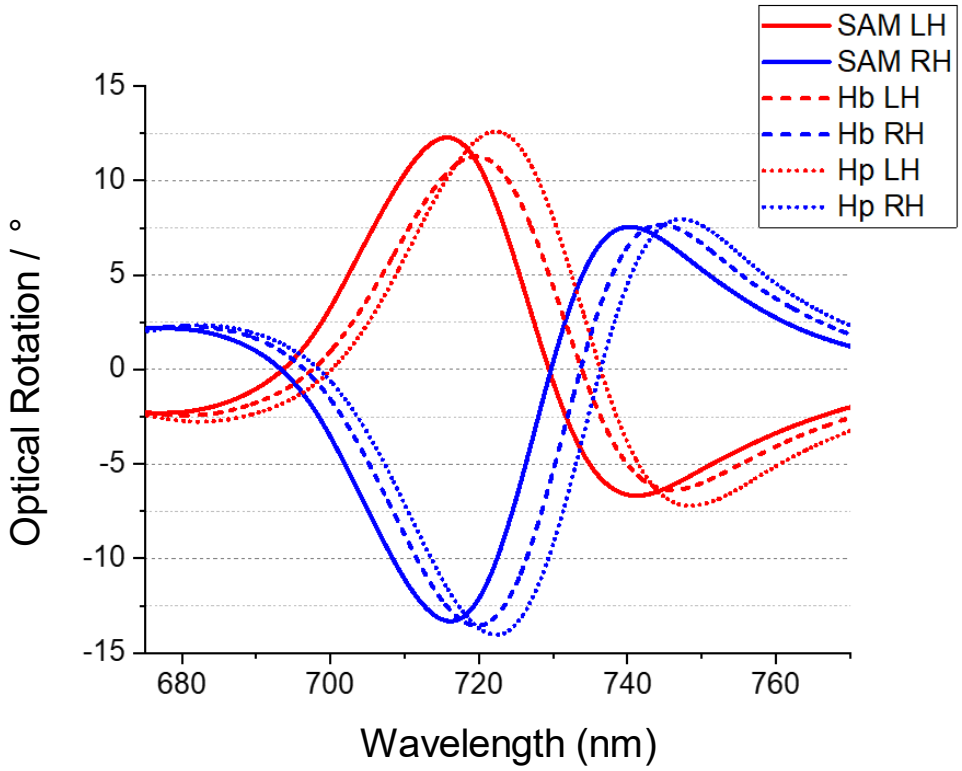

Figure 4-17 ORD data for CT(PEG)$_{12}$ and MT(PEG)$_4$ SAM (solid line), followed by Hb functionalised onto SAM using EDC/NHS protocol (dashed line). 10 µM Hp was then added to the surface (dotted line). All measurements taken post-rinsing.

	Peak 1		Peak 2	
	LH	RH	LH	RH
SAM	715.9	716.1	740.8	740.2
Hb	719.7	719.6	745.3	744.4
Hp	722.4	722.3	747.8	747.3

	Peak 1		Peak 2	
	LH	RH	LH	RH
Δλ Hb	3.8	3.5	4.5	4.2
Δλ Hp	6.5	6.2	7.0	7.1

	Peak 1 (LH-RH)	Peak 2 (LH-RH)
ΔΔλ Hb	0.3	0.3
ΔΔλ Hp	0.3	-0.1

Table 4-4 ORD minima/maxima peak resonance positions for Hb/Hp experiment from DPA sample (regions EL and ER) treated with 10 µM Hp.

The EDC/NHS functionalisation strategy shows good results with Hb binding to the DPA surface, inducing a mean change in resonance $\Delta\lambda$ of 3.8, 3.5 (Peak 1), 4.5, and 4.2 nm (Peak 2)

compared to initial SAM values for LH and RH structures, respectively. Hp, being of a protein of comparable size to that of Hb (64.5 *versus* 86.0 kDa), induced further 2.7, 2.7 (Peak 1), 2.5, and 2.9 nm (Peak 2) $\Delta\lambda$ relative to haemoglobin. These values being lower than those achieved from Hp binding could be explained by fewer Hp molecules binding to the surface; likely due to some non-specifically adsorbed Hb molecules which experience distortions in their protein shape, reducing affinity to Hp [70]. Additionally, as electric field strength decreases exponentially as the distance from the DPA increases, it follows that $\Delta\lambda$ values diminish as Hp molecules will be further from the DPA surface compared to Hb.

Figure 4-18 and Table 4-5 shows the ORD mean $\Delta\lambda$ data from Hb functionalised DPA samples treated with varying concentrations of Hp. From these graphs it is evident that there is some concentration dependence on the resonance shift values based on the Hp concentration. For the 0.05 μM Hp trial, mean resonance shift values were 0.0 and 0.4 nm for Peak 1 and Peak 2 respectively, with a data range of -0.3 – 0.5 nm and -0.1 – 0.8. Such low $\Delta\lambda$ values indicate that a 0.05 μM (4.3 mg L^{-1}) Hp concentration is close to the LoD value using this methodology, although more repeats are required to fully confirm this. At higher Hp concentrations, $\Delta\lambda$ values increase expectedly, with the highest $\Delta\lambda$ values of 2.6 and 2.8 nm for Peak 1 and Peak 2 obtained from the DPA sample treated with 5 μM Hp. Doubling the Hp concentration to 10 μM yielded no further increase in resonance position, with $\Delta\lambda$ values even being slightly lower than the 5 μM haptoglobin experiment. These findings indicate that the DPA surface reaches saturation at around 5 μM Hp concentrations. This is of course highly dependent on not only on the sensor but also the functionalisation strategy.

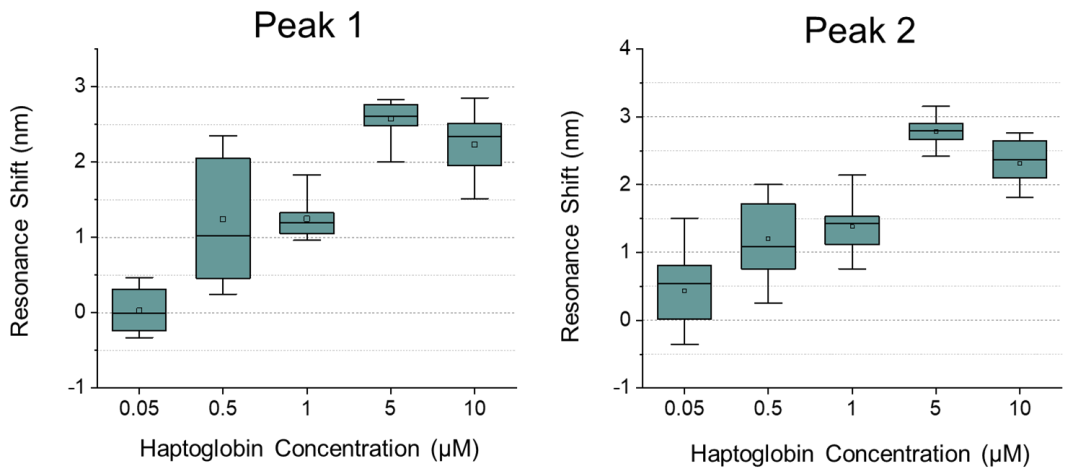

Figure 4-18 Boxplots showing Peak 1 and Peak 2 ORD Δλ data from Hb functionalised DPA samples treated with varying concentrations of Hp.

Hp Concentration (μM)	0.05		0.5		1		5		10	
	Peak 1	Peak 2	Peak 1	Peak 2	Peak 1	Peak 2	Peak 1	Peak 2	Peak 1	Peak 2
Mean Δλ	0.0	0.4	1.3	1.1	1.3	1.5	2.6	2.8	2.2	2.3
Min Δλ	-0.3	-0.1	0.7	0.6	1.0	0.8	2.1	2.4	1.5	1.8
Max Δλ	0.5	0.8	1.9	1.8	1.6	2.2	2.8	3.2	2.9	2.8

Table 4-5 Mean, min, and max Δλ values for all Hp concentration experiments. Units in nm.

Data spreads in the Hb-Hp experiments are quite large, especially for the experiment conducted using 0.5 μM Hp concentration. This can be due to inconsistencies between samples and differences in protein surface coverage, which is one of the main challenges in biosensor development [71]. However, as the post-infection Hp levels range of 52-323 mg L^{-1} (0.6-4 μM) for cow milk samples falls into the DPA dynamic range of detection [60], the variance of the Δλ values may not be an issue as long as positive and negative Hp samples, and therefore mastitis, can be differentiated.

More Hp concentrations are required to construct a complete calibration curve for the Hb-Hp system. However, using the obtained results, approximate lines of best fit can be added to estimate DPA Hp sensitivity (Figure 4-19 and Figure 4-20). The sensitivity can be calculated from the slope of the function, which is fitted for the lower concentration range (0-2 μM). This range is often referred to as the *dynamic range*, at which the sensitivity of the sensor can be assumed to be quasi-constant and measuring under optimal conditions [72, 73]. Considering that

resonance shift values are lower on average for 10 μM Hp concentrations than for 5 μM Hp, it can be assumed that sensor saturation occurs around the 5 μM or 0.4 mg ml^{-1} Hp mark.

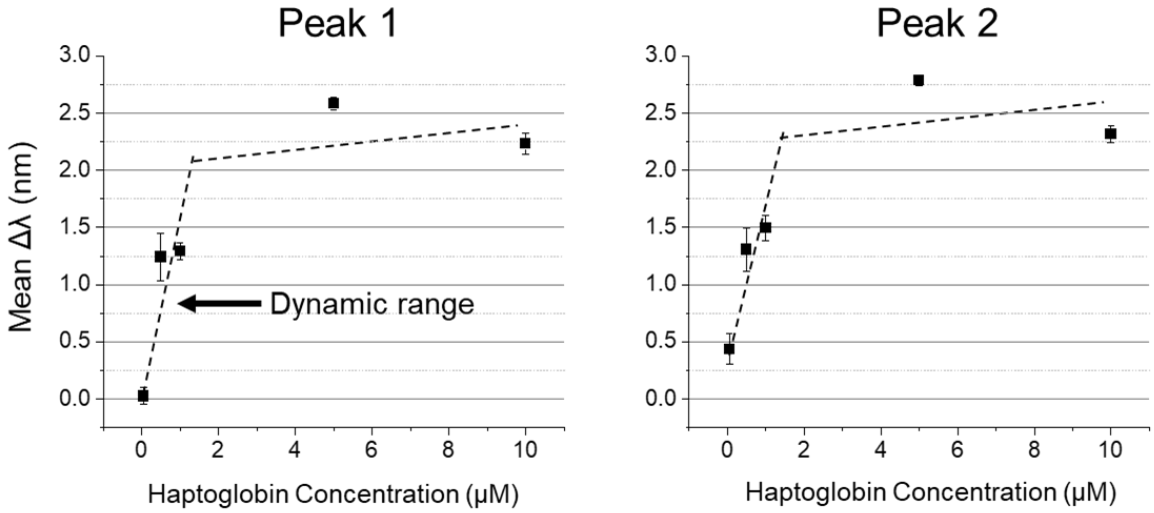

Figure 4-19 Mean resonance shift Δλ values for Peak 1 (P1) and Peak 2 (P2) from haemoglobin functionalised DPA samples treated with varying concentrations of haptoglobin. Dotted lines show approximate line of best fit, with the lower concentration range representing the dynamic range before sensor saturation. Error bars represent standard error.

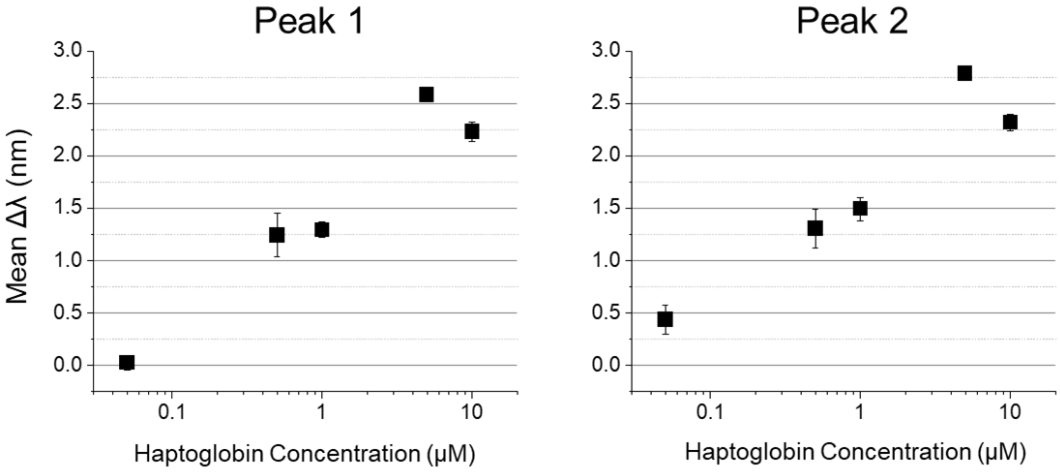

Figure 4-20 Log graph of Figure 4-19.

From the estimated dynamic range functions of Figure 4-20, the sensitivity of the DPA Hb-Hp system is 1.6 nm μM^{-1} (14.5 nm mg^{-1} ml^{-1}) and 1.5 nm μM^{-1} (13.6 nm mg^{-1} ml^{-1}) for Peak 1 and Peak 2, respectively. Another plasmonics based label-free biosensor developed by Calvo-Lozano *et al*. detected SARS-CoV-2 antibodies using a SPR sensor chips functionalised with either Receptor-Binding Domain (RBD) or Nucleocapsid (N) viral proteins, reported sensitivities of 261 and 50 nm ml^{-1} mg^{-1} for RBD- and N- samples respectively [74]. While these sensitivities

are markedly higher than what was achieved with the DPA haptoglobin sensor, they are of the same order, and the added benefit is that the DPA experimental set-up does not require a microfluidic system as is the case with SPR machines.

To improve the sensitivity of Hp detection using DPAs, future work could investigate the DPAs as a competitive biosensor, as performed by Åkerstedt *et al* [75]. A competitive sensor in this case would functionalise the DPA surface with Hp instead of Hb, and then mixing the sample to be tested with Hb. A mastitis negative sample would experience a change in surface mass as the Hb mixed into the sample binds to the surface, which would be observed by resonance shifts. A mastitis positive sample would not show any changes in resonance, as the mixed Hb would bind to Hp and be unable to bind to the sensor surface (Figure 4-21). The proposed benefit of this method is that as a larger molecule, Hp (86 kDa) has better exposure on the sensor surface compared to Hb (64.5 kDa).

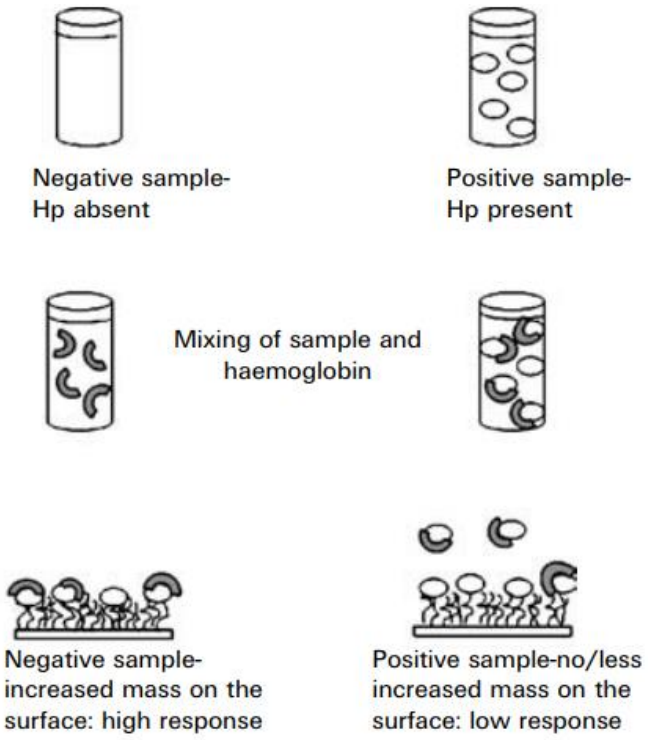

Figure 4-21 Schematic illustration of competitive biosensor assay. Figure from Åkerstedt et al [75].

4.6 Conclusion

Chapter 4 demonstrates the potential of DPAs as a mass manufacturable route to cheaper and reliable label-free biosensors for diagnostic applications. In the previous chapter, DPA samples were shown to possess attributes and refractive index sensitivities found in both LSPR and SPR sensors, with measured values of 466 and 468 nm/RIU for Peak 1 and Peak 2, respectively. The biosensing results prove the validity and accuracy of multiplexed plasmonic biosensing using DPAs.

DPA samples in conjunction with the imaging polarimetry microscope set-up were used to successfully detect protein-ligand (biotin-streptavidin) and protein-protein (antibody-antigen and Hb-Hp) interactions with high sensitivity at the gold nanostructured surface. While chiral asymmetry parameters $\Delta\Delta\lambda$ values proved to average around zero for all experiments, the work shown here suggests that DPA platforms are still useful for biosensing purposes owing to their unique resonance mechanisms and refractive index sensitivities.

In Section 4.3 DPA samples were functionalised with multiple functionalities for S1- and streptavidin-antibody subsequent target detection in the presence of several other proteins, demonstrating for the first time the multiplexing potential of DPAs in complex serum-substitute conditions. As a proof of concept, these results prove that separate DPA regions can be individually functionalised with almost any protein using his-tagging methodology.

In addition to proteins and antibody detection, the direct detection of SARS-CoV-2 virions using $F(ab')_2$ antibody fragments, and without virus lysing or any additional labelling steps was demonstrated in Section 4.4.1. These results broadened the scope of DPA applications from proteins to much larger virus particles. As antibody fragmentation requires several experimental steps and extensive centrifugation, further experiments utilised the Protein A/G fusion protein to bind whole antibodies to detect live Zika virus and Noro VLPs. While virus $\Delta\lambda$ values were significantly lower using Protein A/G based SAMs, specific detection of these viruses was still possible on a single DPA sample.

The final section of this chapter demonstrated how DPA samples can be functionalised using simple EDC/NHS conjugation chemistry with Hb protein to detect Hp levels in solution. Increasing Hp concentrations yielded higher resonant shift responses, allowing for the

construction of a concentration curve and the estimation of sensitivity. The lower limit of Hp detection was found to be around 0.05 μM, which only gave a mean positive resonant shift values for Peak 2 of 0.4 nm, and resonant shift values were highest at 5 μM Hp concentrations, after which $\Delta\lambda$ values did not increase, suggesting DPA surface saturation. Considering that the dynamic range of Hp concentration is reported to be 0.6-4.0 μM, these results indicate that the Hb functionalised DPA sample could successfully detect mastitis. However, further experimentation is required with complex solutions and surface chemistry optimisation strategies. Using the EDC/NHS conjugation system, it is possible to bind any protein onto the DPA surface, allowing for the development of other APP biosensing systems.

4.7 References

1. Gupta, N., et al., *Point-of-care PCR assays for COVID-19 detection.* Biosensors, 2021. **11**(5): p. 141.
2. Mahmood, Z., et al., *Investigating virological, immunological, and pathological avenues to identify potential targets for developing covid-19 treatment and prevention strategies.* Vaccines, 2020. **8**(3): p. 443.
3. Hendry, E., et al., *Ultrasensitive detection and characterization of biomolecules using superchiral fields.* Nature nanotechnology, 2010. **5**(11): p. 783-787.
4. Tullius, R., et al., *"Superchiral" spectroscopy: detection of protein higher order hierarchical structure with chiral plasmonic nanostructures.* Journal of the American Chemical Society, 2015. **137**(26): p. 8380-8383.
5. Tarun, K., et al., *Superchiral near fields detect virus structure.* Light: Science and Applications, 2020. **9**(1).
6. Han, T., et al., *Recent advances in detection technologies for COVID-19.* Talanta, 2021. **233**: p. 122609.
7. Advocacy, A., *ASM Expresses Concern about Coronavirus Test Reagent Shortages.* American Society for Microbiology, 2020.
8. Mercer, T.R. and M. Salit, *Testing at scale during the COVID-19 pandemic.* Nature Reviews Genetics, 2021. **22**(7): p. 415-426.
9. Sachs, J.D., et al., *The Lancet Commission on lessons for the future from the COVID-19 pandemic.* The Lancet, 2022. **400**(10359): p. 1224-1280.
10. Dhama, K., et al., *Coronavirus disease 2019–COVID-19.* Clinical microbiology reviews, 2020. **33**(4): p. e00028-20.
11. Letko, M., A. Marzi, and V. Munster, *Functional assessment of cell entry and receptor usage for SARS-CoV-2 and other lineage B betacoronaviruses.* Nature microbiology, 2020. **5**(4): p. 562-569.
12. Huang, Y., et al., *Structural and functional properties of SARS-CoV-2 spike protein: potential antivirus drug development for COVID-19.* Acta Pharmacologica Sinica, 2020. **41**(9): p. 1141-1149.
13. Duan, X., et al., *Quantification of the affinities and kinetics of protein interactions using silicon nanowire biosensors.* Nature nanotechnology, 2012. **7**(6): p. 401-407.
14. Sedlak, S.M., et al., *Streptavidin/biotin: tethering geometry defines unbinding mechanics.* Science advances, 2020. **6**(13): p. eaay5999.
15. Ahlers, M., et al., *Specific recognition and formation of two-dimensional streptavidin domains in monolayers: applications to molecular devices.* Thin Solid Films, 1989. **180**(1-2): p. 93-99.
16. Weber, P.C., et al., *Structural origins of high-affinity biotin binding to streptavidin.* Science, 1989. **243**(4887): p. 85-88.
17. Dundas, C.M., D. Demonte, and S. Park, *Streptavidin–biotin technology: improvements and innovations in chemical and biological applications.* Applied microbiology and biotechnology, 2013. **97**: p. 9343-9353.
18. Lowe, B.M., et al., *Field-effect sensors–from pH sensing to biosensing: sensitivity enhancement using streptavidin–biotin as a model system.* Analyst, 2017. **142**(22): p. 4173-4200.

19. Dong, J., et al., *Recent progress on plasmon-enhanced fluorescence.* Nanophotonics, 2015. **4**(4): p. 472-490.
20. Tullius, R., et al., *Superchiral plasmonic phase sensitivity for fingerprinting of protein interface structure.* ACS nano, 2017. **11**(12): p. 12049-12056.
21. Crut, A., et al., *Optical absorption and scattering spectroscopies of single nano-objects.* Chemical Society Reviews, 2014. **43**(11): p. 3921-3956.
22. Foerster, B., et al., *Chemical interface damping depends on electrons reaching the surface.* ACS nano, 2017. **11**(3): p. 2886-2893.
23. Szekrényes, D.n.P., et al., *Chemical Interface Damping as an Indicator for Hexadecyltrimethylammonium Bromide Replacement by Short-Chain Thiols on Gold Nanorods.* The Journal of Physical Chemistry C, 2020. **124**(36): p. 19736-19742.
24. Zijlstra, P., et al., *Chemical Interface Damping in Single Gold Nanorods and Its Near Elimination by Tip-Specific Functionalization.* Angewandte Chemie International Edition, 2012. **33**(51): p. 8352-8355.
25. Kelly, C., et al., *Chiral plasmonic fields probe structural order of biointerfaces.* Journal of the American Chemical Society, 2018. **140**(27): p. 8509-8517.
26. Abdulrahman, N.A., et al., *Induced chirality through electromagnetic coupling between chiral molecular layers and plasmonic nanostructures.* Nano letters, 2012. **12**(2): p. 977-983.
27. Govorov, A.O. and Z. Fan, *Theory of chiral plasmonic nanostructures comprising metal nanocrystals and chiral molecular media.* ChemPhysChem, 2012. **13**(10): p. 2551-2560.
28. Genevet, P., et al., *Controlled steering of Cherenkov surface plasmon wakes with a one-dimensional metamaterial.* Nature Nanotechnology, 2015. **10**(9): p. 804-809.
29. Doms, R.W., *Basic concepts: A step-by-step guide to viral infection*, in *Viral pathogenesis*. 2016, Elsevier. p. 29-40.
30. Sato, S., et al., *Alcohol abrogates human norovirus infectivity in a pH-dependent manner.* Scientific Reports, 2020. **10**(1): p. 15878.
31. Suomalainen, M. and U.F. Greber, *Uncoating of non-enveloped viruses.* Current opinion in virology, 2013. **3**(1): p. 27-33.
32. Blut, A., *Influenza virus.* Transfusion Medicine and Hemotherapy, 2009. **36**(1): p. 32.
33. Yao, H., et al., *Molecular architecture of the SARS-CoV-2 virus.* Cell, 2020. **183**(3): p. 730-738. e13.
34. Anfossi, L., et al., *Multiplex lateral flow immunoassay: An overview of strategies towards high-throughput point-of-need testing.* Biosensors, 2018. **9**(1): p. 2.
35. Li, L., et al., *All inkjet-printed amperometric multiplexed biosensors based on nanostructured conductive hydrogel electrodes.* Nano letters, 2018. **18**(6): p. 3322-3327.
36. Jarockyte, G., et al., *Multiplexed nanobiosensors: current trends in early diagnostics.* Sensors, 2020. **20**(23): p. 6890.
37. Lillehoj, E.P., et al., *Cellular and molecular biology of airway mucins.* International review of cell and molecular biology, 2013. **303**: p. 139-202.
38. Mathew, J., P. Sankar, and M. Varacallo, *Physiology, blood plasma.* 2018.
39. Janeway Jr, C.A., et al., *The structure of a typical antibody molecule*, in *Immunobiology: The Immune System in Health and Disease. 5th edition*. 2001, Garland Science.
40. Kim, J.-M., et al., *Identification of coronavirus isolated from a patient in Korea with COVID-19.* Osong public health and research perspectives, 2020. **11**(1): p. 3.

41. Park, W.B., et al., *Virus isolation from the first patient with SARS-CoV-2 in Korea.* Journal of Korean Medical Science, 2020. **35**(7).
42. Musso, D. and D.J. Gubler, *Zika virus.* Clinical microbiology reviews, 2016. **29**(3): p. 487-524.
43. Robilotti, E., S. Deresinski, and B.A. Pinsky, *Norovirus.* Clinical microbiology reviews, 2015. **28**(1): p. 134-164.
44. Lee, L.A., Z. Niu, and Q. Wang, *Viruses and virus-like protein assemblies—Chemically programmable nanoscale building blocks.* Nano Research, 2009. **2**: p. 349-364.
45. McNaught, A.D. and A. Wilkinson, *Compendium of chemical terminology*. Vol. 1669. 1997: Blackwell Science Oxford.
46. Cennamo, N., et al., *SARS-CoV-2 spike protein detection through a plasmonic D-shaped plastic optical fiber aptasensor.* Talanta, 2021. **233**: p. 122532.
47. Chiavaioli, F., et al., *Towards a uniform metrological assessment of grating-based optical fiber sensors: From refractometers to biosensors.* Biosensors, 2017. **7**(2): p. 23.
48. Seo, G., et al., *Rapid detection of COVID-19 causative virus (SARS-CoV-2) in human nasopharyngeal swab specimens using field-effect transistor-based biosensor.* ACS nano, 2020. **14**(4): p. 5135-5142.
49. Ahmed, S.R., et al., *In situ self-assembly of gold nanoparticles on hydrophilic and hydrophobic substrates for influenza virus-sensing platform.* Scientific reports, 2017. **7**(1): p. 44495.
50. Devarakonda, S., et al., *Cost-effective and handmade paper-based immunosensing device for electrochemical detection of influenza virus.* Sensors, 2017. **17**(11): p. 2597.
51. Peto, T., et al., *COVID-19: Rapid antigen detection for SARS-CoV-2 by lateral flow assay: A national systematic evaluation of sensitivity and specificity for mass-testing.* EClinicalMedicine, 2021. **36**.
52. Xu, M., et al., *Recent advances of representative optical biosensors for rapid and sensitive diagnostics of SARS-CoV-2.* Biosensors, 2022. **12**(10): p. 862.
53. Faye, O., et al., *One-step RT-PCR for detection of Zika virus.* Journal of Clinical Virology, 2008. **43**(1): p. 96-101.
54. Martins, S.A., et al., *Biosensors for on-farm diagnosis of mastitis.* Frontiers in bioengineering and biotechnology, 2019. **7**: p. 186.
55. Abb-Schwedler, K., et al., *Feeding mastitis milk to organic dairy calves: effect on health and performance during suckling and on udder health at first calving.* BMC veterinary research, 2014. **10**(1): p. 1-11.
56. YALÇIN, C., *Cost of mastitis in Scottish dairy herds with low and high subclinical mastitis problems.* Turkish Journal of Veterinary & Animal Sciences, 2000. **24**(5): p. 465-472.
57. Carinelli, S., et al., *Hemoglobin-modified nanoparticles for electrochemical determination of haptoglobin: Application in bovine mastitis diagnosis.* Microchemical Journal, 2022. **179**: p. 107528.
58. Alayash, A.I., *Oxygen therapeutics: can we tame haemoglobin?* Nature reviews Drug discovery, 2004. **3**(2): p. 152-159.
59. Windria, S., et al., *Development of ELISA against milk haptoglobin for diagnosis of subclinical mastitis in goats.* Heliyon, 2021. **7**(2): p. e06314.

60. Grönlund, U., et al., *Haptoglobin and serum amyloid A in milk and serum during acute and chronic experimentally induced Staphylococcus aureus mastitis.* Journal of dairy research, 2003. **70**(4): p. 379-386.
61. Sharma, N., V. Pandey, and N. Sudhan, *Comparison of some indirect screening tests for detection of subclinical mastitis in dairy cows.* Bulgarian Journal of Veterinary Medicine, 2010. **13**(2).
62. Lam, T., et al., *Mastitis diagnostics and performance monitoring: a practical approach.* Irish Veterinary Journal, 2009. **62**(4): p. 1-6.
63. Barnum, D. and F. Newbould, *The use of the California mastitis test for the detection of bovine mastitis.* The Canadian Veterinary Journal, 1961. **2**(3): p. 83.
64. Sharma, N., N. Singh, and M. Bhadwal, *Relationship of somatic cell count and mastitis: An overview.* Asian-Australasian Journal of Animal Sciences, 2011. **24**(3): p. 429-438.
65. Persson, Y. and I. Olofsson, *Direct and indirect measurement of somatic cell count as indicator of intramammary infection in dairy goats.* Acta Veterinaria Scandinavica, 2011. **53**(1): p. 1-5.
66. Polticelli, F., et al., *Human haptoglobin structure and function–a molecular modelling study.* The FEBS journal, 2008. **275**(22): p. 5648-5656.
67. Hwang, P.K. and J. Greer, *Interaction between hemoglobin subunits in the hemoglobin. haptoglobin complex.* J Biol Chem, 1980. **255**(7): p. 3038-3041.
68. Andersen, C.B.F., et al., *Structure of the haptoglobin–haemoglobin complex.* Nature, 2012. **489**(7416): p. 456-459.
69. Mattson, G., et al., *A practical approach to crosslinking.* Molecular biology reports, 1993. **17**: p. 167-183.
70. Ozboyaci, M., D. Kokh, and R. Wade, *Three steps to gold: mechanism of protein adsorption revealed by Brownian and molecular dynamics simulations.* Physical Chemistry Chemical Physics, 2016. **18**(15): p. 10191-10200.
71. Oliverio, M., et al., *Chemical functionalization of plasmonic surface biosensors: a tutorial review on issues, strategies, and costs.* ACS applied materials & interfaces, 2017. **9**(35): p. 29394-29411.
72. Lavín, Á., et al., *On the determination of uncertainty and limit of detection in label-free biosensors.* Sensors, 2018. **18**(7): p. 2038.
73. Standardization, I.O.f., *Capability of Detection, Part 1: Terms and Definitions*. 1997, ISO Geneva.
74. Calvo-Lozano, O., et al., *Label-free plasmonic biosensor for rapid, quantitative, and highly sensitive COVID-19 serology: implementation and clinical validation.* Analytical chemistry, 2021. **94**(2): p. 975-984.
75. Åkerstedt, M., et al., *Biosensor assay for determination of haptoglobin in bovine milk.* Journal of Dairy Research, 2006. **73**(3): p. 299-305.

Chapter 5 - Enantiomeric Discrimination Using Chirally Dependent SERS

This chapter progresses from biosensing using ORD measurements to exploring chiral discrimination through the more near field-sensitive technique of SERS with DPA samples. By employing SERS, the chiral nature of the DPA shuriken shape will become paramount, giving rise to the phenomenon of chirally dependent SERS. The chapter begins by introducing the concepts of near field and far field domains in plasmonic resonators, followed by a description of the two experimental setups that demonstrate chirally dependent SERS in this work. Subsequently, the chapter is divided into two sections, each presenting and discussing the results from the respective experimental systems.

5.1 Background

The terms ‘near field’ and ‘far field’ are often used when describing EM field regions around a plasmonic resonating object, such as DPA nanostructure. Most experimental techniques used to characterise the optical properties of plasmonic nanostructures rely on far field measurements, such as reflectivity, absorption, and ORD. The far field of a resonating structure is generally described as the region a distance away from the structure where EM fields behave as a classical propagating wave [1]. It can be viewed as the “normal” light which is detected with conventional microscopes. Conversely, near field regions are described as being non-radiative, which are close to the resonating structure. These near field regions range from nanometres to a wavelength unit from the structure, after which far field behaviour begins to dominate. Near field light is non-propagating and confined close to the resonant structure surface [1]. The differences in scale between near and far fields is illustrated in Figure 5-1.

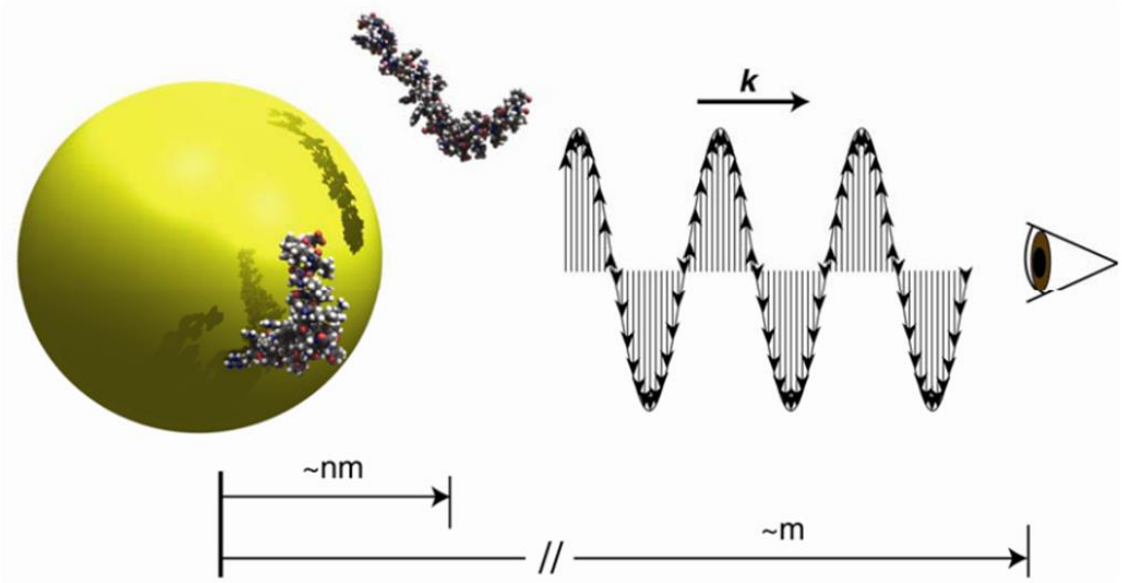

Figure 5-1 Illustration of a plasmonic nanoparticle surrounded by biomolecules, on which near-field effects occur close to the surface in the nm range. However, common measurement techniques are taken in the far field at a much greater distance. Image from Ross et al. [1].

Previous studies have shown that far field measurements are less sensitive to asymmetric changes in the presence of a chiral medium when compared to near field techniques [2] [3]. This is because near field techniques are more sensitive to local changes in optical chirality as opposed to far-field light scattering measurements. Tabouillot *et al.* demonstrated this using plasmonic circularly polarised luminescence to detect chiral asymmetric responses of peptides which was undetectable with classical light scattering based measurements [2]. Hajji *et al.* reported similar findings of asymmetric luminescence when introducing antibody molecules to a shuriken metafilm with added quantum dot emitters, demonstrating chiral detection of antibodies at femto- and zeptomolar levels by monitoring luminescence spectral line shapes between LH and RH structures [3].

In addition to photoluminescence, SERS is a powerful and sensitive near field technique suitable for the detection of asymmetric changes in local plasmonic near field environments. SERS is considered a near field technique as it relies on the interaction of molecules and plasmonic substrates at close distances, which is where the enhancement of the Raman signal predominantly occurs [4]. Furthermore, SERS signals arise solely from the molecule(s) of interest, devoid of interference from background gold or unfunctionalised regions. This property

simplifies the monitoring of changes in the analyte or the surrounding EM fields, rendering SERS as a sensitive and valuable technique.

In this work, the chiral EM field environments are generated by the DPA shuriken nanostructures. By utilising chiral nanoparticles or molecules, asymmetric changes in the near field EM environments of the DPAs can be achieved, which will be reflected by differential SERS intensities. This phenomenon can be described as the *chiral SERS effect*, or *chirally dependent SERS*. While recent studies have explored this effect [5-7], a comprehensive understanding of its underlying mechanisms have yet to be explored in-depth. While the biosensing experiments in the previous chapter were conducted using P5 region DPA nanostructures, SERS enhancement factors were discovered to be the highest for the P3 region. This finding is further explored and discussed later in Section 5.3.1. Resultingly, P3 regions were exclusively used for all SERS experiments.

The chiral SERS effect is demonstrated using 2 separate experimental systems, the first of which involves the creation of differential EM hotspots between DPA nanostructures and deposited gold chiral Helicoid Nanoparticles (HNPs). The two plasmonic systems are linked together using a linear achiral dithiol molecule, biphenyl-4,4’-dithiol (BPDT), which serves as both a linker for the gold substrates as well as the Raman reporter of the EM near field intensities. Far field ORD and reflectivity measurements taken from DPA samples functionalised with BPDT and HNPs are shown to not possess observable asymmetry, demonstrating the limitations of such techniques. However, with SERS measurements the asymmetry becomes apparent. This is the first known report of chirally dependent SERS using diastereomeric combinations of chiral metal nanostructures/nanoparticles.

The second experimental system demonstrating the chiral SERS effect uses silver sputter coated DPA samples for the enantiomeric discrimination of various molecules using a common Raman system. The silver sputter coating process was found to be essential to provide adequate SERS enhancement. Subsequent spin-coating of molecular enantiomers allowed for the detection and enantiomeric discrimination of a variety of molecules. This experimental system is expanded upon further in Section 5.3.

5.2 Enantiomeric Discrimination of Chiral Helicoid Nanoparticles Using Chirally Dependent SERS

5.2.1 Chiral Helicoid Nanoparticles

To investigate the physical phenomenon of the chirally dependent SERS response, rhombic dodecahedral shaped chiral HNPs (Figure 5-2) were proposed as an experimental system that could be paired with DPA shurikens to investigate the coupling of chiral EM-fields between the two chiral plasmonic systems. This essentially creates diastereomeric combinations of plasmonic structures.

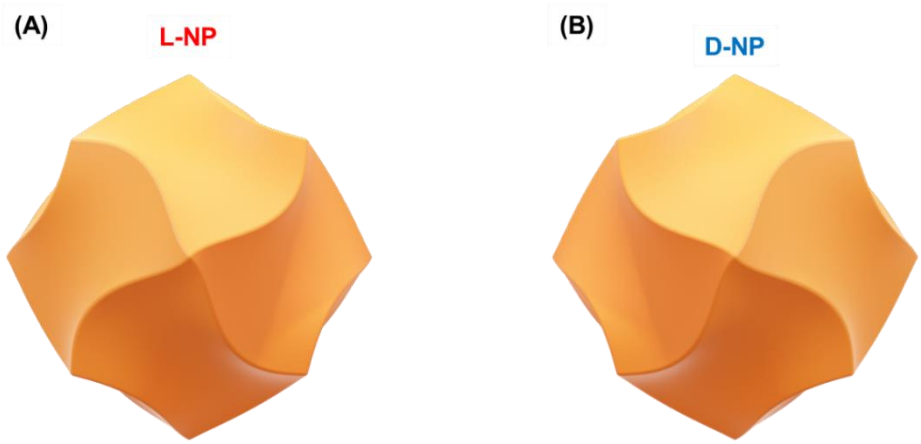

Figure 5-2 Idealised geometry of enantiomeric HNPs.

HNPs have been investigated extensively in other studies to explore the fabrication of asymmetric structures using solution-phase chemistry and amino-acid/peptide shape-directing additives [8, 9]. To synthesise HNPs, a two-step growth method is used. Firstly, 2 nm precursor spherical gold nanoparticles are grown in a growth solution containing cetyltrimethylammonium bromide (CTAB), ascorbic acid (AA), and tetrachloroauric (III) trihydrate in water for 15 minutes to yield 50 nm sized cuboctahedron shaped nanoparticles. The cuboctahedron shape arises from the influence of CTAB and AA cooperation on nanoparticle growth; CTAB inhibits growth on the {100} surface while AA promotes growth in the {111} direction. Tuning the CTAB and AA reagent ratios as well as reaction time allows for the precise control over size and shape of nanoparticles [10]. In the second growth step, the 50 nm cuboctahedron nanoparticles are grown in a growth solution containing CTAB, AA, tetrachloroauric(III) trihydrate, and cysteine for 1 hour. The cysteine molecules continuously attach to the gold nanoparticles through

thiol interactions, and depending on the choice of cysteine enantiomer, one direction of growth is favoured over the other, resulting in the final HNPs. The morphological evolution of the second growth stage over time in addition to the measured CD spectra is presented in Figure 5-3 [9].

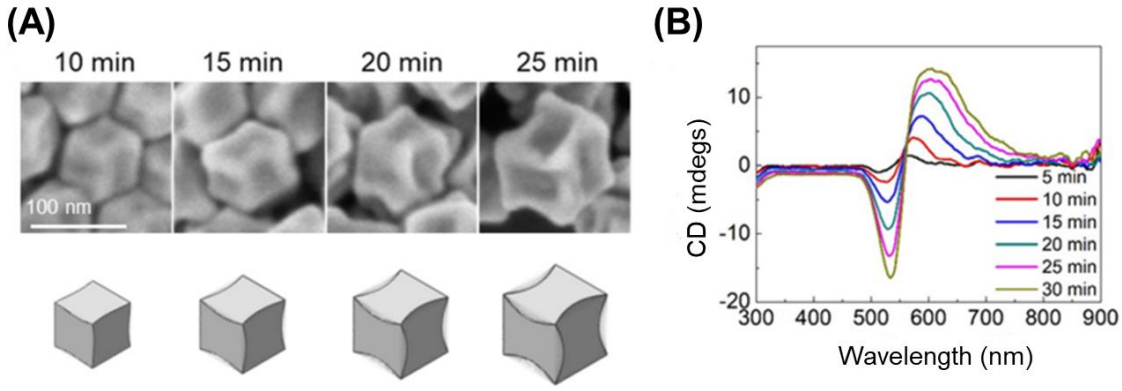

Figure 5-3 (A) SEM images depicting the morphological development of cuboctahedron nanoparticles grown in cysteine growth solution for different time periods. (B) CD spectra of nanoparticles in aqueous solution. Images and spectra from study by Lee et al. [9].

The CD spectra from the L- and D-HNPs in aqueous solution used in the following experiments is presented in Figure 5-4. Using the Kramers-Kronig relation, the corresponding ORD spectra were calculated as well. The main CD resonance peak was discovered to be around 575 nm, which coincides closely to the resonance features of the HNPs synthesised by Lee *et al*. [9].

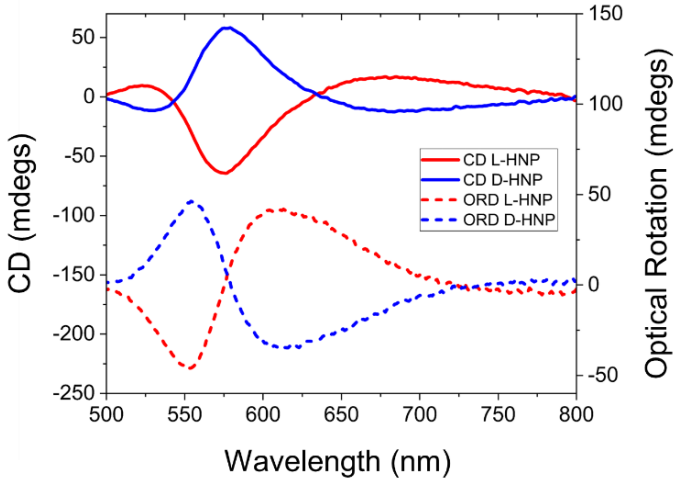

Figure 5-4 CD and corresponding ORD (calculated using Kramers–Kronig transform) spectra for L- (red) and D- (blue) HNPs in aqueous solution.

To link the synthesized HNPs with DPA samples, DPAs were first rinsed with methanol and plasma cleaned for 5 minutes at 100 W power. DPAs were then immersed in a 3 mM methanol

solution of BPDT (95%) (Sigma-Aldrich) for 24 hours to form a SAM. After rinsing and drying the shurikens with methanol a solution of either L- or D-HNPs in DI was added. The samples were left on a shaker for 24 hours, then washed with deionised water and dried with N_2 gas (Figure 5-5).

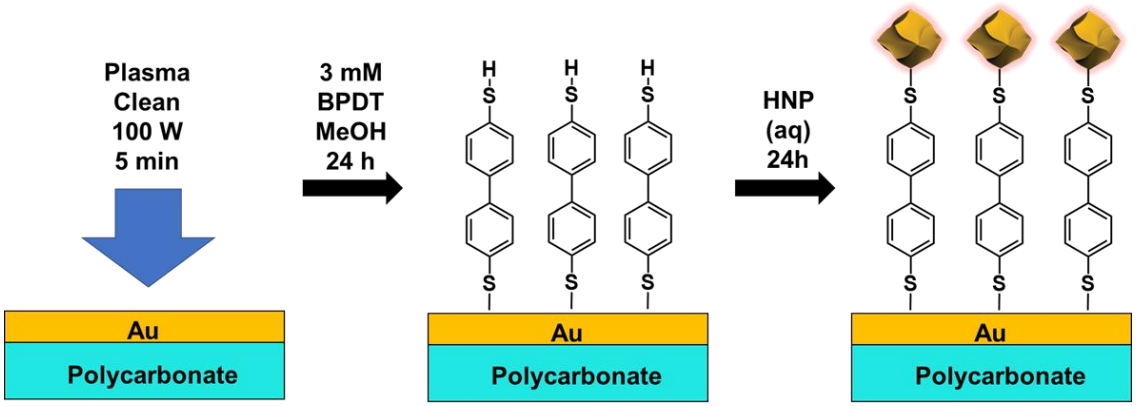

Figure 5-5 Functionalisation strategy of gold DPA metafilms with BPDT and HNPs.

For convention, a two-lettered labelling system was adopted to describe the different combinations of shuriken and HNP: 'LL', 'LR', 'RL', and 'RR', where the first letter describes the handedness of the shuriken nanostructure and the second letter the handedness of the nanoparticle. For simplicity, a D-HNP is considered a RH particle and referred to by the letter '*R*', and a L-HNP as a LH particle referred to by the letter '*L*'. SEM images of the HNP functionalised DPA samples for all four combinations of shuriken and HNP are presented in Figure 5-6. From the images, relatively even coverage of bright HNP particles on all DPA samples are observed. While there are areas present which do not possess HNPs, the 633 nm Raman laser spot-size diameter of around 100 μm ensures the illumination and excitation of multiple shurikens linked with HNPs in an area.

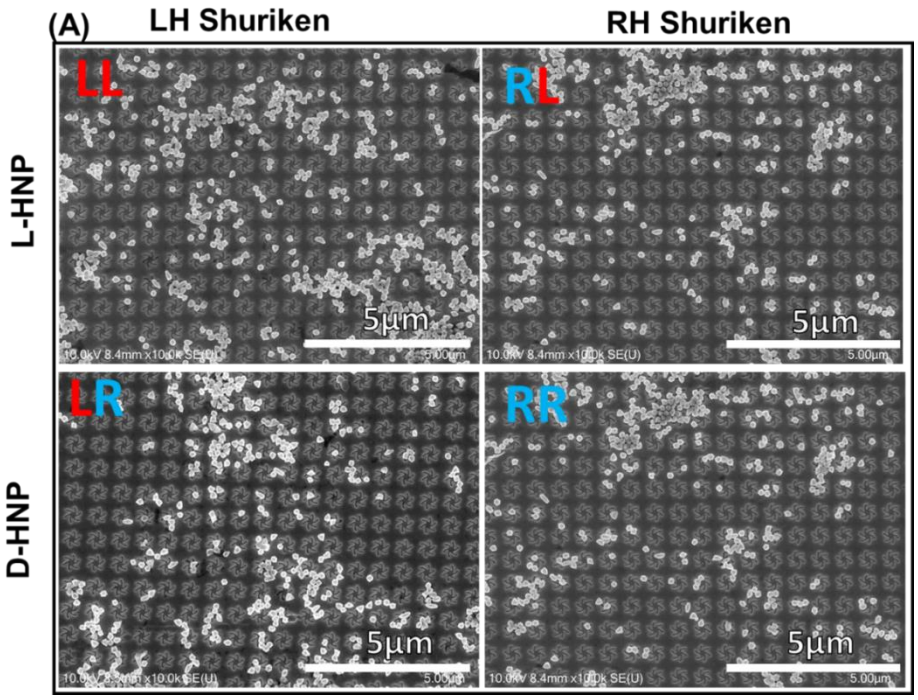

Figure 5-6 SEM images of LH and RH nanostructures functionalized with BPDT and HNPs.

5.2.2 Optical Properties of HNP Functionalised DPA Samples

The optical properties of BPDT SAM and HNP functionalised DPA samples were measured to investigate levels of asymmetry detectable with far field measurements. Both reflectivity and ORD spectra were acquired using the single-spot polarimetry microscope described in Section 3.3.2 from P3 DPA regions on the E array (LH and RH) locations. For each spectrum, 8 measurements were performed from which the mean was calculated and the background measurement from plain gold subtracted. The reflectivity spectra and their associated resonance peak positions for pristine, BPDT, and L- or D-HNP functionalised DPA samples are shown in Figure 5-7 and Table 5-1.

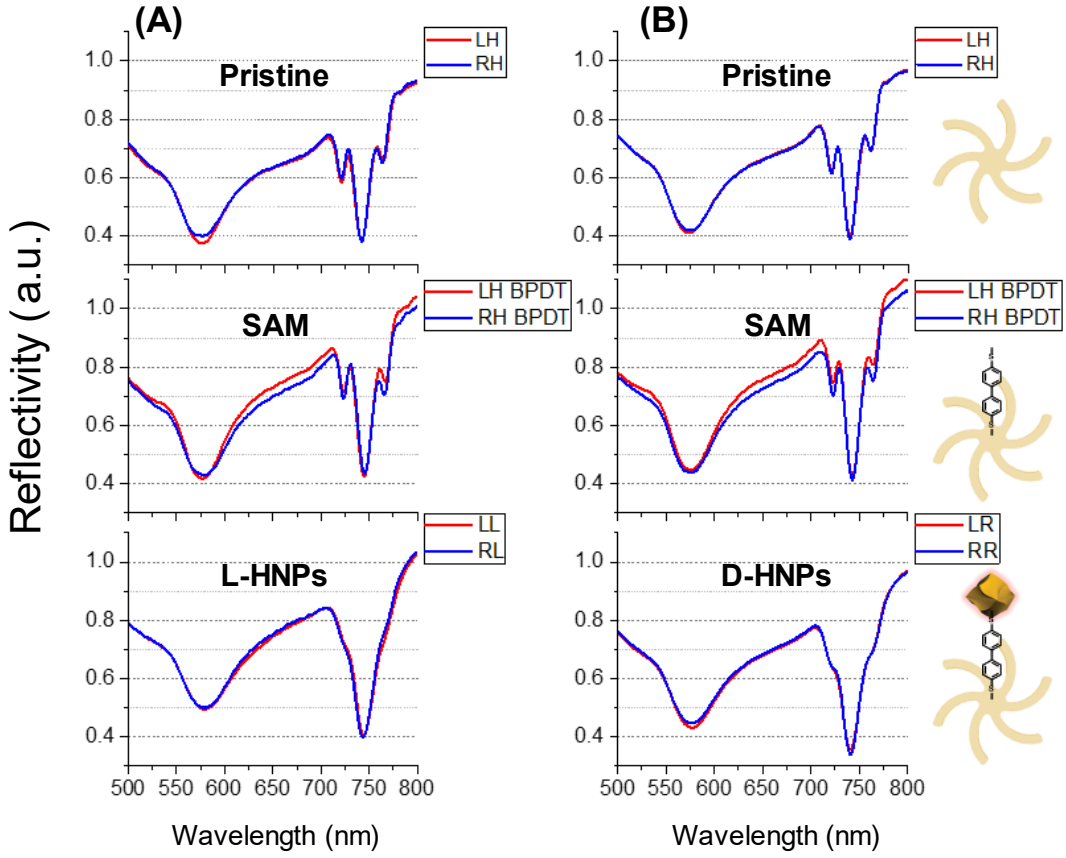

Figure 5-7 Reflectivity spectra from samples used for (A) L- and (B) D-HNP samples for LH (red) and RH (blue) shuriken metafilm samples throughout each experimental stage: Pristine sample prior to any surface modification, after BPDT SAM functionalization, and after L- or D-HNP addition.

		Broad Resonance Position (nm)				Sharp Resonance Position (nm)			
		L-HNP Sample		D-HNP Sample		L-HNP Sample		D-HNP Sample	
		LH	RH	LH	RH	LH	RH	LH	RH
Experimental Stages	Pristine	576.5	576.3	573.7	574.0	741.9	741.8	740.0	740.0
	BPDT	577.7	577.9	575.1	575.4	744.8	745.1	742.7	742.8
	HNP	579.7	579.6	577.2	577.4	744.4	744.0	742.3	742.0
Resonance Shift	Δλ BPDT	1.2	1.6	1.4	1.4	2.9	3.3	2.7	2.8
	Δλ HNP	3.2	3.3	3.5	3.4	2.5	2.2	2.3	2.0
Asymmetry (LH-RH)	ΔΔλ BPDT	-0.4		0.0		-0.4		-0.1	
	ΔΔλ HNP	-0.1		0.1		0.3		0.3	

Table 5-1 Reflectivity spectra resonance peak positions from DPA samples for all experimental stages: Pristine, BPDT SAM, and L- or D-HNP functionalised. Resonance shift and asymmetry parameters (LH-RH) relative to pristine samples are also shown.

Upon BPDT SAM application, the resonance features in the reflectivity spectra do not change significantly. Resonance positions do shift however, with an approximate 1.4 nm increase in the broad resonance peak in the 575 nm region, and a 2.9 nm shift in the sharp resonance peak in the 740 nm region. Following HNP functionalisation the reflectivity spectra broaden significantly in the 710-760 nm region. This is most likely a result of plasmonic hybridisation and damping mechanisms between the plasmon modes of the shurikens and HNPs [11]. The broad resonance peak experienced a further mean 2.0 nm shift, whereas the sharp resonance experienced a relative mean 0.6 nm blue-shift in position relative to BPDT.

By comparing the difference of the resonance shift values between LH and RH DPA structures, the asymmetry parameter, $\Delta\Delta\lambda$, was calculated (LH-RH). With the chiral nature of HNPs, an asymmetric optical response would be expected between different handedness of shuriken nanostructures. However, a lack of observable asymmetry is noted in the reflectivity spectra as both LH and RH measurements are near identical for all experimental stages, with asymmetry parameters not exceeding $\pm$ 0.4 nm.

The ORD spectra and the Peak 1 and Peak 2 resonance peak positions for pristine, BPDT, and L- or D-HNP functionalised DPA samples are shown in Figure 5-8 and Table 5-2.

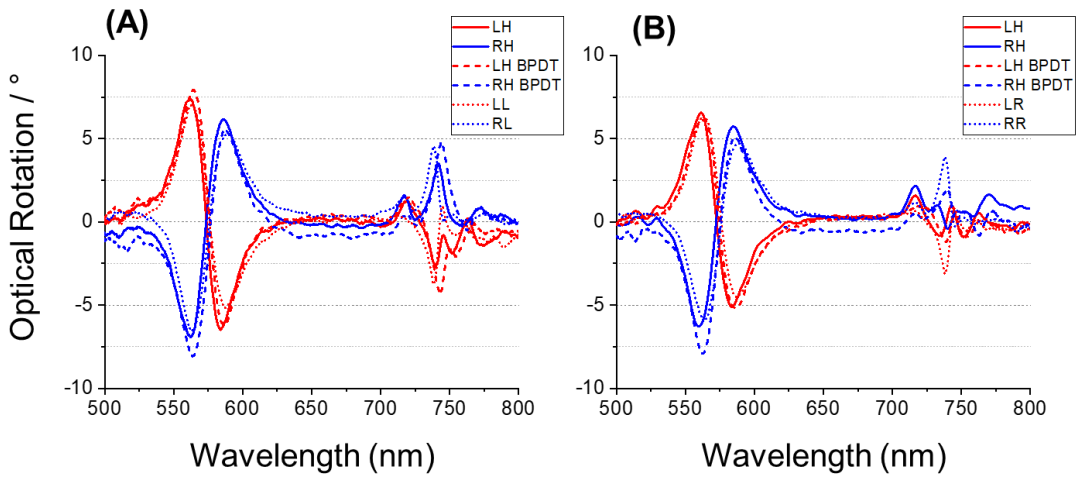

Figure 5-8 ORD spectra for LH (red) and RH (blue) shuriken metafilm samples throughout each experimental stage: Pristine sample prior to any surface modification (solid lines), after BPDT SAM functionalization (dashed lines), and after L- or D-HNP addition (dotted lines).

		Peak 1				Peak 2			
		L-HNP Sample		D-HNP Sample		L-HNP Sample		D-HNP Sample	
		LH	RH	LH	RH	LH	RH	LH	RH
Experimental Stages	Pristine	561.8	562.3	561.5	560.8	585.1	586.4	583.9	584.8
	BPDT	564.3	564.2	563.6	562.5	586.9	587.8	586.1	586.3
	HNP	563.4	563.6	563.4	563.2	587.7	588.5	586.8	587.2
Resonance Shift (nm)	Δλ BPDT	2.5	1.9	2.1	1.7	1.8	1.4	2.2	1.5
	Δλ HNP	1.6	1.3	1.9	2.4	2.6	2.1	2.9	2.4
Asymmetry (LH - RH) (nm)	ΔΔλ BPDT	0.6		0.4		0.4		0.7	
	ΔΔλ HNP	0.3		-0.5		0.5		0.5	

Table 5-2 ORD spectra resonance peak positions from DPA samples for all experimental stages: Pristine, BPDT SAM, and L- or D-HNP functionalised. Resonance shift and asymmetry parameters (LH-RH) relative to pristine samples are also shown.

From the ORD spectra, a mean 2.1 and 1.7 nm red shift in the resonance positions of Peak 1 and Peak 2 were observed upon BPDT SAM application, respectively. These values are comparable to the resonance shift values of the broad reflectivity peak to which these ORD resonances correspond to. Upon HNP functionalisation, resonance shift values decreased a mean value of 0.3 nm for Peak 1 and increased a mean value of 0.8 nm for Peak 2 compared to BPDT.

The peak positions from the resonance features located in the 710-760 nm regions were not tabulated due to their sporadic line shapes. A noteworthy observation from the ORD peaks in this region is that upon HNP functionalisation resonance features tend to blue shift. This is evident

most clearly in the case of the L-HNP functionalised sample, where an approximate 3 nm blue-shift is observed compared to the pristine sample measurements. This blue shift, observed in both reflectivity and ORD, can arise through the hybridisation of the two plasmonic systems [12]. In this case the plasmonic resonators are the DPA nanostructures and the HNPs. If one of the resonances is out of phase with the other, then the resulting coupled resonance would require a higher driving frequency compared to the single resonator, leading to resonance positions at lower wavelengths.

Looking at the asymmetry parameters from the ORD spectra, no combination of HNP or DPA shuriken leads to significant or opposite asymmetry, with asymmetry values falling between $\pm$ 0.5 nm. The small differences that exist in the ORD and reflectivity spectral peak shapes between L- and D-HNP functionalised samples can be attributed to sample inhomogeneity and small differences in the number of surface-bound HNPs.

In conclusion, the far field optical spectra of ORD and reflectivity obtained from BPDT and L- or D-HNP functionalised DPA samples did not reveal significant levels of asymmetry. A more direct probe of the EM near field environments is required, such as is available with the technique of SERS.

5.2.3 SERS Results and Discussion

An example SERS spectrum of BPDT taken with 633 nm laser excitation using the Raman spectrometer outlined in Section 3.3.5 is presented in Figure 5-9. The most prominent BPDT Raman bands are located at 1084, 1285, and 1589 cm^{-1}, which coincide with the in-plane vibration of the C-S bond, inter-ring C-C stretching, and C-C stretching, respectively. The full characterisation of all BPDT Raman bands is presented in Appendix B.1.

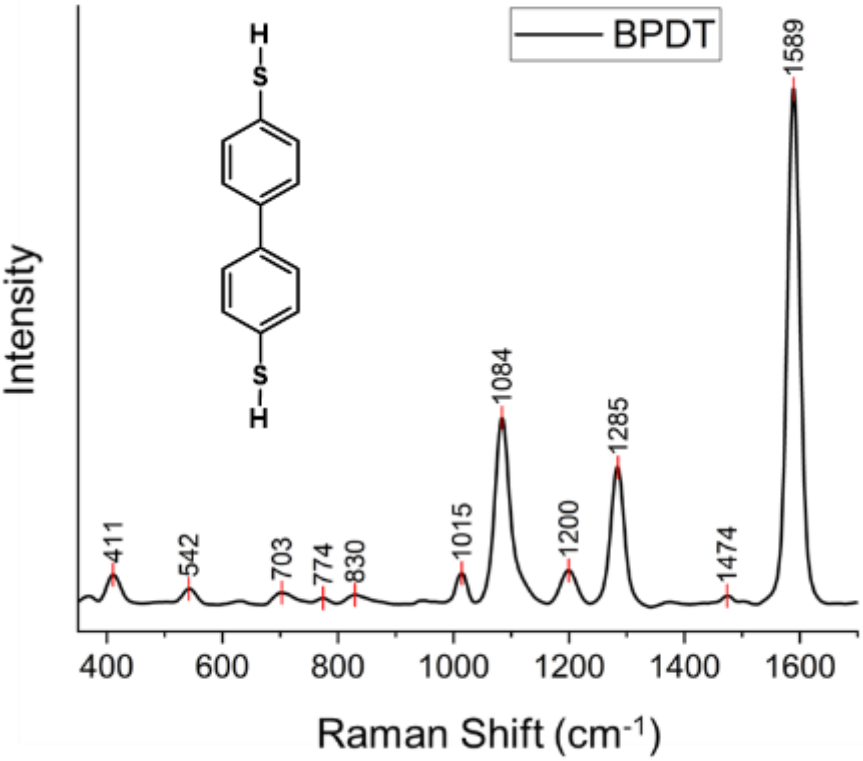

Figure 5-9 Molecular structure of BPDT, with an example SERS spectrum of adsorbed collected from DPA metafilm taken with 633 nm laser excitation.

To investigate the SERS response of BPDT in the absence of HNPs, SERS spectra of a BPDT SAM functionalised DPA sample were collected from plain gold (Au), as well as from the 9 LH and 9 RH P3 DPA surfaces. A signal accumulation time of 10 seconds per measurement was used with a laser power of 35 mW. Excitation and collection of Raman scattered light was perfomed using a 20× objective with an estimated spot size of 100 μm. The resultant mean SERS spectra are presented in Figure 5-10, with the shaded bands representing standard error.

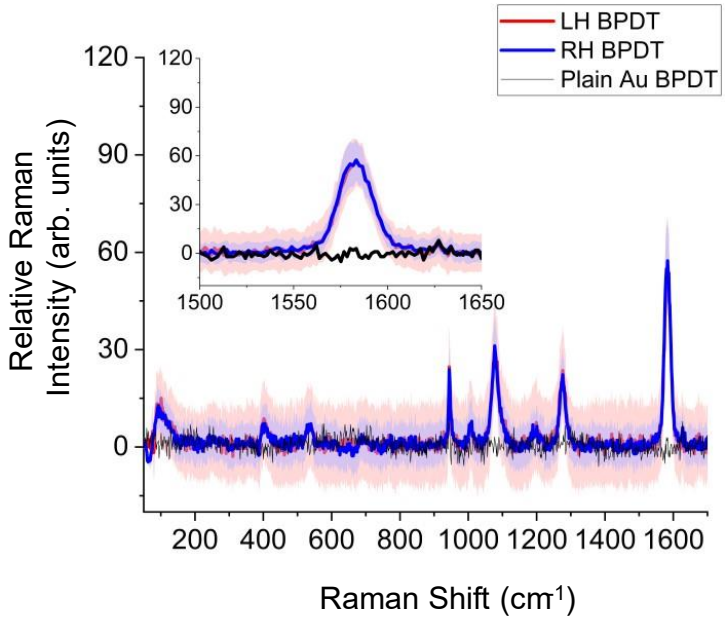

Figure 5-10 SERS spectra of BPDT on plain gold (black), and LH (red) and RH (blue) DPA nanostructured surfaces. Shaded regions represent standard error. Measurements taken with 633 nm laser excitation.

Raman measurements from plain gold surfaces on the DPA samples yield no observable SERS response from the BPDT SAM, indicating that the plain gold surface on its own does not have high enough SERS enhancement to generate adequate signals. Raman peaks become apparent when measuring from LH and RH DPA nanostructured surfaces as a result of the plasmonic resonances and EM field enhancement at these locations. Although the SERS signals are weak, they exhibit distinct peaks that correspond to those of BPDT. A noteworthy observation is that the LH and RH BPDT SERS spectra are near identical in intensity, with significant overlap in their standard error regions. These results align with expectations, as the achiral structure of BPDT on its own would not generate differential near field intensities on shuriken nanostructures of opposite handedness.

The next stage of experimentation was to incorporate the HNPs to the DPA surface using the BPDT SAM. Following the functionalisation procedures outlined in Section 5.2.1, SERS measurements were first acquired from the plain gold surfaces with attached HNPs to investigate the change in SERS response. 9 Raman measurements each were performed from L- and D-HNP functionalised plain gold surfaces, with mean Raman intensities and standard error calculated (Figure 5-11).

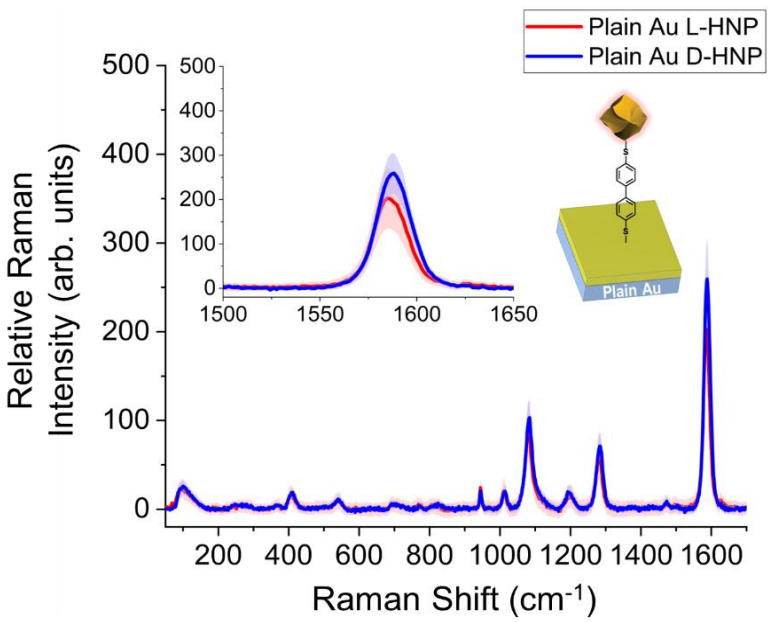

Figure 5-11 Mean BPDT SERS spectra from L- (red) and D-HNP (blue) functionalised samples on unstructured plain gold films. Solid lines show the mean values of the 9 data sets and shaded bands represent standard error.

BPDT Raman intensities from L- and D-HNP functionalised plain gold surfaces were noticeably stronger compared to BPDT measurements from nanostructured surfaces. This outcome is not entirely unexpected, as the close gap between the HNP and gold surface is expected to generate a strong plasmonic hotspot with intensified EM fields, leading to higher SERS intensities.

As observed in the case of BPDT on LH and RH DPA nanostructures, mean SERS intensities obtained from BPDT with added L- or D-HNPs were nearly identical, with overlapping standard error regions. Once more, this result can be attributed to the fact that the different handed HNPs do not create differential EM fields when on top of plain gold surfaces, resulting in equal SERS enhancement of BPDT signals from both HNP case.

Following control experiments, SERS measurements were then acquired from LH and RH P3 DPA regions functionalised with both BPDT and HNPs. SERS spectra were collected from an individual E array pair, with 10 measurements taken from each LH and RH array, effectively covering the whole array area (Figure 5-12C). The mean SERS spectra for all HNP and DPA shuriken handedness combinations are presented in Figure 5-12A-B, with shaded bands representing standard error.

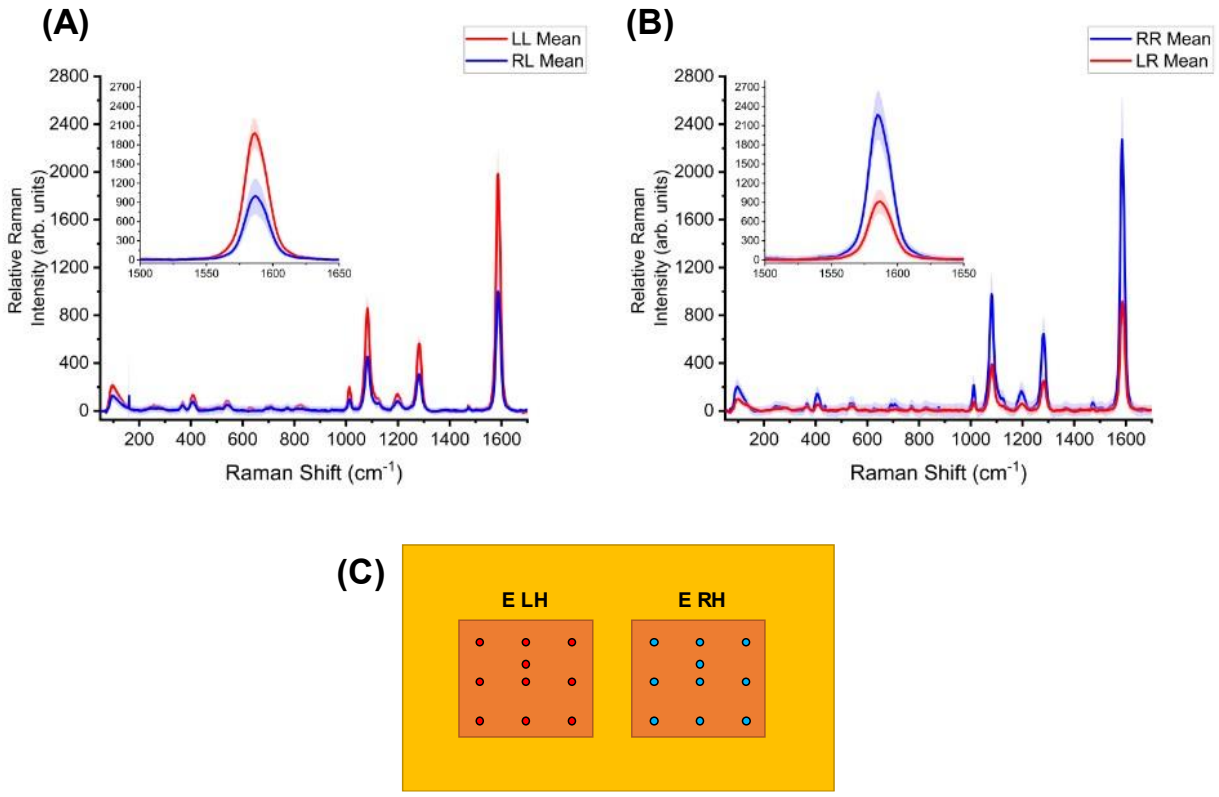

Figure 5-12 BPDT SERS spectra for (A) L-HNPs and (B) D-HNPs on LH (red) and RH (blue) E array DPA nanostructures, where solid lines show the mean values of the 10 data sets and shaded bands represent standard error. Inset graphs zoom on to the largest peaks (1589 cm^{-1}) from the spectra for clarity. (C) The 10 positions where SERS spectra were collected on LH and RH nanostructures from E region arrays.

The central finding presented in this work is the dependency of the SERS spectrum intensity on the symmetry properties between the diastereomer combinations of the DPA shurikens and the HNPs. In Figure 5-12A comparison spectra from L-HNP on both LH and RH shuriken combinations are shown (LL and RL, respectively). The opposite configurations from D-HNPs are shown in Figure 5-12B (LR and RR). The SERS spectra show clear and significant differences between combinations, with matched combinations of LL and RR resulting in higher Raman signal intensities compared to the mismatched counterparts of LR and RL**.** The shaded bands represent standard error, with the relatively close ranges indicating that the spread of SERS data is small, especially in the case of the LR combination. This signifies that SERS

intensities do not vary greatly from different regions of the sample and there is relatively good homogeneous coverage of HNPs.

To confirm that this observed chirally dependent SERS effect was consistent across the entirety of the P3 DPA regions, SERS measurements were also acquired from all P3 array pairs A-I. Additionally, the approximate 100 μm laser spot size meant that multiple measurements taken from the single array pair were experiencing significant overlap in the measured areas. By taking single measurements from each array, it is ensured that the laser spot is located entirely on the DPA nanostructured areas. The approximate laser spot-size is depicted in Figure 5-13C-D. Thus, using this method, a total of 9 measurements for each LH and RH A-I array set was obtained. The mean SERS spectra for all diastereomeric HNP and DPA shuriken handedness combinations collected this way are presented in Figure 5-13A-B, with shaded bands representing standard error.

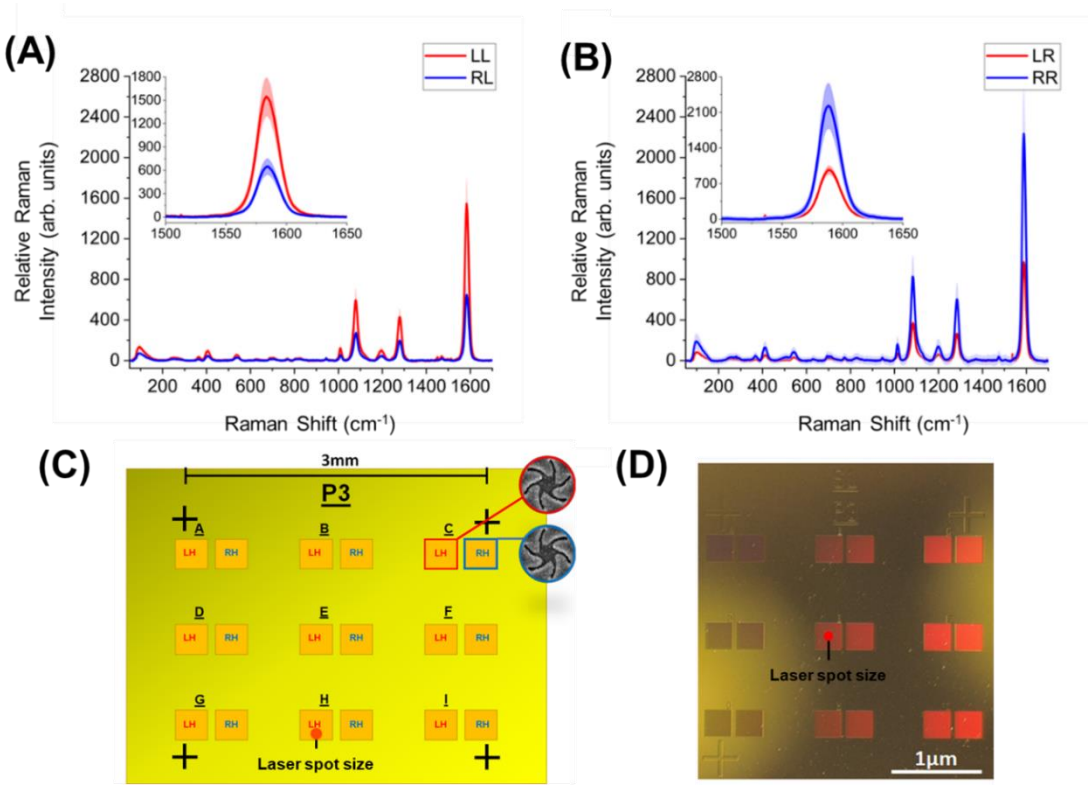

Figure 5-13 BPDT SERS spectra for (A) L-HNPs and (B) D-HNPs on LH (red) and RH (blue) DPA nanostructures, where solid lines show the mean values of the 9 data sets and shaded bands represent standard error. Inset graphs zoom on to the largest peaks (1589 cm^{-1}) from the spectra for clarity. (C) Diagram and (D) photographic representation of DPA P3 sample surface, with Raman laser spot size diameter shown as reference to shuriken nanostructure array size.

The resultant mean SERS spectra show the same asymmetric response as shown in the previous set of measurements from a single array pair in Figure 5-12, with the signal intensities within standard error of each other. These results indicate that the HNP surface coverage across samples is relatively even for SERS measurements, and that measurements from single array pairs as well as from pairs across the entire sample produce the same chiral SERS effect.

To quantify the difference in SERS intensities of BPDT between all diastereomeric nanostructure/nanoparticle combinations, the peak intensity ratios for all the characteristic BPDT Raman bands were calculated. This was performed by taking the intensities from all the BPDT Raman bands in Figure 5-13A-B and calculating the ratios from the RL/LL and LR/RR combinations. These results are presented in Table 5-3.

	Peaks RL										
Peak Position (cm^{-1})	411	542	703	774	830	1015	1084	1200	1285	1474	1589
Intensity (arb. Units)	46	30	15	11	14	53	271	46	190	20	636

	Peaks LL										
Peak Position (cm^{-1})	411	542	703	774	830	1015	1084	1200	1285	1474	1589
Intensity (arb. Units)	94	53	26	20	21	125	589	101	426	40	1538

Ratio (RL/LL)	0.49	0.57	0.58	0.55	0.67	0.42	0.46	0.46	0.45	0.50	0.41

Mean Ratio RL/LL	**RL/LL**
	0.50
SE	0.02

	Peaks LR										
Peak Position (cm^{-1})	411	542	703	774	830	1015	1084	1200	1285	1474	1589
Intensity (arb. Units)	54	35	21	13	18	70	368	58	254	21	953

	Peaks RR										
Peak Position (cm^{-1})	411	542	703	774	830	1015	1084	1200	1285	1474	1589
Intensity (arb. Units)	127	85	38	30	28	159	820	140	595	37	2218

Ratio (LR/RR)	0.43	0.41	0.55	0.43	0.64	0.44	0.45	0.41	0.43	0.57	0.43

Mean Ratio	**LR/RR**
	0.47
SE	0.02

Table 5-3 Relative Raman intensities for all characteristic BPDT bands for each nanostructure and HNP combination. The RL/LL and LR/RR ratios are presented, and the mean ratios and standard error (SE) calculated.

The calculated mean values for the RL/LL and LR/RR combinations were found to be 0.50 ± 0.02 and 0.47 ± 0.02, respectively. These values are expected to be the similar, as the RL/LL and LR/RR pairs are related by mirror symmetry. These values also indicate that on average the relative Raman intensities were approximately twice as high for the matched combinations of LL and RR compared to the mismatched LR and RL combinations.

To visualise the difference in SERS intensities between all types of measurements, the mean magnitudes of SERS responses between experiments are summarised in Figure 5-14, with the overall trend of BPDT Raman intensities observed as:

$$Plain\ gold\ < Shuriken\ only < HNP + Flat\ gold\ substrate\ < HNP + Shurikens \quad (5.2.1)$$

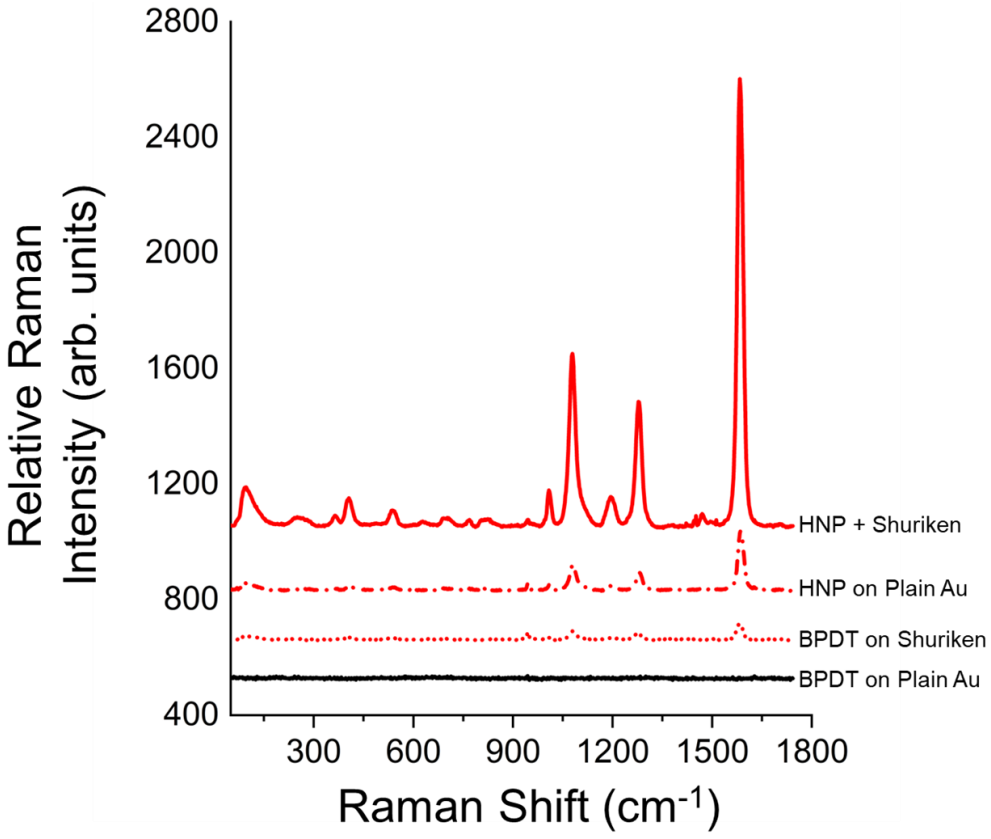

Figure 5-14 Comparison of SERS intensities between HNP functionalised on shurikens, HNPs on plain gold, BPDT on the shurikens and BPDT on plain gold.

The average Raman signal from HNP + shurikens was found to be approximately 7.5 times greater than that from HNP on plain gold films, which is in turn approximately 4.5 times greater than the BPDT SAM response on DPA shurikens.

5.2.4 HNP EM Simulations

The differential BPDT SERS signals arise due to the interplay of symmetry properties between the DPA metafilm and HNPs. The different symmetry combinations result in distinct EM environments, leading to the observed variations in the BPDT SERS signals. A widely accepted relation regarding SERS Enhancement Factor (EF) is [13, 14]:

$$EF \approx \left|\frac{E_{loc}}{E_i}\right|^4 \tag{5.2.2}$$

Where E_{loc} is the electric local field amplitude at the Raman active site (or hot spot) and E_i is the amplitude of the incident excitation. Hence, Equation 5.3.1 relates the EF to intensities of hotspot regions in the EM environment. Consequently, the presented hypothesis in this work is that the local electric fields between matched LL and RR nanostructure and nanoparticle combinations are higher in intensity compared to mismatched LR and RL combinations, which can be written as:

$$\left|\frac{E_{loc}}{E_i}\right|_{LL,RR} > \left|\frac{E_{loc}}{E_i}\right|_{LR,RL} \tag{5.2.3}$$

This argument presented in Equation 5.3.2 was validated by numerical EM simulations.

EM simulations were performed by positioning a single HNP with and end-to-end length of 160 nm in close vicinity to a shuriken nanostructure and applying periodic boundary conditions, resulting in a simplified model representation of the experimental samples. Shuriken nanostructure dimensions (30 nm arm width) and periodicity (720 nm) were chosen in accordance with P3 nanostructure geometry. Mesh element sizes were regulated so that regions of interest – namely the HNP, shuriken gold film, and the area between HNP and shuriken – had smaller element sizes and therefore higher accuracy. All symmetry combinations, LL, LR, RL, and RR, between HNPs and shuriken were simulated using the experimental 633 nm wavelength excitation, with two different locations chosen for the HNP: in the centre of the shuriken and on a resonating arm of the shuriken - Figure 5-15A and Figure 5-15C, respectively.

To calculate electric field strengths in the regions of interest between the HNP and shuriken nanostructures, a rectangular box was defined containing these regions (Figure 5-15B and Figure 5-15D).

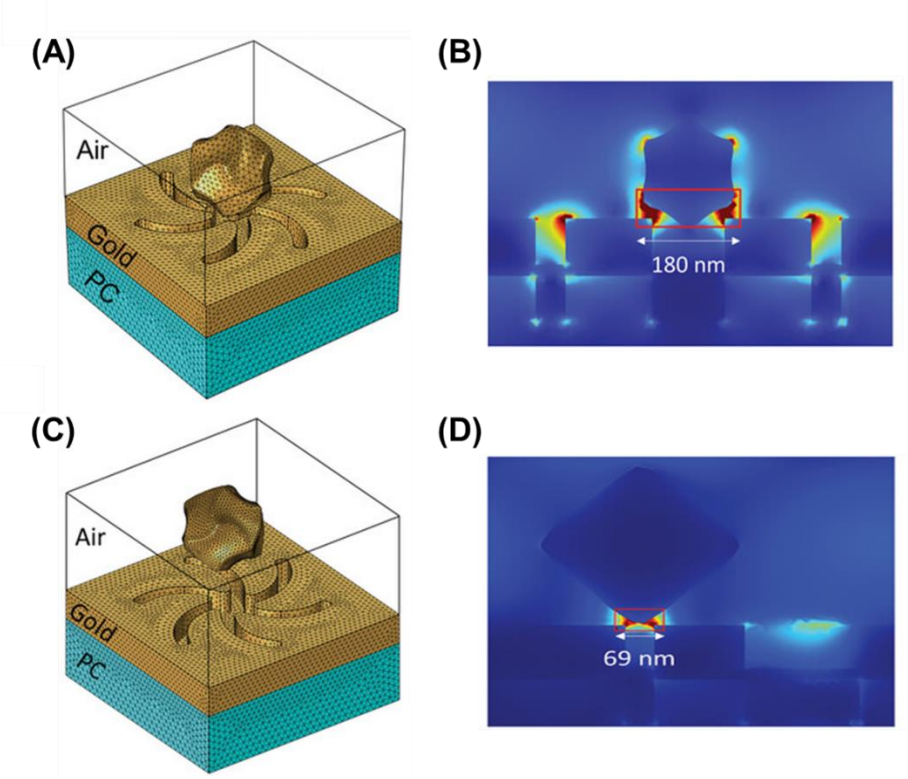

Figure 5-15 Idealized structural model examples used in the simulations of a HNP on the centre (A) and arm (C) of a DPA nanostructure on a polycarbonate (PC) substrate. (B) Side view of a slice of the simulated electric field for the RR diastereomeric combination of (A), with the red box (55 × 180 nm) highlighting the region with the most intense hotspots. (D) Side view of a slice of the simulated electric field for the LL diastereomeric combination of (C), with the red box (35 × 69 nm) highlighting the region with the most intense hot spots.

By calculating the mean electric field values in the defined areas for each HNP and shuriken symmetry combinations, the final $\left|\frac{E_{loc}}{E_i}\right|^4$ values could be obtained for each simulation (Figure 5-16).

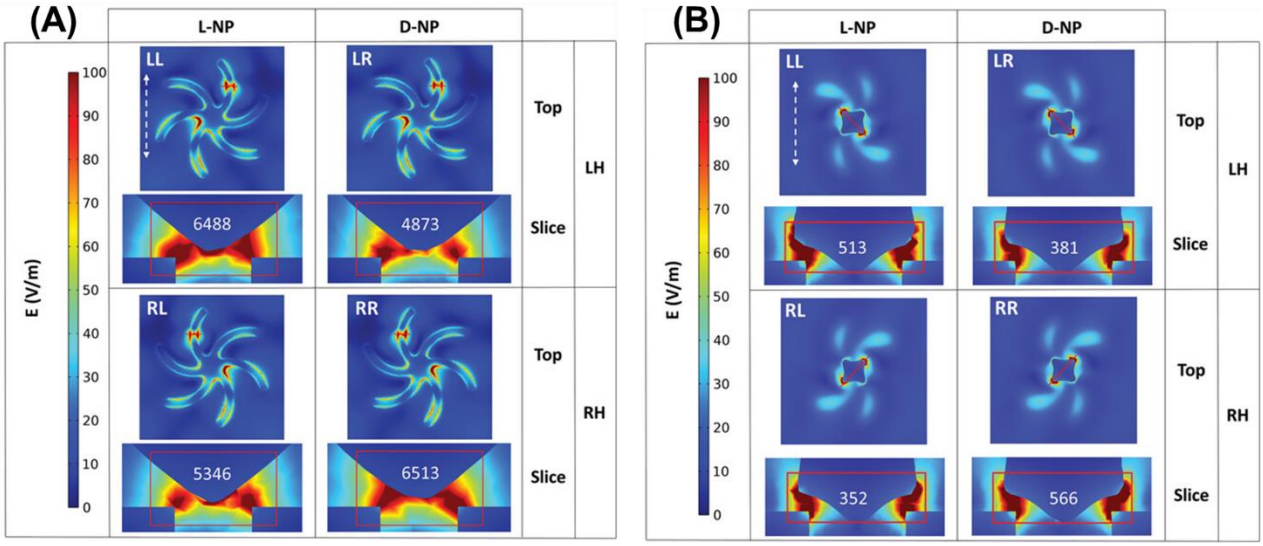

Figure 5-16 Simulated maps of electric fields for the 4 diastereomeric combinations for HNPs situated on the centre (A) and arm (B) of a DPA shuriken nanostructure, with the values representing calculated $\left|\frac{E_{loc}}{E_i}\right|^4$ *values. The polarization of the incident light is highlighted with the dashed white arrow in the top left panels of (A) and (B).*

The simulation results from both HNP locations show that the most intense hotspots, and therefore the strongest Raman responses, are produced by diastereomeric combinations formed from matched pairs LL and RR. There are slight differences in values between the mirror symmetry related combinations, which is unexpected considering the EM environments of RR and LL (and RL and LR) combinations should be the same. These differences can arise from computational constraints placed on the mesh element size, as separate simulations will have slightly different meshing geometries.

Considering that the highest Raman response is expected from the observed EM hotspots and that the signal is dependent on the term $\left|\frac{E_{loc}}{E_i}\right|^4$, the calculated ratios using the values in Figure 5-16A for LR/RR and RL/LL are 0.67 and 0.69, and for Figure 5-16B are 0.75 and 0.82, respectively. These values are significantly greater than the ratios obtained from the experimental samples. However, these regions from which $\left|\frac{E_{loc}}{E_i}\right|^4$ are calculated also contain

areas without significant EM fields, which artificially raises the calculated ratio values. Considering this, the ratios obtained from these simulations are within reasonable agreement with the experimentally obtained intensity ratio values of 0.43 and 0.46.

To summarise, the results obtained from numerical EM simulations, while based on highly idealised models, support the hypothesis that different diastereomer combinations of HNP and DPA shurikens, which are not related by mirror symmetry, possess different EM near field environments. Nanostructure and nanoparticle pairs which are related by mirror symmetry were found to possess near identical EM intensities, which those of matching handedness (LL and RR) possessing the highest EM intensities compared to mismatched (LR and RL) combinations.

5.2.5 Conclusion

Enantiospecific recognition of chiral HNPs is demonstrated through the creation of "cooler" and "hotter" EM hotspots through the coupling of the nanoparticles with DPA nanostructures. While asymmetric changes were not apparent in the far field optical spectra of ORD or reflectivity, SERS – which has its intensity directly dependent on the plasmonic near field environment – is able to discriminate between the resultant diastereomeric combinations of HNP and chiral shuriken nanostructures. The different EM environment strengths were measured through SERS intensities which are resultant from the BPDT molecules used to link HNPs to the DPA surface.

Obtained SERS results indicated that when HNPs and DPA nanostructures were of matching handedness, characteristic BPDT Raman bands were on average twice as high in intensity as opposed to combinations of mismatched handedness. Control experiments in the absence of HNPs or DPA nanostructures were performed, which confirmed that both chiral systems are required for SERS enhancement and differential SERS response. The electric field strengths between all HNP and shuriken combinations were further investigated by simulations, with HNPs situated on 2 separate locations. In both cases, electric field strength was found to be higher in intensity for the matched LL and RR combinations, supporting experimental observations.

These results differ from work where metamaterials have been used to amplify SEROA measurements, as the SERS data collected here was not intrinsically optically active [15]. The advantage in this case of using what can be called metamaterial diastereomers in this study is that

the asymmetric SERS intensity response is two orders of magnitude greater than observed in SEROA.

5.3 Enantiomeric Discrimination of Enantiomers Using Chirally Dependent SERS

While HNPs present a unique approach to discriminating diastereomeric pairs of plasmonic systems, the ability to rapidly distinguish between molecular enantiomers is more relevant in various industries, including drug development, environmental, and food quality monitoring [16-18]. Conventional chiroptical techniques such as CD and ORD are universally used in this regard for the analysis of molecules ranging from small organic compounds to proteins and protein structure [19-22]. However, such methods do not provide detailed information regarding molecular structure. SERS, in addition to being a near field sensitive technique, offers detailed information regarding the molecular structure of the analyte.

The chiroptical counterpart technique to Raman spectroscopy of ROA possesses the same weaknesses as CD and ORD, namely that it is inherently weak; typically three to four magnitudes smaller than a conventional parent Raman spectrum [23]. While SEROA is a useful alternative to boost ROA intensities, it suffers from the weak dependence of the local metal plasmon polarisation on the initial light polarisation [24]. This means that molecules placed on the SEROA platform experience non-circular polarisation from the plasmonic near-field and there is little contribution of chirality from the exciting hotspots.

Indeed, the interpretation of SEROA spectra can be challenging, as the EM field in a SEROA signal is affected by the metal surface in multiple ways, such as in magnitude, polarisation, direction, and spatial dependence [25]. All these factors influence SEROA measurements, making the interpretation and reproducibility of results a complex task. Consequently, there have been fewer experimental studies using SEROA compared to SERS and is why chirally dependent SERS using metamaterials may be an alternative technique.

To enable the differentiation of molecular enantiomers using SERS, a substrate which supports chiral plasmons is required. In this regard, DPAs with their chiral shuriken nanostructures emerge as a suitable candidate. However, DPAs alone do not exhibit sufficiently high SERS EFs essential for measurements. One method to increase EFs is to increase the DPA surface roughness and plasmonic activity with a technique known as sputter coating, or sputter deposition, with silver metal. This technique bombards a solid silver target with energetic ions,

generating a silver vapour which is directed towards the substrate surface [26]. Consequently, a thin silver film layer is formed on the DPA surface. This results in a thin silver film on the DPA substrate, increasing surface roughness and augmenting SERS efficiency.

Through the silver sputter coating process, additional plasmonic hotspots are created on the DPA surface. These fields then couple to the chiral fields generated by the DPA shurikens, which when interacting with further deposited chiral compounds lead to an observed chiral SERS effect. This effect was found to be dependent on the handedness of both the shuriken nanostructure and enantiomer molecule, as well as the Raman excitation laser wavelength chosen. Enantiomers of the amino acids, namely cysteine and methionine, as well as the drug molecule thalidomide were measured using the silver functionalised DPA samples. A larger chiral DNA molecule was measured to demonstrate the versatility of this system.

5.3.1 SERS Optimisation Using Silver

Initial SERS experiments using DPA samples spin-coated with a test molecule Rhodamine 6G (R6G) discovered that DPA samples on their own did not show adequate levels of SERS activity. R6G is a common fluorescent dye molecule with a high Raman cross-section ideal for SERS studies [27]. The problem of R6G fluorescence is avoided by using a 785 nm Raman excitation laser, which does not overlap with the fluorescence excitation peak of 525 nm. To increase SERS activity, a thin layer of silver was sputter-coated onto DPA gold surfaces to increase surface roughness (Figure 5-17). The silver was deposited onto DPA samples using a vacuum sputtering method, using a Direct Current (DC) argon plasma with a gas purity of 99.995%, gas pressure of 4 Pa, and a discharge power of 7.5 W. 4 different sputter times were tested to determine the optimum silver layer thickness, starting from 50 seconds, increasing with increments of 50 seconds up to 200 seconds.

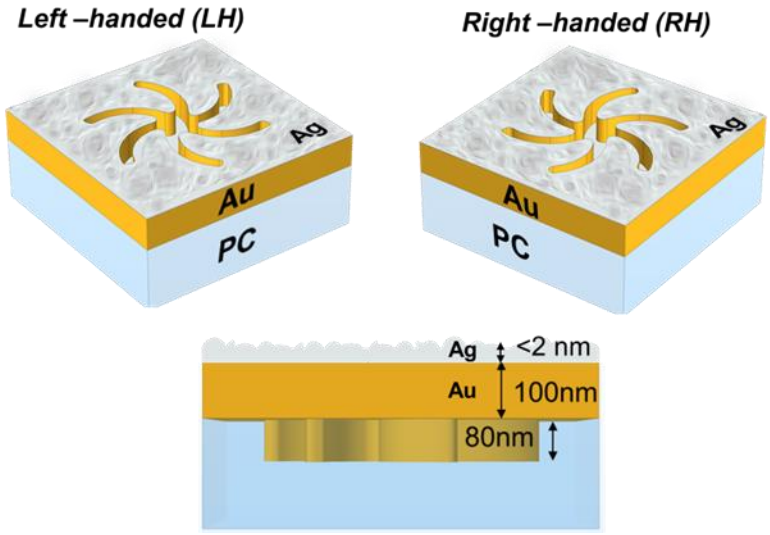

Figure 5-17 Diagram of a gold (Au) LH DPA shuriken nanostructure on its polycarbonate (PC) substrate, sputter coated with a thin layer of silver.

All P1-P6 DPA regions spin-coated with R6G solution were measured using the Raman system described in Section 3.3.6 to investigate which nanostructure geometry exhibited the best SERS EFs (Figure 5-18). Different silver sputter coating times led to silver film thicknesses ranging from $0.5 - 1.8$ nm (Figure 5-18B).

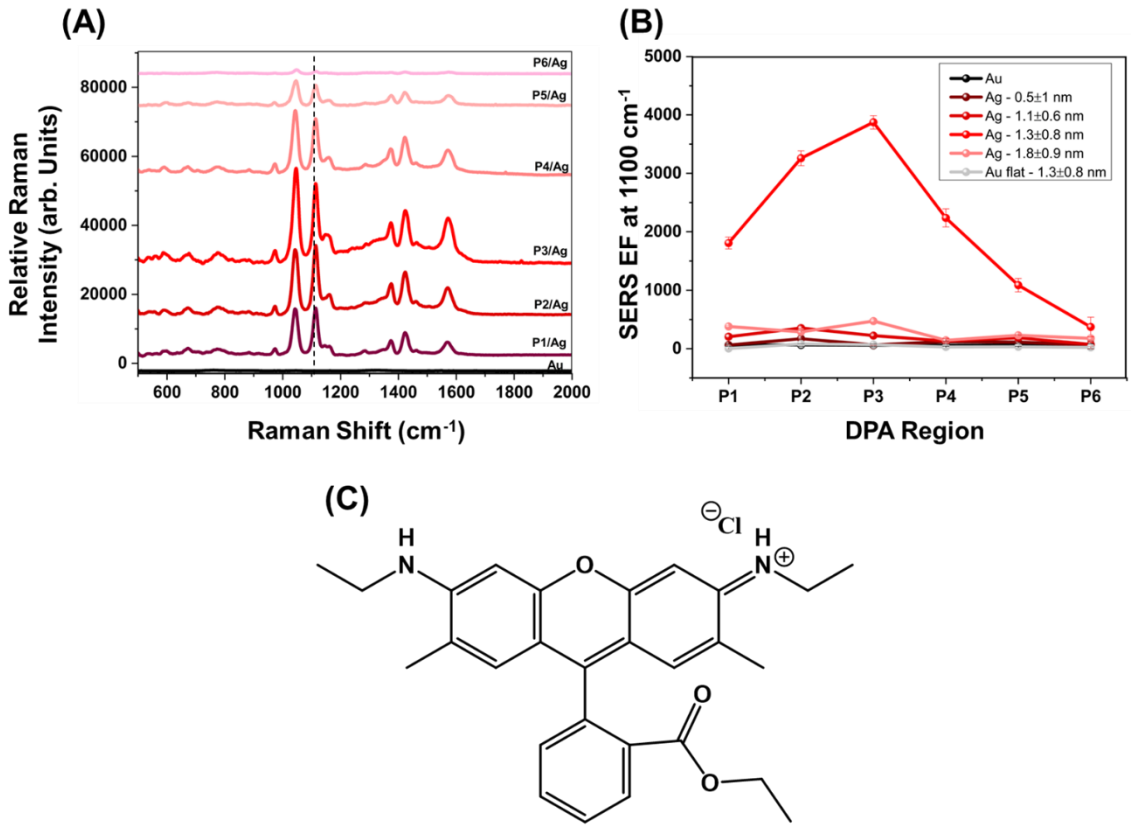

Figure 5-18 (A) Stacked SERS spectra of R6G measured at 785 nm excitation wavelength on RH silver-coated DPA structures from P1-P6 regions, as well as on flat gold. Dashed line shows R6G characteristic Raman band at 1114 cm^{-1}. (B) Dependence of SERS enhancement factor (EF) on P1-P6 region shuriken geometry (and flat gold) and effective silver thickness. (C) Chemical structure of R6G.

The SERS spectra of R6G displays a characteristic Raman band at 1114 cm^{-1}, associated with the C-C stretching vibration (Figure 5-18A) [28]. Using the different intensities of this band, the EF was calculated for all DPA sample regions P1-P6 with different silver layer thicknesses (Figure 5-18B). EF is calculated as the ratio of the intensity of the Raman signal in the presence of the resonator, in this case the DPA nanostructures, to the power of the signal in its absence [29].

From Figure 5-18B, the optimal silver layer thickness for SERS enhancement was found to be 1.3 ± 0.8 nm and was thus chosen as the optimal thickness for further experiments. Any additional deposition was detrimental to SERS activity due to the merging of silver nanoparticle clusters to a more uniform layer. There is evidence that silver layers this thin can be approximated as surface bound nanoparticles which possess their own plasmonic dipoles and therefore aid in enhancing SERS activity [30].

At the optimal 1.3 nm silver coating thickness, P5 and P6 regions displayed the lowest EFs below 1200. P2 and P4 had moderate EFs at 2247 and 3250, respectively. P3 displayed the highest EF at 3852 and was chosen as the platform for continuing SERS experiments. The discovered correlations among various EFs offer evidence supporting the existence of plasmon coupling between shurikens and silver nanoparticle clusters. Additionally, the observed variations in SERS efficiency due to the subtle differences in shuriken nanostructure geometry suggest that the plasmonic coupling might possess resonant characteristics.

The increase in surface roughness as a result of silver sputter coating was confirmed using Atomic Force Microscopy (AFM). AFM is used to examine the surface topography of materials and is an excellent technique for measuring nanoscale parameters such as surface depth and roughness (Figure 5-19 and Figure 5-20) [31].

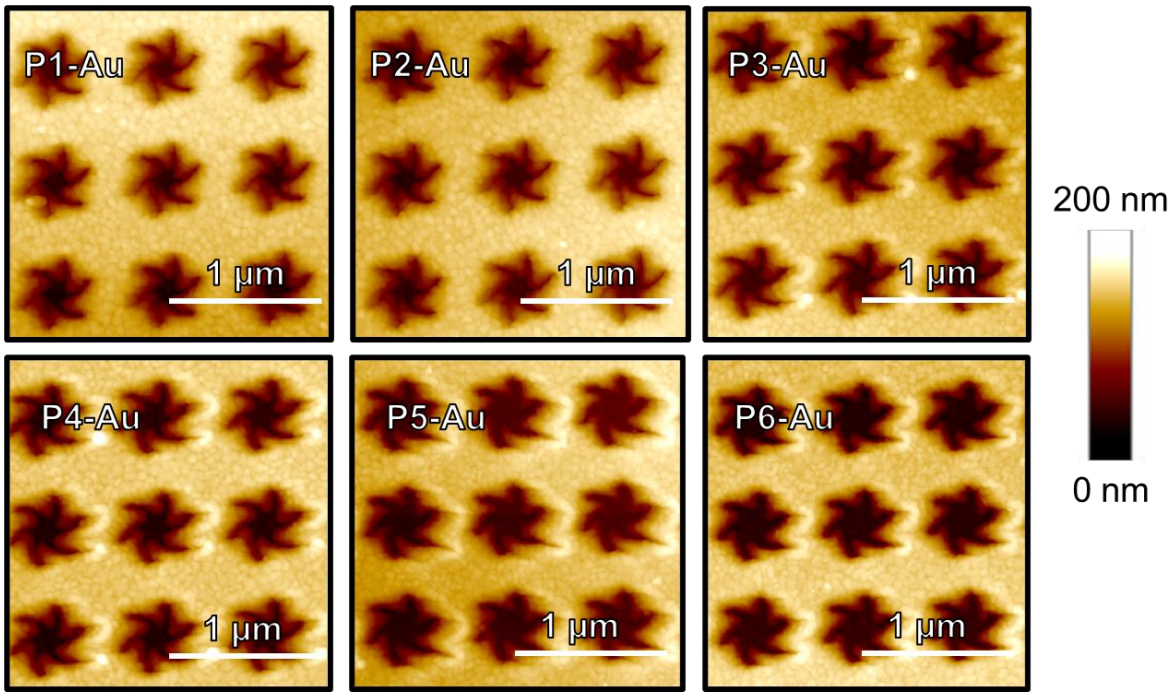

Figure 5-19 AFM images of pristine LH DPA sample regions P1-P6 before silver sputter coating. Legend shows height of DPA sample surface.

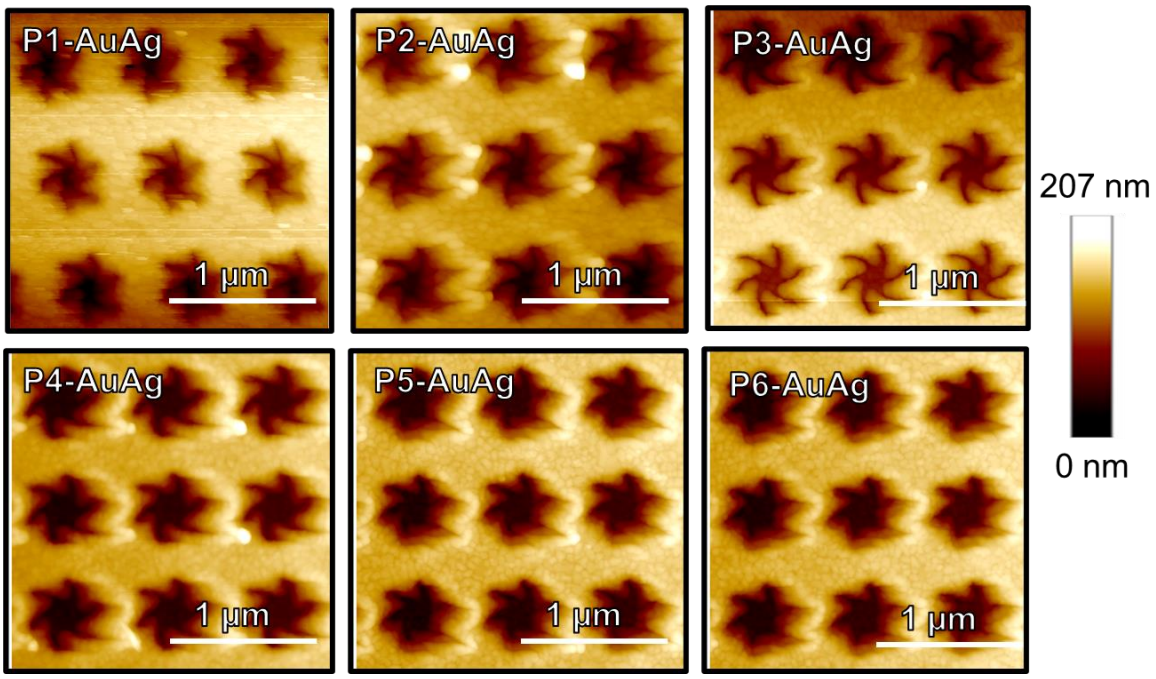

Figure 5-20 AFM images of pristine DPA sample regions P1-P6 after silver sputter coating. Legend shows height of silver coated DPA sample surface.

AFM imaging reveals that the general shuriken geometries remain unchanged following silver sputter coating. However, the silver-coated samples do exhibit noticeable bright spots, indicating an increase in height variation and minor surface inhomogeneities. These observations are typical when applying thin layers of silver, where slight variations are expected. To assess the level of surface change before and after silver coating, AFM measurements were performed on the inside cavity of a P3 region LH shuriken nanostructure before and after 1.3 nm silver deposition (Figure 5-21).

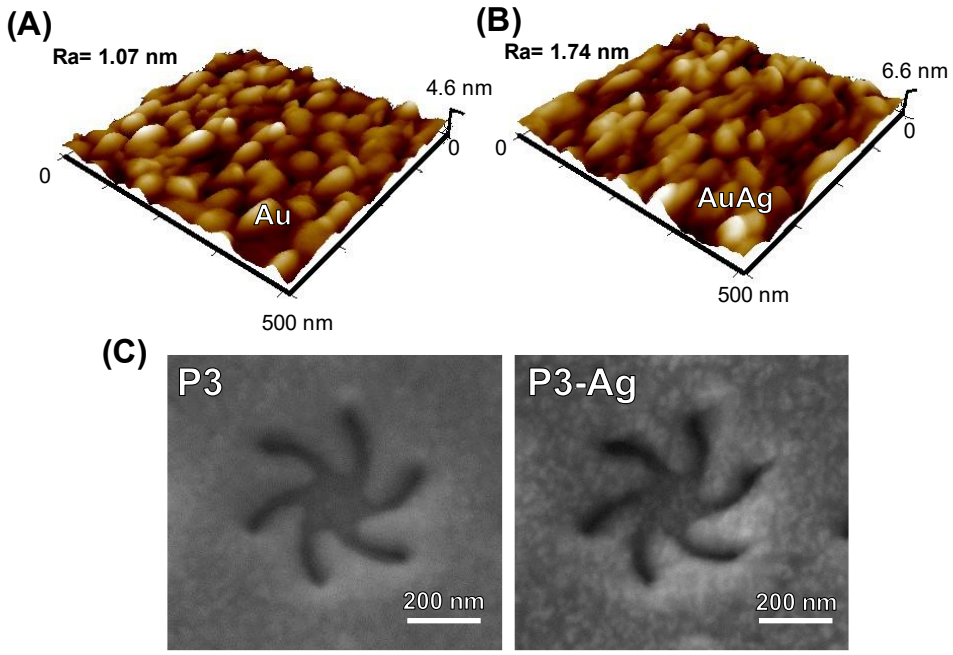

Figure 5-21 AFM images from P3 LH shuriken cavity before (A) and after (B) silver sputter coating, with corresponding SEM images shown (C).

The surface roughness was measured in units of "Ra", which stands for "arithmetic average roughness". This is a common parameter of surface roughness which quantifies the mean deviation of a surface profile from its mean line over a sample length [32]. The mean Ra, and therefore surface roughness, was found to increase from 1.07 to 1.74 nm following silver coating, a significant 67.3% increase. The reason behind P3 exhibiting the highest SERS enhancement factor is not easily determined. However, it is possible that the optical properties of the silver-coated samples can provide insight to this phenomenon.

5.3.2 Optical Properties of Silver Coated DPA Samples

The optical properties of the DPA samples will naturally change with the addition of a silver layer. The change in resonance is important to follow as the choice of laser frequency is often significant in Raman spectroscopy and SERS. The chosen laser wavelength impacts several features such as Raman scattering intensity, levels of background fluorescence, and acquisition times [33]. The most common laser wavelength for Raman spectroscopy is 785 nm due to its ability to provide relatively low background fluorescence and good Raman scattering intensity [33, 34]. Other common laser wavelengths include 532, 633, and 830 nm.

The ORD and reflectivity spectra of silver coated DPA samples were measured from all regions P1-P6 following silver coating. As P3 regions showed the highest SERS EFs, only the ORD and reflectivity for the P3 DPA region is shown below in Figure 5-22. The changes in reflectivity spectra for P1, P2, P4, P5, and P6 region DPA structures following silver deposition were small, with the corresponding spectra available in Appendix B.2.

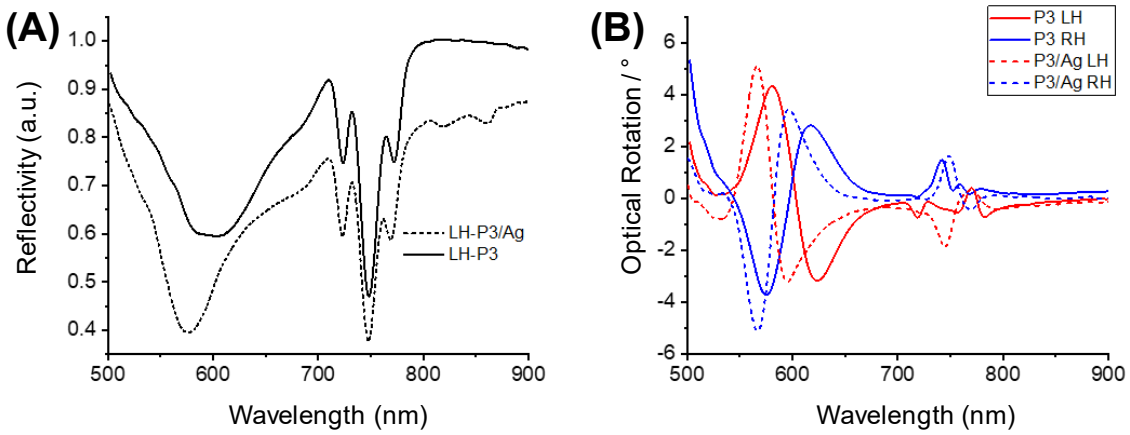

Figure 5-22 Reflectivity (A) and ORD (B) spectra from pristine (solid lines) and silver sputter-coated (dashed lines) P3 DPA samples. E LH (red) and RH (blue) locations measured.

Comparing ORD and reflectivity spectra before and after silver deposition for the P3 region indicates small red shifts in the resonances located in the 700-800 nm range. Slight broadening in the reflectivity spectrum is also observed, accompanied by a decrease in reflectivity, corresponding to higher absorption. An interesting observation is that the strongest resonance region at the 550-650 nm region experiences a significant blue shift upon silver coating. Similar to the blue-shift observed in the ORD spectra of HNP functionalised DPA samples in Section 5.2.2, this can arise through the plasmonic hybridisation of the two plasmonic systems [12]. Furthermore, silver sputter coating led to a significant increase in absorption in the reflectivity spectrum. This effect was greater than for any other DPA region. Higher absorption indicates stronger resonance conditions, which could lead to the higher SERS EFs shown by P3 structures.

The changes in both resonance positions and increase in absorption as a result of silver coating are the most likely explanations as to why P3 showed the highest SERS EFs at 785 nm excitation with R6G as a test molecule. By plotting the common Raman laser excitation wavelengths along

with the ORD and reflectivity spectra of the silver coated P3 DPA sample, the proximity of the different lasers to the resonance mode positions can be seen (Figure 5-23).

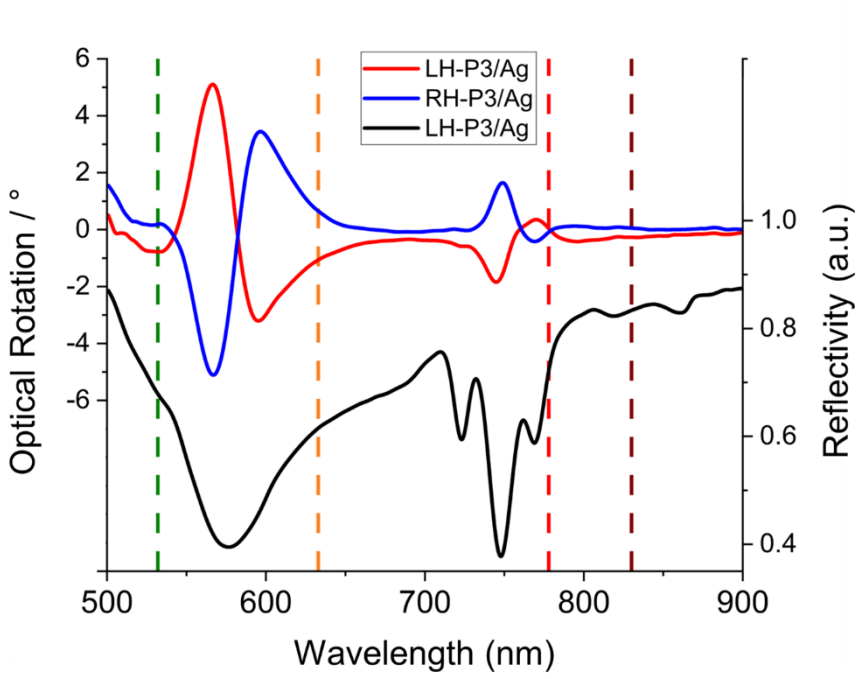

Figure 5-23 Reflectivity (black) and ORD spectra from LH (red) and RH blue) silver coated P3 DPA nanostructures, with common Raman laser wavelengths shown with dashed lines.

The most common laser excitation wavelength of 785 nm is close to the right-most reflectivity resonance mode and passes through a region of minor optical activity in the ORD spectra. It should be noted that upon the deposition of R6G (or any other analyte), the resonances are expected to further red shift by some nanometres and would thus be more in line with the excitation laser than shown here, leading to higher SERS enhancement. The higher laser wavelength of 830 nm is not in a region of absorption or optical activity, and therefore is not expected to exhibit significant SERS response. Towards the lower laser excitation wavelengths, 532 nm is at a region with moderate absorption and weak optical activity, though it should be stated that ORD measurements at such low wavelengths may be unreliable due to the lower sensitivity of the spectrometer. The 633 nm excitation wavelength lies in a region of both moderate absorption and optical activity, from which SERS response is expected.

Based on these observations, the best SERS responses are predicted to arise from the 785 and 633 nm lasers, as these wavelengths lie closest to the resonance positions. Furthermore, for

enantiomeric discrimination of molecules using SERS, excitation wavelengths should generate chiral EM fields, which are present, but not strongest, at 785 and 633 nm. Ideally, lasers with wavelengths at or closer to the exact resonance positions would be available, as at these energies the absorption of light as well as optical activity is the highest. However, acquiring lasers of such different wavelengths is unfeasible for the Raman systems used in this work due to lack of availability. With this information, the 785 nm Raman laser was chosen for the bulk of the enantiomer discrimination experiments as it is the most common laser used and near the resonance positions. However, the other 3 laser wavelengths were also trialled, with results presented later in Section 5.3.4.

5.3.3 Results and Discussion - L/D-Cysteine Enantiomer Discrimination

Following DPA modification for optimum SERS enhancement, the silver coated DPA samples were spin-coated with varying concentrations of L- or D-cysteine in methanol solutions to investigate SERS responses between LH and RH shurikens. The spin coating parameters were chosen such that a thin-film homogeneous and amorphous layer of cysteine would form on the DPA surface. To evaluate the homogeneity of the cysteine on the DPA surface, a technique known as Energy Dispersive X-ray (EDX) mapping was performed. EDX is a useful tool employed for elemental analysis. It operates by directing an incident electron beam onto a sample, inducing X-ray emission. The X-ray photons possess quantised energy levels that are characteristic to the electron orbital transitions occurring within the elements [35]. By measuring the energies of the emitted X-rays, the precise elemental composition of the sample can be determined. EDX mapping images, with reference SEM images, show the elemental distribution of sulphur in the colour of green (Figure 5-24). From these images, the homogeneous coverage of sulphur, and therefore cysteine, is observed.

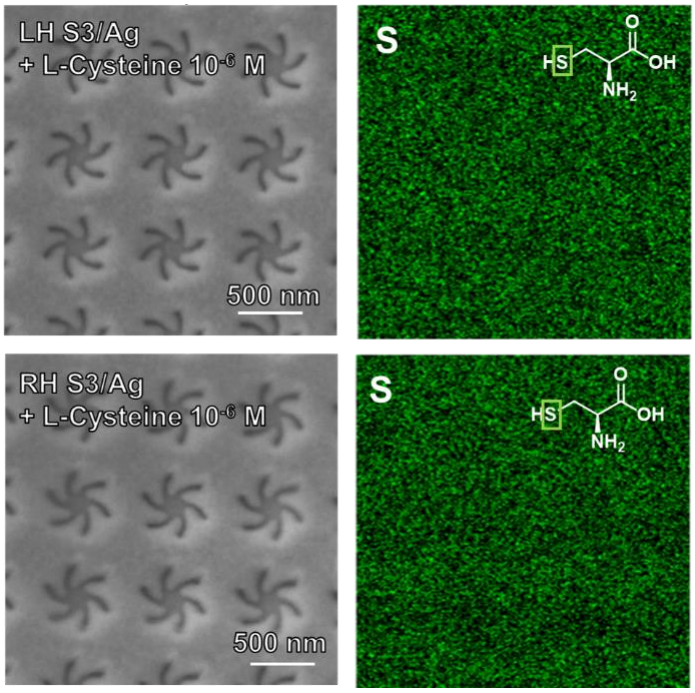

Figure 5-24 SEM images (left) of LH and RH P3/Ag DPA nanostructures taken after cysteine spin-coating (10^{-6} M concentration), with corresponding EDX maps (right) taken to image sulphur atom distribution.

Another technique to confirm the amorphous character of the cysteine layer is X-Ray Diffraction (XRD). Having an amorphous layer over a crystalline layer is important as crystalline structures are anisotropic and heterogenous in character. Crystalline structures possess a periodic arrangement of atoms, from which characteristic X-ray diffraction patterns can be obtained, providing information about atomic arrangements [36] [37]. By measuring XRD from the deposited cysteine layer on the DPA samples, it is possible to ascertain whether the cysteine is crystalline or amorphous in nature by the presence of XRD peaks Figure 5-25.

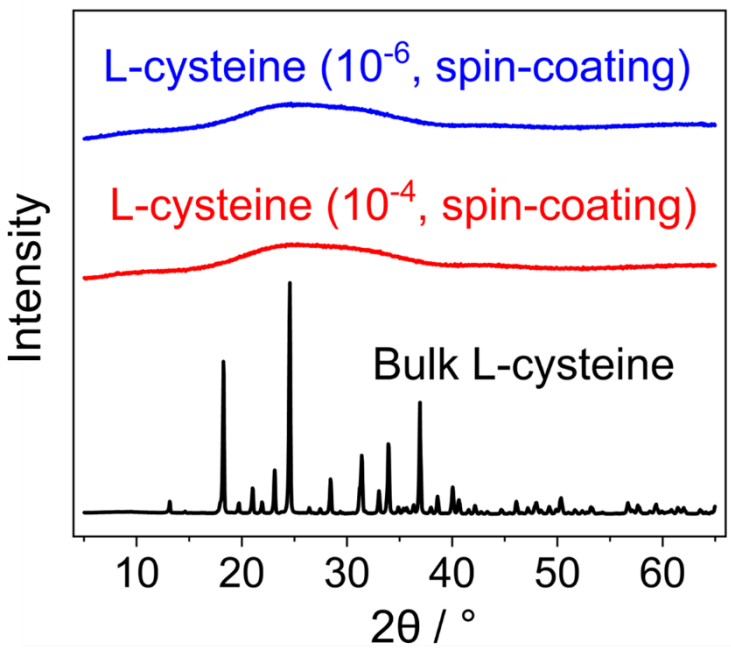

Figure 5-25 XRD patterns of spin coated L-cysteine layer on DPA sample for 10^{-6} (blue) and 10^{-4} (red) M concentrations, with reference bulk crystalline L-cysteine (black) shown as reference.

The x-axis of the XRD pattern is measured with what is known as Bragg angle (2θ), which represents the scattering angle of the X-rays interacting with the sample, measured in degrees [38]. XRD measurements of bulk cysteine confirm its crystalline nature as there is an abundance of diffraction peaks. Conversely, XRD from cysteine spin coated DPA samples show no cysteine-related diffraction peaks, confirming the amorphous character and the lack of any polycrystalline structure.

Following the characterisation of the silver sputter coated and cysteine spin coated DPA samples, Raman measurements were performed. Raman measurements were taken as described in Section 3.3.6 using 785 nm laser excitation, with 10 random points analysed on each LH or RH DPA shuriken array. The mean SERS spectra results from L- and D-cysteine enantiomer measurements is presented in Figure 5-26A.

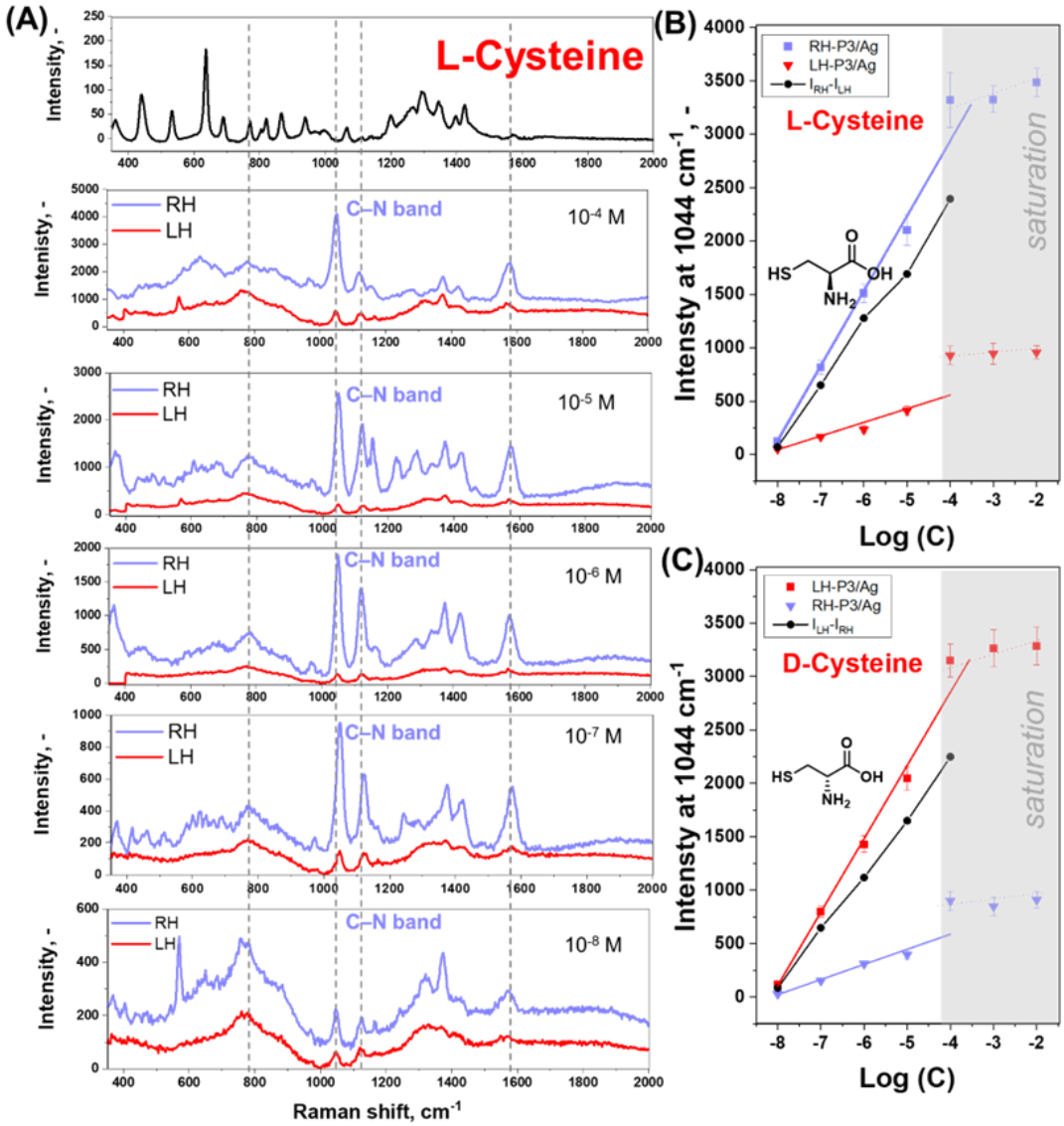

Figure 5-26 (A) Stacked SERS spectra of L-cysteine enantiomer deposited on LH- or RH P3/Ag substrates from methanol solutions with various initial concentrations ($10^{-4} – 10^{-8}$ M range) measured at 785 nm excitation wavelength; (B) and (C) the characteristic L-cysteine and D-cysteine SERS band (1044 cm^{-1}) intensity as a function of the initial enantiomer concentrations and LH (red) or RH (blue) shuriken substrate.

Cysteine SERS intensity was found to largely depend upon the enantiomer conformation and shuriken nanostructure handedness. SERS bands were noticeably higher in intensities for L-cysteine on RH shurikens in comparison to D-cysteine. Conversely, the opposite effect was observed with D-cysteine, which displayed higher SERS intensities on LH shurikens. This differential SERS effect was observed for cysteine concentrations ranging from 10^{-4} to 10^{-8} M. Higher concentrations of cysteine lead to the saturation of SERS intensities. Figure 5-26 B-C plots the intensity of the characteristic cysteine Raman band at 1044 cm^{-1} as a function of the enantiomer concentrations and LH and RH shuriken handedness: showing this trend clearly. For cysteine concentration higher than 10^{-4} M SERS signal intensities became saturated and no further increases were apparent. These findings show that the coupling of DPA shurikens with a SERS active silver thin film can be applied for the enantiomeric discrimination of small molecules up to nanomolar (10^{-8} M) concentration scales with a common Raman spectrometer.

The homogeneity of SERS signals from silver and cysteine coated DPA samples was further investigated using Raman mapping measurements by comparing 1044 cm^{-1} band intensities across the DPA sample (Figure 5-27A). For the mapping measurement, an area of 0.85×0.45 mm^2 was scanned, and the characteristic Raman band intensity interpolated using the Clough-Tocher method. This interpolation method is a numerical technique which approximates values at points in a grid based off known values at scattered data points [39]. This method is a variant of the FEM, introduced in Section 2.8.

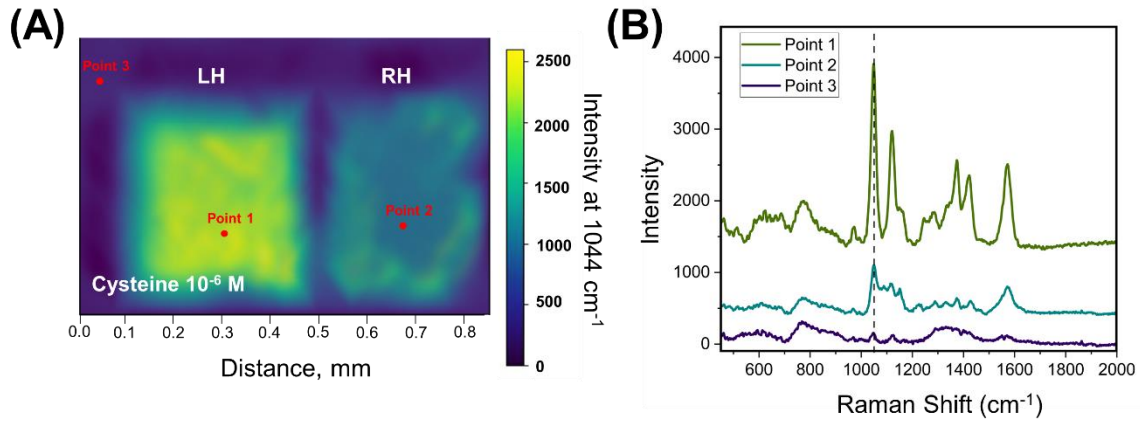

Figure 5-27 (A) SERS map of D-cysteine (10^{-5} M) on RH- and LH P3/Ag structures measured at 785 nm excitation wavelength; (B) stacked SERS spectra from measurement points 1-3 designated on (A).

Figure 5-27 shows the results of the SERS mapping measurement across a DPA sample sputter coated with silver and spin-coated with D-cysteine, with colour intensity related to the Raman intensity of the cysteine characteristic 1044 cm^{-1} band. The SERS map clearly shows that LH shuriken (Point 1) nanostructures possess overall higher signal intensities when compared to their RH counterparts (Point 2). Additionally, it was observed that on flat gold and silver surfaces surrounding the square LH and RH nanostructure arrays (Point 3) there is very little SERS signal, which is expected due to the lack of plasmonic activity and EM enhancement.

5.3.4 Impact of SERS Excitation Wavelength

To assess the influence of Raman laser excitation wavelength position on the chirally dependent SERS phenomenon with DPA substrates, L-cysteine coated samples measured in the previous section under 785 nm laser excitation were also measured in a similar fashion with 532, 633, and 830 nm lasers, with their associated laser powers and accumulation times outlined in Section 3.4.5. The corresponding SERS spectra results for each laser wavelength are presented in Figure 5-29. For reference, the ORD and reflectivity spectra of silver coated P3 DPA samples with laser wavelengths is repeated here for ease of results interpretation (Figure 5-28).

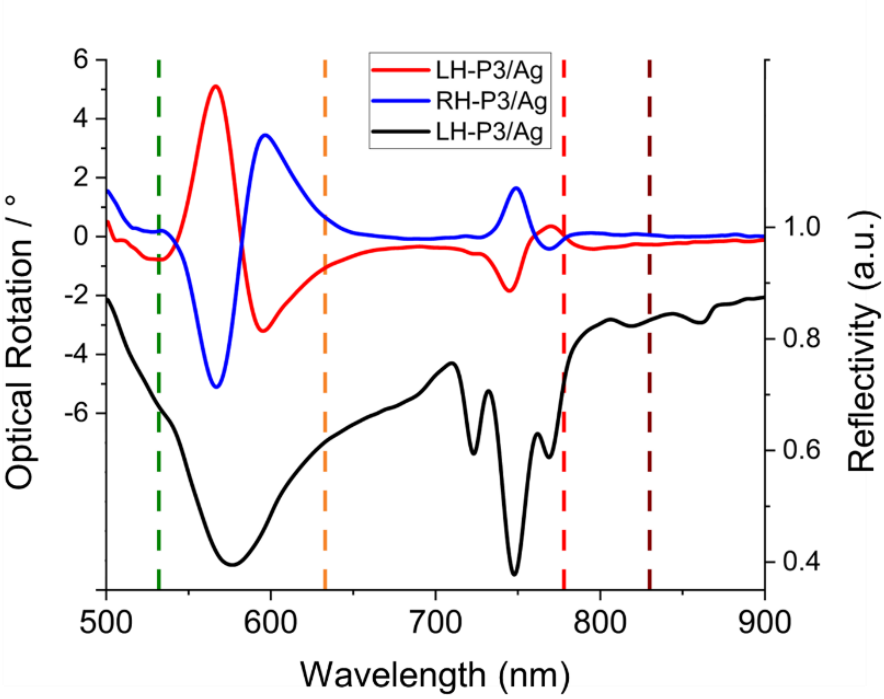

Figure 5-28 Reflectivity (black) and ORD spectra from LH (red) and RH (blue) silver coated P3 DPA nanostructures, with common Raman laser wavelengths shown with dashed lines.

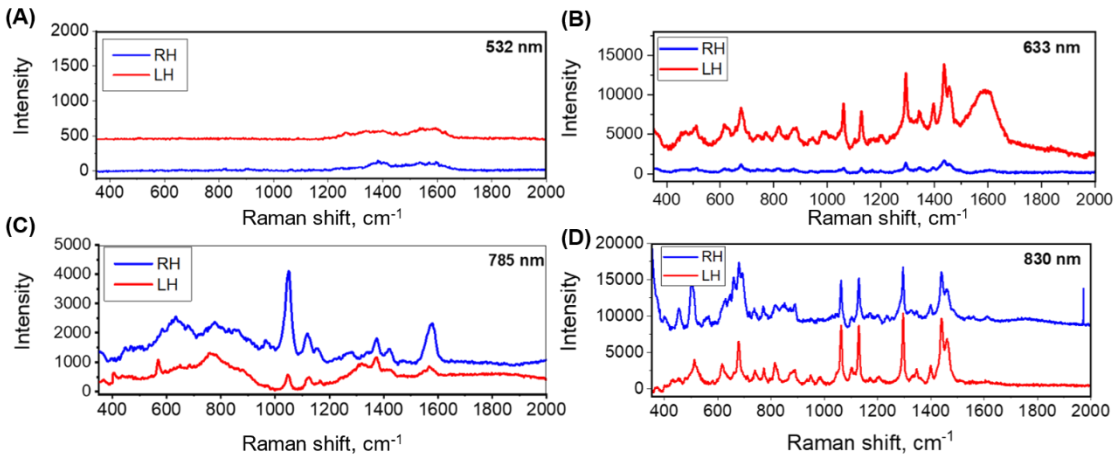

Figure 5-29 Stacked SERS spectra of 10^{-4} M L-cysteine deposited on LH and RH silver coated P3 DPA structures measured with (A) - 532 nm, (B) - 633 nm, (C) – 785 nm, and (D) – 830 nm excitation wavelengths.

Under 532 nm laser excitation, there are no discernible cysteine Raman bands observed from either LH or RH regions. This result is not unexpected, as this wavelength is not near any resonance modes visible in the ORD/reflectivity spectra. As there is little to no plasmonic activity, SERS enhancement is minimal. Under 633 nm laser excitation, the laser wavelength is closer to the broad reflectivity resonance and in a region of moderate optical activity shown by the ORD spectra. As such, Raman bands become apparent, and are much stronger when measured from LH nanostructures. The SERS results obtained from 785 nm excitation have already been discussed. However, what is interesting to see is that the chiral response is flipped compared to the results obtained with the 633 nm laser. This is consistent with the ORD spectral response, where the signs of the respective ORD spectra also flip. These results demonstrate a clear connection between enantiomeric selectivity and excitation wavelength, as the choice of excitation wavelength leads to a selective chiral SERS response due to the inversion of chiral response at different wavelengths. This effect highlights the possibility of achieving tailored SERS responses through the selection of the excitation wavelength in chiral systems. Under 830 nm excitation shows cysteine Raman bands obtained from both LH and RH DPA regions. However, there are no significant differences between the intensities of the two spectra, which is expected considering 830 nm is not in a region of optical activity.

5.3.5 Enantiomeric Discrimination of Other Molecules

To demonstrate the versatility of DPA samples as SERS substrates with enantiomeric discrimination capabilities, additional experiments were conducted using other small compounds: the amino-acid methionine and the drug molecule thalidomide. Following the spin-coating procedure to that of cysteine, 10^{-4} M concentrations of both molecule enantiomers were

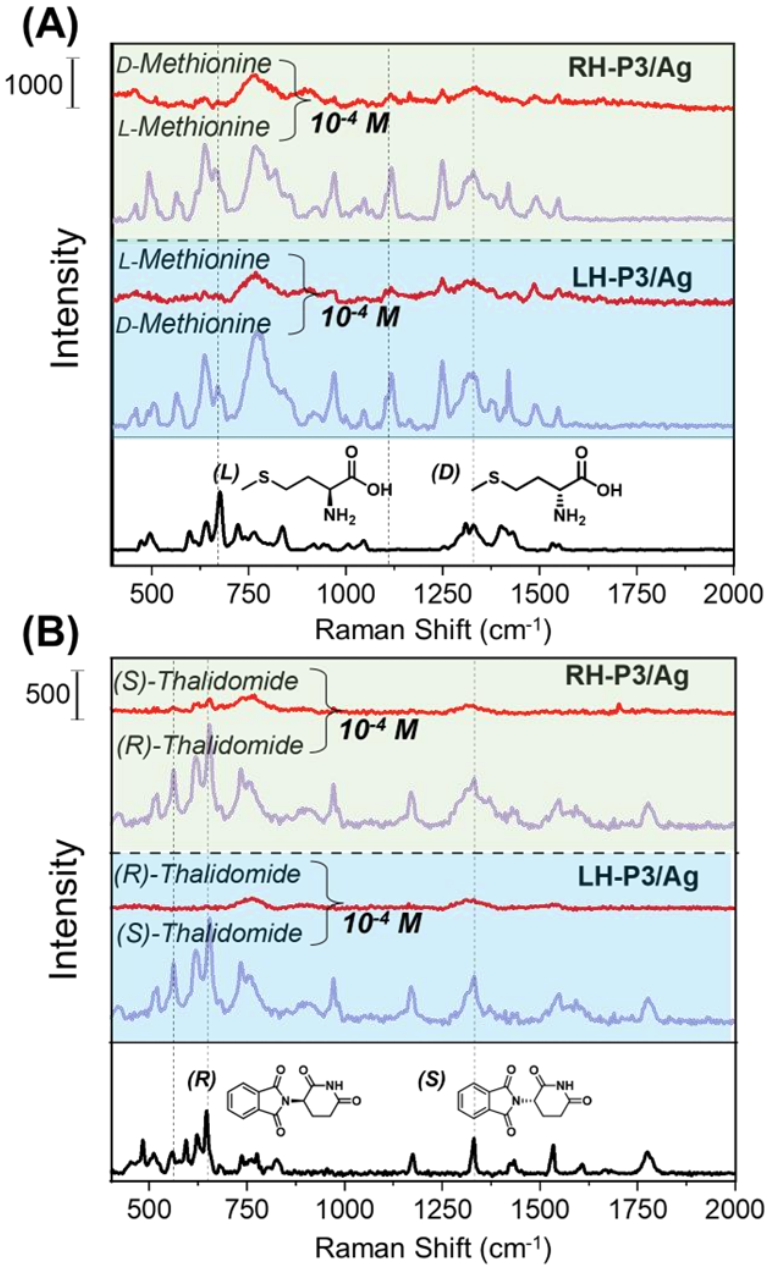

Figure 5-30 Stacked SERS spectra of 10^{-4} M L/D enantiomer solutions of (A) methionine and (B) thalidomide measured from LH and RH P3/Ag samples using 785 nm laser excitation. Bottom (black) spectra show Raman spectra of bulk compounds.

spin coated onto separate silver coated DPA P3 samples, and SERS spectra were collected using 785 nm laser excitation (Figure 5-30).

From Figure 5-30A, SERS intensity of L-methionine on P3 silver coated nanostructures was found to be significantly higher on RH structures compared to LH. This trend was expectedly reversed when measuring D-methionine, which produced higher SERS intensity on LH nanostructures. The same effect was observed in Figure 5-30B for the drug molecule of thalidomide, of which the R-enantiomer which produced higher SERS intensities on RH structures and the S-enantiomer produced higher SERS intensities on LH structures. These results demonstrate that DPA substrates can be utilised for the rapid discrimination of several different molecules and their associated enantiomers.

In addition to small chiral compounds, the applicability of the silver sputter coated DPA samples was also tested with larger biomolecules, namely DNA. The renowned double helix structure of DNA possesses a natural right-handed rotation due to the specific arrangement of nucleotide base pairs (bp), and is therefore chiral [40]. A 20 bp DNA molecules were synthesised by mixing 1 ml of oligonucleotide (5'-CGCCAATACGACCAAATCCG-3') at a concentration of 5×10^{-9} M with 1 ml of annealing buffer (10 mM Tris, pH 7.5, 50 mM NaCl, 1 mM EDTA) and 1 ml of complimentary oligonucleotide (5'-GCGGTTATGCTGGTTTAGGC -3') at a concentration of 5×10^{-9} M. The resulting solution was heated to 90 °C for 2 minutes, and gradually cooled to

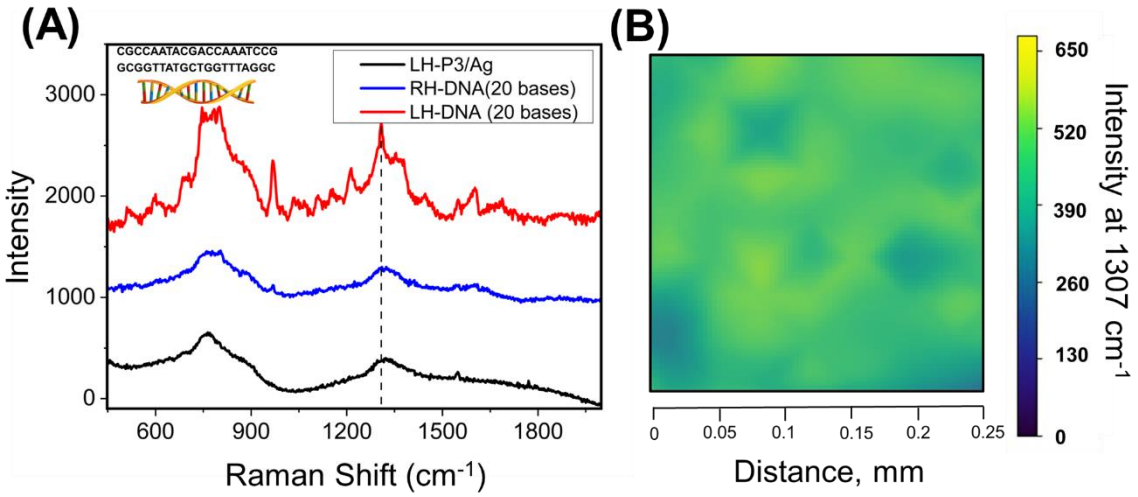

Figure 5-31 (A) Stacked SERS spectra of 20 bp DNA recorded on RH (blue) and LH (red) P3/Ag DPA substrates using 785 nm laser excitation. Bottom (black) spectrum shows a background measurement from a Pristine LH P3/Ag DPA substrate with no DNA. (B) SERS mapping measurement of 20 bp DNA on LH P3/Ag DPA substrates.

25 °C at a rate of 1.5 °C per minute. From the resulting DNA solution, 100 µl was drop-deposited onto a silver coated P3 DPA surface and left in a refrigerator (4 °C) until dry. Raman spectra of the sample were then recorded using 785 nm laser excitation with 40 mW power and accumulation time of 200 seconds. Raman mapping measurements were scanned on an area of 0.25×0.25 mm^2. The SERS results of DNA experiments are presented in Figure 5-31.

Figure 5-31A shows the SERS spectra recorded from LH (red) and RH (blue) silver coated P3 DPA nanostructures. Raman band intensities are significantly higher on LH nanostructures as opposed to RH nanostructures, which shows only extremely weak Raman bands. The strong characteristic peak at 1307 cm^{-1} (Figure 5-31B dashed line) is assigned to deoxyguanosine and deoxyadenosine (dG and dA) heterocycle ring stretching frequencies [41, 42]. The Raman mapping measurement based on the intensity of the 1307 cm^{-1} in Figure 5-31B shows the relatively even coverage of DNA across an area on the LH P3 nanostructures. These results demonstrate that, in addition to small molecules, chiral discrimination can be performed using silver coated DPA substrates on chiral molecules as large as 20 bp length DNA.

5.3.6 EM Simulations

EM simulations were performed to better understand the behaviour and interactions between chiral fields generated by the DPA shurikens and the deposited silver nanocluster layer. Initial simulations investigated and compared the reflectivity/transmission, optical chirality values, and electric field strengths of two different plasmonic structures in air: a LH shuriken DPA metafilm, and a dimer of nanorods. The LH shuriken simulation was constructed using P3 shuriken nanostructure dimensions across a wavelength range of $500 - 898$ nm in steps of 6 nm, as described in Section 3.4.

As a reminder, the optical chirality parameter *C* measures the degree of chiral asymmetry, and the time-independent form can be calculated as [43]:

$$C = \frac{\varepsilon_0 \omega}{2} Im(E^* \cdot B) \tag{5.6.1}$$

Where ε_0 is the vacuum permittivity, ω is the angular frequency of light, and E^* and B are the imaginary components of the complex electric and magnetic field amplitudes, respectively. Obtained *C* values are then normalised against *C* values for RH CPL propagating in air at the same wavelength. This normalisation process is important to reduce the effects from different meshing elements across different simulations, allowing for the accurate comparison of results. The resultant reflectivity plots obtained from the shuriken and nanorod dimer simulations are presented in Figure 5-32. In addition to reflectivity, optical chirality, *C*, and electric field plots taken from the surface of the shuriken metafilm and an x-y plane passing through the centre of the nanorod dimer are also shown. through the highest intensity of near fields are also shown.

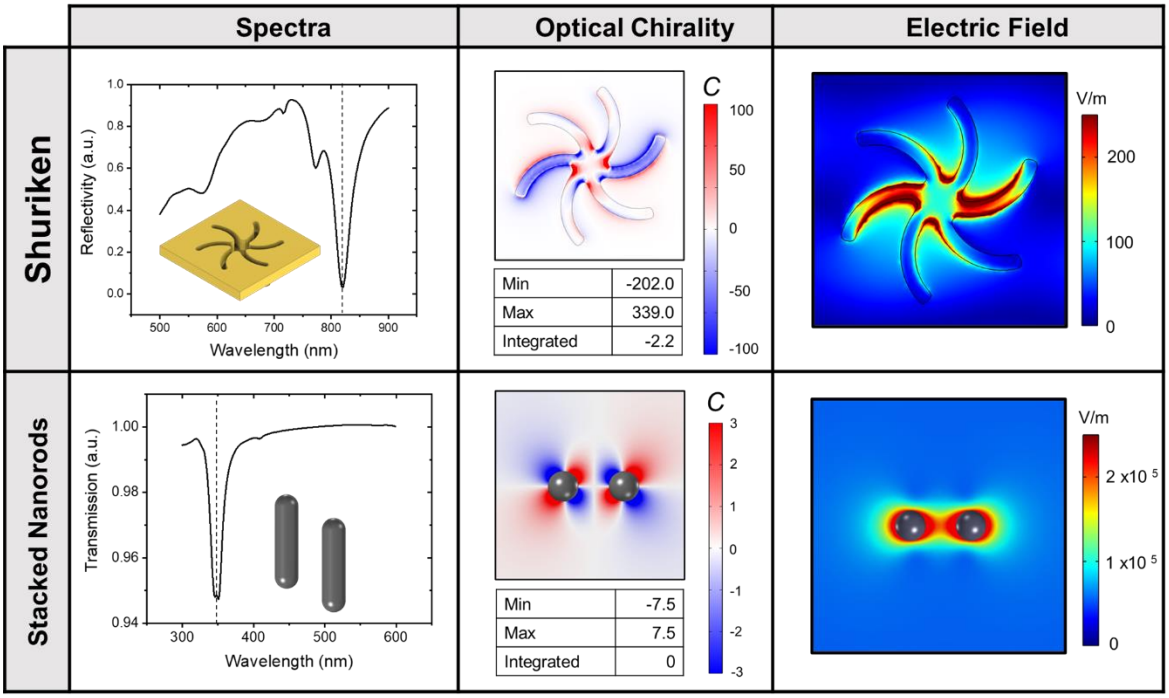

Figure 5-32 Comparison of simulated LH shurikens (Top) and nanorods (Bottom) generating chiral fields at their peak resonance. For each structure, the optical chirality parameter, C, and electric field (V/m) plots are shown on Integrated C values are presented in their respective tables below the optical chirality plots.

The simulated reflectivity plot for the shuriken metafilm shows a strong resonance around 820 nm, with an adjacent weaker mode at 770 nm. The difference in resonance position compared to experimental reflectivity spectra can be attributed to the idealised geometry of the constructed simulated model, which does not possess rounded and smoothed edges which arise during the nanofabrication processes. The simulated transmission plot for the nanorod dimer shows a single resonance mode around 350 nm. Only one resonance mode is present due to the simple geometry of the nanorods.

By investigating the optical chirality, *C*, parameters at each respective simulation resonance wavelength, the significance of structural symmetry with regards to the generation of chiral EM fields can be demonstrated. Comparing the shuriken metafilm to the nanorod dimer, the former is found to exhibit regions with *C* values approximately two orders of magnitude larger than the latter. Additionally, when analysing the integrated *C* values across the simulated shuriken surface, an overall net negative value of -2.2 is observed. In contrast, while the achiral nanorods do produce EM regions with non-zero C values, the magnitude is significantly smaller compared

to the chiral structures. Moreover, due to the quadrupolar symmetry of the oscillating fields between the nanorods, the integrated *C* values sum up to a net zero value. These findings indicate that shuriken metafilms generate EM fields with far greater chiral asymmetry than achiral counterparts. They also highlight the role of structural asymmetry in nanostructures to create plasmonic regions with an overall net chiral fields effect.

The next stage of simulations was to add silver nanoclusters onto the shuriken unit cell surface to simulate the silver sputter coating process and to investigate the EM properties instilled by the shuriken onto the silver. Continuing with the consideration that the thin film of sputter coated silver can be approximated as a collection of nanoparticles or nanoclusters [30], a total of 8 hemispherical silver nanoparticles were introduced onto the gold shuriken surface to simulate the effect of chiral near fields on a thin sputter coated silver layer (Figure 5-33A). The electric field intensity at the plasmon resonance wavelength was visualised from a cut plane 5 nm above the gold surface, cutting through approximately half of the silver nanoparticles which were simulated at 10 nm height (Figure 5-33B).

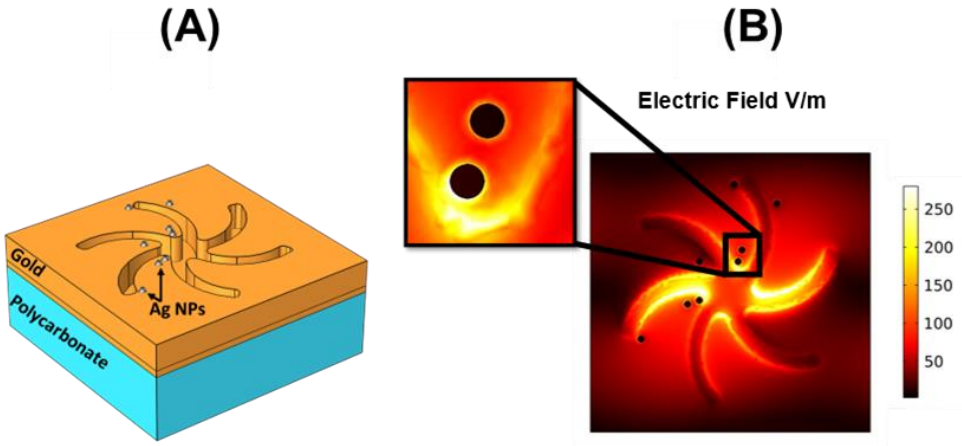

Figure 5-33 (A) Simulation schematic of 8 added silver nanoparticles on the shuriken surface. (B) Electric field plot of shuriken at 824 nm mode, from a cut plane 5 nm above the shuriken surface. Inset shows two silver nanoparticles affected by strong electric fields near shuriken centre and arms.

The electric field intensity plot shows that at this resonance position, the two horizontal shuriken arms possess regions with the strongest plasmonic activity, and thus the highest electric field intensities. Figure 5-33B also shows how silver nanoclusters, or in this case nanoparticles,

resonate on their own, evident by the elevated electric field values surrounding them. However, the important conclusion of this simulation is that the silver nanoparticles couple to the field generated by the shuriken when close to the strongest resonating regions. This means that as the EM fields generated by the shuriken are chiral in nature, shown earlier in Figure 5-32, the resultant coupled field between silver nanoparticle and gold shuriken is chiral in nature as well.

To visualise the influence of chiral fields on the simulated silver nanoparticles**,** the normalised optical chirality parameter, *C*, was calculated at two opposite points for 3 of the simulated nanoparticles within the resonating regions. These 3 nanoparticles were labelled Point 1, 2, and 3 **(**Figure 5-34 and Table 5-4).

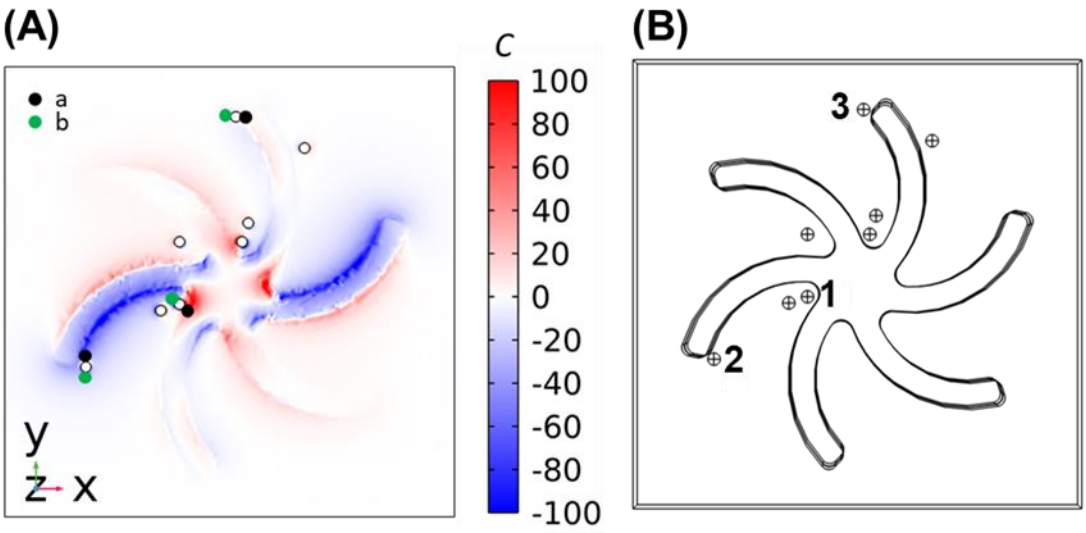

Figure 5-34 (A) Optical chirality parameter, C, values calculated at the surface of shuriken nanostructure ($z = 105$ nm). Black/green regions represent locations from which C values taken for Table 5-4. (B) Outline of shuriken and silver nanoparticle locations, with Points 1, 2, and 3 highlighted.

	Optical Chirality Parameter, C		Net Value, C
Point	**a**	**b**	**(a+b)**
1	79.0	-23.5	55.5
2	-30.4	-15.9	-46.3
3	4.75	-4.23	0.5

Table 5-4 Normalised C values from points a and b on opposite sides of simulated silver nanoparticles. a and b regions selected such that they are parallel to resonating directions.

The *C* values were measured from opposite ends of Points 1, 2, and 3, with the region placed alignment parallel to the direction of shuriken arm alignment. This procedure was performed to assess the symmetry of the chiral fields surrounding the nanoparticles. The silver nanoparticle at Point 1 is close in proximity to the shuriken resonating field and is therefore strongly influenced by both LH (red) and RH (blue) EM fields. This results in large values of *C* surrounding the nanoparticle, with the overall net *C* value being positive, suggesting that the resonance of this nanoparticles is dominated by LH fields. The silver nanoparticle at Point 2 is near the end of the shuriken arm also in a region of strong resonance and plasmonic fields. At this location the net *C* value is negative, suggesting that the nanoparticle resonance is dominated by RH fields. The silver nanoparticle at Point 3 is not located in a region of strong resonance or plasmonic fields. This particle is shown to weakly resonate on its own, but the net *C* values are low and near zero, suggesting that the overall net nature of the fields surrounding this nanoparticle are achiral.

Based on these simulation results, it can be inferred that nanoparticles deposited on the shuriken metafilm surface which are in close vicinity to excited resonating regions, such as nanoparticles on Point 1 and 2, experience significantly higher exposure to chiral EM fields. This exposure results in the development of a net positive or negative chiral field surrounding these nanoparticles. Conversely, nanoparticles not in the vicinity of shuriken resonating regions, such as Point 3, mostly have equal and opposite symmetry around them with a net $C \approx 0$. These findings provide further evidence to the idea that shuriken nanostructures influence the chiral characteristics of nearby achiral nanoparticles, thus modulating their EM behaviour.

Considering the approximation of a silver layer to represent silver nanoparticles and recognizing that silver is responsible for the enhanced SERS response, these EM simulations show that the nanoparticle fields are also likely to be chiral in nature when located in the proximity of the shuriken resonating regions. It is thus possible that it is these chiral plasmonic fields coupling between the gold metamaterial and silver which are responsible for the differential SERS response experimentally observed from chiral molecules.

5.3.7 Conclusion

The enantiomeric discrimination capabilities of molecules using silver sputter coated DPA samples is demonstrated using SERS. Clear differences in SERS spectra were observed for small

organic enantiomers of cysteine, methionine, thalidomide, as well as large 20 bp DNA biomolecules. This differential SERS effect was found to be dependent on the handedness of both the enantiomer and DPA shurikens. Enantiomeric discrimination was also dependent on a variety of other factors, including silver layer thickness, shuriken geometry, and Raman laser excitation wavelength. Different excitation wavelengths were found to be more suitable for chiral SERS if located in a region of resonance and optical activity.

The precise mechanism responsible for the observed chiral SERS response is challenging to determine. 4 possible theories are suggested [44]:

1. **Coupling of the silver nanoparticle dipole fields with chiral EM fields generated by the shuriken metafilm.**
   In this case, the energy of the incident photons is converted into a chiral plasmon with enhanced asymmetry by the shuriken. This energy is then transferred into the silver nanoparticles, creating silver plasmonic hotspots which are chiral in nature. Resultingly, it can be expected that deposited molecules will experience a higher degree of local circular electric field polarisation, leading to resonant differences between enantiomers – and therefore a difference in SERS intensity. This concept has also been demonstrated by Liu *et al.* who used chiral gold nanofiber metafilms to determine enantiomeric excess of a variety of molecules [5].
2. **Polarisation dependency on SERS signal.**
   Studies have shown that SERS enhancement is dependent on the direction of polarisation when using non-spherical nanostructures [45]. If the shuriken structures induce an overall chiral polarisation on the deposited analytes scattering tensor, the Raman coefficient is expected to change. Thus, this effect is similar to that of the case with HNPs and BPDT, where certain enantiomer and shuriken combinations lead to higher or lower scattering. This additional induced molecular polarisation has been shown to increase SERS intensity by a factor of $10 - 10^2$ [46], which coincides well with the experimental data.
3. **Chirality transfer between achiral silver nanoparticles and chiral dielectric cysteine layer.**
   This assumes that chirality is conveyed by the surrounding molecular cysteine layer to the achiral silver plasmon. This effect was demonstrated by Abdulrahman *et al*, who

showed how chiroptical behaviour can be induced by coupling between achiral metallic nanoparticles and an isotropic chiral layer of flavin mononucleotide [47]. This phenomenon can then be enhanced through the coupling with chiral near fields generated by the DPA shurikens.

4. **Differential shifts of plasmonic resonances.**
   The addition of chiral analytes to the DPA surface is expected to induce differential shifting of the plasmonic resonance, which may or may not be apparent in far field optical measurements. These changes in resonance positions would mean that the excitation laser used would be more aligned with one resonance over the other, leading to differential SERS intensities.

The extent to which each proposed mechanism is responsible for the chirally dependent SERS effect is uncertain and is likely to be influenced by the simultaneous interaction of multiple mechanisms working synergistically. Further theoretical and experimental research is required to fully elucidate the mechanism(s) of the observed phenomena. However, with respect to experimental applicability, it is clear that the silver coated DPA samples enable enantioselective SERS measurements. SERS measurements can be performed using standard Raman spectrometers and without the need of more complex and expensive ROA equipment. Furthermore, the disposable aspect of DPAs allows for the scalable production of multiple samples at low cost.

5.4 References

1. Ross, B.M., S. Tasoglu, and L.P. Lee. *Plasmon resonance differences between the near- and far-field and implications for molecular detection*. in *Plasmonics: Metallic Nanostructures and Their Optical Properties VII*. 2009. SPIE.
2. Tabouillot, V., et al., *Near-Field Probing of Optical Superchirality with Plasmonic Circularly Polarized Luminescence for Enhanced Bio-Detection.* ACS photonics, 2022. **9**(11): p. 3617-3624.
3. Hajji, M., et al., *Chiral Quantum Metamaterial for Hypersensitive Biomolecule Detection.* ACS nano, 2021. **15**(12): p. 19905-19916.
4. Pettinger, B., et al., *Tip-enhanced Raman spectroscopy: near-fields acting on a few molecules.* Annual review of physical chemistry, 2012. **63**: p. 379-399.
5. Liu, Z., et al., *Enantiomeric Discrimination by Surface-Enhanced Raman Scattering–Chiral Anisotropy of Chiral Nanostructured Gold Films.* Angewandte Chemie, 2020. **132**(35): p. 15338-15343.
6. Sukmanee, T., et al., *Distinguishing Enantiomers by Tip-Enhanced Raman Scattering: Chemically Modified Silver Tip with an Asymmetric Atomic Arrangement.* Angewandte Chemie International Edition, 2020. **59**(34): p. 14564-14569.
7. Zhang, W., et al., *Plasmonic chiral metamaterials with sub-10 nm nanogaps.* ACS nano, 2021. **15**(11): p. 17657-17667.
8. Lee, H.-E., et al., *Amino-acid-and peptide-directed synthesis of chiral plasmonic gold nanoparticles.* Nature, 2018. **556**(7701): p. 360-365.
9. Lee, H.-E., et al., *Cysteine-encoded chirality evolution in plasmonic rhombic dodecahedral gold nanoparticles.* Nature communications, 2020. **11**(1): p. 1-10.
10. Ahn, H.-Y., et al., *Extended gold nano-morphology diagram: synthesis of rhombic dodecahedra using CTAB and ascorbic acid.* Journal of Materials Chemistry C, 2013. **1**(41): p. 6861-6868.
11. Dahmen, C., B. Schmidt, and G. von Plessen, *Radiation damping in metal nanoparticle pairs.* Nano letters, 2007. **7**(2): p. 318-322.
12. Pelton, M. and G.W. Bryant, *Introduction to metal-nanoparticle plasmonics*. 2013: John Wiley & Sons.
13. Kneipp, K., et al., *Surface-enhanced Raman scattering and biophysics.* Journal of Physics: Condensed Matter, 2002. **14**(18): p. R597.
14. Xu, H., et al., *Unified treatment of fluorescence and Raman scattering processes near metal surfaces.* Physical review letters, 2004. **93**(24): p. 243002.
15. Xiao, T.-H., et al., *All-dielectric chiral-field-enhanced Raman optical activity.* Nature communications, 2021. **12**(1): p. 3062.
16. D'Orazio, G., et al., *Chiral separations in food analysis.* TrAC Trends in Analytical Chemistry, 2017. **96**: p. 151-171.
17. H Brooks, W., W. C Guida, and K. G Daniel, *The significance of chirality in drug design and development.* Current topics in medicinal chemistry, 2011. **11**(7): p. 760-770.
18. Ye, J., et al., *Enantioselectivity in environmental risk assessment of modern chiral pesticides.* Environmental Pollution, 2010. **158**(7): p. 2371-2383.
19. Barron, L.D., *The development of biomolecular Raman optical activity spectroscopy.* Biomedical Spectroscopy and Imaging, 2015. **4**(3): p. 223-253.

20. Keiderling, T.A., *Structure of condensed phase peptides: Insights from vibrational circular dichroism and Raman optical activity techniques.* Chemical reviews, 2020. **120**(7): p. 3381-3419.
21. Lee, Y.Y., et al., *Plasmonic metamaterials for chiral sensing applications.* Nanoscale, 2020. **12**(1): p. 58-66.
22. Ostovar Pour, S., et al., *Through-space transfer of chiral information mediated by a plasmonic nanomaterial.* Nature Chemistry, 2015. **7**(7): p. 591-596.
23. Baranska, M. and K. Chruszcz-Lipska, *Raman optical activity: a powerful technique to investigate essential oil components.* Natural Product Communications, 2010. **5**(9): p. 1934578X1000500914.
24. Born, M. and E. Wolf, *Principles of optics: electromagnetic theory of propagation, interference and diffraction of light*. 2013: Elsevier.
25. Efrima, S., *Raman optical activity of molecules adsorbed on metal surfaces: theory.* The Journal of chemical physics, 1985. **83**(3): p. 1356-1362.
26. Depla, D., S. Mahieu, and J. Greene, *Sputter deposition processes*, in *Handbook of deposition technologies for films and coatings*. 2010, Elsevier. p. 253-296.
27. Jensen, L. and G.C. Schatz, *Resonance Raman scattering of rhodamine 6G as calculated using time-dependent density functional theory.* The Journal of Physical Chemistry A, 2006. **110**(18): p. 5973-5977.
28. Pristinski, D., et al., *In situ SERS study of Rhodamine 6G adsorbed on individually immobilized Ag nanoparticles.* Journal of Raman Spectroscopy: An International Journal for Original Work in all Aspects of Raman Spectroscopy, Including Higher Order Processes, and also Brillouin and Rayleigh Scattering, 2006. **37**(7): p. 762-770.
29. Goel, R., et al., *Design of Polarization Independent SERS Substrate with Raman Gain Evaluated Using Purcell Factor.* Plasmonics, 2021. **16**(4): p. 1365-1373.
30. Goetz, S., et al., *Ultrathin sputter-deposited plasmonic silver nanostructures.* Nanoscale Advances, 2020. **2**(2): p. 869-877.
31. Giessibl, F.J., *Advances in atomic force microscopy.* Reviews of modern physics, 2003. **75**(3): p. 949.
32. Thomas, T., *Characterization of surface roughness.* Precision Engineering, 1981. **3**(2): p. 97-104.
33. Alajtal, A., et al., *The effect of laser wavelength on the Raman Spectra of phenanthrene, chrysene, and tetracene: Implications for extra-terrestrial detection of polyaromatic hydrocarbons.* Spectrochimica Acta Part A: Molecular and Biomolecular Spectroscopy, 2010. **76**(1): p. 1-5.
34. Yang, S., et al., *Laser wavelength dependence of background fluorescence in Raman spectroscopic analysis of synovial fluid from symptomatic joints.* Journal of Raman spectroscopy, 2013. **44**(8): p. 1089-1095.
35. Scimeca, M., et al., *Energy Dispersive X-ray (EDX) microanalysis: A powerful tool in biomedical research and diagnosis.* European journal of histochemistry: EJH, 2018. **62**(1).
36. Chauhan, A. and P. Chauhan, *Powder XRD technique and its applications in science and technology.* J Anal Bioanal Tech, 2014. **5**(5): p. 1-5.
37. Bunaciu, A.A., E.G. UdriŞTioiu, and H.Y. Aboul-Enein, *X-ray diffraction: instrumentation and applications.* Critical reviews in analytical chemistry, 2015. **45**(4): p. 289-299.

38. Pope, C.G., *X-ray diffraction and the Bragg equation.* Journal of chemical education, 1997. **74**(1): p. 129.
39. Clough, R.W. *Finite element stiffness matricess for analysis of plate bending*. in *Proc. of the First Conf. on Matrix Methods in Struct. Mech.* 1965.
40. Klug, A., *The discovery of the DNA double helix.* Journal of molecular biology, 2004. **335**(1): p. 3-26.
41. Deng, H., et al., *Dependence of the Raman signature of genomic B-DNA on nucleotide base sequence.* Biopolymers: Original Research on Biomolecules, 1999. **50**(6): p. 656-666.
42. Wu, C.Y., et al., *Surface enhanced Raman spectra of oligonucleotides induced by spermine.* Journal of Raman Spectroscopy: An International Journal for Original Work in all Aspects of Raman Spectroscopy, Including Higher Order Processes, and also Brillouin and Rayleigh Scattering, 2006. **37**(8): p. 799-807.
43. Tang, Y. and A.E. Cohen, *Optical chirality and its interaction with matter.* Physical review letters, 2010. **104**(16): p. 163901.
44. Guselnikova, O., et al., *Coupling of plasmonic hot spots with shurikens for superchiral SERS-based enantiomer recognition.* Nanoscale Horizons, 2023. **8**(4): p. 499-508.
45. Ko, H., S. Singamaneni, and V.V. Tsukruk, *Nanostructured surfaces and assemblies as SERS media.* Small, 2008. **4**(10): p. 1576-1599.
46. Alessandri, I. and J.R. Lombardi, *Enhanced Raman scattering with dielectrics.* Chemical reviews, 2016. **116**(24): p. 14921-14981.
47. Abdulrahman, N.A., et al., *Induced chirality through electromagnetic coupling between chiral molecular layers and plasmonic nanostructures.* Nano letters, 2012. **12**(2): p. 977-983.

Chapter 6 - Summary and Outlook

This thesis has presented the applicability of high-throughput injection moulded DPAs for both biosensing and Raman spectroscopy purposes. This final chapter will summarise the presented results, as well as consider possible future prospects for these DPA applications.

6.1 DPAs for Biosensing

Chapter 4 of this thesis highlights the versatility of DPA surface functionalisation techniques in numerous biosensing experiments. Initial experiments focused on biotin-streptavidin interactions, providing valuable insights into the optimal concentrations of SAMs to minimize non-specific binding and the $\Delta\lambda$ values achieved upon binding streptavidin, a protein with a molecular weight of approximately 55 kDa. At this stage, it was observed that the introduction of chiral proteins did not result in significant observable $\Delta\Delta\lambda$. This lack of asymmetry can be attributed to factors such as the disordered orientation of bound proteins, leading to an overall isotropic protein layer, and the unavoidable collection of light from multiple angles, which leads to changes in ORD spectrum shape, as demonstrated by EM simulations. Additionally, the deformation of the envelope structure in the case of virus particles could also contribute to the absence of useful asymmetry measurements in virus experiments. Despite these limitations, DPAs still exhibited high refractive index sensitivity and ORD responses suitable for biosensing applications.

Building upon the biotin-streptavidin experiments, the chapter progressed to utilise NTA SAMs to bind his-tagged streptavidin and COVID-19 S1 proteins simultaneously on a single DPA sample, enabling the first multiplexing experiment for the detection of both streptavidin and S1 antibody targets. This experiment successfully detected both antibodies with minimal non-specific binding interactions. However, the expensive cost of NTA-PEG thiols and histidine tag requirement renders this functionalisation strategy unsuitable for large-scale production and commercial use.

To overcome the limitations associated with his-tagged proteins and NTA SAMs, and to avoid virus lysing reagent requirements, $F(ab')_2$ antibody fragments mixed with spacer thiols were explored as a method to create a DPA sensor capable of detecting whole inactivated SARS-CoV-

2 virus particles. The large size of the virions facilitated significant ORD resonance shifts, over 6 nm for Peak 2, even after sample rinsing, confirming the specific binding of virus particles.

In addition to $F(ab')_2$ antibody fragments as target binders, the use of cysteine-tagged Protein A/G was explored as an alternative method for antibody binding and the detection of whole virus particles. Using this methodology, fewer experimental steps for antibody binding are required. The multiplexing experiment carried out with Zika and norovirus antibodies were able to distinguish between applied live Zika virus and norovirus VLPs.

To expand the multiplexing capabilities of DPAs, future work aims to develop these sensors for large target screening assays in analytical laboratories or point-of-care diagnostics, particularly for the detection of major respiratory viruses. However, a key challenge lies in enhancing DPA sensitivity. Clinical respiratory samples from SARS-CoV-2 infected individuals were found to contain a wide range of viral loads, spanning from 641 to 1.34×10^{11} pfu (virus copies) mL^{-1} [1]. Considering that the sample concentration tested with DPA samples was approximately 3×10^{5} pfu mL^{-1}, it is unlikely that the current sensitivity would enable the detection of infections at lower viral load ranges. Various strategies, such as the use of nanocatalysts, sample concentration techniques, and fluid mixing, can enhance the sensitivity of optical biosensors, but each method carries its own drawbacks [2]. Therefore, careful consideration must be given to selecting the optimal sensitivity enhancement technique while maintaining the high-throughput, low reagent, and reduced experimental steps requirements that DPAs currently offer.

Another area of improvement lies in the optimisation of the Protein A/G functionalisation methodology for various viruses. The ORD resonance shift values were significantly lower compared to those received from the SARS-CoV-2 virus experiment. To improve upon this, several factors can be investigated, such as reagent concentrations, incubation times, temperature conditions, pH, buffers, and spacer to Protein A/G ratios. All these variables can be altered, with the ultimate objective being that of a well-orientated antibody layer while minimising steric hindrance effects. Such conditions have been shown to be the most advantageous for biosensing purposes [3, 4].

In a study by Kausaite-Minkstimiene *et al*, this was demonstrated by comparing the human growth hormone antibody (anti-HGH) binding activity in two cases [3]: The first approach used EDC/NHS conjugation chemistry to directly link anti-HGH to a carboxy-terminated 11-

mercaptoundecanoic SAM. The second by using EDC/NHS conjugation to first link Protein G to the SAM, followed by the introduction of anti-HGH. They discovered that the direct conjugation of anti-HGH without Protein G led to higher surface concentrations of antibodies, but more random antibody orientation, leading to diminished antigen binding capacity. On the other hand, by employing Protein G antibody surface coverage was lower, but had better orientation and therefore more antibody activity. In light of these findings, it is possible that the Protein A/G with a cysteine terminus used in this thesis has reduced antibody affinity. This could be attributed to the cysteine linker's inadequacy in distancing the protein from the gold surface, leading to a degree of detrimental conformational changes and deformation [5]. Future work using Protein A/G on DPA samples can explore the EDC/NHS conjugation avenue to monitor whether antibody conjugation is improved.

Virus biosensing experiments were concluded by calculating an estimated LoD value for the Protein A/G and anti-Zika virus antibody system used to detect Zika virus. This was performed by constructing a concentration curve by using functionalised DPA samples to measure several different concentrations of Zika virus. From the curve, the LoD value was obtained using the initial linear dependency of Zika virus concentration on ORD resonance shift.

In the final section of Chapter 4, EDC/NHS and maleimide chemistry was used to create the basis of a haptoglobin biosensor by functionalising the DPA surface with haemoglobin. Testing various haptoglobin concentrations produced a concentration curve which provided insights into DPA sensitivity and dynamic range. It should be noted that these parameters will be change if using different proteins. The benefit of EDC/NHS functionalisation is that virtually any protein with free lysine residues can be conjugated to the gold surface. This allows for potential future work to investigate other protein-protein interactions, particularly for proteins released during inflammation. For example, Alpha-1 antitrypsin (A1AT) is a glycoprotein which binds to neutrophil elastase, which is an enzyme released during inflammation by immune cells and capable of causing tissue damage [6].

Another key objective to focus on for future experiments using the EDC/NHS conjugation methodology would be to improve upon protein conjugation rates to achieve a homogeneous protein layer on the DPA surface. One way of accomplishing this would be to develop a microfluidic system, which would enhance the kinetics of the conjugation reactions [7].

In addition to sensitivity enhancement, future work may involve the development of a more complex fluidic chamber system that allows for the multiplexing of more than four antigen targets on DPA samples. This requires designing of a new DPA layout with increased spacing between array locations to accommodate the flow of functionalisation solutions adequately. Furthermore, modifications to the imaging polarimetry microscope optics are necessary to create a larger field of view, enabling the imaging of greater DPA areas.

In conclusion, the biosensing work presented in this thesis establishes a novel technological platform that bridges the gap between research and in-field applications, with the potential to significantly contribute to modern diagnostics and precision medicine. The versatility and capabilities of DPAs, despite certain limitations, lay the foundation for further advancements in biosensing technology using plasmonic nanostructures.

6.2 DPAs for SERS

6.2.1 DPAs and HNPs

In Chapter 5 of this thesis, the Raman and SERS applications of DPAs were explored. The first results section of this chapter, Section 5.2, utilised chiral HNPs linked to DPA samples to investigate the differential Raman response of the achiral linker BPDT reporter molecules. The areas in between that of the HNPs and shuriken were found to have EM strengths that were dependent on the symmetry combinations of HNP and DPA shuriken, with LL and RR matching combinations supporting stronger fields, and thus higher SERS intensities, as opposed to mismatched LR and RL combinations. By analysing the Raman peak intensity ratios among the HNP and DPA combinations, it was determined that matched combinations exhibited an average intensity approximately twice as high. These findings were supported using numerical EM simulations of all symmetry combinations. These simulations enabled the calculation of electric field strengths within the resonating regions between L- or D-HNP and LH or RH DPA shurikens. The electric field strength values, while obtained from idealised models, supported the hypothesis that the different diastereomeric HNP and DPA shuriken pairs possess different EM near field environments.

Using this strategy, the rapid recognition of chiral nanoparticles can be performed using a simple Raman spectrometer with small sample quantities. The ability to create and control the strength

of near field environments may also find use in other applications, such as the development of plasmonic nanoantennas [8]. Future work may look to employ this SERS based strategy with chiral compounds instead of HNPs, as these would also influence changes in the local near fields of the DPA substrates. Other interesting research topics might involve the use other chiral nanoparticle geometries and dithiol reporters. Additionally, the manufacture of chiral metamaterials with resonances exactly at Raman laser wavelengths would provide more insight on whether the chiral SERS effect can be amplified with enhanced light-matter interactions and higher optical activity.

6.2.2 DPAs and Chiral Molecules

Finally, in the second half of Chapter 5, the focus shifted to using SERS for the enantiomeric discrimination of molecules. To achieve this with DPAs, a sputter coated layer of silver was required to increase the DPA SERS EFs for adequate Raman signals. Different sputter coating times were tested to discover the optimal thickness at which SERS efficiency from the R6G Raman reporter was maximised, with the optimum silver layer thickness being 1.3 nm. The measured optical properties from the silver coated DPA samples indicated that no major changes in resonance properties, indicating that the chiroptical properties of the DPA shurikens were largely unaffected. Through analysis of the optical spectra, it was possible to infer the Raman laser wavelengths which coincide with regions exhibiting optical activity and absorption. This allowed for the prediction of which excitation wavelengths the chiral SERS effect would be manifested.

The primary emphasis of the experiment focused on the SERS measurements of cysteine enantiomers spin coated onto DPA substrates, which displayed clear Raman intensity dependency on the enantiomer and DPA shuriken handedness. This effect was shown for several cysteine spin coating solution concentrations using 780 nm laser excitation, ranging from $10^{-8} - 10^{-4}$ M. SERS mapping images were also able to visually determine intensity differences of the cysteine characteristic Raman band 1044 cm^{-1} between coated LH and RH DPA shuriken arrays. Investigating other common and available Raman laser wavelengths, the chiral SERS effect was only observed with the 633 nm laser. The 532 nm laser did not show any observable Raman signal, and while the 830 nm laser did provide appreciable Raman spectra, there was no significant difference between LH and RH DPA measurements.

The chiral SERS effect was also demonstrated with other chiral compounds of methionine and thalidomide, as well as the large biomolecule of DNA. In all cases, the chiral EM fields created by the DPA shurikens couple and interact differentially with the applied molecular enantiomers, leading to the same chiral SERS effect as observed with cysteine and BPDT with HNPs.

EM simulations were performed to investigate the interaction of chiral EM fields with representative idealised silver nanoclusters, which were approximated as hemispheres on the DPA simulation surface. Results showed that the silver does indeed couple with the chiral EM fields generated by the DPA shurikens. This was shown by measuring the optical chirality parameter, *C*, values from different locations. Silver nanoparticles which were located near the resonating regions of the simulated shuriken were found to possess an unequal distribution of LH or RH chiral fields, suggesting that the resonating fields which lead to SERS enhancement are likely to be chiral in nature.

The proposed mechanism(s) for this effect were discussed, and it was concluded that the chiral SERS intensity dependence most likely arises from the synergistic combination of several mechanisms. One of the main challenges in determining which mechanism is most responsible lies in determining whether it is the superchiral fields interacting differentially with the enantiomers, or the differential changes in plasmonic resonances induced by the enantiomers which lead to the chiral SERS effect.

Future work regarding enantiomeric discrimination using chiral metamaterials could look to creating designs with resonance positions at the 780 nm Raman laser wavelength, as evidence presented here suggests this would maximise the chiral SERS effect. Furthermore, designs can be altered to include nanogaps, which would create plasmonic hotspots capable of producing strong SERS signals [9]. This would retain the chiral field characteristics as well as circumvent the need for silver sputter coating. Another way of increasing SERS enhancement without relying on sputter coating would be to electrochemically roughen the DPA gold surface. This can be accomplished by cycling the potential of the gold surface in an ionic solution, such as KCl [10, 11].

Investigating the chiral SERS effect with other large biomacromolecules would also be an interesting avenue. Only one handedness of DNA was used in this work, and to fully confirm the chiral response the other LH, or “Z-DNA” should be trialled [12]. In addition to DNA, other

chiral macromolecules, such as proteins, can be investigated. While performing Raman spectroscopy on proteins can be challenging, due to their relatively large and complex structures, Raman has proven useful for the analysis and understanding of protein structure and conformational changes [13]. By utilising DPA samples as SERS substrates, the chiral nature of proteins can also be probed, as certain Raman signals may be more (or less) evident based on the nanostructure handedness. To accomplish this however, SERS measurements should be performed in solutions in which proteins maintain their native conformations, which would require design of optimisation of experimental conditions.

To investigate the extent to which mechanism leads to the observed chiral SERS effect, one method would be to remove plasmonics from the equation by creating superchiral fields without metal substrates. This can be accomplished utilising the methodology proposed by Tang and Cohen in their first study describing superchiral light [14]. By simply using an imperfect mirror, the reflection of left CPL at normal incidence leads to reflected right CPL with the same frequency and phase, but with slightly lower amplitude. At certain distances above the mirror surface, standing waves with enhanced chiral asymmetry are created. A thin film of chiral molecules can then be localised on the mirror surface to study the change in chiroptical interactions. From such a substrate, Raman measurements could be taken to investigate the chiral SERS (or this case Raman) effect without plasmonic substrates or changes in resonance conditions.

In conclusion, chiral SERS dependency was demonstrated with both HNPs as well as molecular enantiomers using DPA substrates. This research introduces a pioneering approach for discriminating between chiral plasmonic systems, while also extending the scope of DPA utility for discriminating between enantiomers.

6.3 References

1. Pan, Y., et al., *Viral load of SARS-CoV-2 in clinical samples.* The Lancet infectious diseases, 2020. **20**(4): p. 411-412.
2. Kim, Y., J. Gonzales, and Y. Zheng, *Sensitivity-Enhancing Strategies in Optical Biosensing.* Small, 2021. **17**(4): p. 2004988.
3. Kausaite-Minkstimiene, A., et al., *Comparative study of random and oriented antibody immobilization techniques on the binding capacity of immunosensor.* Analytical chemistry, 2010. **82**(15): p. 6401-6408.
4. Oh, B.-K., et al., *Immunosensor for detection of Legionella pneumophila using surface plasmon resonance.* Biosensors and bioelectronics, 2003. **18**(5-6): p. 605-611.
5. Moulin, A., et al., *Measuring surface-induced conformational changes in proteins.* Langmuir, 1999. **15**(26): p. 8776-8779.
6. Carrell, R.W., *alpha 1-Antitrypsin: molecular pathology, leukocytes, and tissue damage.* The Journal of clinical investigation, 1986. **78**(6): p. 1427-1431.
7. Asiaei, S., B. Smith, and P. Nieva, *Enhancing conjugation rate of antibodies to carboxylates: Numerical modeling of conjugation kinetics in microfluidic channels and characterization of chemical over-exposure in conventional protocols by quartz crystal microbalance.* Biomicrofluidics, 2015. **9**(6).
8. Schnell, M., et al., *Controlling the near-field oscillations of loaded plasmonic nanoantennas.* Nature Photonics, 2009. **3**(5): p. 287-291.
9. Zhang, W., et al., *Plasmonic chiral metamaterials with sub-10 nm nanogaps.* ACS nano, 2021. **15**(11): p. 17657-17667.
10. Abdelsalam, M.E., et al., *Electrochemical SERS at a structured gold surface.* Electrochemistry Communications, 2005. **7**(7): p. 740-744.
11. Tian, Z.-Q., B. Ren, and D.-Y. Wu, *Surface-enhanced Raman scattering: from noble to transition metals and from rough surfaces to ordered nanostructures*. 2002, ACS Publications. p. 9463-9483.
12. Herbert, A. and A. Rich, *The Biology of Left-handed Z-DNA (∗).* Journal of Biological Chemistry, 1996. **271**(20): p. 11595-11598.
13. Kuhar, N., S. Sil, and S. Umapathy, *Potential of Raman spectroscopic techniques to study proteins.* Spectrochimica Acta Part A: Molecular and Biomolecular Spectroscopy, 2021. **258**: p. 119712.
14. Tang, Y. and A.E. Cohen, *Enhanced enantioselectivity in excitation of chiral molecules by superchiral light.* Science, 2011. **332**(6027): p. 333-336.

Appendix A – Trigonometric Identities

The two trigonometric identities used to convert Equation 2.7.8 into Equation 2.7.9 are:

1. $\cos(2\pi\nu_0 t)\cos(2\pi\nu_{vib}t) = \cos(2\pi\nu_0 t + 2\pi\nu_{vib}t) + \sin(2\pi\nu_0 t)\sin(2\pi\nu_{vib}t)$
2. $\cos(2\pi\nu_0 t)\cos(2\pi\nu_{vib}t) = \cos(2\pi\nu_0 t - 2\pi\nu_{vib}t) - \sin(2\pi\nu_0 t)\sin(2\pi\nu_{vib}t)$

Summing these identities together:

$$\begin{aligned} 2\cos(2\pi\nu_0 t)\cos(2\pi\nu_{vib}t) &= \cos(2\pi\nu_0 t + 2\pi\nu_{vib}t) + \\ &\quad + \sin(2\pi\nu_0 t)\sin(2\pi\nu_{vib}t) \\ &\quad + \cos(2\pi\nu_0 t - 2\pi\nu_{vib}t) - \sin(2\pi\nu_0 t)\sin(2\pi\nu_{vib}t) \\ &= \cos(2\pi\nu_0 t + 2\pi\nu_{vib}t) + \cos(2\pi\nu_0 t - 2\pi\nu_{vib}t) \\ &= \cos[2\pi(\nu_0 + \nu_{vib})t] + \cos[2\pi(\nu_0 - \nu_{vib})t] \\ &\rightarrow \cos(2\pi\nu_0 t)\cos(2\pi\nu_{vib}t) \\ &= \frac{1}{2}[\cos(2\pi(\nu_0 + \nu_{vib})t) + \cos(2\pi(\nu_0 - \nu_{vib})t)] \end{aligned} \qquad (A.1)$$

These two identities were applied to Equation 2.7.8, which is reiterated here (Equation A.2):

$$P = \alpha_0 E_0 \cos(2\pi\nu_0 t) + \frac{\partial\alpha}{\partial Q} Q_0 E_0 \cos(2\pi\nu_0 t)\cos(2\pi\nu_{vib}t) \qquad (A.2)$$

Which lead to the final equation describing Raman scattering (Equation A.3):

$$P = \alpha_0 E_0 \cos(2\pi\nu_0 t) + \left(\frac{\partial\alpha}{\partial Q}\frac{Q_0 E_0}{2}\right)\{cos[2\pi(\nu_0 - \nu_{vib})t] + \cos[2\pi(\nu_0 + \nu_{vib})t]\} \qquad (A.3)$$

Appendix B – BPDT SERS

B.1 Characterisation of BPDT

The Raman spectrum and full characterisation of all BPDT characteristic peaks measured from BPDT SAM functionalised DPA samples are presented in Figure B-1 and Table B-1, respectively.

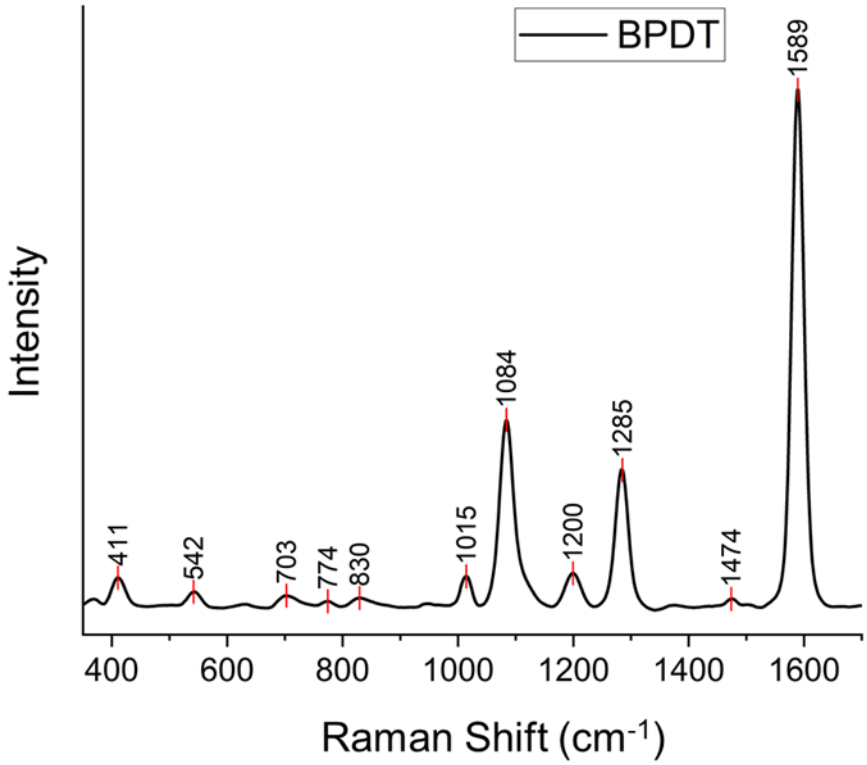

Figure B-1 Example SERS spectrum of adsorbed BPDT collected from gold shuriken metafilm.

These Raman bands and assignments coincide well with data obtained from other studies investigating BPDT [1, 2].

BPDT SERS Spectrum	
Peak (cm^{-1})	**Assignment**
411	C-S v_{asym}
542	C-S v_{sym}
703	Out-of-plane skeletal
774	Ring deformation
830	C-H Out-of-plane
1015	Ring Deformation
1084	C_{ring}-S in-plane
1200	12 C-H in-plane
1285	Inter-ring C-C stretching
1474	C-C stretching
1589	C-C stretching

Table B-1 SERS peak positions and assignments of BPDT measured from DPA samples.

B.2 Optical Spectra from Silver Sputter Coated DPA Samples

The optical spectra from silver sputter coated DPA samples were measured from all P1-P6 regions to investigate which region would be most suitable for SERS enhancement. These spectra are presented in Figure B-2

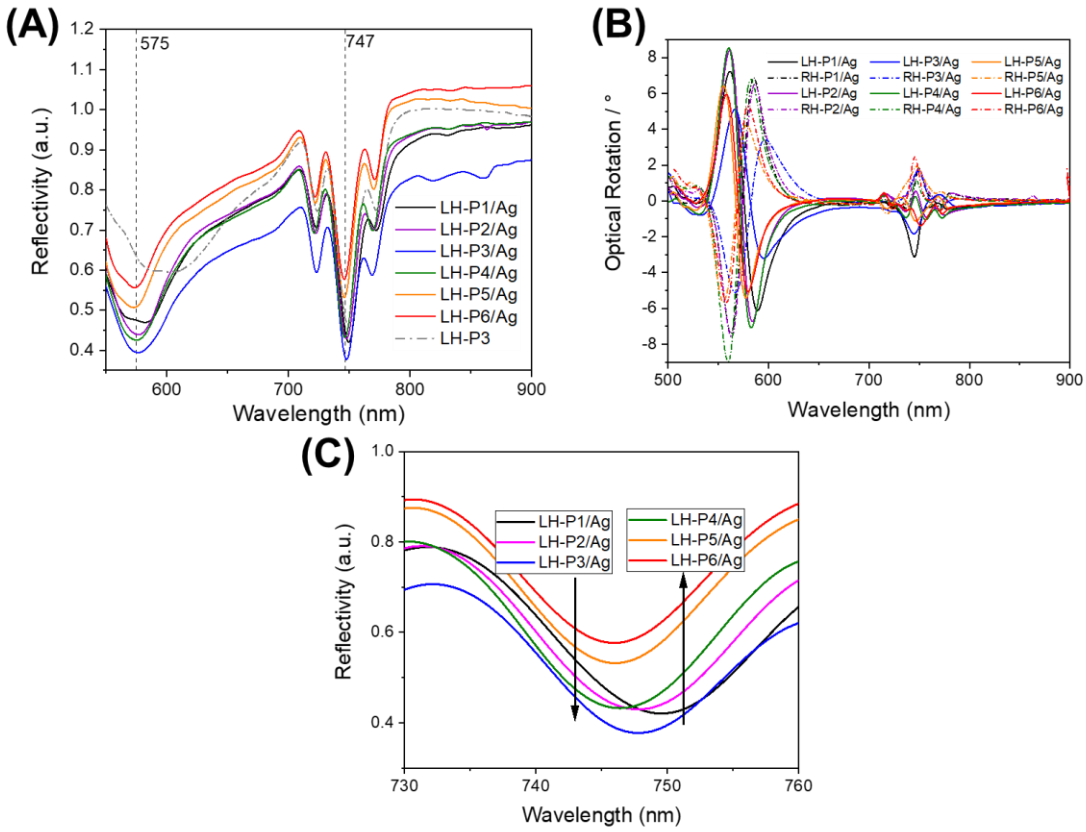

Figure B-2 (A)(C) Reflectivity and (B) ORD spectra of silver coated P1-P6 DPA samples.

The P3 region showed the most prominent change in its reflectivity spectrum following silver deposition, with the broad resonance originally around 575 nm shifting to 600 nm. Furthermore, P3 showed a distinct increase in its absorption, which would potentially lead to an increase in the EM field strengths generated.

References - Appendix

1. Ganbold, E.O. and S.W. Joo, *Raman Spectroscopy of Biphenyl-4, 4'-dithiol and p-Terphenyl-4, 4 "-dithiol on Gold Surfaces.* Bulletin of the Korean Chemical Society, 2015. **36**(3): p. 887-890.
2. Lee, Y.R., M.S. Kim, and C.H. Kwon, *Surface-Enhanced Raman Scattering and DFT Study of 4, 4'-Biphenyldithiol on Silver Surface.* Bulletin of the Korean Chemical Society, 2013. **34**(2): p. 470-474.